Universitat Politècnica de València
Departamento de Máquinas y Motores Térmicos

Analysis of hydrogen fuel cell powerplant architectures for future transport applications

Doctoral Thesis
Presented by:
Marcos López Juárez
Directed by:
Dr. Ricardo Novella Rosa

Valencia, September 12th, 2022

Doctoral Thesis

Analysis of hydrogen fuel cell powerplant architectures for future transport applications

Presented by:	Marcos López Juárez
Directed by:	Dr. Ricardo Novella Rosa

Examining Board:

President:	Prof. Jesús Vicente Benajes Calvo
Secretary:	Prof. Octavio Armas Vergel
Examiner:	Dr. Michele Bardi

Reviewing Board:

Prof. Juan José Hernández Adrover
Dr. Darío López Pintor
Dr. Michele Bardi

Valencia, September 12th, 2022

Nomenclature

Latin

$a_c L_c$	Electrode Roughness
C	Concentration/Mass Transport Loss Coefficient
di/dt	Rate of Change of the Current Density
du/dt	Rate of Change of the Control Variable
E_{act}	Activation Energy
E_b	Energy Stored in the Battery
E_b^o	Best Trajectory for the Energy Stored in the Battery
$\cdot E_b$	Rate of Change of the Energy Stored in the Battery
$ECSA_{loss}$	Percentage of ECSA loss
F	Faraday Constant
$\overline{g}_f$	Average Gibbs Free Energy of Formation
GWP_{CH_4}	CH_4 Global Warming Potential Index
GWP_{CO_2}	CO_2 Global Warming Potential Index
GWP_{N_2O}	N_2O Global Warming Potential Index
H	Hamiltonian Function
i	Current Density
i_0	Exchange Current Density
$i_{0,ref}$	Reference Exchange Current Density
i_{hp}	Minimum Current Density with High-power Degradation
i_l	Limiting Current Density
i_{lp}	Maximum Current Density with Low-power Degradation
i_{min}	Minimum Current Density
i_{ref}	Reference Current Density
I	Current
J	Cost Function
L_1	Limiting Function 1

L_2	Limiting Function 2
m_{CH_4}	CH_4 mass emissions
m_{CO_2}	CO_2 mass emissions
m_{N_2O}	N_2O mass emissions
n_{lc}	Number of Load-change Cycles
n_{ss}	Number of Start-stop Cycles
$\dot{n}_{O_2}$	Oxygen molar flux
p_{cath}	Cathode Pressure
p_{O_2}	Oxygen Partial Pressure
$p_{O_2,ref}$	Reference Oxygen Partial Pressure
p_{sat}	Water Saturation Pressure
P_{batt}	Battery Power Output
P_b	Rate of Change of the Energy Stored in the Battery
P_{dem}	E-motor Power Demand
P_f	Fuel Output
P_{FC}	Fuel Cell Stack Power Output
$P_{FC,deg}$	Degraded Fuel Cell Stack Power Output
P_{FC1}	Fuel Cell Stack 1 Power Output
P_{FC2}	Fuel Cell Stack 2 Power Output
r_{Pt}	Pt Grain Radius
R_{ohm}	Ohmic Resistance
R_{gas}	Ideal Gas Constant
RH	Relative Humidity
RH_{an}	Anode Relative Humidity
RH_{cath}	Cathode Relative Humidity
$\overline{RH}$	Average Relative Humidity
SUV	Sport Utility Vehicle
t	Time
t_0	Initial Time
t_f	Final Time
t_m	Membrane Thickness
T	Temperature
T_{cell}	Cell Temperature
T_{cath}	Cathode Temperature
T_{FC}	Fuel Cell Stack Temperature
T_{ref}	Reference Temperature
u	Control Variable

u_1	Control Variable for FCS 1
u_2	Control Variable for FCS 2
u^o	Best Trajectory for the Control Variable
V_{act}	Activation Voltage Loss
V_{conc}	Concentration/Mass Transport Voltage Loss
V_{deg}	Fuel Cell Degraded Voltage
V_{FC}	Fuel Cell Voltage
V_{loss}	Percentage of Voltage Loss due to ECSA loss
V_{OC}	Open Circuit Voltage
V_{ohm}	Ohmic Voltage Loss
w	Water Content
X	Cost of a 120 kW FCS
X_{H_2O}	Water Vapor Mole Fraction

Greek

γ_c	Pressure dependency factor
δ	Fuel Cell Stack Voltage Loss Ratio
δ_{hp}	High-power Voltage Loss Ratio
δ_i	Initial Fuel Cell Stack Voltage Loss Ratio
δ_{lc}	Load-change Fuel Cell Stack Voltage Loss Ratio
δ_{lp}	Low-power Fuel Cell Stack Voltage Loss Ratio
δ_{nt}	Natural Fuel Cell Stack Voltage Loss Ratio
δ_{ss}	Start-stop Voltage Loss Ratio
ϵ_1	ECSA Calculation Constant Coefficient
η	Relative Humidity Scaling Function
η_{FCS}	Fuel Cell System Efficiency
λ	Dimensionless Co-state
λ^o	Best Trajectory for the Dimensionless Co-state
$\cdot\lambda$	Rate of Change of the Dimensionless Co-state
λ_{cath}	Cathode Stoichiometry
ρ_{Pt}	Platinum Density
ξ_X	Electrochemical Phenomena Scaling Function under X Condition
σ	Membrane Ionic Conductivity
σ_{30}	Membrane Ionic Conductivity at 30°C
τ	Temperature Scaling Function

Acronyms and abbreviations

0D	Zero-dimensional
1D	One-dimensional
ACL	Anode Catalyst Layer
ADR	Assembly, Disposal and Recycling
BEV	Battery-Electric Vehicle
BoP	Balance of Plant
CCL	Cathode Catalyst Layer
CCS	Carbon Capture and Storage
CDCS	Charge Depleting Charge Sustaining
CH_4	Methane
CO_2	Carbon Dioxide
DC	Direct Current
DoE	Department of Energy
e_-	Electron
ECSA	Electrochemical Surface Area
EPSA	Effective Platinum Surface Area
EMS	Energy Management Strategy
EOL	End of Life
FC	Fuel Cell
FCH JU	Fuel Cells and Hydrogen Joint Undertaking
FCREx	Fuel Cell Range-Extender
FCS	Fuel Cell System
FCV	Fuel Cell Vehicle
FCV1	Reference Fuel Cell Vehicle 1
FCV2	Reference Fuel Cell Vehicle 2
FRR	Fluoride Release Rate
GDL	Gas Diffusion Layer
GHG	Greenhouse Gas
GHG-100	Greenhouse Gas with 100 year horizon effect
GWP	Global Warming Potential
H_2	Hydrogen
H_2O	Water
H^+	Hydrogen Atom or Proton
HDDT	Heavy-Duty Diesel Truck
HDV	Heavy-Duty Vehicle
ICE	Internal Combustion Engine
ICEV	Internal Combustion Engine Vehicle

IPCC	Intergovernmental Panel on Climate Change
LCA	Life Cycle Assessment
LCI	Life Cycle Inventory
LCV	Light-Commercial Vehicle
LDV	Light-Duty Vehicle
MEA	Membrane Electrode Assembly
N_2	Nitrogen
N_2O	Nitrous Oxide
NMC	Nickel Manganese Cobalt Oxide
NO_X	Nitrogen Oxides
PEMFC	Proton-Exchange Membrane Fuel Cell
O_2	Oxigen
OC	Optimal Control
PM	Particulate Matter
Pt	Platinum
PMP	Pontryagin's Minimum Principle
PR	Pressure Ratio
RMS	Root Mean Square
SDG	Sustainable Development Goals
SMR	Steam Methane Reforming
SOC	State of Charge
SOFC	Solid-Oxide Fuel Cell
TCO	Total Cost of Ownership
UN	United Nations
US	United States
TRL	Technology Readiness Level
WLTC	World Harmonized Light-duty Vehicle Test Cycle
WLTP	World Harmonized Light-duty Vehicle Test Procedure

Resumen. A la luz de la crisis medioambiental y del creciente interés en el uso del H_2 para avanzar hacia la Economía del Hidrógeno, esta tesis tiene como objetivo analizar y optimizar nuevas arquitecturas de sistemas propulsivos de FCV para aplicaciones en turismos y vehículos pesados en términos de rendimiento, durabilidad e impacto medioambiental. Para ello, se ha desarrollado una plataforma de modelado de FCV multifísica y flexible que integra un modelo de pila de combustible validado junto con los componentes del BoP, los componentes mecánicos y eléctricos del vehículo y el sistema propulsivo, un modelo de degradación de FC semi-empírico informado por tendencias físicas diseñado para ser utilizado en condiciones de conducción y un optimizador de EMS en tiempo real que ofrece el mejor rendimiento dado un diseño de sistema propulsivo y un ciclo de conducción, de tal forma que todas las arquitecturas propuestas para una aplicación determinada sean comparables en términos justos.

La discusión de los resultados puede dividirse en tres partes diferentes. La primera está orientada a la optimización del rendimiento del FCS. Los resultados de esta parte ayudaron a identificar la estrategia de gestión del aire que, dado un conjunto de restricciones impuestas en los componentes del BoP, maximizaba la potencia neta del FCS (eficiencia) para cada valor de densidad de corriente. El balance energético resultante, que comprende la potencia producida por la pila de combustible, las pérdidas electroquímicas y el consumo de los componentes del BoP, fue analizado y utilizado para determinar y diseñar la estrategia de control de los actuadores del BoP para condiciones de conducción.

La segunda parte se centra en la evaluación y optimización, cuando es posible, de la arquitectura FCREx para aplicaciones de turismos y la configuración multi-FCS para aplicaciones de vehículos de transporte pesado. Desde el punto de vista del rendimiento, la arquitectura FCREx ofrecía un consumo mínimo de H_2 con una elevada potencia de la pila de combustible y una gran capacidad de la batería, pero este diseño podría ser prohibitivo en términos de costes. Podía ofrecer hasta un 16.8-25% menos de consumo de H_2 y un 6.8% menos de consumo de energía. La limitación en la dinámica de esta arquitectura aumentó la durabilidad de la FC en un 110% con una penalización en el consumo de H_2 del 4.7%. La arquitectura multi-FCS para aplicaciones pesadas podría funcionar con una dinámica aún menor, con un aumento de la durabilidad de la pila del 471% con una penalización en el consumo de H_2 del 3.8%, ya que el perfil de conducción de los vehículos pesados suele ser menos dinámico. El control y el dimensionamiento diferencial sólo podrían aportar beneficios en términos de impacto ambiental o de coste, pero no de rendimiento.

La última parte considera los resultados obtenidos en términos de rendimiento y durabilidad para analizar el impacto medioambiental de cada arquitectura. La estrategia de producción de H_2 afecta significativamente a las emisiones del ciclo de vida en ambas aplicaciones sobre cualquier otra elección de diseño. El diseño óptimo para la arquitectura FCREx que minimiza las emisiones tiene una alta potencia de la pila de combustible y una capacidad moderada de la batería. En el caso de la aplicación para vehículos pesados, se identificó la dinámica de control óptima para cada diseño y estrategia de producción de H_2, y se determinó que la estrategia de diseño de dimensionado diferencial sólo proporcionaba beneficios si se consideraba

una tecnología de pila de combustible diferente para las distintas pilas integradas en el sistema propulsivo.

Resum. A la llum de la crisi mediambiental i del creixent interés en l'ús de l'H_2 per a avançar cap a l'Economia de l'Hidrogen, aquesta tesi té com a objectiu analitzar i optimitzar noves arquitectures de sistemes propulsius de FCV per a aplicacions en turismes i vehicles pesants en termes de rendiment, durabilitat i impacte mediambiental. Per a això, s'ha desenvolupat una plataforma de modelatge de FCV multifísica i flexible que integra un model de pila de combustible validat juntament amb els components del BoP, els components mecànics i elèctrics del vehicle i el sistema propulsiu, un model de degradació de pila de combustible semiempíric informat per tendències físiques dissenyat per a ser utilitzat en condicions de conducció i un optimitzador d'EMS en temps real que ofereix el millor rendiment donat un disseny de sistema propulsiu i un cicle de conducció, de tal forma que totes les arquitectures proposades per a una aplicació determinada siguen comparables en termes justos.

La discussió dels resultats pot dividir-se en tres parts diferents. La primera està orientada a l'optimització del rendiment del FCS. Els resultats d'aquesta part van ajudar a identificar l'estratègia de gestió de l'aire que, donat un conjunt de restriccions imposades en els components del BoP, maximitzava la potència neta del FCS (eficiència) per a cada valor de densitat de corrent. El balanç energètic resultant, que comprén la potència produïda per la pila de combustible, les pèrdues electroquímiques i el consum dels components del BoP, va ser analitzat i utilitzat per a determinar i dissenyar l'estratègia de control dels actuadors del BoP per a condicions de conducció.

La segona part se centra en l'avaluació i optimització, quan és possible, de l'arquitectura FCREx per a aplicacions de turismes i la configuració multi-FCS per a aplicacions de vehicles de transport pesat. Des del punt de vista del rendiment, l'arquitectura FCREx oferia un consum mínim d'H_2 amb una elevada potència de la pila de combustible i una gran capacitat de la bateria, però aquest disseny podria ser prohibitiu en termes de costos. Podia oferir fins a un 16.8-25% menys de consum d'H_2 i un 6.8% menys de consum d'energia. La limitació en la dinàmica d'aquesta arquitectura va augmentar la durabilitat de la pila en un 110% amb una penalització en el consum d'H_2 del 4.7%. L'arquitectura multi-FCS per a aplicacions pesades podria funcionar amb una dinàmica encara menor, amb un augment de la durabilitat de la pila del 471% i una penalització en el consum d'H_2 del 3.8%, ja que el perfil de conducció dels vehicles pesants sol ser menys dinàmic. El control i el dimensionament diferencial només podrien aportar beneficis en termes d'impacte ambiental o de cost, però no de rendiment.

L'última part considera els resultats obtinguts en termes de rendiment i durabilitat per a analitzar l'impacte mediambiental de cada arquitectura. L'estratègia de producció d'H_2 afecta significativament a les emissions del cicle de vida en totes dues aplicacions sobre qualsevol altra elecció de disseny. El disseny òptim per a l'arquitectura FCREx que minimitza les emissions té una alta potència de la pila de combustible i una capacitat moderada de la bateria. En el cas de l'aplicació per a vehicles pesants, es va identificar la dinàmica de control òptima per a cada disseny i estratègia de producció d'H_2, i es va determinar que l'estratègia de disseny de dimensionament diferencial només proporcionava beneficis si es considerava una

tecnologia de pila de combustible diferent per a les diferents piles integrades en el sistema propulsiu.

Abstract. In light of the environmental crisis and the growing interest in the use of H_2 to advance toward the Hydrogen Economy, this thesis aims at analyzing and optimizing novel FCV powerplant architectures for passenger car and heavy-duty vehicle applications in terms of performance, durability, and environmental impact. For that purpose, a multi-physics flexible FCV modeling platform was developed integrating a validated FC stack model together with the BoP components, the mechanical and electrical components of the vehicle and powertrain, a semi-empirical physics-informed FC degradation model designed to be used in driving conditions and a real-time EMS optimizer that offers the best-performance given a powerplant design and driving cycle so that all the proposed architectures for a given application are comparable.

The discussion of the results can be divided into 3 different parts. The first one is oriented towards the FCS performance optimization. The results in this part helped to identify the air management strategy that, given a set of constraints imposed in the BoP components, maximized the FCS net power output (efficiency) for each value of current density. The resulting energy balance comprising the FC stack power produced, the electrochemical losses, and the consumption of the BoP components was analyzed and used to determine and design the control strategy of the BoP actuators for driving cycle conditions.

The second part is focused on the evaluation and optimization, when possible, of the FCREx architecture for passenger car applications and the multi-FCS configuration for heavy-duty vehicle applications. Performance-wise the FCREx architecture offered minimum H_2 consumption with high FC stack power and high battery capacity, but this design could be prohibitive in terms of costs. It could offer up to 16.8-25% lower H_2 consumption and 6.8% lower energy consumption. Limiting the dynamics of this architecture increased the FC durability by 110% with a penalty in H_2 consumption of 4.7%. The multi-FCS architecture for heavy-duty applications could operate with even lower dynamics, with an increase in the FC durability of 471% with a penalty in H_2 consumption of 3.8%, since the driving profile of heavy-duty vehicles is usually more steady. Differential control and sizing could only provide benefits in terms of environmental impact or cost, not performance.

The last part considers the results obtained in terms of performance and durability to analyze the environmental impact of each architecture. The H_2 production pathway affected significantly the life cycle emissions of both applications over any other design choice. The optimum design for FCREx architecture that minimized emissions had high FC stack power and moderate battery capacity. In the case of heavy-duty application, the optimum control dynamics for each design and H_2 production pathway were identified, and the differential sizing design strategy was determined to only provide benefits if different FC stack technology was considered for the various stacks in the powerplant.

A mis padres, Emilio e Isabel.
Por haberme dado alas, impulso para volar,
y un lugar al que siempre volver.

A mi hermano, Emilio.
Por ser una meta a la que aspirar
y un ejemplo que seguir.

A Marta.
Por haberme ayudado a crecer
y darme la ilusión para seguir haciéndolo.

Agradecimientos

Un gran compañero un día me dijo: un doctorado, más que un título, es un viaje de crecimiento personal. Esas palabras me marcaron en uno de los momentos en los que más las necesitaba y, por esa misma razón, quiero empezar agradeciendo a mi gran director de tesis y amigo Ricardo. Por todo lo que te has implicado más allá de tus responsabilidades y por haberme enseñado a desarrollarme como investigador y como persona. Nunca se me olviadará nuestro mantra, el mantra del éxito: primero las personas.

También me gustaría agradecer a todas las personas con las que he colaborado en el CMT, como Benjamín Pla y Luis Miguel García-Cuevas o Andrés Tiseira, ya que gracias a trabajar con ellos he podido experimentar de primera mano que la unión hace la fuerza. Especialmente, agradezco el apoyo y la fe ciega que José María Desantes, Francisco Payri y Santiago Molina han tenido en mí, aún sin haber trabajado de cerca con todos ellos, no sólo durante el doctorado sino también durante mi carrera universitaria y de máster.

A Álvaro Fogué, Andrés Felgueroso, Brayan Conde y a todos mis compañeros que han hecho de esta etapa de mi vida un viaje inolvidable, con los que he compartido tanto alegrías como momentos de estrés. Sé que si de algo puedo estar orgulloso y presumir delante de todo el mundo, es de mis amigos.

A mis padres, por transmitirme un orgullo más allá de lo que jamás habría imaginado, darme alas, impulso para volar y un lugar al que siempre volver. A mis abuelos, quienes desde la más absoluta humildad nunca se han rendido y han hecho posible mi viaje. A mi hermano, por ser una meta a la que aspirar y un ejemplo que seguir. Y finalmente, a Marta, por haberme ayudado a crecer, darme la ilusión para seguir haciéndolo y haberme acompañado en los momentos en los que más necesitaba un apoyo.

Sin lugar a dudas, soy afortunado de poder contar con todas estas personas para afrontar esta nueva etapa de mi vida, y espero que las siguientes también.

Table of Contents

Index of Figures

Index of Tables

Chapter 1

Introduction

Contents

1.1 Introduction

Global warming, growing population, industrialization and urbanization of emerging countries, digitalization of society, imbalance of natural resources, war, energy dependency and highly-inefficient energy sectors are some of the concepts describing the political, societal, industrial and economical context wordlwide. This set of circumstances define a turbulent era that must be followed by a transition age. The industry, which is in a constant process of renewal, must adapt to a growing population and society that is significantly more dependent on electronic devices than ever. As a consequence, the increase in the energy demand, mostly in developing countries, is rising continuously and is expected to keep growing in the following decades. Unfortunately, with the current power generation technologies and sustainability policies, increasing the energy generation irremediably implies a growing environmental impact that is translated into phenomena such as global warming, affecting million of species worldwide and changing the climate by rising the global average temperature.

In this context, international organizations such as the United Nations (UN) proposed H_2 as the energy vector to correct the imbalances and inefficiency of the energy sector and to promote a sustainable growth of the energy generation infrastructure. The idea behind the utilization of this energy vector is to oversize the infrastructure to produce renewable energy, which excess will be converted into H_2 through water electrolysis to be stored and used later in other sectors. This concept of using H_2 to connect all the sectors and developed a balanced energy generation system is what the experts defined as Hydrogen Economy.

Among the different technologies that can be used to convert the chemical energy in the H_2 molecule bond into mechanical or electrical energy, fuel cells (FC) offer the highest efficiency (over 50% for H_2 FC [1, 2]) and is developed enough to penetrate most of the sectors of the industry. Nevertheless, the experts developing this technology face significant challenges to further refine and improve FC systems (FCS) so that they can be integrated into any application while offering high durability and performance. Particularly, the transportation sector is regarded as one of the main candidates to incorporate this technology in the short-term to be decarbonized, but there are still numerous scientific and technological barriers to overcome to further optimize these systems for transport applications.

This thesis is born to address part of the challenges to integrate FC technology in the transportation sector and bring light to the knowledge gaps that the industry and the scientific community are struggling to fill. The research presented along this document is focused on evaluating and optimizing the integration of FC technology in passenger car and heavy-duty vehicle applications by considering the optimization at different levels of detail: FCS, powertrain architecture, and life cycle environmental impact.

1.2 Context

The context leading to the recent development of H_2 FC technology is complex. Although the reader may think the advantages of using H_2 in FCS compared to any other technologies may be enough in themselves to justify their integration in all the sectors. Truth is that a set of complex circumstances and the necessity of urgent action have had to take place so that this technology moves to the spotlight of the scientific, political and industrial communities.

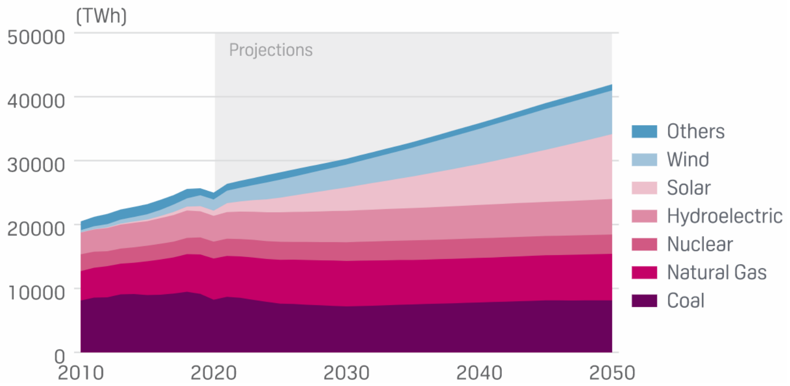

Figure 1.1. *Global net energy generation by source 2010-2050 [4, 5].*

The political context and actions, as the drivers of the recent funding of research projects to develop FC technology, arise from the needs derived from the environmental, industrial, societal and financial contexts.

In general terms, there are several concerns that are affecting the society, the economy and the industry. First, the global population, nowadays counting as 7.6 billion people, is expected to grow to 9.8 billion in 2050 [3], which implies an increment close to 29%. As can be deduced, this increase would imply not only a grow in the human capital but a significant need for natural resources and energy. According to the experts in the US's Energy Information Administration, this may lead to an increase in the global energy demand of 47% by 2050, that would probably be mostly covered by coal and other fossil fuels' energy (figure 1.1), since only 27% of the global energy mix would be from renewable sources, thus implying a global increase in the CO_2 only motivated by the increase in the energy demand.

Although the growth in the population may seem a critical issue to be addressed, there are other complementary factors contributing to the energy demand increase such as the increased urbanization mainly in continents such as Africa, given that currently about 600 million people do not have access to electricity [6]. In this line, other organizations such as the International Energy Agency predict that the energy-related CO_2 emissions would increase from nearly 40 Gt in 2020 to around 55 Gt in 2050, i.e., and increase in the CO_2 emissions of +37.5% (figure 1.2). According to the International Energy Agency, the transportation sector could help mitigate or be responsible for 20% of the increment of the energy-related CO_2 emissions in 2050 [7]. This

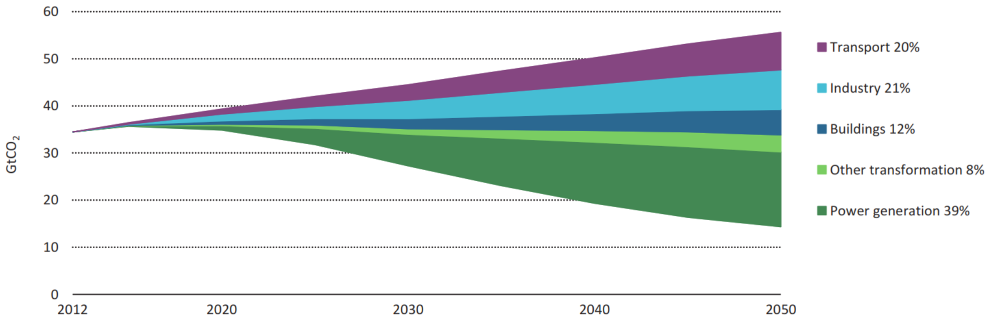

Note: $GtCO_2$ = gigatonnes of carbon dioxide.

Figure 1.2. *Energy-related carbon emission reductions by sector [7].*

means that the transportation sector is key to decrease the global warming impact of the society.

Particularly, for the transportation sector it is expected that the well-to-wheel GHG emissions would increase from 12000 Mt of CO_2 eq. in 2020 to 21000 Mt of CO_2 eq. in 2050 (+75%) [8]. Among the different applications within the transportation sector, heavy-duty vehicles (HDV) and light-duty vehicles (LDV) or passenger cars together with light commercial vehicles are responsible for 30% and 40% of the total well-to-wheel CO_2 emissions in 2020 respectively (figure 1.3), which may be maintained in 2050 if no further action is taken.

Future prospects indicate a growth in human-related GHG emissions that may increase the average global temperature over its natural evolution. The Intergovernmental Panel on Climate Change (IPCC) estimated that human activities are the cause for the current increase in the average global temperature by 0.8-1.2°C with respect to the pre-industrial levels, and it is likely to reach 1.5°C between 2030 and 2052 if no further action is taken and the current rate of increase in the global warming in maintained [9]. These anthropogenic emissions are expected to persist from hundreds to thousands of years and could be responsible for some of the long-term and potentially irreversible changes in the global environment such as the sea level rise, ocean acidification, the threatening of certain ecosystems, the increase in frequency of extreme weather events and deforestation, among others. In order to minimize the effect over the environment of human-related emissions, there seems to be a general consensus that the actions to be taken should be focused on the acceleration and upscaling of multilevel and cross-sectoral climate mitigation strategies to be integrated by the industry and the society as a whole.

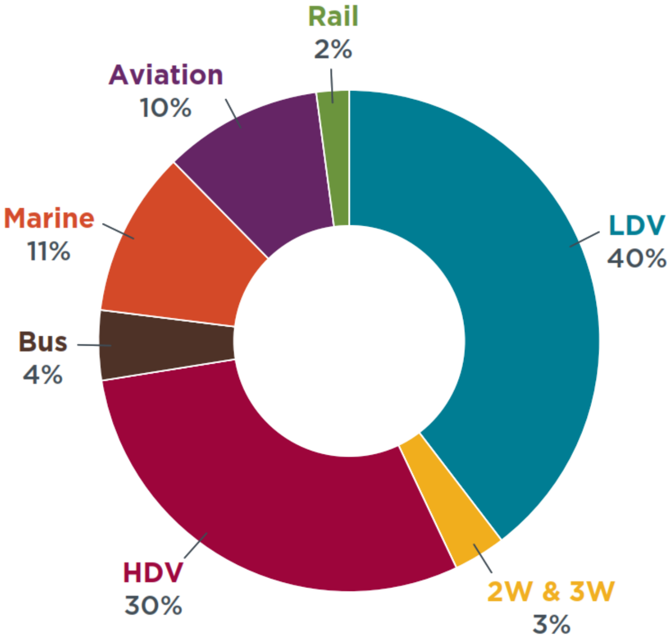

Figure 1.3. *Breakdown of 2020 well-to-wheel CO_2 emissions fin the transportation sector, by application [8].*

The aforementioned keywords define the characteristics of the solution to address global warming. On one hand, it must be as clean as possible, which means that the energy to be used in the future and in the industry for both electricity and heat should have the smallest effect on the environment possible, with a renewable origin not to deplete the natural resources. The concepts *cross-sectoral* and *multilevel* mean that the solution should be widespread across most of the industrial and societal activities, even in the hard-to-abate sectors. This, coupled with the necessity of increasing the efficiency of the energy sector, indicates that clean energy must be distributed with low losses and stored during long periods of time to account for the imbalances in the renewable energy production between seasons. In this context, H_2 rises as the energy vector that could help reach the climate neutrality worldwide by complementing other electric technologies. It can be obtained from water and renewable energy and, if used with FC technology, it only produces water and electricity with roughly double the efficiency obtained with an internal combustion engine (ICE), which fits almost perfectly within definition of a technology that could be the core of a circular economy. H_2 can be stored during long periods of time and, although it can be stored in a variety of states ranging from high-pressure gas to liquid or in solid compounds, the storage technologies are nowadays at the highest technology readiness level and offer higher energy density than lithium batteries, thus being more suitable than batteries for longer range or endurance transport applications.

In light of this situation and with the H_2 solution in mind, almost all countries committed to take actions to maintain the increase in the global average temperature below 2°C through the Paris Agreement which came into force on the 4^{th} of Novemeber 2016.

Later, in December 2019, during the fist stages of the COVID-19 pandemic, the EU adopted the even more ambitious objective of achieving climate neutrality by 2050, which implies net zero GHG emissions. Shortly after, the European Green Deal was supported through a resolution of the European Parliament, enforcing the roadmap towards climate neutrality in 2050 and adding more ambitious targets for 2030 [10]. As a consequence of this support from the EU, the European Comission presented the Hydrogen Strategy for a climate neutral Europe in July 2020, describing 3 phases that dictated the scaling up of renewable H_2 production infrastructure and the actions to take place to decarbonize even the hard-to-abate sectors by 2050 [11].

From this point until today, numerous roadmaps and white papers have been defined to make EU advance towards the Hydrogen Economy by determining specific goals and estimating the required funding to achieve each milestone. At national level, it is possible to find specific roadmaps such as the one devised in Spain *Hoja de Ruta del Hidrógeno: Una apuesta por el hidrógeno renovable* with similar targets adapted to the political and geographical situation of the country [12]. Apart from the roadmaps elaborated by specific countries or set of countries such as the EU, some international organizations such as the International Energy Agency developed their roadmaps with a global perspective [13]. As the example in figure 1.4, these roadmaps define the milestones to be accomplished until 2050 to fulfill the target of emissions reduction for one or several sectors.

Among these roadmaps, the Hydrogen Roadmap Europe elaborated by the Fuel Cells and Hydrogen Joint Undertaking (FCH JU) defines the objectives and practices to achieve the Hydrogen Economy in Europe and is commonly used as the guideline to identify the needs of the industry and decide on the allocation of funding for H_2-related research projects in Europe [14]. The ambitious goals in this roadmap for 2050 include an increase in the renewable energy share in the final energy demand of 24%, the annual abatement of 560 Mt of CO_2, a revenue of 820 billion €, a 15% reduction of other

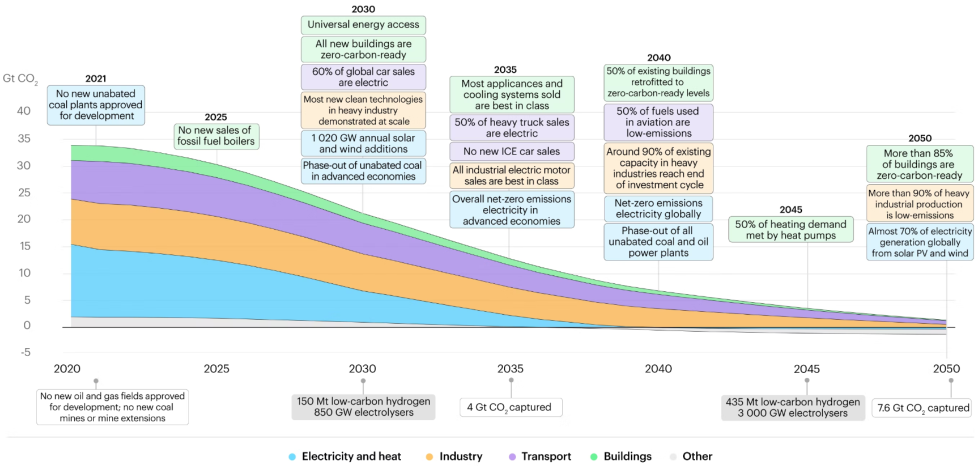

Figure 1.4. *Description of the milestones to achieve net zero emissions in the global energy sector and evolution of the corresponding CO_2 emissions [13].*

local emissions (NO_X) in the road transportation sector, and the generation of 5.4 million jobs related to the H_2 infrastructure development. It also includes a strategy to deploy H_2 refueling stations across Europe to make FC-based transport possible and defined the road transport sector, particularly heavy-duty transportation and passenger car, as essential to decarbonize to maximize the positive impact of the Hydrogen Economy on the environment. Furthermore, among the different technologies to extract the chemical energy from H_2, FC is determined to be optimum for road transport application since it can produce high-enough range with double the efficiency compared to ICE, with much lower refueling times than battery-electric vehicles and zero tailpipe emissions.

In conclusion, given the global environmental needs, the growing energy demand due to the population growth, the inefficiencies in the energy generation sector, and the never-better favorable political context, H_2 in combination with FC technology has enough support and can provide enough benefits so that it penetrates the market effectively and remain in the transportation sector for the decades to come.

1.3 Justification

In light of the aforementioned context, this thesis is born to contribute to the integration of FC technology in the road transportation sector. For such purpose, this thesis aims at analyzing and optimizing, whether possible, novel FC powertrain architecture for both passenger car and heavy-duty vehicle applications. These applications were selected since they are closely related, were determined to be priority in most of the roadmaps to achieve the climate neutrality and are responsible for most of the emissions in the transportation sector, according to figure 1.3.

Nowadays, even though there are commercial FC vehicles (FCV) such as the Toyota Mirai, the Hyundai Nexo or the Hyundai XCIENT FCV, few powertrain architectures have reached the market, mainly due to the lack of research in this area of knowledge. To address this issue, the research work associated to this thesis aims at developing a state-of-the-art FCV modeling framework useful for benchmark purposes with optimum FCS operation (chapter 4, part 1, section 4.2), evaluating the performance and durability of the FC range-extender (FCREx) architecture for passenger car application and the multi-FCS architecture for heavy-duty vehicle application (chapter 4, part 2, sections 4.3 and 4.4), and analyzing the life cycle environmental impact of both novel configurations though an LCA analysis in which the optimum configuration is identified for each H_2 production pathway (chapter 5) to understand what designs could maximize the rate of decrease of global warming emissions in the transportation sector.

1.4 Objectives

The main objective of this thesis is to *analyze and optimize, when possible, the novel FC powerplant architectures for the next generation of* H_2 *FCV in terms of performance, durability and environmental impact.* In this line, the FCREx architecture was considered for a passenger car application while the multi-FCS architecture was evaluated for a heavy-duty vehicle application. The conclusions of each of the studies in this thesis are used, when possible, to extract recommendations for the industry in such a way that this work can contribute to help the FC technology penetrate the transportation sector. In order to achieve the main objective, a set of secondary targets must be fulfilled:

- **Partial Objective 1.** Develop a flexible FCV modeling platform capable of predicting the performance, durability and environmental impact of any light-duty or heavy-duty vehicle in driving cycle conditions. This simulation tool should integrate a balance of plant (BoP) management strategy that ensures the best FCS-performance, an energy management strategy optimizer that offers the lowest possible H_2 consumption with any driving profile, a FC degradation model capable of capturing the the voltage loss of the FC stack depending on the FC management during driving conditions, and a LCA framework that comprises several H_2 production pathways to understand the environmental impact of each FCV design in different scenarios.
- **Partial Objective 2.** Carry out an optimization of the BoP management for the FCS used for passenger car and heavy-duty applications and integrate the BoP management strategy in the control algorithms handling the main actuators in the FCS in such a way that the BoP aims at maximizing the FCS efficiency at each time step during any driving cycle simulation.
- **Partial Objective 3.** Analyze the effect on performance and durability of considering different powertrain component sizing and control dynamics for the FCREx architecture in a passenger car application and the multi-FCS in a long-haul heavy-duty application. Identify optimum designs performance and/or durability wise and determine the sizing and dynamic limits for which these powerplants can fulfill the target operating modes in driving cycle conditions.
- **Partial Objective 4.** Understand the environmental impact of each FCV with the proposed novel architectures when modifying the H_2 production pathway and the powerplant design or control. Identify the optimum architecture depending on the scenarios defined by the H_2 production pathways.

1.5 General outline

The outline of this thesis (figure 1.5) can be clearly divided into 3 different parts, each of which addresses at least one of the partial objectives defined in section 1.4:

1. **Optimized FCV modeling framework development.** The main objective of this part is to develop a FCV modeling framework capable

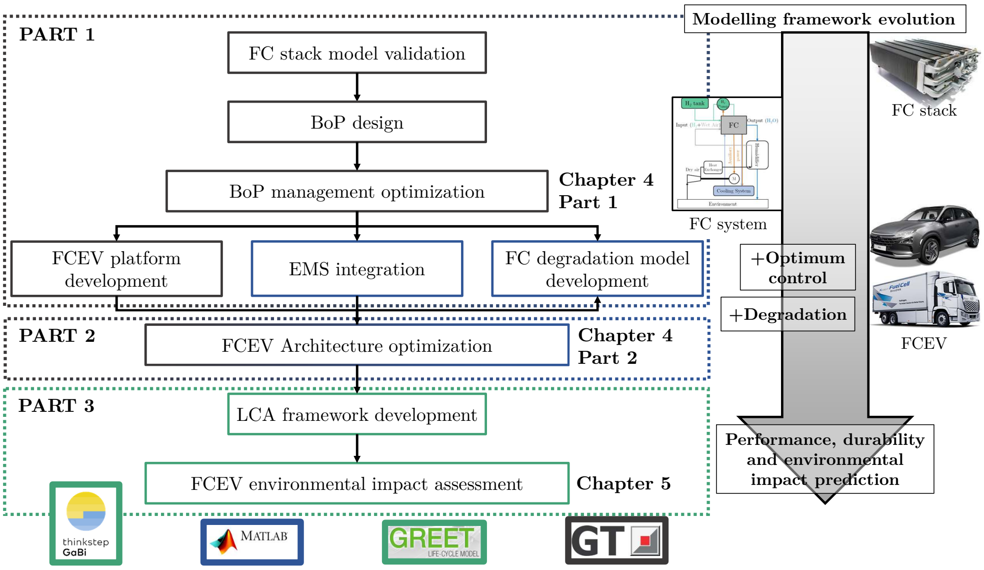

Figure 1.5. *Outline of the activities carried out along this thesis.*

of describing the optimum FCS operation in driving cycle conditions for each of the designs considered. This part integrates not only the development of the modeling tools, but also the results obtained when optimizing the FCS efficiency. This is considered an independent part since it is essential to assure that each design offers the optimum operation to avoid any possible bias induced by a methodological error when comparing different powertrain architectures. As such, it is possible to state that this part comprises both the development of the modeling platform explained in **chapter 3** as well as the results in **chapter 4, part 1, section 4.2** which are clearly related and interdependent as presented in figure 1.5. This part responds to the **Partial Objectives 1 and 2**.

2. **FCV performance and durability optimization.** This part, mainly comprising the analysis carried out in **chapter 4, part 2, sections 4.3 and 4.4**, is aimed at identifying the optimum sizing and control dynamics that maximize performance and durability for the FCREx architecture applied to a passenger car application and the multi-FCS propulsion system applied to a heavy-duty application. Since usually performance and durability can not be optimized simultaneously, the trade-off between them is identified for different powerplant designs so

that it can serve as a basis in the FCV development process. The sizing analysis for the FCREx architecture consists of varying the FC stack maximum power output, the battery capacity and the H_2 tank capacity while for the multi-FCS powerplant the total FCS power was maintained constant by the relative power of the two FCS composing the powertrain was changed. These analyses were carried out by imposing different restrictions in the dynamics and in the operational space to understand how H_2 consumption is affected when considering control strategies aimed at preserving the FC stack durability. The research related to this part is in line with **Partial Objective 3**.

3. **Environmental impact assessment of novel architectures.** This part, mainly comprising **chapter 5**, was focused on understanding the environmental impact of the novel FC-based powerplants in terms of GHG and NO_X emissions. For that purpose, the results in chapter 4, part 2, sections 4.3 and 4.4 are combined with the LCA framework defined in chapter 3 with different H_2 production pathways. Apart from estimating the environmental impact, the optimum architecture designs for each production pathway were identified and compared against the optimum powerplants aimed at minimizing H_2 consumption or FC stack durability. This part directly addresses **Partial Objective 4**.

References

[1] Barbir Frano. *PEM Fuel Cells Theory and Practice Chapter 4 - Main Cell Components, Material Properties, and Processes.* 2013.

[2] Desantes J.M., Novella R., Pla B. and Lopez-Juarez M. "Impact of fuel cell range extender powertrain design on greenhouse gases and NOX emissions in automotive applications". *Applied Energy*, Vol. 302, pp. 117526, 2021.

[3] United Nations. "World population projected to reach 9.8 billion in 2050, and 11.2 billion in 2100", 2017.

[4] U.S. Energy Information Administration. "International Energy Outlook 2021", 10 2021.

[5] Gordon Meghan and Weber Maya. "Global energy demand to grow 472021.

[6] International Energy Agency. "Africa Energy Outlook 2019 World Energy Outlook Special Report".

[7] International Energy Agency. "Technology Roadmap Hydrogen and Fuel Cells".

[8] International Council Of Clean Transportation. "Vision 2050: A strategy to decarbonize the global transport sector by mid-century", 2020.

[9] IPCC. "Special report: global warming of 1.5 °C - Summary for Policymakers", 6 2018.

[10] European Parliament. "European Parliament resolution of 15 January 2020 on the European Green Deal (2019/2956(RSP))", 2020.

[11] European Commission. "A hydrogen strategy for a climate-neutral Europe", 2020.

[12] Ministerio para la Transición Ecológica y el Reto Demográfico (MITERD). "Hoja de Ruta del Hidrógeno: Una apuesta por el hidrógeno renovable", 2020.

[13] International Energy Agency. "Net Zero by 2050 - A Roadmap for the Global Energy Sector", 2021.

[14] Fuel Cells & Hydrogen (FCH). *Hydrogen Roadmap Europe - a Sustainable Pathway for the European Energy Transition.* Publications Office of the European Union, 1st edition, 2019.

Chapter 2

Literature review

Contents

2.1 Introduction

Before delving into the detailed explanation of the tools and results obtained throughout this thesis, it is important to understand the current state-of-the-art of FC technology applied to both passenger car and heavy-duty vehicle applications. This chapter intends to provide a general outlook of the scientific work carried out prior to this research and to provide the basic knowledge to the reader to be able to comprehend the complex concepts used in the following chapters. For that purpose, sections 2.2 and 2.3 explain the fundamental of H_2 FC technology while sections 2.4, 2.5 and 2.6 are aimed at analyzing the recent research on FC powerplants applied to passenger cars, heavy-duty vehicles and the most novel approaches to model FC degradation.

Finally, section 2.7 summarizes the presented recent research and identifies the knowledge gaps filled by this thesis.

2.2 H_2 as an energy carrier

With the general objective of decarbonizing most of the sectors in the industry, H_2 FCVs have recently become relevant and penetrated the market, particularly in the automotive sector [1]. This technology is not only attractive since it can potentially produce zero CO_2 emissions, but also because the energy carrier it works with (H_2) has many advantages, relative to electricity for BEVs.

H_2 utilization could offer many benefits if used as the primary energy carrier in most of the industry sectors. The main advantages of this fuel when used in transportation applications are [1–3]:

- It does not produce tailpipe CO_2 emissions when burned or used in a FC.
- It can be produced through many production pathways such as electrolysis or steam methane reforming (SMR). In the case of the electrolysis the electricity can be obtained from renewable sources and in the case of SMR the H atoms could be extracted from biogas. Therefore, H_2 could also imply zero or negative well-to-wheel emissions.
- When stored in tanks at 700 bar (as commonly done in the automotive sector) it has a higher energy density than batteries.

Nevertheless, despite the benefits of H_2, it also presents some disadvantages when compared against batteries or conventional fuels.

In the energy sector, H_2 can be used to decarbonize the gas grid. Other strategies to decarbonize it include the use of biogas for heating or the electrification of most of the heating processes with electrical heat pumps. However, the former is not expected to be available at the required scale and the latter would be very expensive for old buildings and would produce significant seasonal imbalances in the consumer power demand thus requiring a large-scale power storage mechanism, such as H_2. Integrating H_2 as an energy carrier in the energy sector could maximize the efficiency of the overall energy usage in the electric grid by absorbing the energy peaks (supply over demand) and using the stored energy when the power demand is over the supply. Furthermore, its properties as a gas and storage distribution through pipelines, ships, or trucks, compared to electricity transmission lines imply lower losses and longer storage periods. H_2 transportation could be further optimized to reduce distribution costs and CO_2 emissions if it is transformed into any liquid e-fuel such as methanol or ethanol through CO_2 sequestration or even to ammonia with the N_2 of the atmosphere. These fuels, if produced from renewable H_2, could also be used directly in ICE producing neutral well-to-wheel CO_2 emissions [4–6].

H_2 is considered one of the most promising solutions to decarbonize for both light and heavy-duty transportation applications. Its energy density is lower, even in liquid state, compared to conventional fuels, therefore the range of a H_2-fueled vehicle is lower, particularly if the on-board space available is highly limited. Nowadays, the manufacturing costs of H_2-powered vehicles is higher due to the high-pressure H_2 tanks, capable of withstanding almost 700 bar of pressure difference and the FC system. Nevertheless, in the medium-term, this drawback would be less important once both technologies benefit from the economies of scale. Regarding the relative advantages, H_2 can offer higher flexibility to reduce well-to-wheel emissions as it can be produced from renewable energy sources with electrolysis (green H_2), from SMR without CCS (grey H_2) or with CCS (blue H_2) or electrolysis with the local electricity mix (black H_2), among other production pathways. It can be used either in ICE or in FC. The former propulsion system implies lower manufacturing costs since it is based on a technology that is widely spread in the industry, has high durability and is less sensitive to impurities in H_2 and vibrations. However, compared to FC it may produce other tailpipe emissions besides H_2O such as NO_X if it is not burned together with enough air or exhaust gases (lean) and its efficiency is around half of that offered by FC technology, which aggravates other challenges of FCV such as on-board storage and range. In this line, there are some challenges that still need to be addressed in the H_2 chain such as the development of compact, cheaper and durable on-board storage systems, the lack of H_2 production and distribution infrastructure and the improvement of the H_2 handling systems to avoid embrittlement and leakages. All in all, the primary advantage of H_2 compared to conventional fuels is that its utilization with FC does not produce CO_2 emissions while its main disadvantage is the lower vehicle range. Nevertheless, given the high efficiency of FCS, current FCVs used for light-duty applications (passenger car) are capable of achieving more than 600 km of range with 5 minutes of refueling time and over 400 km in heavy-duty transportation applications with only a refueling duration around 10-20 min, which is not an issue even for long-distance trips [1].

If H_2 is compared against batteries, the other alternative to decarbonize the transport sector, some advantages and disadvantages can be found as well. Regarding the advantages, if H_2 is used together with FC technology and high-pressure storage in gas state it can offer higher energy density, hence higher vehicle range, shorter refueling times (from 30 min to 2 h depending on the C rate and the battery capacity to 5 min), lower requirement of raw materials and rare earths metals for the manufacturing (only small quantities of Pt for the catalysts are required) and the energy losses when stored for long durations are negligible. However, batteries present higher efficiency ($\sim$90% compared to $\sim$50-60%) and they produce lower noise since they do not need an air compressor. Therefore, the main advantages of H_2 over batteries are its higher energy density, both in terms of mas and volume, and the lower refueling time despite the lower efficiency in energy utilisation.

In conclusion for the transportation sector, H_2 can provide higher energy density than batteries, hence enabling long-range operation (>600 km for passenger car and >400 km in heavy-duty vehicles), and potentially lower well-to-wheel and cradle-to-grave emissions than hydrocarbon-fueled vehicles [7], given the large variety of H_2 production pathways. This makes H_2 a suitable option to decarbonize the operation of heavy-duty vehicles, ships, trains, and aircraft while it is a perfect fuel to complement and coexist with batteries and/or neutral CO_2 emissions ICE for light-duty vehicles, enabling high-enough-range and carbon-free transport applications [1, 2].

2.3 Fuel cell technology

FC technology can be devised as a combination or compromise between ICE and batteries. ICE obtain the chemical energy from a fuel that is stored in a separate tank, which implies that the amount of energy stored in the vehicle is decoupled from the ICE size. In this powerplants, the chemical energy is first converted into heat through a combustion process, for which air is required, and then into mechanical energy following a thermodynamic cycle, which ideal and maximum efficiency is that of the Carnot cycle. In contrast, batteries obtain the chemical energy from the reactants stored inside the battery and transform it into electrical energy by an electrochemical process. Electricity can further be turned into mechanical energy with the assistance of an e-motor that usually implies $\sim$5% of power losses, inverter included. The amount of energy stored (energy density) and the maximum power that the battery can supply (specific power) depend on the number of cells composing the battery pack and their internal organization (serial cells to increase the maximum power output and cells in parallel for increased energy capacity). This means that modifying the maximum power output or the energy stored in the battery necessarily implies a change in the weight and the volume of the battery pack. FC are said to be a combination of or *in between* these two technologies since the chemical energy is obtained from a fuel stored in a tank, which is later combined with air to convert the energy stored in the bond of the H_2 molecule into electricity by means of an electrochemical reaction. This implies that the energy stored in the vehicle is decoupled from the FCS size (as in ICE) and the overall efficiency of the process is higher since the chemical energy is extracted following an electrochemical reaction (as in batteries).

The structure of a low-temperature H_2 Proton-Exchange Membrane Fuel Cells or PEMFC (figure 2.1) is mainly composed of the flow channels, whose shape is defined by the bipolar plates, for both the anode and the cathode, and the membrane electrode assembly or MEA. The flow channels carry the reactants (H_2 in the anode and O_2 in the form of air in the cathode) to the MEA and evacuate the products of the reaction (H_2O) so that they do not obstruct the flow channels or any porous media in the MEA. The MEA is used to provide mechanical integrity to the FC, to separate the H_2 and the O_2 thus preventing combustion, and to carry out all the steps required in the electrochemical oxidation of H_2: the uniform distribution of the reactants along the catalyst surface thanks to a porous media (gas diffusion layer or GDL, normally made of carbon compounds such as graphite), the dissociation of H_2 into H^+ in the presence of Pt in the anode catalyst layer, the transport of protons from anode to cathode through a membrane that is only permeable to H^+ and impedes the circulation of e^-, and the recombination of the H^+ with the e^- and O_2 to form H_2O in the cathode catalyst layer.

The process though which electricity is obtained in a FC is a combination of thermofluid and electrochamical phenomena and is ideally limited by the Gibbs free energy of the reaction, as explained in chapter 3. The electricity is generated by the circulation of e^- in a conducting medium, and is only possible since the membrane, made of Nafion, is a polymeric material that is only permeable to H^+ and offers high resistance to the transport of any other gaseous species and e^-, except for liquid H_2O which is transported through capillarity. In reality, the transport of other species is small but not zero, and it is accounted for as crossover or internal currents voltage losses.

Following the outline in figure 2.1, it is possible to explain how the electricity is generated in a FC. Starting from the anode side, H_2 is supplied and distributed along the MEA through a set of channels engraved in the bipolar plates (outer material of any single-cell FC array). Then, H_2 flows to

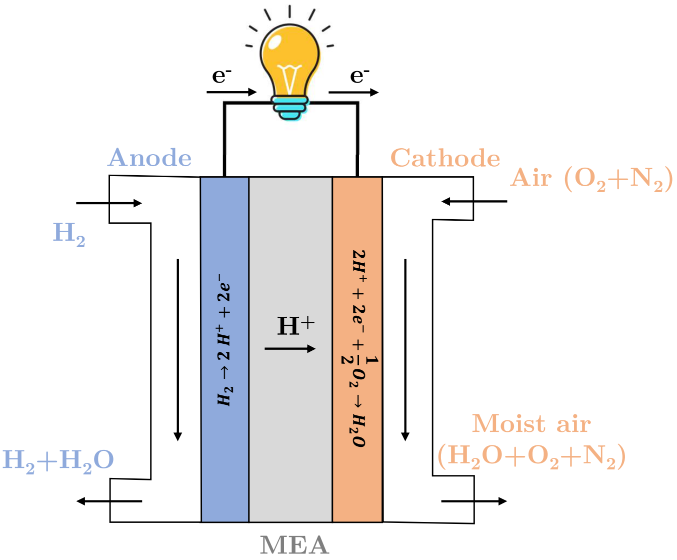

Figure 2.1. *Single-cell PEMFC outline.*

the GDL, a porous medium that distributes it evenly along the anode catalyst layer. When H_2 molecules interact with the Pt in the catalyst layer, they are broken down into H^+ ions or protons and e^- or electrons:

$$H_2 \rightarrow 2H^+ + 2e^-$$

At this point, protons flow through the membrane while electrons that can not be transported through Nafion, follow the least-resistance path, i.e., a conductor (wire) connected to the FC and to an external load (e-motor or any appliance). The split up of H^+ and e^- produces the voltage difference that is perceived as open-circuit cell voltage that is later measured as cell voltage after all the voltage losses are accounted for. Then, when H^+ reach the other side of the membrane, they interact with the e^- (from which they were separated at the anode catalyst layer) and the O_2 at the cathode catalyst layer, thus forming H_2O which is transported to the anode and the cathode flow channels:

$$2H^+ + 2e^- + \frac{1}{2}O_2 \rightarrow H_2O$$

The electrical power of the FC is produced by the circulation of e^- through the conducting material and the voltage difference resulting from the overall electrochemical process. The relation between the current (or current density if divided by the cell active surface area) and the cell voltage is given by the polarization curve of the FC, as defined in section 3.3.1.

These electrochemical and themofluid-dynamics set of processes occur at any cell, and the value of voltage is limited to 1.23 V according to the Gibbs free energy while the current depends on the cell surface area. Therefore, in order to scale-up the cell power, instead of considering a large cell to increase the current, a set of cells with fixed surface are connected in series to form a FC stack. The nature of these stacks is modular since their power can usually be modified by adding or eliminating cells, but require layers of cooling (cell-like layers where coolant is flowed through inserted in between the electrochemical cells) to keep the cell temperature around 70-80°C to maximize the FC efficiency while avoiding degradation. Nevertheless, a FC stack usually can not produce power by itself. It needs a set of auxiliary components to supply and condition the flows in the anode and in the cathode. The set of components required to manage these flows and the cooling system is called the balance of plant (BoP) and its combination together with the FC stack is known as FCS. The FCS is what can be understood as the compromise between the ICE and the battery since it can produce by itself electrical energy from a fuel supplied from a tank. This thesis includes a part of a chapter dedicated to the optimization of the BoP management and the FCS net efficiency (chapter 4, part 1, section 4.2).

2.4 Passenger car FCV

FCVs can be classified according to different criteria such as the H_2 storage method (pressurized or in liquid carriers/state), the electronic configuration (direct or indirect), or the battery characteristics (plug-in or non-plug-in). It is worth noting how, despite the classification of the FCV, all of them are similar to a hybrid electric vehicle that can be either serial or parallel since the connections are mainly electronic and can be switched with ease. Nowadays, the commercial FCVs Honda Clarity, Toyota Mirai, and Hyundai Nexo integrated an indirect-type electronic architecture, the H_2 is stored at 700 bar of pressure, and their batteries are small and can not be recharged with the grid (non-plug-in). For state-of-the art FCV the norm has become to use an indirect-type power architecture since it helps to reduce the size of the FCS and protects it from the DC bus voltage oscillations, and compressed

H_2 because this technology has been reliably demonstrated (high TRL) [8] and can be used to store H_2 for long periods of time. Nevertheless, despite the absence of plug-in passenger cars in the market, they shall not be ignored since they could offer significant advantages compared to non-plug-in vehicles. Some of these benefits include potentially lower FC degradation rate, higher powerplant efficiency, increased operational flexibility, and potentially lower total cost of ownership (TCO) and cradle-to-grave emissions, depending on the scenario.

Plug-in FCVs can have different operation modes, among which they may operate using the FCS as a range extender (FCREx) by keeping the battery state of charge within preset limits. The power fluctuations that the FCS is required to supply in non-plug-in vehicles are highly dynamic and this, coupled with frequent start and stop, increase FC stack degradation [9, 10], hence leading to a decrease in FCS efficiency and performance, and increase of user costs. Similarly, in-depth battery discharge or extremely high state-of-charge (SOC) may lead to decreased battery durability and performance. Therefore, the philosophy of FCREx of keeping the battery SOC in moderate and controlled levels increases its life and decreases the user maintenance and repair/replacement costs [11].

The recent technological assessments of commercial FCVs prove that state-of-the-art FCS are capable of operating under highly dynamic conditions, enough to satisfy the power demand profile of aggressive driving conditions with relatively small batteries, similar to those integrated in parallel-hybrid ICEV [12]. Nonetheless, the high dynamic operation of FCS implies an additional cost in terms of long-term performance, since the maximum power output of any FCS decays as the FC stack degradation is aggravated. That is why, the stable and slower operation of FCS in FCREx vehicles could contribute to preserve the FC stack capabilities longer.

The bigger batteries integrated in FCREx vehicles enable a more flexible operation, permitting purely electrical (BEV-like) mode and hybrid (FCREx) mode, depending on the user and driving profile requirements. This is particularly important in the current worldwide situation, where the cost of H_2 is significantly higher than that of electricity and there are a limited number H_2 refueling stations across the world [2]. In this scenario, FCREx vehicles could operate in BEV mode in cities, where 100 km of range should be enough since the battery may be recharged overnight, and use the FCS to extend the range for inter-urban trips with an approximate range of 500-600 km.

Finally, the TCO might be lower for an FCREx vehicle if the battery pack is not over-sized. TCO analyses usually include the price of the vehicle, the cost of fuel or energy source, the insurance, the maintenance, and various taxes and fees. If it is assumed that the insurance and taxes/fees are the same for FCREx vehicles and conventional FCV, the former could offer lower TCO due to various reasons. First, the FCS maximum net power can be reduced since the battery capacity is comparatively higher, so the power demand peaks could be provided by the battery pack without decreasing significantly its SOC. Hence, the FC stack and all the components of the BoP could have lower power requirements and may be cheaper. Nevertheless, this might be outweighed by the increased production cost of the larger battery. Second, H_2 is nowadays more expensive than electricity from the grid if produced through electrolysis from the electricity mix, therefore, for the moment, the overall operating costs of an FCV are greater than those of a BEV. Considering a mix of electricity and H_2 implies the possibility that FCREx vehicles offer to reduce the TCO compared to conventional FCV. The option of obtaining H_2 from SMR, which should be considerably cheaper than from electrolysis nowadays, is not considered because this process produces CO_2 emissions and therefore it is not a long-term solution to make the FCV portfolio sustainable and advance towards the H_2 economy, unless CCS technology is considered [7].

2.4.1 Fuel cell range-extender architecture

As in any new propulsion system technology, there are several possibilities to integrate it into the overall vehicle architecture that may imply different capabilities and performance of FCVs. This is the case of the FCREx powerplant architecture. FCREx configuration can be considered as a combination of the powerplant in BEVs and FCVs and has not still been extensively explored for passenger car applications but has high potential to improve energy efficiency and may be one of the solutions to extend the actual range of FCVs until there are enough H_2 refueling stations [13]. Currently, the only architecture that was considered for commercial light-duty passenger vehicles combines an FCS with a low-capacity battery. As a consequence, the performance of the FCREx powerplant architecture applied to passenger vehicles and how it may change with the sizing of the components remained unexplored prior to this research, thus ignoring the potential of an FCV powertrain architecture that may be essential in the current scenario, where the availability of H_2 refueling stations is limited.

Sizing the components of the FCREx powerplant is more complex than for a conventional FCV as the battery capacity is added as an additional degree of freedom and it also affects considerably the optimum energy management strategy, the operating cost, and the range. As such, for FCREx vehicles, it is necessary to provide a detailed and broad analysis on the performance, range, and cost of systems for different combinations of FCS, H_2 tank storage capacity and battery capacity to understand and analyze the actual potential and limitations of such architecture, relative to conventional FCVs.

Most of the studies in the literature focus on sizing the components of non-plug-in FCVs [14], but those focused on FCREx architecture [15] are not oriented toward passenger car applications or do not consider the same sizing parameters as those in this research. Therefore, there is a clear knowledge gap regarding the sizing of FCREx powertrains for light-duty passenger vehicles.

The state-of-the-art research work on FCREx powerplants for passenger cars is limited. Hence, it is difficult to analyze the frontier defined by the state-of-the-art in this field by focusing only on light-duty vehicle applications. Namely, the related recent research lines have aimed at utilizing the FCREx concept on bus and heavy-duty transport applications and on the optimization of the energy management of different FCV architectures to maximize vehicle performance. The research focused on the sizing of the components of the FCREx architecture for bus applications considers different control strategies such as the CDCS (charge-depleting and charge-sustaining strategy) or two-step algorithms based on dynamic programming in order to evaluate and optimize the vehicle performance and costs. In this line, it was deduced that, to minimize H_2 consumption in FCREx, the priorities should be in order of relevance: decreasing auxiliary power consumption, enhancing the braking energy recovery, increasing the FC stack efficiency, and decreasing battery losses [16]. Furthermore, it was found that the optimum size of the systems for city buses should be around 150 Ah in terms of battery capacity and 40 kW for the FCS maximum output power [17]. Nevertheless, the conclusions extracted from this research are only applicable to urban buses and the results in terms of consumption are far from those expected for an FCREx architecture applied to light passenger vehicles.

Similar to urban bus applications, FCREx powerplant was also considered for urban-logistics vehicles with tools such as convex programming and fuzzy logic controllers to optimize the sizing of the components. The combination of FCS together with batteries with moderate capacity showed that the range of urban-logistics vehicles could be improved compared to BEV and the H_2 consumption could decrease by half [18]. Different from urban bus applications, the optimum battery capacity was determined to be close to 29 kWh, while the optimum FC stack maximum output power depended on the H_2 price [19], probably due to the different vehicle weight and driving profile. The dependence of FCS power on H_2 cost to minimize the TCO proved how sensitive the efficiency and performance of FCREx vehicles is to the FC stack size as higher FC stack maximum power output implies lower H_2 consumption due to the lower current density and higher FCS efficiency.

Supplementing the FCREx-oriented research work, there have also been several studies aiming at optimizing the EMS in driving cycles simulations or the size of the components in conventional FCV to improve fuel consumption and FC durability, but they used other components such as supercapacitors [20] or low-capacity batteries [21].

In light of the state-of-the-art research for FCREx powerplants, it is important to note that most of the studies consider low-order models to define the FCS performance such as constant polarization curves [20, 22], polynomials only sensitive to the current density [19, 23] or simply straight lines expressing constant FC stack efficiency [21], not even FCS efficiency, that do not represent the physics behind the change of the FCS performance with the operating conditions. In most of these studies, the FCS management was not validated or optimized, and most of the research was focused on the optimization of the control strategies. This implies that the results are not representative of the best FCS performance since the models were only partially-optimized and could be improved.

The outlook of the state-of-the-art research confirm that currently, the FCREx powerplant architecture has mainly been considered for transport applications other than passenger cars. Despite the existence of sizing studies for this architecture, the conclusions and optimal designs of these studies can not be applied to light-duty passenger vehicles. Furthermore, the sizing studies for FCVs do not consider the FCREx architecture.

2.5 Heavy-duty FCV

Given the advantages of integrating FC technology in the heavy-duty transportation sector and the public willingness to decarbonize in the short-term with FCVs not only in EU [1], but also in other countries such as China [24], the scientific community has pushed significantly the state-of-the-art in this research line during the last years, perceiving an increase in the published work of 270% from 2019 to 2021 [25].

In this context, several research lines have recently aimed at quantifying the environmental benefits of powering heavy-duty vehicles with FC-based powerplants through LCA studies. The environmental advantages of replacing the heavy-duty Diesel vehicle fleet by H_2 FCVs were assessed in different scenarios in China, where the GHG emissions produced by this sector are expected to increase. In this line, the penetration of FC technology in the heavy-duty transport sector could imply a decrease in GHG emissions ranging from 63 to 12% in 2050, compared to a no FCV scenario [26]. Other studies based on other regions such as Germany, also point out that the use of FC and battery technologies could decrease CO_2, NO_X and PM emissions by 28%, 19% and 7% in the heavy-duty transport sector, respectively [27]. Finally, in other regions such as America, this technology is also expected to provide significant advantages in terms of environmental impact by reducing well-to-wheel GHG emissions from 20 to 45% considering different H_2 production pathways compared to their Diesel counterpart [28]. These studies suggest that there is a general consensus in the scientific community about the fact that integrating FC technology in heavy-duty transportation applications would undoubtedly bring environmental benefits in most of the regions across the globe.

Among the studies aimed at optimizing the FC-based powertrain for heavy-duty applications, in general they conclude that the integration of FC technology in heavy-duty trucks could provide more advantages than in other applications compared to BEV and ICEV trucks due to the high range and carbon-free emissions that this technology can offer. FC powerplants with moderate or high battery capacity are very compatible with heavy-duty vehicles because they enable flexible operation modes and low consumption. FCREx architectures have also been considered for heavy-duty vehicles since recent research showed that they could decrease the TCO by 1.3% with respect to conventional FCV architectures [29], being the result strongly dependent on H_2 costs. In addition, different control strategies were applied and compared for FCV trucks with the 8*CHTC-HT and 7*C-WTVC Chinese truck driving cycles, thus concluding that convex-optimization-based control strategies could provide minimum H_2 consumption and could be used on-line while driving. In this line, novel cost oriented sizing technologies were developed by other authors, thus providing an optimal powertrain (battery pack and FCS) size for the 2020, 2030 and 2050 scenarios in Europe [30]. This study could serve as the base to start any preliminary heavy-duty FC-based powertrain sizing, to down select the total FCS power and battery pack capacity.

Other heavy-duty applications for which FC technology was considered is mining trucks, where the mitigation of the tailpipe emissions is essential to ensure the safety of underground mining operators, given the narrow available space and the potential gases accumulation. For these vehicles with an optimized FC-battery hybrid powerplant design, the battery life was extended, the H_2 consumption decreased, and the mining cost decreased by 8.7% [22]. Other authors considered FC-based powertrains for captive fleet applications such as heavy-duty yard truck for port logistics [31]. They considered a single FCS with a maximum power output of 70 kW, but mostly operating at 34 kW, thus concluding that the FCV concept accomplished the target port operations outperforming Diesel vehicles in terms of power and energy requirements while providing zero local emissions.

Finally, it is important to note that none of the studies oriented towards heavy-duty applications found in the literature consider a powerplant architecture consisting of multiple FCS or a multi-FCS architecture. Most of the research work consider that the vehicle powerplant comprises only 1 FCS. Therefore, although the performance and cost-oriented sizing analyses are useful to understand which would be the optimum maximum output power of the FC part of the powerplant, there is a clear knowledge gap when deepen into a further level of detail in the FCS configuration, particularly when considering novel architectures such as the multi-FCS configuration with novel design methodologies such as differential sizing and control.

2.6 Fuel cell degradation

Although FCVs are an option acknowledged by the scientific community to decrease the GHG emissions and help mitigate the global warming contribution of the transport sector, FC stacks have relatively low durability, compared to ICE vehicles [32]. Organizations such as the Department of Energy (DoE) of the United States set the durability 2020 targets of FC stack to 40000 h for stationary applications such as decentralized power generation and 5000 h in realistic driving conditions for passenger car applications [33]. As such, the development of high-fidelity FC stack and FC degradation models has been one of the main objectives of the scientific community during the last years [34, 35].

FC degradation needs to be predicted as it leads to the decrease of the FC maximum power output capacity through the increase in the electrochemical irreversibilities such as those producing for activation, ohmic, and concentration voltage losses, among others. It is especially important to be able to capture these phenomena during dynamic operation (driving conditions), where degradation is particularly high due to load cycling. In a vehicle platform, the EMS, that is designed to properly manage the energy flows and the power split sequence when an FCS and a battery are integrated simultaneously in a powerplant, needs to be aware of the FC stack voltage losses (degradation state or state of health) and the change of the degradation rate with the operating conditions to provide the optimum energy consumption and improve durability, if required. Therefore, developing FC degradation models that enable the on-line prediction of how voltage losses change and affect the FC performance is essential as it affects both the energy transformation processes, since the electrochemical losses increase, and the energy management strategy, because the solution provided by control strategy optimization algorithms depends on the degradation state of the powertrain components [36].

The reader should note that the membrane electrode assembly (MEA) is the component of the FC where all the electrochemical mechanisms take place. It comprises the gas diffusion layer (GDL), the anode catalyst layer (ACL), the cathode catalyst layer (CCL), and the membrane. Among the MEA subcomponents, the ACL and CCL are responsible for allowing the fast H_2 break down into protons (H^+) and the water formation when they react with O_2.

The voltage losses that take place at the ACL and CCL are called activation losses. They are due to the additional energy (overpotential) that must be applied over the reacting surface to achieve a desired reaction rate (reactants consumption). Part of the energy lost in the catalyst is not simply transformed into heat but also contributes to catalyst degradation through the loss of electrochemical surface area (ECSA) [37]. Among the catalyst degradation mechanisms, it is possible to identify Pt dissolution, Ostwald ripening, carbon corrosion, Pt particle detachment and Pt agglomeration as the primary degradation phenomena [38]. The rate at which all of these mechanisms influence the FC performance decay is increased at high temperatures [39, 40].

The membrane is the component that permits the H^+ transport from the anode (ACL) to the cathode (CCL) and is where the ohmic losses take place in the FC, primarily produced by its ionic conductivity, which is significantly influenced by the water content of the membrane [41]. The degradation of the properties of the membrane may be due to chemical or mechanical effects such as membrane decomposition or cracking due to abrupt changes in the water content [42]. These two mechanisms work interrelated, so they usually influence each other. The fluoride release rate of the membrane is often measured and used as an indicator to quantify the chemical and overall membrane degradation [43].

The GDL is a porous layer used to distribute homogeneously the reactants to the catalyst layers, to enhance the cell mechanical integrity, to enable the electrons to be conducted to the bipolar plates and to improve heat dissipation and water removal. The main voltage losses that the GDL contributes to are the mass or concentration losses that happen at high current densities. Nevertheless, the effect of GDL degradation on FC performance is minor. Therefore, the catalysts and membrane degradation are usually considered the most important phenomena affecting the FC output power decay [44].

In the last years, there have been considerable research efforts to identify and model all the phenomena responsible MEA degradation. In the scientific community, two different approaches to model FC degradation are usually considered: semi-empirical and analytical/physical. The former is based on obtaining degradation rates from a certain set of experimental data at known reference operating conditions and applies them directly through the use of constant coefficients, thus implying constant degradation rates that are independent of the FC electrochemical behavior and operating conditions. Although this practice is extensively used, this type of model is not suitable for predicting the FC degradation produced during driving conditions, where the FC stack operating conditions may deviate significantly from the reference or standard conditions considered at the experimental aging tests. The second approach could be named analytical/physical and is based on solving the transport equations and source terms to model degradation mechanisms such as the Pt loss in the catalysts or the change in the membrane ionic resistance. These detailed models are usually validated at very specific operating conditions and need very detailed information about the FC inner flows to model degradation such as the time evolution of the H_2 content in the membrane, which can not be predicted by most of the FC stack models and is currently unmeasurable during FC stack operation.

Empirical and semi-empirical FC stack degradation models are mainly based on the data obtained in the studies performed by Pei et. al [45] and Lu et. al [46]. In these studies, they carried out FC aging tests with a FC stack which data was used to develop a degradation model consisting of constant degradation rates. This model was validated with data obtained from an FCV urban bus operated daily for a long period of time. Nonetheless, most of the research work that utilize these coefficients do not know their source, since these studies are not referenced, nor the operating conditions of current density, relative humidity and temperature at which they were determined. Consequently, some authors apply them them directly over the FC stack no matter its operating conditions. These studies mostly consider this FC degradation model to explore different EMS optimizers integrating the FC degradation such as modular EMS considering fuzzy-logic and Rainbow-based SOC prediction [47], Pontryagin's Minimum Principle [48] or min-max game-based EMS [9], among others. Some of these studies modify the initial model to integrate natural degradation and multiply the degradation rates with correction coefficients whose origin is unknown [21].

In the literature, it is possible to find other alternative approaches for semi-empirical FC degradation modeling but they are limited and usually do not include the influence of the FC operating conditions (T and RH) on durability decay [49]. For instance, the model developed by Ou et. al [50] predicts degradation through a time-dependent exponential function acting on the exchange current density (activation losses). Another example is the study carried out by Ma et. al [51], where they used a recurrent neural network optimizer with grid long-short term memory to determine the change in the current due to FC degradation by fitting an activation function and the hyperbolic tangent of the FC state.

Apart from the aforementioned models, there are other semi-empirical degradation models that intend to integrate the FC operating conditions by modifying the degradation rates. The studies in which these models are developed often obtain experimental data from sources other than [45, 46] or self-produce them and use complex optimizers to match the coefficients of the functions they propose to scale the degradation rates. This is the case of the study carried out by Chen et al. [52], in which a FC degradation model was developed by fitting semi-empirical functions that relate the FC degradation to the FC current, temperature, relative humidity, and pressure to experimental data through genetic algorithms, extreme machine learning and wavelet analysis. Among these optimizing algorithms, that combining the wavelet analysis for multi-scale decomposition with genetic algorithms and extreme machine learning to develop the model of each sub-waveform offered a mean absolute relative error below 0.05%. Nonetheless, the scaling functions, although they were applicable to the specific FC used to produce the experimental data, lacked of a direct relation with the physical tendencies describing how the properties of the catalyst and the membrane decay, which implies that the fitted linear functions should need to be recalibrated for each FC stack. Bressel et al. [53] carried out a similar work by considering an extended Kalman filter to fit the linear function $\alpha(\mathrm{t})$ that was used to modify the FC ohmic resistance and the limiting current density defining the polarization curve by directly multiplying these parameters by and scaling factor. This model was initially calibrated using steady-state experimental data with constant load, therefore it was not useful for dynamic FC operation. Nonetheless, the authors further improved the model to integrate the effect of FC load change on performance decay [54].

The other approach to model FC degradation can be named the physical or analytic approach, as it intends to capture the detailed evolution of the degradation mechanisms, and describe them through analytical equations. The studies that consider this approach are mostly focused only the catalyst degradation [55, 56], or membrane degradation [57, 58], are validated in a very specific set of FC operating conditions of current density, relative humidity, temperature, dynamic/steady behavior,... and usually imply significant computational cost since some of them require solving additional transport equations.

2.7 Summary and conclusions

Along this chapter, the fundamentals of H_2 FC technology were presented together with a dedicated literature review focused on FC powertrains applied to passenger cars and heavy-duty applications, as well as on the modeling approaches to FC degradation.

Significant work has been performed in the last years to push forward the state-of-the-are of FC technology applied to passenger cars. The main research lines aimed at developing control strategies to minimize parameters such as the TCO, H_2 or energy consumption. Nonetheless, most of the research was focused on conventional FCV configurations and alternative powerplant architectures such as the FCREx powertrain were not analyzed for light-duty vehicle applications. Furthermore, among the presented studies, FCV models were too simple and could not replicate the change in the FC stack performance with the operating conditions or did not use an adequate EMS designed for benchmarking purposes. Even though the FCREx powertrain was considered for different applications, it was detected that further work with detailed models was required to understand how this powerplant architecture should be designed in terms of the size of the components and the control dynamics for passenger car applications to maximize performance and durability while minimizing its cradle-to-grave environmental impact. This constitutes the first main knowledge gap to be filled by this thesis.

Regarding the heavy-duty FCV applications, there has been significant advancements in understanding the environmental benefits this technology could offer in different scenarios such as China, America and Europe. Furthermore, different performance and cost-oriented analyses were identified in the literature considering different driving cycles, not only for long-haul transport applications by for other heavy-duty vehicles such as mining or port logistics trucks. Nevertheless, in all theses studies, the FC part of the powertrain comprised a single FCS, thus including several FCS as the industry trend indicates was not explored or optimized. As such, the second knowledge gap this thesis intends to cover is the optimization in terms of performance, durability and environmental impact of the multi-FCS powerplant architecture for heavy-duty vehicle applications by considering novel design approaches such as differential sizing and control, which remains unexplored in the literature.

A dedicated section to FC degradation models was included to highlight the necessity of developing semi-empirical physics-informed degradation models that can be applied to FC stack operated in realistic driving conditions. It was found that most of the semi-empirical models in the literature consisted of constant degradation rates that were not aware of the FC stack operating conditions while the physical/analytical models were only applicable to a very specific set of operating conditions and could imply significant computational cost. Therefore, the development of the semi-empirical physics-informed FC degradation model presented in this thesis intends to fill the knowledge gap defined by the absence of such models.

This thesis constitutes the first one focused in FC technology in the institute CMT-Motores Térmicos. As such, the work developed in this documents is intended to serve as the basis for a new research line in the department that is aligned with the new topics of interest in the automotive sector, the scientific community and the society through the sustainable development goals (SDG). The knowledge generated through the articles associated to this thesis constitute the early-life background

References

[1] Fuel Cells & Hydrogen (FCH). *Hydrogen Roadmap Europe - a Sustainable Pathway for the European Energy Transition.* Publications Office of the European Union, 1st edition, 2019.

[2] International Energy Agency. "The Future of Hydrogen". Technical Report June, 2019.

[3] Verhelst Sebastian and Wallner Thomas. "Hydrogen-fueled internal combustion engines". *Progress in Energy and Combustion Science*, Vol. 35 n^o 6, pp. 490–527, 2009.

[4] Benajes J., Antonio Garcia, Monsalve-Serrano Javier, Balloul Iyad and Pradel Gérard. "Evaluating the reactivity controlled compression ignition operating range limits in a high-compression ratio medium-duty diesel engine fueled with biodiesel and ethanol". *International Journal of Engine Research*, Vol. 18, pp. 60–88, 02 2017.

[5] García Antonio, Monsalve-Serrano Javier, Villalta D., Lago Sari Rafael, Gordillo Zavaleta Victor and Gaillard Patrick. "Potential of e-Fischer Tropsch diesel and oxymethyl-ether (OMEx) as fuels for the dual-mode dual-fuel concept". *Applied Energy*, Vol. 253, pp. 113622, 2019.

[6] García Antonio, Monsalve-Serrano Javier, José Sanchís Enrique and Fogué-Robles Álvaro. "Exploration of suitable injector configuration for dual-mode dual-fuel engine with diesel and OMEx as high reactivity fuels". *Fuel*, Vol. 280, pp. 118670, 2020.

[7] Desantes J. M., Molina S., Novella R. and Lopez-Juarez M. "Comparative global warming impact and NOX emissions of conventional and hydrogen automotive propulsion systems". *Energy Conversion and Management*, Vol. 221, pp. 113137, 2020.

[8] Teng Teng, Zhang Xin, Dong Han and Xue Qicheng. "A comprehensive review of energy management optimization strategies for fuel cell passenger vehicle". *International Journal of Hydrogen Energy*, Vol. 45 n^o 39, 2020.

[9] Sun Zhendong, Wang Yujie, Chen Zonghai and Li Xiyun. "Min-max game based energy management strategy for fuel cell/supercapacitor hybrid electric vehicles". *Applied Energy*, Vol. 267, pp. 115086, 2020.

[10] Zhang Hongtao, Li Xianguo, Liu Xinzhi and Yan Jinyue. "Enhancing fuel cell durability for fuel cell plug-in hybrid electric vehicles through strategic power management". *Applied Energy*, Vol. 241 n^o January, pp. 483–490, 2019.

[11] Wikner Evelina and Thiringer Torbjörn. "Extending battery lifetime by avoiding high SOC". *Applied Sciences (Switzerland)*, Vol. 8 n^o 10, 2018.

[12] Argonne National Laboratory. "Technology Assessment of a Fuel Cell Vehicle: 2017 Toyota Mirai Energy Systems Division". *US DOE -Energy Systems Division*, 2017.

[13] Lane Blake, Shaffer Brendan and Samuelsen Scott. "A comparison of alternative vehicle fueling infrastructure scenarios". *Applied Energy*, Vol. 259 n^o June 2019, pp. 114128, 2020.

[14] Feroldi Diego and Carignano Mauro. "Sizing for fuel cell/supercapacitor hybrid vehicles based on stochastic driving cycles". *Applied Energy*, Vol. 183, pp. 645–658, 2016.

[15] Pourabdollah M., Egardt B., Murgovski N. and Grauers A. "Convex Optimization Methods for Powertrain Sizing of Electrified Vehicles by Using Different Levels of Modeling Details". *IEEE Transactions on Vehicular Technology*, Vol. 67 n^o 3, pp. 1881–1893, 2018.

[16] Xu Liangfei, Ouyang Minggao, Li Jianqiu, Yang Fuyuan, Lu Languang and Hua Jianfeng. “Optimal sizing of plug-in fuel cell electric vehicles using models of vehicle performance and system cost”. *Applied Energy*, Vol. 103, pp. 477–487, 2013.

[17] Xu Liangfei, Mueller Clemens David, Li Jianqiu, Ouyang Minggao and Hu Zunyan. “Multi-objective component sizing based on optimal energy management strategy of fuel cell electric vehicles”. *Applied Energy*, Vol. 157, pp. 664–674, 2015.

[18] Lü Xueqin, Wang Peisong, Meng Lingzheng and Chen Chao. “Energy optimization of logistics transport vehicle driven by fuel cell hybrid power system”. *Energy Conversion and Management*, Vol. 199 n^o June, pp. 111887, 2019.

[19] Wu Xiaohua, Hu Xiaosong, Yin Xiaofeng, Li Lei, Zeng Zhaowei and Pickert Volker. “Convex programming energy management and components sizing of a plug-in fuel cell urban logistics vehicle”. *Journal of Power Sources*, Vol. 423 n^o March, pp. 358–366, 2019.

[20] Gaikwad Shrihari D. and Ghosh Prakash C. “Sizing of a fuel cell electric vehicle: A pinch analysis-based approach”. *International Journal of Hydrogen Energy*, Vol. 45 n^o 15, pp. 8985–8993, 2020.

[21] Hu Zunyan, Li Jianqiu, Xu Liangfei, Song Ziyou, Fang Chuan, Ouyang Minggao, Dou Guowei and Kou Gaihong. “Multi-objective energy management optimization and parameter sizing for proton exchange membrane hybrid fuel cell vehicles”. *Energy Conversion and Management*, Vol. 129, pp. 108–121, 2016.

[22] Feng Yanbiao and Dong Zuomin. “Integrated design and control optimization of fuel cell hybrid mining truck with minimized lifecycle cost”. *Applied Energy*, Vol. 270 n^o March, pp. 115164, 2020.

[23] Wu Xiaohua, Hu Xiaosong, Yin Xiaofeng, Peng Yiqiang and Pickert Volker. “Convex programming improved online power management in a range extended fuel cell electric truck”. *Journal of Power Sources*, Vol. 476 n^o 2019, pp. 228642, 2020.

[24] Yan Jianjun and Zhao Jia. “Willingness to pay for heavy-duty hydrogen fuel cell trucks and factors affecting the purchase choices in China”. *International Journal of Hydrogen Energy*, 2022.

[25] de las Nieves Camacho María, Jurburg Daniel and Tanco Martín. “Hydrogen fuel cell heavy-duty trucks: Review of main research topics”. *International Journal of Hydrogen Energy*, 7 2022.

[26] Liu Feiqi, Mauzerall Denise L., Zhao Fuquan and Hao Han. “Deployment of fuel cell vehicles in China: Greenhouse gas emission reductions from converting the heavy-duty truck fleet from diesel and natural gas to hydrogen”. *International Journal of Hydrogen Energy*, Vol. 46, pp. 17982–17997, 5 2021.

[27] Breuer Janos Lucian, Samsun Remzi Can, Stolten Detlef and Peters Ralf. “How to reduce the greenhouse gas emissions and air pollution caused by light and heavy duty vehicles with battery-electric, fuel cell-electric and catenary trucks”. *Environment International*, Vol. 152, 7 2021.

[28] Lee Dong Yeon, Elgowainy Amgad, Kotz Andrew, Vijayagopal Ram and Marcinkoski Jason. “Life-cycle implications of hydrogen fuel cell electric vehicle technology for medium- and heavy-duty trucks”. *Journal of Power Sources*, Vol. 393, pp. 217–229, 7 2018.

[29] Sim Kyuhyun, Vijayagopal Ram, Kim Namdoo and Rousseau Aymeric. “Optimization of component sizing for a fuel cell-powered truck to minimize ownership cost”. *Energies*, Vol. 12 n^o 6, 2019.

[30] Anselma Pier Giuseppe and Belingardi Giovanni. "Fuel cell electrified propulsion systems for long-haul heavy-duty trucks: present and future cost-oriented sizing". *Applied Energy*, Vol. 321, 9 2022.

[31] Ilio G. Di, Giorgio P. Di, Tribioli L., Bella G. and Jannelli E. "Preliminary design of a fuel cell/battery hybrid powertrain for a heavy-duty yard truck for port logistics". *Energy Conversion and Management*, Vol. 243, 9 2021.

[32] McKinsey. "A portfolio of power-trains for Europe: a fact-based analysis - The role of Battery Electric Vehicles, Plug-in Hybrids and Fuel Cell Electric Vehicles". Technical report, 2020.

[33] Office of energy efficiency and renewable energy - Department of Energy. "Durability Working Group - Hydrogen and Fuel Cell Technologies Office".

[34] Qin Yanzhou, Liu Guokun, Chang Yafei and Du Qing. "Modeling and design of PEM fuel cell stack based on a flow network method". *Applied Thermal Engineering*, Vol. 144 n^o August, pp. 411–423, 2018.

[35] Pan Tianyao, Shen Jiong, Sun Li and Lee Kwang Y. "Thermodynamic modelling and intelligent control of fuel cell anode purge". *Applied Thermal Engineering*, Vol. 154 n^o March, pp. 196–207, 2019.

[36] Li Huan, Ravey Alexandre, N'Diaye Abdoul and Djerdir Abdesslem. "Online adaptive equivalent consumption minimization strategy for fuel cell hybrid electric vehicle considering power sources degradation". *Energy Conversion and Management*, Vol. 192 n^o March, pp. 133–149, 2019.

[37] Chen Ben, Cai Yonghua, Shen Jun, Tu Zhengkai and Chan Siew Hwa. "Performance degradation of a proton exchange membrane fuel cell with dead-ended cathode and anode". *Applied Thermal Engineering*, Vol. 132, pp. 80–86, 2018.

[38] Cherevko Serhiy, Kulyk Nadiia and Mayrhofer Karl J.J. "Durability of platinum-based fuel cell electrocatalysts: Dissolution of bulk and nanoscale platinum". *Nano Energy*, Vol. 29, pp. 275–298, 2016.

[39] Zheng Weibo, Xu Liangfei, Hu Zunyan, Ding Yujie, Li Jianqiu and Ouyang Minggao. "Dynamic modeling of chemical membrane degradation in polymer electrolyte fuel cells: Effect of pinhole formation". *Journal of Power Sources*, Vol. 487 n^o December 2020, pp. 229367, 2021.

[40] Moein-Jahromi M. and Kermani M. J. "Three-dimensional multiphase simulation and multi-objective optimization of PEM fuel cells degradation under automotive cyclic loads". *Energy Conversion and Management*, Vol. 231 n^o February, pp. 113837, 2021.

[41] Terada Ichiro and Nakagawa Hideki. "Polymer Electrolyte Fuel Cell". *Kobunshi*, Vol. 57 n^o 7, pp. 498–501, 2008.

[42] Shi Shouwen, Sun Xiaoyi, Lin Qiang, Chen Jian, Fu Yuanjie, Hong Xiaodong, Li Cong, Guo Xiang, Chen Gang and Chen Xu. "Fatigue crack propagation behavior of fuel cell membranes after chemical degradation". *International Journal of Hydrogen Energy*, Vol. 45 n^o 51, pp. 27653–27664, 2020.

[43] Yuan Xiao Zi, Nayoze-Coynel Christine, Shaigan Nima, Fisher David, Zhao Nana, Zamel Nada, Gazdzicki Pawel, Ulsh Michael, Friedrich Kaspar Andreas, Girard Francois and Groos Ulf. "A review of functions, attributes, properties and measurements for the quality control of proton exchange membrane fuel cell components". *Journal of Power Sources*, Vol. 491 n^o January, pp. 229540, 2021.

[44] Chen Huicui, Song Zhen, Zhao Xin, Zhang Tong, Pei Pucheng and Liang Chen. "A review of durability test protocols of the proton exchange membrane fuel cells for vehicle". *Applied Energy*, Vol. 224 n^o April, pp. 289–299, 2018.

[45] Pei Pucheng, Chang Qianfei and Tang Tian. "A quick evaluating method for automotive fuel cell lifetime". *International Journal of Hydrogen Energy*, Vol. 33 n^o 14, pp. 3829–3836, 2008.

[46] Lu Languang, Ouyang Minggao, Huang Haiyan, Pei Pucheng and Yang Fuyuan. "A semi-empirical voltage degradation model for a low-pressure proton exchange membrane fuel cell stack under bus city driving cycles". *Journal of Power Sources*, Vol. 164 n^o 1, pp. 306–314, 2007.

[47] Peng Fei, Zhao Yuanzhe, Chen Ting, Zhang Xuexia, Chen Weirong, Zhou Donghua and Li Qi. "Development of robust suboptimal real-time power sharing strategy for modern fuel cell based hybrid tramways considering operational uncertainties and performance degradation". *Applied Energy*, Vol. 226 n^o April, pp. 503–521, 2018.

[48] Song Ke, Wang Xiaodi, Li Feiqiang, Sorrentino Marco and Zheng Bailin. "Pontryagin's minimum principle-based real-time energy management strategy for fuel cell hybrid electric vehicle considering both fuel economy and power source durability". *Energy*, Vol. 205, pp. 118064, 2020.

[49] Zhou Yue, Obeid Hussein, Laghrouche Salah, Hilairet Mickael and Djerdir Abdesslem. "A novel second-order sliding mode control of hybrid fuel cell/super capacitors power system considering the degradation of the fuel cell". *Energy Conversion and Management*, Vol. 229 n^o September 2020, pp. 113766, 2021.

[50] Ou Mingyang, Zhang Ruofan, Shao Zhifang, Li Bing, Yang Daijun, Ming Pingwen and Zhang Cunman. "A novel approach based on semi-empirical model for degradation prediction of fuel cells". *Journal of Power Sources*, Vol. 488 n^o December 2020, pp. 229435, 2021.

[51] Ma Rui, Yang Tao, Breaz Elena, Li Zhongliang, Briois Pascal and Gao Fei. "Data-driven proton exchange membrane fuel cell degradation predication through deep learning method". *Applied Energy*, Vol. 231 n^o July, pp. 102–115, 2018.

[52] Chen Kui, Laghrouche Salah and Djerdir Abdesslem. "Degradation model of proton exchange membrane fuel cell based on a novel hybrid method". *Applied Energy*, Vol. 252 n^o May, pp. 113439, 2019.

[53] Bressel Mathieu, Hilairet Mickael, Hissel Daniel and Ould Bouamama Belkacem. "Extended Kalman Filter for prognostic of Proton Exchange Membrane Fuel Cell". *Applied Energy*, Vol. 164, pp. 220–227, 2016.

[54] Jha Mayank Shekhar, Bressel Mathieu, Ould-Bouamama Belkacem and Dauphin-Tanguy Genevieve. "Particle filter based hybrid prognostics of proton exchange membrane fuel cell in bond graph framework". *Computers and Chemical Engineering*, Vol. 95, pp. 216–230, 2016.

[55] Kregar Ambrož, Tavčar Gregor, Kravos Andraž and Katrašnik Tomaž. "Predictive system-level modeling framework for transient operation and cathode platinum degradation of high temperature proton exchange membrane fuel cells â". *Applied Energy*, Vol. 263 n^o February, pp. 114547, 2020.

[56] Li Yunqi, Chen Xiran, Liu Yuwei, Xiong Danping, Li Jing, Yin Sha, Chen Liang, Li Congxin and Xu Jun. "Analytical modeling framework for performance degradation of PEM fuel cells during startup-shutdown cycles". *RSC Advances*, Vol. 10 n^o 4, pp. 2216–2226, 2020.

[57] Kwon Jun Hwa, Jo Seunghyun, Cho Ki Yeop and Eom Kwang Sup. "Deconvolution of the dehydration degradation mechanism in polymer electrolyte membrane fuel cells using electrochemical impedance analysis combined with the transmission line model under low humidity". *Journal of Power Sources*, Vol. 473 n^o March, pp. 228587, 2020.

[58] Futter Georg A., Latz Arnulf and Jahnke Thomas. "Physical modeling of chemical membrane degradation in polymer electrolyte membrane fuel cells: Influence of pressure, relative humidity and cell voltage". *Journal of Power Sources*, Vol. 410-411 n^o November 2018, pp. 78–90, 2019.

Chapter 3

Methodology

Contents

3.1 Introduction

In this chapter, the tools, techniques and procedures followed in this thesis to obtain the results discussed in chapters 4 and 5 are described. In general terms, the modeling framework can be divided into 3 different parts: the development of the FCV modelling platform (sections 3.3-3.6), the development of the FC stack degradation model 3.7, and the description of the LCA framework 3.8. After all these sections are explained, a last part (section 3.9) is used to elaborate on what driving cycle simulations were carried out for this work and how the different numerical models described communicate between each other in real time during the simulations.

3.2 Methodology Outline

The process followed along this thesis is fairly linear, although some analyses do not require the whole modeling framework described in this chapter. As can be perceived, the results in chapters 4 and 5 are based on simulations. As such, it is critical to ensure that the numerical tools are both representative of the physics and useful to extract meaningful conclusions.

In general terms, the first step of this work was to develop and validate 0D-1D FC stack and system models that can be later combined with more complex modeling frameworks (sections 3.3 and 3.4). The interaction between these models was optimized in such a way that the management of the BoP could ensure maximum efficiency at each current density (chapter 4, part 1, section 4.2). Then, they were integrated in a vehicle simulation platform consisting of other components such as the vehicle body, the battery and the electric motor (section 3.5). Note that this last vehicle platform was developed for two different applications: a passenger car and a heavy-duty vehicle. At this point, the interaction between the different elements of the powertrain had to be optimized to ensure minimum H_2 consumption, for which an energy management strategy (EMS) optimizer was embedded as the FCS controller (section 3.6). With this, a fully integrated FCV simulation platform was operative and could be used to carry out part of the simulations of this thesis. Nonetheless, in order to analyze and identify the main causes of performance loss along the life of a FC stack for automotive applications, a FC stack degradation model was developed and incorporated with the rest of the models to predict FC durability when subjected to driving conditions (section 3.7). Once all the models were combined and operative in the same simulation platform, all the driving cycle simulations related to architecture optimization were carried out (chapter 4, part 2, sections 4.3 and 4.4). Finally, after defining the LCA framework (section 3.8), the results from chapter 4, part 2, sections 4.3 and 4.4 were used to calculate the environmental impact of the architectures considered in this thesis (chapter 5), thus providing a further than the state-of-the-art insight on how the FCV should be designed to maximize performance, durability and minimize the environmental impact in both passenger car and heavy-duty vehicle applications. An outline of this process was previously presented in figure 1.5.

The FCV modeling framework was developed in GT-Suite v2020 software using the already-existing sub-models for PEMFC stacks and BoP components. GT-Suite is a 0D-1D modeling program commonly used in the automotive sector. As such, it is capable of reproducing complex thermofluid-dynamics phenomena through solving the energy, momentum, and mass conservation equations mixed with empirical correlations. 0D-1D modeling software is appropriate for sizing and optimization studies as they may be used to generate trustworthy conclusions at the expense of relatively low computational cost. However, particularly for any FCS, they must be calibrated using experimental data.

Complementary to this model, the EMS optimizer and the FC stack degradation model were developed in MATLAB Simulink and connected to

GT-Suite to ensure constant information exchange between all the models during the simulation of the vehicles in driving cycle conditions.

3.3 Fuel cell stack model

3.3.1 Numerical description

The polarization curve of the FC stack model utilized in this research is specified as follows:

$$V_{FC} = V_{OC} - V_{act} - V_{ohm} - V_{conc} \tag{3.1}$$

$$V_{OC} = \frac{-\Delta \bar{g}_f}{2F} \tag{3.2}$$

$$V_{act} = \begin{cases} \frac{R_{gas}T}{2F}\left(\frac{i}{i_0}\right) \\ \frac{R_{gas}T}{2\alpha F} ln\left(\frac{i}{i_0}\right) \end{cases} \tag{3.3}$$

$$V_{ohm} = R_{ohm}\, I \tag{3.4}$$

$$V_{conc} = -C\; ln\left(1 - \frac{i}{i_l}\right) \tag{3.5}$$

where V_{OC} is the open voltage circuit and V_{act}, V_{ohm} and V_{conc} are the activation, ohmic and mass transfer losses. Advanced losses modeling was utilized to incorporate the sensitivity of the ohmic resistance and the exchange current density to the FC operating conditions. The ohmic resistance R_{ohm} was modeled according to [1] by examining the change in the ionic conductivity of the membrane as a function of the membrane relative humidity/water content, temperature, and membrane properties:

$$\sigma_{30} = 0.005139w - 0.00326(w > 1) \tag{3.6}$$

$$\sigma(T_{cell}) = \sigma_{30}\; exp\left[1268\left(\frac{1}{303} - \frac{1}{273 + T_{cell}}\right)\right] \tag{3.7}$$

$$R_{ohm} = \int^{t_m} \frac{dz}{\sigma} \tag{3.8}$$

Where w is the local membrane water content, σ_{30} and $\sigma(T_{cell})$ are the protonic conductivity of the membrane at 30°C and at T_{cell} respectively, T_{cell} is the cell temperature, and t_m is the membrane thickness.

Analogously, the exchange current density was approximated as a function of the FC temperature, the oxygen partial pressure, the electrochemical activation energy, the electrode surface roughness and the reference exchange current density $i_{0,ref}$ [2].

$$i_0 = i_{0,ref} a_c L_c \left(\frac{p_{O_2}}{p_{O_2,ref}} \right)^{\gamma_c} exp \left[\frac{-E_{act}}{R_{gas} T_{FC}} \left(1 - \frac{T_{FC}}{T_{ref}} \right) \right] \tag{3.9}$$

Where $a_c L_c$ is the electrode roughness (defined by the material properties), p_{O_2} is the oxygen partial pressure, γ_c is the pressure dependency factor (which value is 1, as in [2]), E_{act} is the electrochemical reaction activation energy (66 kJ mol^{-1} for O_2 reduction on Pt), R is the ideal gas constant, and T_{FC} is the stack temperature.

The parameters which can be used to calibrate this model of the polarization curve (section 3.3.2) are the mass transfer loss coefficient α, the exchange current density $i_{0,ref}$, the limiting current density i_l and the open circuit losses, already included into V_{OC}. Note that although the usual expression for V_{OC} is that defined in equation 3.2, in the model used in this work V_{OC} was calibrated as part of the validation process so that it does not only include the losses attributed to the variation of the mean Gibbs potential but also other phenomena present in the experimental polarization curve at low current density such as the internal currents and the H_2 crossover.

Even though this model was calibrated to experimental results, it still has several drawbacks that are not important for the investigation. For instance, N_2 crossover was not modeled since the simulations of the WLTC 3b driving cycle only last 30 min (computational time), so the effect of N_2 on efficiency and degradation is minimum in such a short timespan. Furthermore, FC degradation was accounted for with a separate FC degradation model (section 3.7) that predicted the voltage loss as a functions of the operating conditions and the eletrochemical behavior of the degradation mechanisms. Nevertheless, FC degradation due to poisoning was not accounted for since most of the degradation of the state-of-the-art FC technology is produced from dynamic voltage cycling [3].

3.3.2 Validation

The calibration of an FC stack model using experimental data is essential to prove the validity of the model. Given the formulation of the polarization curve, there are numerous coefficients that have to be calibrated (eq. 3.1).

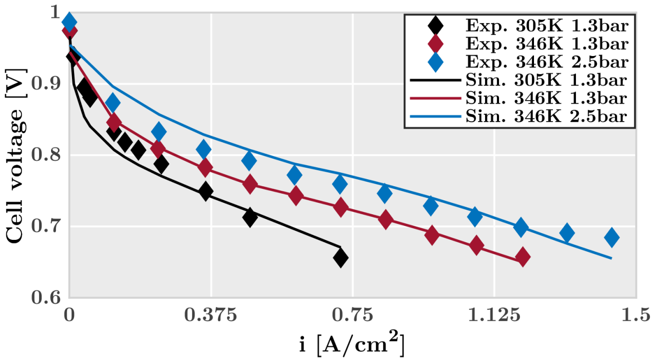

Figure 3.1. *Calibration/validation results at different conditions of pressure and temperature.*

As such, there are various combinations of parameters that may define the same polarization curve and, depending on the value of these coefficients, the sensitivity of the polarization curve to the boundary and operating conditions varies. In order to validate effectively any FC stack model, it is necessary to collect data regarding how the polarization curve evolves with temperature and pressure, i.e., the calibration should be valid for a broad range of operating conditions.

The experimental results from [4, 5] were utilized to calibrate and validate the FC stack model. These data were acquired from an 80-cell, 20 kW PEMFC stack at an experimental facility under temperature, stoichiometry and pressure-controlled conditions. Active surface area was estimated to be 250 cm^2. These data show how the polarization curve was determined at varying cathode pressure and temperature. Therefore, the data is suitable not only to capture the polarization curve but also capture and calibrate the sensitivity to temperature and pressure of the model.
Genetic algorithms were utilized to determine the calibration parameters and coefficients characterizing the polarization curve simultaneously under various operating conditions: $T_{cath} = 346\,K$ & $p_{cath} = 1.3\,bar$, $T_{cath} = 305\,K$ & $p_{cath} = 1.3\,bar$ and $T_{cath} = 346\,K$ & $p_{cath} = 2.5\,bar$ (figure 3.1). Anode pressure was constantly maintained 0.3 bar higher than cathode pressure and inlet H_2 was at ambient temperature (287 K). Stoichiometry was modified according to the experimental results [4, 5]. In order to assure convergence of genetic algorithms, 25 generations of solutions were employed. Following this process, it was feasible to decrease the total error of the model from

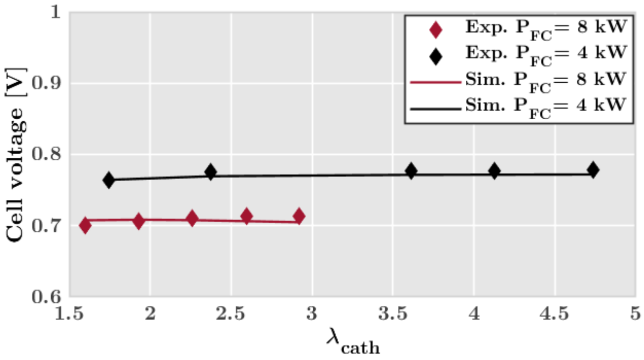

Figure 3.2. *Comparison between single-cell voltage experimental data and simulation results when varying cathode stoichiometry.*

experimental data to 2%. The largest deviations were recorded at low temperature and low current density. However, the deviation under these conditions was minor. The calibration of the model also included the effect of cathode stoichiometry over the cell voltage, defined as:

$$\lambda_{cath} = \frac{\dot{n}_{O_2}|_{supplied}}{\dot{n}_{O_2}|_{consumed}} \tag{3.10}$$

Where $\dot{n}_{O_2}$ is the molar flux of O_2. This parameter has significant impact on FC efficiency through the oxygen partial pressure affecting the activation losses. Therefore, in order to minimize the error in FC voltage prediction, the sensitivity of the FC stack model must match that of the experimental stack. Figure 3.2 shows how the sensitivity of the FC stack model to cathode stoichiometry matches the experimental data in [4] at 4 kW and 8 kW of load. At both loads, the model was able to reproduce the voltage sensitivity with stoichiometry. The maximum error (1.3%) was found at 4.7 of cathode stoichiometry and 4 kW of output power. Nonetheless, the FC stack was not expected to operated under such a high cathode stroichiometry and the simulation of a WLTC class 3b driving cycle with optimized EMS showed that cathode stoichiometry oscillated mostly between 1.5 and 2 where the deviation between the experiments and the simulations was lower than 1%.

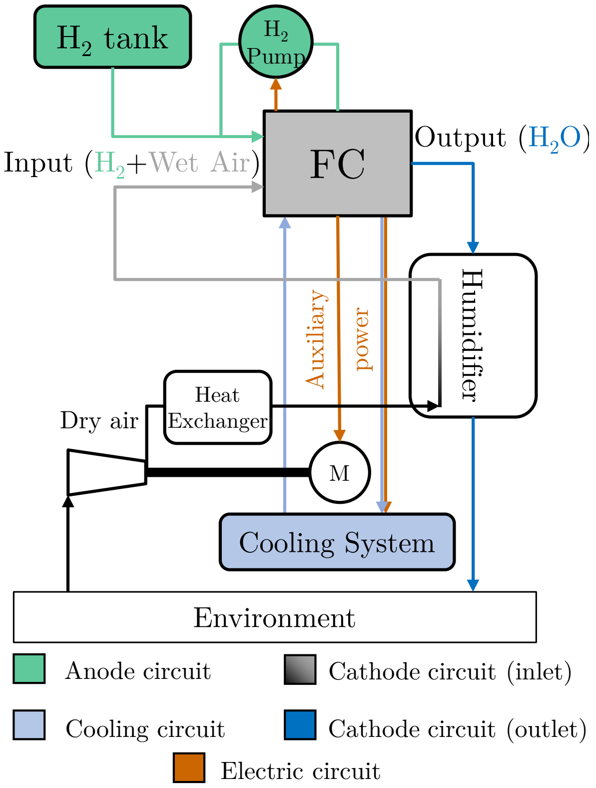

Figure 3.3. *Fuel cell system outline integrating all the inner circuits.*

3.4 Fuel cell system model

3.4.1 Balance of plant outline

As in any internal combustion engine (ICE), the design of the BoP is crucial to guarantee optimal performance of the engine. Different from ICE, in FCS, the design of the BoP appears independent from the FC stack as it may create electricity if just oxygen and H_2 are provided. However, the performance of such a system would be low as the FC stack efficiency is strongly influenced by cathode/anode pressure, temperature stoichiometry, and relative humidity (RH). As such, to increase the performance of any FCS, the BoP must be developed to supply the stack with the correct flow conditions and mass flow rate that maximize the FCS efficiency for the given FC stack size.

The schematic of the FCS is presented in figure 3.3. In this layout, 4 separate circuits may be differentiated: the anode, cathode, cooling and electric circuits. Among these, the electric circuit was solely utilized to power the devices of the BoP using the power acquired from the FC stack. The remainder of the circuits have different roles:

- The cathode circuit was in charge to feed air to the FC stack with a particular mass flow, pressure, temperature and relative humidity. To accomplish so, the air is drawn from the environment and compressed using a centrifugal compressor. The model for the centrifugal compressor was a parametric model. This was important to make the BoP model entirely scalable with the FC stack maximum output power. The compressor was driven by an electric motor attached to the FC stack. The regulation of the compressor operation was handled by 2 PIDs regulating a valve at the exit of the cathode circuit (after the humidifier) and the power given to the electric motor. After the compressor the air was cooled down using a heat exchanger before entering the humidifier. In the heat exchanger, the cooling liquid at 70°C was utilised as a cold reservoir. In the humidifier, the exit gases from the FC (extremely high RH) are utilized to raise the RH at the cathode intake. This component was modeled as 7000 pairs of parallel pipes with very small diameter coupled with a thermal mass and water injectors/ejectors to replicate the heat and water transmission. The humidifier was employed to maintain the cathode inlet at RH=80% when feasible. This value of RH was used to maximize the ionic conductivity of the membrane (decrease ohmic losses) during normal operation without saturating the membrane and prevent flooding effects (potentially present at higher RH), which were not in the scope of this modeling framework.

- The anode circuit supplies H_2 to the FC stack at a set pressure and flow rate from a 700 bar H_2 tank. In addition, H_2 is recirculated by means of an active recirculation loop, thereby increasing fuel usage and permitting relatively high dynamics in the anode circuit compared to passive recirculation. The pressure was managed using a valve at the exit of the H_2 tank while the mass flow rate was controlled with the H2 pump, even though the operation on both components is closely connected and impacts both pressure and mass flow rate. The pump was modeled using an isentropic efficiency of 0.8.

- The cooling circuit was mainly employed to maintain the FC stack working temperature within optimal settings to enhance its performance and preserve its integrity. The cooling system, albeit not depicted in figure 3.3 was made of a centrifugal liquid pump and a liquid-to-air radiator. The pump was regulated by a PID to guarantee that the coolant temperature was preserved to 70-75°C at the cathode exit of the FC stack.

The FC stack for the basic configuration is that mentioned in the preceding section (20 kW PEMFC, 80 cells). Due to the absence of data supplied by Corbo et al. [4, 5] used in the FC stack calibration (figure 3.1), the electrochemical active surface area and the pressure losses were modeled using the data of Ballard FCVelocity-9SSL fuel cell [6]. An indirect-type architecture is adopted for the vehicle, as such, a DC/DC converter is employed at the output of the FCS and at the output of the battery. The DC/DC converter for the FCS is modeled assuming 95% of energy conversion efficiency.

For the sizing studies, the mass flow rate across each element was multiplied by a scaling factor, thus scaling also the hardware design parameters for such mass flow rates. This scaling factor was also used to act on the number of cells of the FC stack.

3.4.2 Balance of plant limitations

Various limits in the BoP management were implemented in order to protect the integrity of the FCS and assure high efficiency. These constraints were:

- The PIDs controlling the valve of the H_2 tank were adjusted such that the difference in pressure between the anode and the cathode was equal or lower than 0.3 bar to reduce internal stress on the membrane and GDLs.
- The objective signal for the PID regulating the mass flow rate through the compressor by adjusting the power input to the electric motor was restricted such that cathode stoichiometry (λ_{cath}) was always greater than or equal to 1.8. This is especially critical when the FCS operation is very dynamic as rapid changes in load may have the FC stack suffer from starvation (λ_{cath} <1), thus causing the degradation of its performance.
- Cathode inlet pressure was maintained always higher to 1.2 bar to guarantee that the flow always can overcome the FC stack pressure losses. The highest limit of the cathode pressure was set at 2.5 bar to protect the mechanical integrity of the stack.

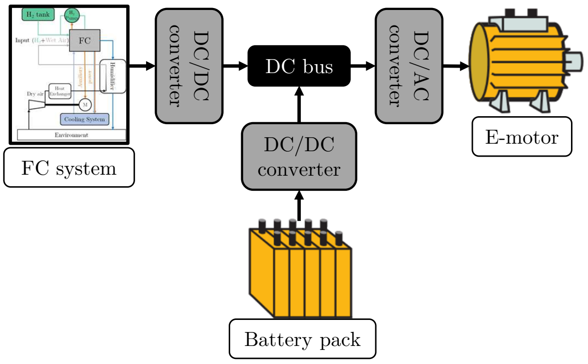

Figure 3.4. *Fuel cell vehicle indirect-type electronic architecture outline.*

- Anode stoichiometry was kept equal to 3 to increase FC stack efficiency and prevent anode starvation.

These limits were imposed not only in the simulations carried out to optimize the FCS efficiency by developing BoP management strategies but also in driving cycle simulations.

3.5 Fuel cell electric vehicle platform

The vehicle electronic architecture was selected to be indirect (figure 3.4). This arrangement, while it might be less efficient than the direct configuration, helps to improve the FC durability because the stack is shielded from the electric oscillations of the system bus and to downsize the FCS due to the DC/DC converter it is attached to [7]. As indicated earlier, the conversion efficiency of each DC/DC converter was considered constant and equal to 95% to account for these power losses. In contrast, the efficiency of the DC/AC converter or inverter required to supply electrical energy from the FCS or the battery to the e-motor was integrated in the e-motor map.

A Li-ion battery was chosen for the FCREx vehicle owing to the high energy density they have relative to other battery technologies. This battery was represented as a set of cylindrical cells in the form of 100 serial cells (to supply adequate power for the purely electric mode) and $n_{parallel}$ of parallel cells to impose the battery capacity. Each cylindrical cell had a nominal voltage of 3.6 V and a nominal capacity of 3.35 Ah and is modeled using an equivalent electric circuit (RC) whose open-circuit voltage and resistance depend on the state of charge and the battery temperature. A lumped mass thermal model was employed to verify that no overheating is generated in the battery. However, owing to the absence of data, the influence of temperature on the battery was not accounted for.

3.5.1 Passenger car

An FCREx vehicle needs relatively high storage capacity or volume to integrate the FCS, the H_2 tanks and the batteries. As such, a car body comparable to that of Hyundai Nexo (SUV) was utilized in the passenger-car related studies of this thesis. After an initial exploratory calculation, it was concluded that the car has adequate capacity to integrate rather high-size batteries, considering the trunk volume. The vehicle dry mass without the FCS, the H_2 tanks and the battery was calculated as 1400 kg, with a frontal area of 2.58 m^2 and a drag coefficient of 0.329, based on the technical specification of the Hyundai Nexo FCV [8]. The device powering the shaft is an electric motor with 120 kW of maximum power whose torque-power curve delivers highly-enough torque even at high load. As such, the connection between the e-motor and the shaft was arranged as a direct drive. In the vehicle mechanical model, integrated in GT-Suite v2020, other data such as the vehicle dimensions and the tires and axle characteritics such as the moment of inertia (0.625 kg/m^2) were also included to approach a realistic vehicle body behaviour during simulations. The sizing study for a passenger car application, which results are presented in section 4.3, comprised the variation of the H_2 tank capacity, the battery energy stored and the FC stack maximum power output. Given that the maximum power of the passgener car is limited by the e-motor, these components were sized to understand the change in H_2, energy consumption and range depending on the design choice. Particularly, these components were sized withing the following limits:

- H_2 tank capacity: [1, 5] kg
- Energy stored in the battery: [30, 60] kWh
- FC stack maximum power: [20, 100] kW

By definition, the mass and volume of these components change with their sizing. Therefore, the change in these parameters should be accounted for in the total mass of the vehicle to provide an accurate calculation of the power demand along the driving cycle. Volume was estimated only to

System	Data used to estimate Mass - Volume
FCS	Linear correlation - 175 kg and 286 l for a 30 kW system - 250 kg and 614 l for a 70 kW system
H_2 tank	0.045 kg H_2/kg system (700 bar) 0.03 kg H_2/l system
Battery	220 Wh/kg 600 Wh/l

Table 3.1. *Mass and volume data for the fuel cell system, H_2 tank and the battery [9–12].*

verify that these systems may fit into the vehicle body. The used values for the specific power, power density, specific energy, energy density and gravimetric/volumetric capacity of each component are those in table 3.1.

3.5.2 Heavy-duty vehicle

The heavy-duty fuel cell vehicle modeling platform was based on the first of its type to be commercialized, i.e., the Hyundai XCIENT fuel cell truck [13]. In terms of the propulsion system, the main difference between this vehicle and the passenger car is that this integrates 2 FCS working in parallel instead of 1. This is mainly motivated by the higher degree of flexibility this novel architecture offers in terms of optimizing performance and durability and due to the current trend in the FC market of standardize the 100 kW FC size so that if a particular application requires more than 100 kW of electrical power, "n" FCS are used instead of a FCS with a specific maximum power output. The most relevant data for the Hyundai XCIENT's body was extracted from [13] and can be found in table 3.3.

Note that, for the heavy-duty modeling platform, the mass during the driving cycle was kept constant with a value of 18000 kg instead of changing it with the sizing of the components. This was due to the fact that in the sizing of the multiple FCS, the sum of the maximum power output of all the FCS was maintained always at 240 kW:

	Max. stack power 1 ($\mathbf{P_{FC1}}$)	**Max. stack power 1 ($\mathbf{P_{FC2}}$)**
Design 1	120 kW	120 kW
Design 2	140 kW	100 kW
Design 3	160 kW	80 kW

Table 3.2. *Maximum stack power output of the multiple FCS configurations considered for the sizing of the HDFCV.*

For all these designs, the H_2 tank and battery capacity were kept constant to the values in table 3.3. Note that the only other parameter affecting the mass of the vehicle that could be change is the cargo and it does not affect the architecture of the powertrain. The total vehicle mass was then set to 18000 kg for the driving simulations for comparison purposes since the reference vehicle (Hyundai XCIENT fuel cell) was capable of providing a total range of 400 km under such conditions.

3.6 Energy management strategy

The energy management in a propulsion system with diverse energy sources mainly consists of identifying the pattern of power split that fulfils the design goals with minimal cost [14]. It is a fundamental feature influencing, to a large degree, the performance of the overall system [15]. In this regard, an incorrect power split scheme may alter the benchmark between various sizing combinations, consequently leading to a biased assessment on which is the superior powertrain sizing. Optimal Control (OC) is a tool particularly suited to design the energy management strategy in a benchmark investigation such as the ones provided in this thesis, as it naturally offers the optimal energy split for every powertrain evaluated. Accordingly, all the designs under study will be compared under the best scenario [16].

In accordance with the preceding idea, the OC problem that consists of determining the powertrain control law that minimizes a cost index across the selected driving cycles has been solved for every architecture analyzed. Regarding the control variable, given the powertrain model provided in previous sections, and specifically the energy balance in the DC bus (figure 3.4), leads to:

$$P_{dem} = P_{batt} + P_{FC} \tag{3.11}$$

	Dimensions
Wheel base	5.13 m
Length	9.745 m
Width	2.515 m
Height	3.73 m
	Weight
Empty vehicle	9795 kg
Normal driving	18000 kg
	H_2 tank
Filling pressure	350 bar
Capacity	32.09 kg
	Battery
Technology	NMC Li-ion
Capacity	1 pack of 73.2 kWh
	Other
Transmission	ATM S4500 (Allison) / 6 forward speed and 1 reverse speed
Configuration	4x2

Table 3.3. *Reference data for the heavy-duty FCV based on the Hyundai XCIENT fuel cell vehicle [13].*

where the electrical power needed by the motor to move the vehicle (P_{dem}) may be provided by the battery (P_{batt}), the FC (P_{FC}), or a mix of both. Note that the evolution of P_{dem} solely relies on the driving cycle and hence considering the FC power as control parameter ($u = P_{FC}$) the electrical power demanded to (or supplied by) the battery ($Pbatt$) may be computed as:

$$P_{batt} = P_{dem} - P_{FC}(u) \tag{3.12}$$

Concerning the optimization objective, the fuel consumption (H_2) was chosen as the cost to be minimized, although similarly, the fuel cost, the total energy consumed or CO_2 emissions associated to battery charging or H_2 production could be used. In this sense, all the simulations carried out in the frame of this thesis offer the minimum H_2 consumption, given the vehicle architecture and the limitations over the EMS. Durability, which was also considered as an optimization target, was optimized by imposing restrictions in the control strategy to prevent the FC from operating with high dynamics to minimize H_2 consumption.

The relation $P_{FC} = f(u)$ depends simultaneously on the FC stack current density and on the cathode and anode conditions (pressure, temperature and stiochiometry). This mathematical relation was generated in chapter 4, part 1, section 4.2 after optimizing the management of the BoP for each FCS and integrating a control protocol that allowed the FCS adapt the operation of its components based on the current density to maximize the FCS efficiency. Nonetheless, these data was obtained in steady-state, hence discrepancies may arise when this EMS optimizer is applied over a dynamic or a steady-state/mean value FCS mode (see section 3.9). Therefore, to minimize this source of error and integrate a dynamics-informed EMS optimizer, the relation $P_{FC} = f(u)$ was made dependent on the parameter that was identified the most influential in the FCS efficiency during dynamic simulations: the cathode pressure. As a consequence, this numerical space was transformed into $P_{FC} = f(u, p_{cath})$ in such a way that each time step $\mathrm{p_{cath}}$ is evaluated as a function of the control variable in the previous time step $u(t - dt)$ and used as a constant input to obtain P_{FC}. This methodology can only be used when the simulation time step is small enough, to hold the hypothesis that the cathode pressure does not change significantly between two consecutive time steps, and allowed to decrease the deviation between the FCS dynamic and steady-state models in WLTC 3b driving cycle simulations from 2.5-5% to lower than 0.5.

Given the chosen control variable and optimization criteria, the OC problem can be defined as finding the control sequence $u\left(t\right)$ over time t that minimises the cost:

$$J = \int_{t_0}^{t_f} P_f\left(u\left(t\right), t\right) \mathrm{dt} \tag{3.13}$$

where P_f represents the fuel (H_2) power consumed as a function of the control variable (u), which in this case is the FC current density. Because P_f is proportional to the amount of fuel consumed, minimizing equation 3.13 will inevitably reduce the amount of fuel consumed. The full FC model described in sections 3.3 and 3.4 was reduced to a look-up table ($P_f = P_f(u)$) that provided the fuel power P_f as a function of the FC stack current density, i.e. the control variable u.

The only state in the system, given the univocal relationship between u and P_f, is the energy stored in the battery (E_b), defined as:

$$\dot{E}_b = -P_b \tag{3.14}$$

being P_b the fluctuation in the energy state of the battery (which is considered negative when the battery is being charged an positive when the battery is being discharged). It's worth noting that P_b may be determined using P_{batt} and the battery model defined in 3.5.

Finally, since during a driving cycle simulation grid charging is not taken into account and all energy must come from the FC, the net battery charge change in a long-enough cycle should be zero in order to evaluate battery charge sustaining mode and to enable a fair comparison of the powertrains investigated in this thesis. This is considered in the optimization problem as follows:

$$\int_{t_0}^{t_f} P_b\left(u\left(t\right), E_b\left(t\right), t\right) \mathrm{dt} = 0 \tag{3.15}$$

Pontryagin's Minimum Principle (PMP) permits solving the global optimization problem described in equations 3.13-3.15 as a series of local optimization problems. Particularly, the PMP asserts that if u^* and E_b^* are the best trajectories of the control and battery energy across the driving cycle, then:

$$H\left(u^*, E_b^*, \lambda^*, t\right) \leqslant H\left(u, E_b^*, \lambda^*, t\right) \forall u \in U, t \in \left[t_0, t_f\right] \tag{3.16}$$

where H is the Hamiltonian function, defined as:

$$H = P_f - \lambda \dot{E}_b = P_f\left(u\left(t\right), t\right) + \lambda\left(t\right) P_b\left(u\left(t\right), E_b\left(t\right), t\right) \tag{3.17}$$

Note that since P_f and P_b have the same units, the co-state λ becomes dimensionless. PMP relates the value of λ with the evolution of the Hamiltonian (H) with regard to the state (E_b):

$$\dot{\lambda} = \frac{\partial H}{\partial E_b} \tag{3.18}$$

Replacing equation 3.17 into 3.18 and introducing P_{batt} yields:

$$\dot{\lambda} = \lambda \frac{\partial P_b}{\partial E_b} = \lambda P_{batt} \frac{\partial\left(P_b/P_{batt}\right)}{\partial E_b} \tag{3.19}$$

where the electrical power produced by the battery (P_{batt}), according to equation 3.12, depends on $u\left(t\right)$ but not on E_b. The ratio P_b/P_{batt} reflects the battery efficiency. Since the sensitivity of the battery attributes (open circuit voltage and internal resistance) on changes in E_b is low, λ may be considered to be constant for the considered system [17]. Therefore, the optimization problem is simplified to selecting the right constant value of λ which meets the problem constraint (equation 3.15) to maintain the charge-sustaining mode. A comprehensive analysis of the application of PMP to the Energy Management of Hybrid Electric Vehicles can be found in [14] and references therein.

Since the driving cycle simulations carried out in this thesis are known in advance, λ can be found by any iterative process by considering different values of λ until the constraint (equation 3.15) is met. An initial guess to the value λ can be obtained by applying the condition of minimum to equation 3.17, which leads to:

$$\lambda = -\frac{\left(\frac{\partial P_f}{\partial u}\right)}{\left(\frac{\partial P_b}{\partial u}\right)} \tag{3.20}$$

where terms in numerator and denominator are directly related to the efficiencies of FC and battery respectively, and $\left(\frac{\partial P_b}{\partial u}\right)$ is negative due to equation 3.12. Therefore, the ratio between FC and battery average efficiencies can be used as a good first guess for λ.

In this work, different restrictions on the EMS were imposed depending on the application of study. For passenger cars, the work was focused on understanding the effect on performance and durability when imposing restrictions on the dynamics and the operational space. These limits were imposed over the rate of change of the current density and over the mathematical space that determines the values the current density can acquire at any time step. The selection of the current density as the variable whose behaviour should be limited is motivated by two reasons. On one hand, the current density is directly proportional to the H_2 and air consumption, which means that the flow management strategies on the FCS to maintain a certain stoichiometry should depend on it. On the other hand, this variable represents the load of any FCS system regardless on the number of cells of the stack, which implies that any conclusion extracted from acting on the current density for a given stack could be more easily applied to other stack with different number of cells for sizing purposes. Therefore, the restrictions on $|\mathrm{di/dt}|$ and $\mathrm{i_{min}}$ were accounted for by means of step functions affecting the cost function J. In contrast, for the heavy-duty application only dynamic restrictions ($|\mathrm{di/dt}|$) were considered but they were imposed simultaneously in two different FCS.

In this sense, the Hamiltonian function, to be minimized each time step, is replaced by:

$$H = P_f - \lambda \dot{E}_b + L_1 + L_2 \tag{3.21}$$

where L_1 and L_2 are the limiting functions that increase the cost function value to infinite for the values of the control variable u (current density) out of the imposed bounds at each time step so that the EMS optimizer discards the operation at these points. Since these limits on the EMS change with the applications, $\mathrm{L_1}$ and $\mathrm{L_2}$ should change as well. For the passenger car application, their definition are only applied over the only FCS composing the propulsion system and are as follows:

$$L_1 = \begin{cases} 0 & u \geqslant i_{min} \\ inf & u < i_{min} \end{cases} \tag{3.22}$$

$$L_2 = \begin{cases} 0 & |\mathrm{du/dt}|(t+dt) \leqslant |\mathrm{di/dt}|_{max} \\ inf & |\mathrm{du/dt}|(t+dt) > |\mathrm{di/dt}|_{max} \end{cases} \tag{3.23}$$

For the heavy-duty application, in which 2 different FCS were considered to be working in parallel with potentially different stack sizing and dynamics, $\mathrm{L_1}$ and $\mathrm{L_2}$ turn into:

$$L_1 = \begin{cases} 0 & |\mathrm{du_1/dt}|(t+dt) \leqslant |\mathrm{di/dt}|_{max_1} \\ inf & |\mathrm{du_1/dt}|(t+dt) > |\mathrm{di/dt}|_{max_1} \end{cases} \tag{3.24}$$

$$L_2 = \begin{cases} 0 & |\mathrm{du_2/dt}|(t+dt) \leqslant |\mathrm{di/dt}|_{max_2} \\ inf & |\mathrm{du_2/dt}|(t+dt) > |\mathrm{di/dt}|_{max_2} \end{cases} \tag{3.25}$$

where $\mathrm{u_1}$ and $\mathrm{u_2}$ are the current densities of the each FCS. Note that for the algorithms controlling the EMS optimizer for the heavy-duty application, there are two control variables ($\mathrm{u_1}$ and $\mathrm{u_2}$) that need to be determined at each time step. In this case, the fuel power consumption affecting the cost function ($\mathrm{P_f}$) represents the fuel consumed by both FCS, which depends on the current density of each FCS. Therefore, the decision spaces for both $\mathrm{u_1}$ and $\mathrm{u_2}$ can be represented with the following matrices:

$$u_1 = \begin{bmatrix} u_{11} & u_{12} & \cdots & u_{1n} \\ u_{11} & \ddots & & u_{1n} \\ \vdots & \ddots & & u_{1n} \\ u_{11} & \cdots & & u_{1n} \end{bmatrix} \tag{3.26}$$

while the decision space for u_2 is the transpose of u_1:

$$u_2 = \begin{bmatrix} u_{21} & u_{21} & \cdots & u_{21} \\ u_{22} & \ddots & \ddots & \vdots \\ \vdots & & & \\ u_{2n} & u_{2n} & u_{2n} & u_{2n} \end{bmatrix} \tag{3.27}$$

Arranging the decision spaces of length n in this manner allows simplifying the selection of the control variables to just selecting the position on these matrices that provides the minimum value of the Hamiltonian function, turned into a matrix. Note that the selected position (column and row, same for both matrices) determines a value of u_1 and u_2, P_f, and H.

Finally, it is important to note that the lowest and highest values in the discrete decision space of u, for the passenger car application, and for u_1 and u_2, for the heavy-duty application were always 0 and 1.3 A/cm^2 but the mathematical space was significantly refined in the range of u, u_1 and u_2 in which L_1 and L_2 were 0 to minimize both deviations coming from discretization errors and computational cost.

3.7 Fuel cell degradation model

The goal of the degradation model developed in this thesis is to determine, quantify and integrate on FC models the degradation influence on the performance of any PEMFC working under dynamic conditions. This model may be utilized both in experimental and simulation applications. For experimental activities, the model may evaluate fundamental data from the FC stack and offer a diagnostic regarding how much the FC stack has been deteriorated throughout its operation, i.e., the model would be executed and implemented off-line. In contrast, for the simulation activities, the degradation model may be connected in parallel to the FC stack model and adjust the voltage output of the system by evaluating in real-time the operating conditions of the FC stack, i.e., this would be the case of an on-line implementation. For the latter scenario, the energy management strategy optimizer should be aware of how the degradation model influences the voltage and power output of the FCS so that the controller may adjust the FC stack current density for a certain power demand or regard the voltage and the current as independent outputs to produce power. In this particular instance, the output voltage of the FC stack in the FCS modelling platform should be decreased by applying the degraded voltage ratio or FC stack voltage loss ($\delta = 1 - V_{deg}/V_{FC}$), predicted by the degradation model, thus implying a decrease in the power-production capabilities of the stack. In this regard, the FCS and degradation model should function in parallel in such a manner that the degraded voltage ratio is updated each time step depending on the operation of the FC.

In the literature, most of the physical PEMFC degradation models focus on difficult or impossible-to-measure and monitorize parameters such as the concentration of H_2 in the membrane while the empirical or semi-empirical degradation models only depend on the current density of the FC and apply constant degradation rates without considering the physical conditions nor electrochemical behavior of the stack. This degradation model was designed as a hybrid of both approaches: semi-empirical and semi-physical, also called semi-empirical physics-informed. As such, the output of the degradation model is the FC stack voltage loss (δ) and/or the degraded FC voltage (V_{deg})) while the inputs may vary depending on the application. When used off-line, the inputs are the FC current density (i), temperature (T_{FC}), and cathode and anode relative humidity (RH_{an} & RH_{ca}). For the on-line application, the same inputs plus the FC stack voltage (V_{FC}) and the initial degradation state of the stack (δ_i) are required (figure 3.5).

The primary objective of this degradation model is to scale-up or scale-down reference degradation rates derived from a known experimental procedure, where the testing protocol characteristics (i and its temporal history) are known and operating conditions (T_{FC} and RH) are monitored. This model architecture would allow for the direct application of the research results from the state-of-the-art FC stack technology and the standardized durability protocols. This type of approach is required because these tests are carried out under very specific conditions that are very different from those that occur whenever an FCS is used in a real application [18, 19]. Therefore, in order to incorporate these functionalities, the architecture of this model consists of three distinct layers, each of which is represented by a set of linearly independent equations. The first layer represents the degradation

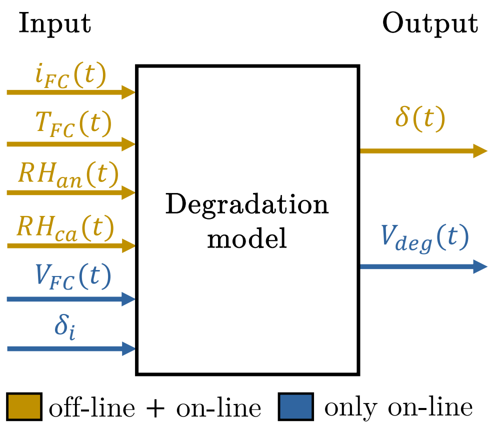

Figure 3.5. *Inputs-outputs diagram for the FC degradation model.*

rate at a specific condition, while the second and third layers, respectively, represent the effect of electrochemical and physical phenomena on FC voltage degradation. The layers are applied to predict the total voltage degradation described by the independent effects of low-power/idle (δ_{lp}), load-change (δ_{lc}), high-power (δ_{hp}), medium-power/natural (δ_{nt}), and start-stop (δ_{ss}) conditions on degradation following the set of equations [20]:

$$\delta = \int_0^t \left[\left.\frac{d\delta}{dt}\right|_{lp} + \left.\frac{d\delta}{dt}\right|_{lc} + \left.\frac{d\delta}{dt}\right|_{hp} + \left.\frac{d\delta}{dt}\right|_{nt} \right] dt + \frac{d\delta_{ss}}{dn_{ss}} n_{ss} \tag{3.28}$$

$$\left.\frac{d\delta}{dt}\right|_{lp} = \left.\frac{d\delta}{dt}\right|_{lp,ref} \cdot \xi_{lp}(i) \cdot \tau(T_{FC}) \cdot \eta(\overline{RH}) \tag{3.29}$$

$$\left.\frac{d\delta}{dt}\right|_{lc} = \left.\frac{d\delta}{dn_{lc}}\right|_{ref} \cdot \xi_{lc}\left(\frac{di}{dt}\right) \cdot \tau(T_{FC}) \cdot \eta(\overline{RH}) \tag{3.30}$$

$$\left.\frac{d\delta}{dt}\right|_{hp} = \left.\frac{d\delta}{dt}\right|_{hp,ref} \cdot \xi_{hp}(i) \cdot \tau(T_{FC}) \cdot \eta(\overline{RH}) \tag{3.31}$$

$$\begin{aligned} \left.\frac{d\delta}{dt}\right|_{nt} = {} & \frac{\left.\frac{d\delta}{dt}\right|_{hp,ref} \xi_{hp}(i_{hp}) - \left.\frac{d\delta}{dt}\right|_{lp,ref} \xi_{lp}(i_{lp})}{i_{hp} - i_{lp}} (i - i_{lp}) \\ & + \left.\frac{d\delta}{dt}\right|_{lp,ref} \xi_{lp}(i_{lp}) \end{aligned} \tag{3.32}$$

$$\frac{d\delta_{ss}}{dn_{ss}} = \left.\frac{d\delta}{dn_{ss}}\right|_{ref} \tag{3.33}$$

where i, $\frac{di}{dt}$, T_{FC} and $\overline{RH}$ are dependent on time because they are derived from the operating conditions as well as from the BoP management. $\overline{RH}$ is the mean relative humidity between the cathode and the anode, n_{ss} is the number of start-stop cycles in a given driving profile, i_{lp} is the maximum current density for which low-power degradation affects the voltage decay, and i_{hp} is the minimum current density for which high-power degradation has some effect of the performance of the system. Note that ξ, τ, and η are scaling functions whose value is 1 when the FC is operated under the identical reference conditions as in the testing protocols where the reference degradation rates were measured. In this model, the natural degradation rate is not altered by the operating conditions of temperature and relative humidity because, by definition, it has effect no matter how the FC is operated. Nonetheless, it is modeled by considering the hypothesis that it is proportional to the flow of protons throughout the membrane and the catalysts and varies uniformly through the polarization curve.

In the literature, it is a standard practice to regard the V_{FC} as the parameter representing the load of the FCS. However, the voltage of FC stacks is a consequence of many factors such as the cathode/anode conditions, the stack temperature, and, mainly, the current density which defines the flow of protons going through the membrane, the amount of H_2 dissociated at the anode catalyst layer and the reaction rate of water formation at the cathode catalyst layer. As a result, it looks more reasonable to regard the current density as the variable indicating the FC load and the effect of the electrochemical processes on degradation rates. In this model, the equations were built to be dependent on the current density. Therefore, the voltage-based data in the literature was transformed to current-density-dependant using empirical data for the proposed model [21].

The phenomena described in each layer and a thorough discussion of the equations above is conducted in section 3.7.1. The 1^{st} layer is described by the reference values $\delta_{x,ref}$ obtained from experimental degradation test procedures, the 2^{nd} is described by the ξ functions which represent the normalized scaling function of the degradation rate with the operating conditions by considering the electrochemical nature of FC degradation, and the 3^{rd} layer is described by the τ and η functions representing the rate of change of the degradation phenomena with temperature and relative humidity. The voltage degradation specified in the preceding equations is applied across a reference current density (i_{ref}) and then distributed throughout the polarization curve as discussed in section 3.7.5.

3.7.1 Degradation model outline

As described before, the model structure consists of 3 different layers, being the 1st layer composed by degradation rates obtained experimentally at very reference conditions while the 2nd and the 3rd layers are used to scale-up or scale-down the reference degradation rates. In this section, every layer of the model is described and the equations used to scale the degradation rates are presented. Note that all the scaled degradation rates are expressed as the degraded voltage over the non-degraded or nominal FC voltage at 1 A/cm^2, in accordance with DoE 2020 objectives for PEMFC durability [22].

The propagation of the voltage losses along the polarization curve, which are not constant, is not described in this section as it is not anything impacting the degradation rates but an integration method. As such, although it is part of the model structure and may be called a 4th layer, it was separated and discussed in section 3.7.5.

The reader must note that all the experimental data utilized in this research were acquired from diverse sources in the literature. As such, each figure and table bears in the title a reference for the paper used to gather the data.

3.7.2 1st layer: reference degradation rates

The 1st layer of the model comprises the reference degradation rates, which are a fraction or % of voltage loss as a function of time under a specific condition (low-power, medium-power or high-power) or per number of cycles (load-change or start-stop). These degradation rates correspond to those that should be derived from standard durability testing protocols, under controlled conditions of T_{FC} and RH. Note that it is necessary to know the values of the reference conditions throughout the experimental procedure so that the scaling functions of the 2nd and the 3rd layer are calibrated to be 1 at these values. In particular, the degradation rates employed in this model were acquired from actual laboratory testing (table 3.4) [23, 24]. These degradation tests were performed at $T_{FC} \sim 50°\text{C}$ and $\overline{RH} \sim 80\%$ and their results have been widely used in the literature [25–29], despite being used as constant degradation rates that do not consider how they ought to change with the FC stack operating conditions. This may create some inaccuracy in the actual degradation rate forecast since the T_{FC} and $\overline{RH}$ of the FC stack deviates considerably from those values under driving cycle conditions. In addition, these degradation rates were determined at 1 A/cm^2 (corresponding to ~0.7 V in the considered FCS [21]) for the high-power condition, at 0.01 A/cm^2

Condition	δ [fraction V loss]
Low power [/h] $\left(\frac{d\delta}{dt}\Big\|_{lp,ref}\right)$	$8.84\cdot10^{-6}$
Load change [/cycle] $\left(\frac{d\delta}{dn_{lc}}\Big\|_{ref}\right)$	$5.93\cdot10^{-7}$
High power [/h] $\left(\frac{d\delta}{dt}\Big\|_{hp,ref}\right)$	$1.03\cdot10^{-5}$
Start-stop [/cycle] $\left(\frac{d\delta}{dn_{ss}}\Big\|_{ref}\right)$	$1.96\cdot10^{-5}$

Table 3.4. *Reference degradation rates (1st layer) to be scaled.*

for the idle/low-power condition and with a load-change cycling amplitude, in terms of current density, going from the idle/low-power to the high-power conditions.

Note that, in this work, the coefficient for the high-power condition was modified with respect to their original value in [23] after the calibration process since the experimental data structure from which these reference degradation rates were acquired did not consider any natural degradation, albeit it is undoubtedly present during normal FC operation. This indicates that the steady-state natural degradation should be incorporated into the steady-state measurements of the degradation rate at low-power and high-power condition in [23]. As a result, the reference degradation rates for these conditions were overestimated and should be reevaluated to the values in table 3.4 to enable the inclusion of PEMFC natural decay.

The degradation rates in table 3.4 were utilized in this model for calibration and validation purposes. The model was developed in such a manner that these coefficients might be modified by state-of-the-art degradation rate coefficients to update the model to simulate the degradation behavior of modern PEMFC technology. In order to do so, the testing conditions at which the new degradation coefficients were acquired should be known and the scaling functions $\tau(T_{FC})$ and $\eta(\overline{RH})$ changed such that their value is 1 at those conditions.

The degradation rates in table 3.4 are those used for the initial calibration of the model to the experimental data in [23]. Nonetheless, the reason for using constant degradation rates in this 1_{st} layer is to be able to update the model when new degradation rates are obtained from durability testing protocols from state-of-the-art FC technology. As such, in this thesis the analysis pertaining to the passenger car application, aimed at detecting trends on FCV performance and durability when imposing different restrictions on the EMS, use the original degradation rates table 3.4. Nevertheless, for the studies related to the heavy-duty application on which longer lifetimes are required, the reference degradation rates were compared and updated to state-of-the-art values in such a way that they are in line with the targets set by the DoE. Among them, low-power, high-power and start-stop degradation rates are in the range of what is required of a FC stack for automotive application, but the load-change degradation rate (responsible for most of the voltage losses) is higher than required. As a consequence, for the heavy-duty application the load-change degratadation rate was updated to $4.94 \cdot 10^{-7}$. This value was calculated based on the PEMFC durability testing protocol defined by the DoE in table P.1 of document [30]. In this table, the maximum voltage loss after aging testing was set to 30 mV at 0.8 A/cm^2 after 30000 voltage cycles at RH=100% and T_{FC}=80°C, which for the FC used in this thesis is translated to a degradation ratio of $1.755 \cdot 10^{-6}$ at 1 A/cm^2 after applying the relation found in figure 3.11 and to $4.94 \cdot 10^{-7}$ at the reference conditions of RH and T_{FC} of the degradation model after dividing it by the value of the RH and T_{FC} scaling functions (equations 3.43 and 3.41) at 100% and 80°C, respectively.

3.7.3 2nd layer: electrochemical phenomena

The 2nd layer is designed to grant the model the capability of being able to apply the degradation rates measured at a specific current density (low-power, medium-power and high-power) or current density cycling amplitude (load-change) along the polarization curve by scaling them with the main electrochemical degradation-related phenomena and how they are affected by the FC operating conditions (physical trends). In this part, the origin and definitions of ξ_{lp}, ξ_{lc} and ξ_{hp} are discussed.

3.7.3.1 Low-power/idle condition

PEMFC stack degradation is largely due to the change in the properties of the membrane and the catalysts. Membrane degradation rate may be monitored using fluoride release rate (FRR), impacting the membrane chemical composition through the reduction in the fluoride concentration and therefore the membrane ionic conductivity (ohmic resistance) [31, 32]. Catalyst degradation does have a direct effect on the electrochemical surface surface area (ECSA) and the effective platinum surface area (EPSA), thus affecting PEMFC performance, in the form of voltage loss, through the increase in the activation potential [33]. Note that the decrease in the FC

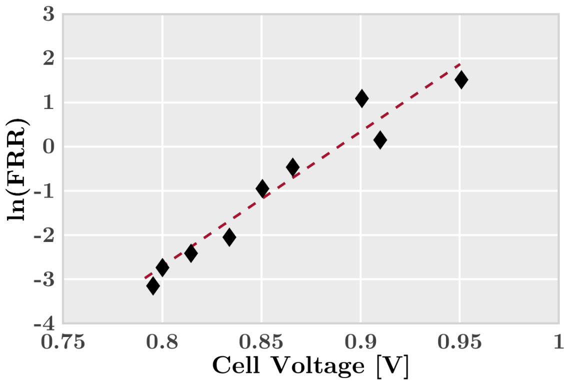

Figure 3.6. *Fluoride release rate evolution with cell potential. Data adapted from [3].*

performance due to ECSA loss is more significant than that due to membrane degradation [34].

The operation at low current densities implies high cell voltage (>0.8 V), which is translated into greater electrochemical energy for degradation processes. Under this scenario, at steady-state operation, the FRR was discovered to rise with voltage, i.e., decrease with current density [3]. This pattern is depicted in figure 3.6 and demonstrates how the membrane degradation rate changes with the FC load.

At this condition, surface carbon oxidation affects the catalyst, the gas diffusion layer, and the material of the bipolar plates, having a considerable impact on PEMFC performance. This performance decline was observed by monitoring anodic peak currents using the cyclic voltammetry approach after holding the PEMFC at 0.8, 1, and 1.2 V for a given amount of time by Kangasniemi et al. [35]. Since the rise in the anodic peak current is directly connected to the PEMFC performance loss, it is also reflective of the increase in the degradation rate.

The data shows the membrane [3] and catalysts [35] degradation phenomena was converted to current-density-dependent, weighted considering that 20% of the degradation is produced in the membrane and 80% in the catalyst, and normalized so that the combined scaling function has a value close to 1 at 0.01 A/cm^2, where the low-power degradation rate was measured. As a consequence, the normalized scaling function $\xi_{lp}(i)$ was defined as:

$$\xi_{lp}(i) = -0.176 \cdot \ln i + 0.169 \tag{3.34}$$

Note that this scaling function is only valid for low-power, i.e., when $i < i_{lp}$. When the PEMFC is running at other loads (medium or high) the value of this function becomes 0 to disable the degrading mechanisms pertaining to the low current density/high voltage operation. The threshold i_{lp} is calibrated on section 3.7.6 to define the limits on which each degradation mechanism dominates the PEMFC ageing based on the experimental data.

3.7.3.2 Load-change condition

The degradation owing to load-change condition is largely due to quick changes in i, T_{FC}, $\overline{RH}$, stoichiometry,... The key phenomena responsible for the degradation of the membrane and catalysts the are the problems related to anode starvation, flows, and water management. These phenomena are attributable to the lag between the characteristic time of the flow and the characteristic time of the electrochemical and electric phenomena [3]. Understanding this, it is feasible to deduce that cause of the load-change degradation is continuous, i. e., it is impossible to define it by means of discrete voltage cycles. However, forecasting such particular issues of the FC stack inner flows management is not computationally inexpensive in the frame of 0D-1D FC models. As a consequence, in those studies where the degradation rate due to the load-change condition is intended to be predicted with 0D-1D FC models, the researchers mostly try to detect the current density cycles (n_{lc}) or the time at which the FC is under the load-change condition without indicating a criterion to detect or scale such load-change degradation and apply the corresponding voltage loss at reference testing condition per load-change cycle or unit of time [26, 36]. Nevertheless, the voltage oscillations that an FC stack endures during driving conditions are far from near to those to which FC stacks are exposed to during voltage cycling testing (standardized durability tests). In order to overcome this difference, a discrete phenomenon such as the voltage cycling was again turned to a continuous degradation problem, nearer to its true nature. To achieve so, this degradation model monitors the fluctuation of the current density each time step.

With just this sensing approach, the degradation under load-change situations is treated again as a continuous phenomenon. Nonetheless, this is only helpful to identify the existence of the degrading state, not to quantify the deterioration rate at various load-changing cycles. In order to address this problem, it is assumed that the intensity of the degradation phenomenon scales with the amplitude of the load change for a given time-step, i.e., with the magnitude of di/dt, from the reference condition. With these assumptions, the appropriate analytical formulation of ξ_{lc} is:

$$\xi_{lc}\left(\frac{di}{dt}\right) = \frac{dn_{lc}}{dt}\frac{\frac{d\delta}{dt}}{\frac{d\delta}{dt}\Big|_{lc,ref}} \tag{3.35}$$

$$\begin{aligned} \frac{d\delta}{dt}\bigg|_{lc,ref} = \frac{d\delta}{di}\,\frac{di}{dt}\bigg|_{lc,ref} &= \frac{d\delta}{di}\,\frac{di}{dn_{lc}}\bigg|_{lc,ref}\,\frac{dn_{lc}}{dt} \\ &= \frac{d\delta}{di}\frac{dn_{lc}}{dt}\,2\left|\Delta i\right|_{ref} \end{aligned} \tag{3.36}$$

$$\frac{d\delta}{dt} = \frac{d\delta}{di}\frac{di}{dt} = \frac{d\delta}{di}\left|\Delta i\right|_{dt} \tag{3.37}$$

where $|\Delta I|_{ref}$ is the reference current density amplitude for the voltage cycling test per voltage cycle (0.99 A/cm^2) while $|\Delta I|_{dt}$ is the absolute value of the current density variation for a particular time step dt. Note that $|\Delta I|_{dt}$ is used in absolute value and $|\Delta I|_{ref}$ is multiplied by 2 to account for the FC degradation when increasing (possible starvation) and decreasing (possible water management problems) the current density in voltage cycling tests and driving cycle conditions. The term dn_{lc}/dt is added in ξ_{lc} to convert the discrete voltage degradation rate under reference conditions ($d\delta/dn_{lc}|_{ref}$) to a continuous degradation rate dependent on time. Deriving the aforementioned equation, the final expression for ξ_{lc} is:

$$\xi_{lc}\left(\frac{di}{dt}\right) = \frac{dn_{lc}}{dt}\frac{\frac{d\delta}{dt}}{\frac{d\delta}{dt}\Big|_{lc,ref}} = \frac{\left|\Delta i\right|_{dt}}{2\left|\Delta i\right|_{ref}} \tag{3.38}$$

3.7.3.3 High-power condition

FC stack degradation mechanisms are often less significant under high-power conditions compared to low-power or load-change conditions. However, under high-power conditions, the ohmic and activation losses of the FC stack are considerable, which increases the inefficiencies, and therefore the heat losses, of the FC stack. The rise in T_{FC} at this situation may raise the intensity of the degradation phenomenon, possibly leading to larger degradation rates than under low-power settings. The degradation phenomena that are intrinsic to the high-power state include the occurrence of partial oxygen starvation, high membrane water content (accelerating oxidation and corrosion mechanisms), and a general rise of the kinetic, ohmic, and mass transport losses. All these phenomena only occur from a particular current density and scale with the flow of protons across the membrane, which is precisely proportional to the current density during normal operation. As such, the degradation mechanism in high-power conditions without considering the independent impact of T_{FC} and $\overline{RH}$ should scale with the current density following:

$$\xi_{hp} = \frac{i}{i_{hp}} \tag{3.39}$$

where i_{hp} is the lowest current density at which the high-power degradation becomes noticeable (calibrated to experimental results to 1 A/cm^2). This scaling function (ξ_{hp}) has a value of 0 when $i < i_{hp}$, thereby triggering the high-power degradation diagnostic only at high-power conditions.

3.7.3.4 Medium-power/natural degradation

Natural degradation in FC is commonly utilized in the literature to describe the natural deterioration of the FC stack components during the steady-state or low-dynamics operation. These degradation phenomena are noteworthy for any FC that is used for power production but merely a tiny portion of the overall degradation for a FC that operates under dynamic conditions, such as those found in transportation applications. As mentioned previously, this model assumes the natural degradation to be independent conditions of T_{FC} and $\overline{RH}$ but proportional to the flow of protons across the membrane and the catalysts, i.e., to the current density (equation 3.32). Natural degradation is generally described as a steady voltage decrease with time because it is highly time and resources intensive to monitor [37]. As a result, natural degradation rates are only recorded at a certain current density, hence the impact of increasing the current density on natural degradation on the same FC type and under the same conditions is unknown. However, it is anticipated that the FC natural decay scales with the rate at which the electrochemical processes are taking place in the membrane and the catalyst. This impact was incorporated in this model as in equation 3.32 and was validated in the validation section such that it reflects steady-state degradation rates that provide ∼40000 h till the end of life, in accordance with DOE 2020

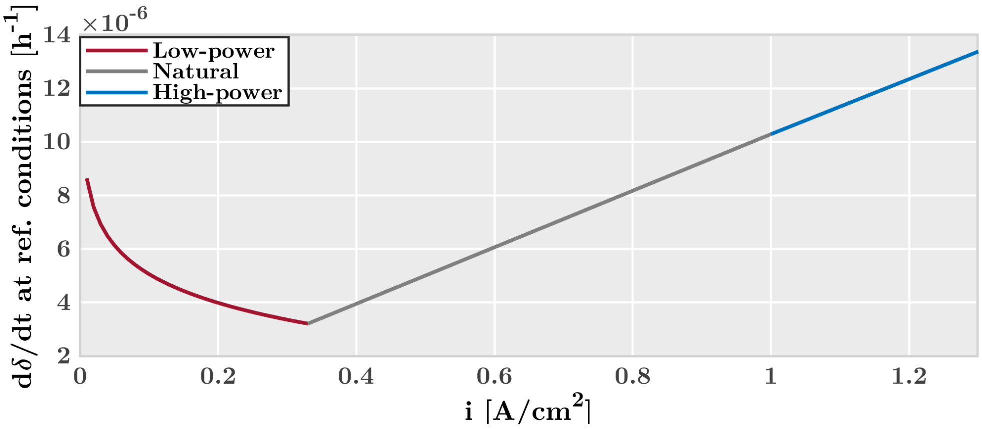

Figure 3.7. *Evolution of $d\delta/dt$ at reference conditions of T_{FC} and $\overline{RH}$.*

objectives [19]. This implementation technique implies that the degradation rate at reference conditions is continuous (figure 3.7) and that part of it is incorporated in the low-load and high-power situations.

3.7.4 3rd layer: physical conditions

Once the reference degradation rates have been scaled with the electrochemical phenomena, they need to be scaled with the physical conditions of the FC stack. Among the different conditions that affect the PEMFC stack degradation rates, the stack temperature (T_{FC}) and the membrane relative humidity have the most significant impact via the increase of the reaction kinetics of the degradation-associated chemical reactions and the change in the cathode catalyst layer properties (Pt grain size, thickness, and carbon corrosion). In this model, the average value of the relative humidity between the anode and the cathode ($\overline{RH}$) was used instead of the membrane relative humidity as it is not quantifiable and relies on other submodels that may create additional uncertainty. The approach of considering the average RH is in line with the extended method of calculating the membrane water content in 0D-1D FC models, which is predicted assuming equilibrium from the activity of the vapor phase of the inlet flows/relative humidity (RH=$X_{H_2O} \cdot p/p_{sat}$) [1, 38] as the average of the water content between the anode and the cathode catalyst layers [39]. Selecting locally the anode or the cathode relative humidity at the stack inlet would make the degradation rates depend significantly on the anode/cathode humidification strategy and

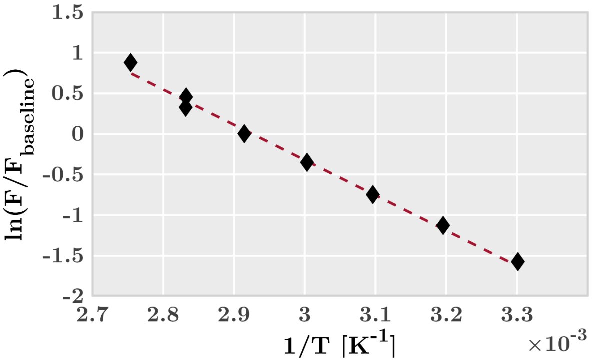

Figure 3.8. *Fluoride release rate relationship with temperature using DuPont Nafion® 112. Data retrieved from [3].*

system, which may differ from the actual conditions of water content at the membrane that are affected by the water production at the cathode catalyst layer. This is accounted for in the RH at the anode and the cathode by solving the mass transport equation. The feature of using $\overline{RH}$ helps on the applicability as it is can be acquired through simulations.

3.7.4.1 Effect of temperature on degradation

The influence of temperature on degradation rate is described by the $\tau(T_{FC})$ function and is universal to all the degradation rates at various conditions. Operation temperature has the largest impact on the degradation processes and the FC contamination. Analogous to the influence of low-power electrochemical mechanisms over degradation, this model addresses the effect of T_{FC} over membrane and cathode catalyst degradation processes. In the case of membrane degradation, it is due to chemical reactions that yield non-zero fluoride release rates and follows an Arrhenius relation with temperature (figure 3.8).

For catalyst degradation, the temperature has a direct influence on the ECSA, i.e., Pt surface loss, via Pt dissolution and grain growth. This model employs the data collected by Bi et al. [40] at 40, 60, and 80°C where the residual ECSA was assessed after 110 h of potential cycling testing (46, 29, and 26% respectively). This residual ECSA was then transformed to equivalent V loss by relating the ECSA loss to voltage loss at 1 A/cm^2 under voltage

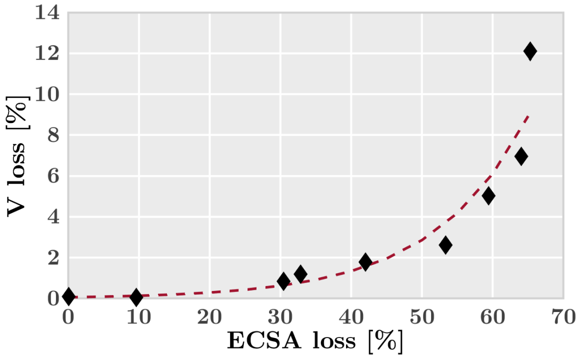

Figure 3.9. *Correlation between V_{loss} [%] and $ECSA_{loss}$ [%] approximated from data from [3, 41] by measurements at 1 A/cm^2 after voltage cycling tests.*

cycling tests from 0.6 V to 1.3 V from the experimental results obtained by Jia et al. [3, 41] with the following expression (figure 3.9):

$$V_{loss}\ [\%] = 0.06447e^{0.0758 \cdot ECSA_{loss}\ [\%]} \tag{3.40}$$

The voltage loss derived from the catalyst degradation and the FRR was normalized so that their value is 1 at reference temperature (50°C) and combined making the assumption that 20% of degradation comes from the membrane and 80% from the catalyst degradation. From this data, the function that scales the degradation phenomenon with the stack temperature is defined as:

$$\tau(T_{FC}) = -5.390 \cdot 10^{-4} T_{FC}^2 + 0.399 \cdot T_{FC} - 71.576 \tag{3.41}$$

being it valid in the range of $T_{FC} \in [310, 373.15]$ K.

3.7.4.2 Effect of relative humidity on degradation

High relative humidity levels have substantial influence on electrode degradation. Namely, high RH influences the catalyst layers by boosting the degrading mechanisms linked with Pt grain growth [42], Pt loss, [43] and CCL thickness [44]. Among these three factors, the ECSA degradation rate is predominantly controlled by the Pt grain size increase. In order to evaluate the influence of RH on Pt grain size growth rate, voltage cycling testing was performed under different value of RH by [44] (figure 3.10). From these data, it was feasible to detect the detrimental influence of RH on electrode assembly's performance decay. Nonetheless, to apply these results to this model, it is necessary to convert them into an equivalent reduction of the ECSA, then to equivalent voltage loss, and finally normalize them into a function $\eta(\overline{RH})$ whose value is 1 at reference conditions ($\overline{RH} = 80\%$). The relation between the ECSA and the radius of the Pt particles in the catalytic layer (r_{Pt}) is [45]:

$$ECSA = \epsilon_1 \frac{3}{r_{Pt}\rho_{Pt}} \tag{3.42}$$

where ρ_{Pt} is the Pt density. Note that ϵ_1 and ρ_{Pt} are constant parameters. Therefore, the reduction in the ECSA is inversely related to the rise in Pt grain size growth.

The remaining ECSA is then estimated using the data in figure 3.10 and the equation 3.42. Finally, $\eta(\overline{RH})$ is derived by translating the ECSA loss into voltage loss by equation 3.40 and normalizing the resultant function such that it is 1 at $\overline{RH} = 80\%$:

$$\eta(\overline{RH}) = 0.10646e^{0.028 \cdot RH\ [\%]} \tag{3.43}$$

This equation is valid for RH up to 100% because membrane flooding and its influence on voltage loss is not within the scope of this model and it normally does not happen under normal operation if the inflows are regulated appropriately. For RH higher than 100%, it is hypothesized that additional degradation processes, such as gas diffusion layer wear or increased catalyst corrosion [46], increase the rate of degradation.

3.7.5 Degradation model integration

3.7.5.1 Integration along the PEMFC polarization curve

As it is generally known, the FC voltage along the polarization curve varies with the current density dependent on the ohmic, activation, concentration, and internal current losses. As a result, applying a the same ΔV or δ caused by degradation across two distinct current densities has different consequences

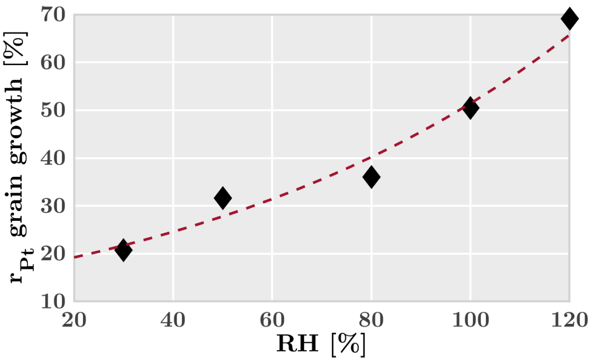

Figure 3.10. *Evolution of catalyst Pt grain size growth after 3000 voltage cycles. Data extracted from [3, 44].*

on the FC performance. In the majority of the research work in the literature, the degradation effect is considered to be uniformly distributed over the polarization curve, which has been demonstrated not to be the case [47]. In order to tackle this issue and also provide a more realistic and physical distribution of the degradation voltage loss effect over the polarization curve, this model was designed to determine all the degradation rates (section 3.7.1) as the voltage loss at a reference current density of 1 A/cm^2 and then distribute the voltage loss along the polarization curve from experimental data.

The data utilized for this purpose was that available in [47]. In this work, Bezmalinovic et al. conducted accelerated stress voltage cycling tests over a PEMFC and assessed the polarization curve before the testing, and after 1000, 3000, and 5000 cycles. From such experimental polarization curves, it was feasible to determine how the voltage along the polarization curve varies for each current density at various degradation levels.

In order to distribute the degradation effect from the reference current density (1 A/cm^2) to the rest of the polarization curve, the variation of the voltage at each current density of the experimental polarization curve in [47] was compared against the voltage loss at the reference current density (figure 3.11). From this comparison, it was established that the change of the voltage owing to degradation at any current density changed linearly with the voltage decay at the reference current density of 1 A/cm^2. As such, the experimental data in figure 3.11 was utilized to distribute the value of δ across the polarization curve. Note that this data also includes highly advanced deterioration states when the PEMFC has already reached the end of life.

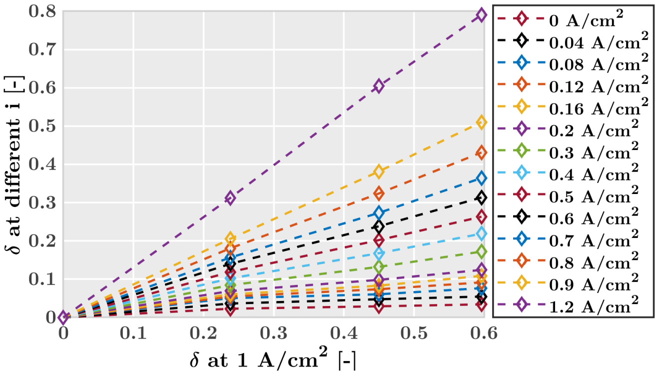

Figure 3.11. *Relation between voltage loss δ at reference current density and δ along the polarization curve. Data extracted from [47].*

3.7.5.2 Integration with PEMFC models

As described earlier in section 3.7, this model was meant to be a plug-in tool in any PEMFC simulation environment. Two distinct techniques might be followed in order to integrate this appropriately into an FC model, depending on the FC management strategy.

In the first scenario, if the FC control is handled by means of power demand, the variable δ at the associated current density for each time step might be applied directly over the electrical power supplied by the FC as a power-decreasing factor:

$$P_{FC,deg} = P_{FC} \cdot (1 - \delta) \tag{3.44}$$

Note that, in this situation, the system controller should be aware of the power loss due to deterioration and modify constantly the current density to meet the power requirement considering the degradation effects. This technique is useful to comprehend the power decay and perform calculations about the rise in H_2 consumption due to the degradation state. Nevertheless, the EMS is not aware of the degradation impacts over the power-generating capacities of the PEMFC.

The second approach is useful, particularly in dynamic simulations such as driving cycles where the energy fluxes should be appropriately handled to attain the optimal global efficiency. It consists of integrating this model both in the PEMFC and into the EMS in such a manner that the EMS optimizer is completely aware of the true H_2 consumption and power-generation capabilities at each current density. In this situation, the internal and basic PEMFC models that the EMS generally have must include this degradation model and utilize it to adjust the mathematical decision space. The value of δ might be applied over the voltage or over the FC electrical power. Although this technique entails some duplicity, it is suggested since merely putting the degradation effects on the PEMFC model but not in the EMS would generate some discrepancy between the models, generating numeric inaccuracies. This second approach was used in the simulations carried out in the frame of this thesis, since the decision space of both the passenger car and heavy-duty FCVs were described in terms of the current density so that dynamic and operation contraints could be placed during driving cycle simulations.

3.7.6 Validation

The validation of the model was conducted using the data in [23], considering the simulation of an FC-powered bus running in actual driving cycle scenarios. Figure 3.12 depicts the power demand of the FC under actual driving conditions obtained experimentally from a city bus running on a daily route. To conduct the validation of the model, a scale version of the FCS model described in section 3.4 was employed. This model was adjusted to have the same characteristics as the FC stack in the bus (280 cm^2 of active surface area and comparable power output). This stack was subsequently incorporated into a balance of plant such that the flow conditions of the FC stack were similar to those found in an FCV.

After simulating this driving cycle and determining the evolution of the current density, the temperature, and the cathode and anode relative humidity, the predicted and experimental degradation rates were compared by source (figure 3.13). The experimental results produced by Pei et. al incorporated two separate degradation sources under steady-state settings (low-power/idle and high-power conditions) but did not take into consideration the natural degradation rate of the FC stack. As such, the experimental results they presented that accounted for the steady-state deterioration must have implicitly incorporated the natural degradation. The validation method in this work involves comparing the degradation originating from load-changing cycling and steady-state operation to the related experimental data. In this sense, the combination of the low-power, high-power, and

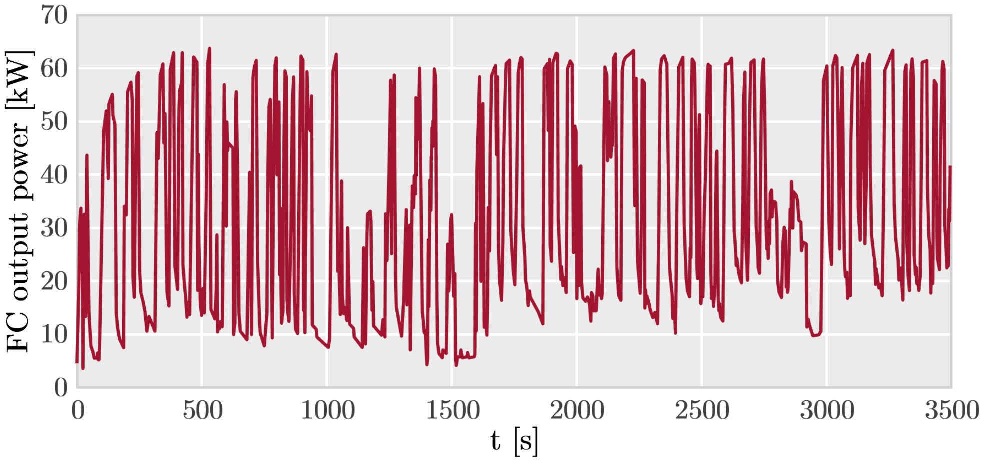

Figure 3.12. *FC stack power demand under the real driving cycle used for validation, retrieved from [23, 24].*

medium-power/natural degradation in the model should match the sum of the low-power and high-power degradation experimental data, indicated as *Experimental steady-state degradation* in figure 3.13. As the final step, the degradation rate derived from the natural degradation mechanisms was confirmed to be compatible with the average life of PEMFC operating under steady-state operation. Note that the start-stop degradation rate, defined as a function of the number of start-stop cycles, was set to the same value as in the experimental data supplied by Pei et al. [23] (see table 3.4).

Figure 3.13 depicts the development of the degradation state by source compared to the experimental degradation estimated by Pei et al. [23] at the completion of the bus operation based on the breakdown of the degradation rate by source. From the data in this figure, compared to the FC output power evolution in figure 3.12, it is possible to recognize how the model reacts properly to the FC operation, i.e., the degradation due to load-change increases with variations in the FC current density and is the highest source of degradation, low-power/idle degradation is more significant in the first half of the driving in which the power reaches lower values and slows after 1600 s, and natural and high-power degradation increase nearly constantly due to the frequent load changes during the vehicle operation. Some time intervals, such as 1000 s to 1250 s, indicate how high-power degradation does not rise when the FC model does not run under high-load situations. This is also observed, for example, from 3000 s when low-power degradation stays constant (degradation rate owing to low-power operation is 0).

In order to calibrate the model to approach the experimental results, the model parameters i_{lp} and i_{hp}, defining the boundary between different degradation conditions (figure 3.7), were calibrated in such a way that the deviation in the degradation rate for each power source is lower than 0.1%. The calibrated values of i_{lp} and i_{hp} are 0.33 A/cm^2 and 1 A/cm^2 respectively. These two parameters have been chosen as the calibration parameters as they correspond to the maximal current density for which the low-power/idle degradation mechanism is regarded significant (i_{lp}) and the lowest current density for which high-power degradation is accounted for (i_{hp}). As such, they describe the range of current densities in which the scaling functions $\xi_{lp}(i)$ and $\xi_{hp}(i)$ are non-zero, and the change of the natural degradation with the current density.

Finally, in order to detect if the natural degradation rate was modeled correctly, the total life of the PEMFC stack owing to simply the natural degradation was estimated assuming the end of life when $\delta = 0.1$ at 1 A/cm^2. In the validation example, degradation rate attributable to natural degradation was $2.57 \cdot 10^{-4}$ % V loss/h, which indicates a life of ~39600 h, in accordance with DoE 2020 objectives [48].

3.8 Life cycle assessment

This section, combined with its accompanying subsections, is focused on discussing the LCA methodology after calculating the H_2 and electricity consumption values as inputs from the driving cycle simulations for both passenger car and heavy-duty FCV. Most of the emissions-related data were collected from the GREET® model v2019 as well as from other sources of data in the literature. The emissions metrics for each H_2 production pathway are those derived in [49] for the scenario with the current EU electricity generation mix so that the conclusions are reflective of the short-term scenario. In this LCA study, all the pathways involved in the cradle-to-grave process were included, i.e., the LCA analysis encompasses the fuel production and distribution cycle, the vehicle manufacturing cycle and the operation cycle.

3.8.1 Boundaries and environmental flows

A diagram of the system boundaries and the elementary flows comprised in this research for the cradle-to-grave process considering electrolysis, steam

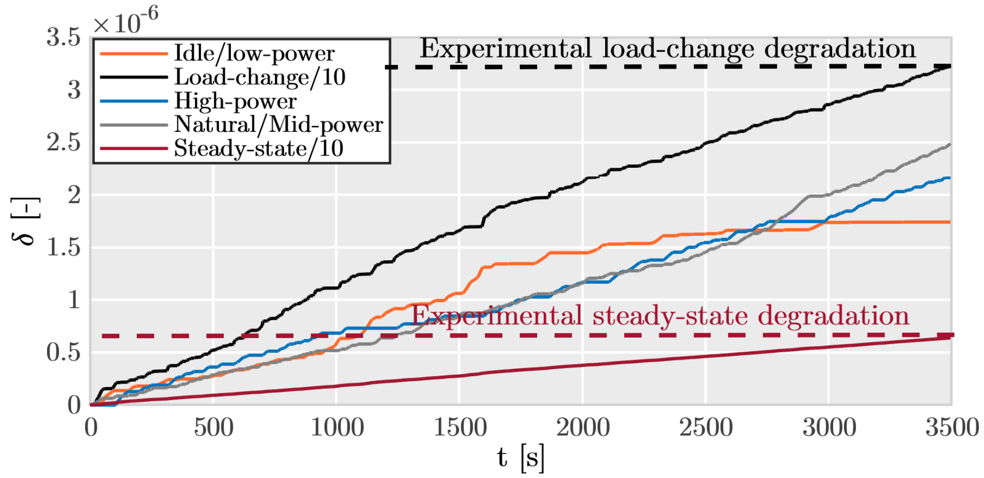

__Figure 3.13.__ Validation results: comparison of experimental [23] degradation rate sources at the end of the driving operation in figure 3.12 with model degradation rate sources. Steady-state degradation comprises low-power, high-power, and natural (medium-power) degradation. Load-change and steady-state voltage loss ratio (δ) evolution were divided by 10 to improve readability.

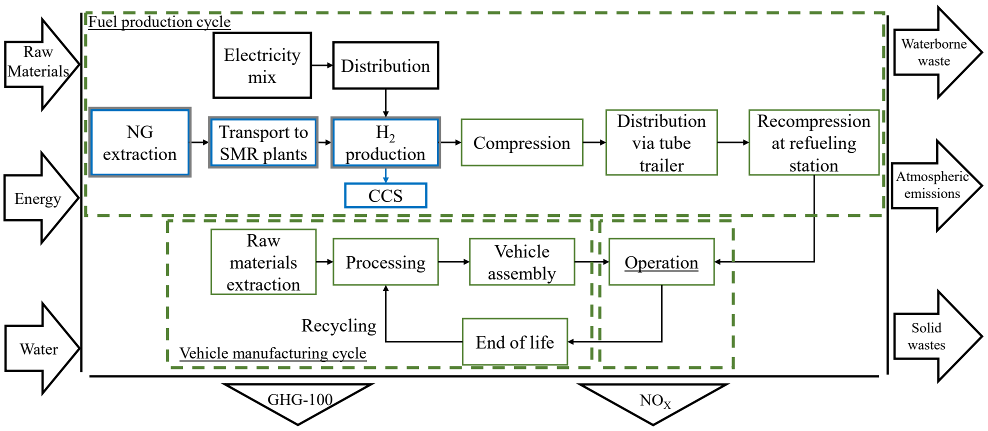

__Figure 3.14.__ System boundaries and elementary flows for the cradle-to-grave process considering electrolysis, SMR and SMR with CCS as the H_2 production pathways. Processes unique to electrolysis production pathway are in __black__, those unique to SMR are in gray, and those unique to SMR with CCS are in blue.

methane reforming (SMR) and SMR with carbon capture and storage (CCS) is presented in figure 3.14. In the present work while various outputs of the cradle-to-grave process such as waterborne waste and other emissions such as SO_X were computed, the analysis solely includes the GHG-100 and NO_X emissions as the system outputs.

3.8.2 Functional unit

The functional unit in this research was adjusted according to the process under study to enhance readability. The functional unit for the emissions in the vehicle production cycle was 1 unit of such vehicle. For the emissions generated in the fuel production cycle, the functional unit was 120000 km of vehicle average useful life for the passenger car application and 1000000 km for the heavy-duty vehicle. In the case of passenger car, the life was chosen significantly lower than the generally used for hydrocarbon-fuelled ICEV (150000 km) as the batteries and FC durability are lower. Finally, in the cradle-to-grave process, the functional unit was both 1 unit of vehicle and the number of km considered for each vehicle of useful life, i.e., the total emissions over the vehicle life.

In the case of section 3.8.4, where the life cycle inventories are shown, in the case of the fuel production cycle, the emissions are reported in terms of kWh of energy source, because multiple energy sources are being considered (H_2 and electricity). These values are then multiplied by the entire-life H_2 and electricity consumption to get the fuel production cycle emissions during the complete vehicle life.

The values of table 3.6 are expressed as a function of the component sizing factor (kWh of energy stored in the case of the battery and the H_2 tank and kW of maximum stack power for the FCS) so that they can be directly transformed into emissions by knowing the sizing parameters.

3.8.3 Impact categories

In the current analysis, GHG-100 was the primary impact category studied as the main purpose of expanding the usage of FCV is to lessen the global warming impact of the transport sector. GHG-100 is an impact category that indicates the global warming potential of various gases over a period of time of 100 years. According to this classification, each greenhouse gas is assigned a value of global warming potential (GWP) that indicates the relative influence on global warming of 1 kg of such gas compared to the effect of 1 kg of CO_2.

The GHG-100 were estimated by taking into account CO_2, CH_4 and N_2O emissions with their GWP of 1, 28, and 265 kg CO_2 equivalent, respectively [50]:

$$\text{GHG-100} = m_{CO_2} \cdot GWP_{CO_2} + m_{CH_4} \cdot GWP_{CH_4} \tag{3.45}$$

$$+m_{N_2O} \cdot GWP_{N_2O} \tag{3.46}$$

where m_{CO_2}, m_{CH_4} and m_{N_2O} are the CO_2, CH_4 and N_2O mass emissions, respectively.

Furthermore, NO_X emissions, while they are not an impact category, were also estimated because of the negative impacts they pose to human health, as well as, their influence on ozone depletion at high altitudes and ozone formation at low altitudes [51].

3.8.4 Life cycle inventory

The life cycle inventory (LCI) data was mostly extracted from the GREET® v2019 model, however some data was updated and supplemented from the literature. This model is extensively utilized in the automobile industry and has been the source of data of numerous research [52–55]. In this section, unless otherwise noted, the reported data was acquired using the GREET® model.

The life cycle inventory may be segmented according to the phase of the cradle-to-grave process it is considered to provide data: fuel production cycle, vehicle manufacturing cycle and operation cycle (figure 3.14).

3.8.4.1 Fuel production LCI

The fuel production cycle encompasses all the processes from the raw material extraction till the vehicle refueling. It may be also known as the well-to-tank process. Three distinct H_2 production pathways were considered: electrolysis using power from the current EU electricity mix, SMR and SMR with CCS. In these three pathways, the H_2, after being generated, is compressed and delivered by tube trailers to be re-compressed at the refueling station (figure 3.14). These production pathways combined with the distribution process and the EU electricity mix were chosen as they reflect the closest-to-present situation. Green H_2 and distribution through pipeline are not explored owing to the huge infrastructure it takes to be practicable at

Production pathway	GHG-100 emissions [kg CO_2 eq./kWh]	NO_X emissions [kg/kWh]
H_2-Electrolysis/EU mix (**black**)	0.489	$5.1 \cdot 10^{-4}$
H_2-SMR (gray)	0.343	$1.5 \cdot 10^{-4}$
H_2-SMR w/ CCS (blue)	0.111	$2.0 \cdot 10^{-4}$
H_2-Electrolysis/solar (green)	0.056	$6.8 \cdot 10^{-5}$
Electricity	0.316	$3.6 \cdot 10^{-4}$

Table 3.5. *Fuel cycle LCI data: GHG-100 and NO_X emissions. Functional unit is kWh of energy source (H_2 or electricity produced).*

an acceptable scale, which implies they are not viable at the short-term. In contrast, creating H_2 with distributed electricity or via SMR with or without CCS is relatively immediate since most of the H_2 at the moment is generated through SMR, whose plants may be altered to incorporate CCS techniques. In the case of CCS technology, a CO_2 sequestration capacity of 90% was estimated, based on the literature data [56].

Besides H_2, there is another energy source in FCREx vehicles: the electricity stored in the battery. The GHG-100 emissions per kWh of electricity were derived from [57] assuming a 6.5% of distribution and transmission losses [58]. Table 3.5 illustrates the GHG-100 and NO_X emissions per kWh of energy source for each manufacturing route, considering all the activities indicated. Total emissions were computed with a refueling efficiency of 1.

3.8.4.2 Vehicle manufacturing LCI

The emissions generated in the vehicle manufacturing cycle are susceptible to major variations in this research since the vehicle design changes in the sizing analyses. The emissions related to the manufacturing of each component were scaled to those comparable with those produced for a 1400 kg vehicle body, in the case of the passenger car application. The vehicle manufacturing cycle comprises the manufacturing of mechanical components (transmission system, chassis, electronic controller, traction electric motor, vehicle tire replacement and vehicle body), the assembly, disposal and recycling (ADR) processes, the fluids production (brake, transmission, coolant, windshield and adhesives), the battery (NMC111 Li-ion), the FCS and the H_2 tank (type

System	GHG-100 emissions [kg CO_2 eq.]	NO_X emissions [kg]
Battery capacity [/kWh]	26.07	$3.9 \cdot 10^{-2}$
FC stack power [/kW]	7.84	$8.7 \cdot 10^{-3}$
H_2 tank capacity [/kg H_2]	424	$4.9 \cdot 10^{-1}$
H_2 tank capacity [/kWh]	12.73	$1.46 \cdot 10^{-2}$

Table 3.6. *Vehicle manufacturing cycle LCI: GHG-100 and NO_X emissions. Emissions given per unit of sizing parameter.*

IV carbon fiber for 700 bar). The information related with the recycling of the FCS and the H_2 were not included since emissions associated with the FC stack recycling are negligible [59] and there is not enough data in the literature about the emissions produced during the recycling of H_2 high-pressure tanks. In the case of the heavy-duty application, the emissions related to the production of the vehicle and all the elements not conforming the powertrain were obtained from GaBi database. The emissions data for the components whose specifications vary in the design spaces (sizing) are supplied in table 3.6 per unit of sizing variable. The sizing parameters, or those controlled to vary the components sizing, are the FC stack maximum power (kW) the battery capacity (kWh) and the H_2 tank capacity (kWh of H_2 or kg of H_2).

The raw materials (inputs in figure 3.14) included for the manufacturing of the vehicles were steel, magnesium, aluminum, zinc, copper wires, plastic product, glass, carbon-fiber-reinforced plastic, styrene-butadiene rubber, lithium and other vehicle materials. The emission related to the processing of raw materials and the extraction of elementary materials such as bauxite, sand water, zinc ore, ore, etc, were analyzed whereas those created during the transport of such materials to the manufacturing facilities were disregarded [60].

3.8.4.3 Operation cycle LCI

The operation cycle might alternatively be named the tank-to-wheel process. In this cycle, different from traditional ICE vehicles, the emissions generated by FCV and their influence on the environment are negligible. The only substantial tank-to-wheel emission of FCS is H_2O. In this research, the H_2O emissions of the FCVs while running in the range-extender mode and their influence on global warming were analyzed. For that purpose, the effective global warming potential of water was defined as $5{\cdot}10^{-4}$ kg CO_2 eq. [61]. This number is the consequence of two opposite impacts of near-surface generated water vapor: the effect of water as a GHG-100 emission and the reduction in temperature owing to the creation of low-altitude clouds that enhance the atmospheric reflectivity.

3.9 Driving cycle simulation procedure

As commented before, the focus of this work is on passenger car and heavy-duty vehicle applications. For each type of vehicle, different parametric analyses were performed to optimize architecture of their propulsion system based on the emerging design FC-based powertrain concepts. In the case of the passenger car application, the studies were mainly focused on identifying the optimum powetrain sizing and control constraints in terms of life cycle emissions, FC stack durability, H_2 and energy consumption. In contrast, in the heavy-duty application, the trend of the industry of modularizing the FCS technology and use "n" of them to scale-up the maximum power output of any propulsion system brings out additional degrees of freedom in terms of design and control. As a consequence, the simulations carried out in this work are focused on identifying the benefits in terms of consumption, durability and life cycle emissions of further optimizing this architecture by considering differential sizing and control of the 2 FCS composing the propulsion system. In order to evaluate such indicators, the WLTC 3b and HDDT (heavy-duty Diesel truck) driving cycles were used for the passenger car and heavy-duty vehicle applications, respectively.

The large amount of simulations required to carry out the aforementioned parametric studies may imply prohibitive computational time if high-detail dynamic powertrain models are considered. As a consequence, once the complete FCS model was optimized in chapter 4, part 1, section 4.2 for each application, it was simplified to a high-fidelity mean values model capable of reproducing the performance of the dynamic model with a deviation in H_2

consumption lower than 0.5%. This was accomplished by adding a dynamics-informed decision space in the energy management strategy optimizer, as commented in section 3.6, thus decreasing the simulation time of a WLTC 3b driving cycle from 4 h to 10 s in the case of the passenger car application.

Nonetheless, the use of steady-state models usually imply the loss of capabilities and some information. In this case, in which durability needs to be predicted as a function of physical variables such as the FC stack temperature whose evolution is not steady-state due to the thermal inertial of any real body, a simple mean values model may induce significant error in the FC stack degradation prediction. In order to address this issue, each FCS steady-state mean values model included a thermal mass in contact with an environment temperature source through a convection heat transfer boundary condition with a heat source term coming from the FC stack net heat transfer (heat due to electrochemical losses minus heat transferred to the coolant, air and H_2 channels). The parameters characterizing the thermal nodes (mass, distance to the mass center, coss-sectional area, convection coefficient evolution with the current density, FC external area) and a correction multiplier for the heat source term were calibrated with a genetic algorithm optimizer for each FCS ranging from 20 to 100 kW for the passenger car application and from 80 to 160 kW for the heavy-duty application. The calibration process was carried out by comparing the FC stack temperature evolution of the dynamic model in the WLTC 3b and HDDT driving cycles depending on the application with the temperature evolution provided by the steady-state model and adjusting the thermal mass characteristics to minimize the RMS error across each driving profile. The calibration results for the passenger car model can be seen in figure 3.15 and imply an overall RMS devation ranging from 0.3 to 1.2%

Once the models were calibrated in terms of temperature evolution, a different set of simulations were carried out for each study and application.

For the passenger car application, the three different studies correspond to those in sections 4.3.1, 4.3.2 and 4.3.3. For the first analysis (section 4.3.1), driving cycle simulations were carried out with FC stack infinite dynamics by varying the sizing of the H_2 tank, battery capacity and FC stack maximum power, as defined in section 3.5.1, which implied a total of 720 designs for which the iterative process to get the right value of λ in the EMS was repeated each time (8-12 driving cycle simulations per design). This analysis study aims at understanding the effect over H_2 and energy consumption of changing such components in the FCREx architecture.

The second study (section 4.3.2) considers a fixed design of a FC stack of 60 kW, a battery capacity of 30 kWh and a H_2 with a capacity of 5 kg close to

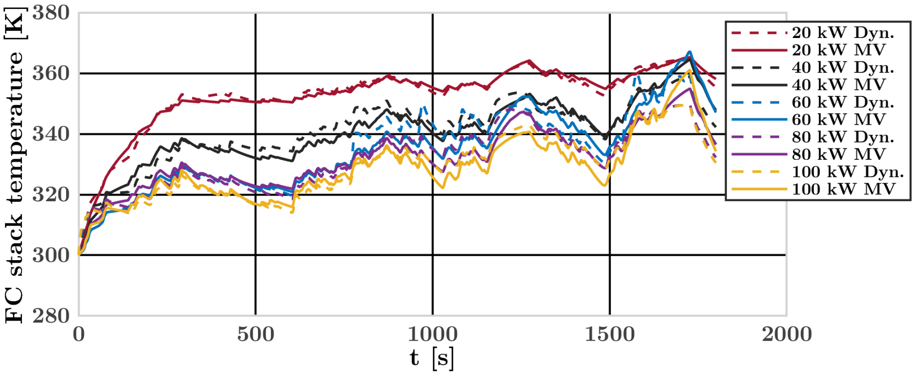

Figure 3.15. *Results of the thermal calibration for the passenger car application: evolution of the FC stack temperature across a WLTC 3b driving cycle of dynamic and mean values (MV) calibrated models.*

the optimum design in terms of performance obtained in section 4.3.1 since it was identified that increasing the battery capacity would incur in a prohibitive vehicle cost. With this design, a series of WLTC 3b driving cycle simulations were carried out by imposing limits on the dynamics ($|\mathrm{di/dt}|_{\mathrm{max}}$) and the minimimum current density ($\mathrm{i}_{\mathrm{min}}$) to understand how these control parameters influence performance and durability following the simulation matrix in table 3.7.

In the third study (section 4.3.3), the first and second analyses were combined by imposing different dynamic restrictions on designs with different FC stack maximum power to understand how the FC stack size and a less-dynamic operation influences the consumption and durability of each design. In this sense, the designs with a FC stack maximum output power of 40, 60, 80 and 100 kW were simulated by imposing the dynamic restrictions on the current density of 1, 0.1, 0.01 and 0.001 $\mathrm{A/cm^2s}$.

The analysis carried out for the heavy-duty application is broken down in a similar structure as in the passenger car application. The first study (section 4.4.1) is focused in the fixed desgin composed by 2 FCS of 120 kW and on understanding how a the differential control (imposing dynamics restrictions of 0.1, 0.01 and 0.001 $\mathrm{A/cm^2s}$ on each FCS) may influence consumption and degradation. Finally, the third study in section 4.4.2 combines the differential control with the differential sizing (with the designs in table 3.2) of both FCS to analyze the implications of applying them simulataneously over the heavy-duty vehicle architecture.

Dynamic limitation [A/cm^{2}s] \ i_{min} [A/cm^2]	0	0.1	0.15	0.2
Inf	X	X	X	X
0.1	X	X	X	X
0.05	X	X	X	X
0.01	X	X	X	X
0.005	X	X	X	X
0.001	X	X	X	X
0.0005	X	X	X	X

Table 3.7. *Simulation matrix defining the EMS restrictions in terms of the dynamic limitation and the minimum current density for each simulation for the study in section 4.3.2.*

In each of these applications, both the EMS, the FCS, the vehicle and the degradation (when required) models were running in parallel (outline in figure 3.16). The flow of information during any simulation was that of a closed loop or with feedback. The driving profile was applied over the vehicle mechanical model, which produced a torque and speed requirement for the electric motor. In parallel, the degradation model evaluates the historic of current densities (defined by the EMS) and operating conditions of the FCS and sends a value for the FC stack voltage loss to both the EMS and the FCS. The resulting electrical power demand obtained from the e-motor map and the FC voltage loss are then sent to the EMS which, being aware of how the FCS and the battery may operate depending on the load imposed on each, chooses for each time step the optimum value for the current density for the FCS (or a set of current densities for the 2 FCS composing the heavy-duty vehicle powertrain). Finally, the FCS model operates under such current density in the following time step, thus producing new operating conditions to feedback the degradation model and the EMS optimizer.

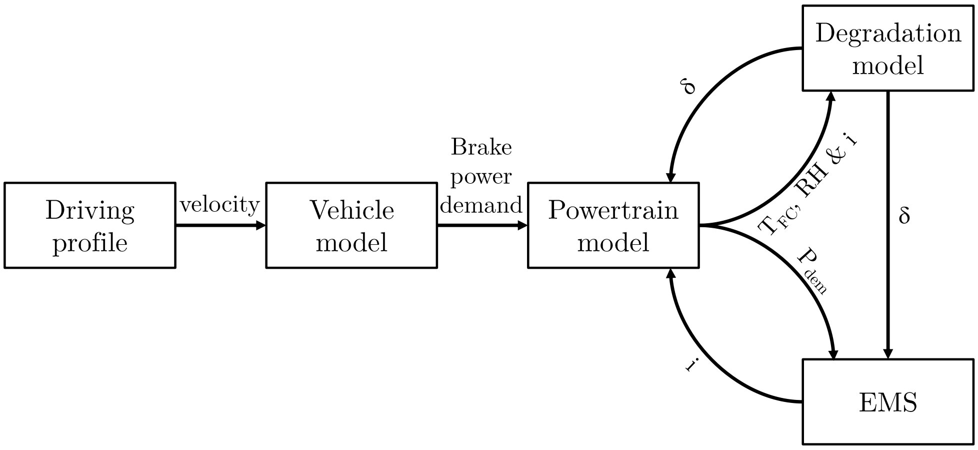

Figure 3.16. Outline of the communcation between the different models composing the simulation platform during driving cycle operation.

3.10 Summary and conclusions

Along this chapter, the methodology followed along this thesis was extensively explained together with all the tools that were used. The modeling framework employed in this thesis consists of a set of models that address each of the relevant systems and scales that are required to ensure a high accuracy and physical consistency. The validated FC stack under different conditions of temperature and pressure was integrated into a scalable BoP thus constituting the FCS model. This FCS model was then integrated in two different vehicle platforms together with the corresponding battery and e-motor models, one for the passenger car and the other for the heavy-duty vehicle application. The control of each component in the powertrain was determined by an EMS optimizer that could ensure that the power split among the subsystems could offer the lowest H_2 consumption. In order to predict degradation, a semi-empirical physics-informed FC degradation model was integrated in the modeling platform to predict the performance decay during realistic operation. This set of models was tested under different driving conditions and applied along the research associated to this thesis to produce the results in the following chapters.

References

[1] Terada Ichiro and Nakagawa Hideki. “Polymer Electrolyte Fuel Cell”. *Kobunshi*, Vol. 57 n^o 7, pp. 498–501, 2008.

[2] Murschenhofer Dominik, Kuzdas Dominik, Braun Stefan and Jakubek Stefan. “A real-time capable quasi-2D proton exchange membrane fuel cell model”. *Energy Conversion and Management*, Vol. 162 n^o January, pp. 159–175, 2018.

[3] Knights S. *Polymer Electrolyte Membrane and Direct Methanol Fuel Cell Technology: 6 - Operation and durability of low temperature fuel cells.* Woodhead Publishing Limited, 2012.

[4] Corbo Pasquale, Migliardini Fortunato and Veneri Ottorino. “Experimental analysis and management issues of a hydrogen fuel cell system for stationary and mobile application”. *Energy Conversion and Management*, Vol. 48 n^o 8, pp. 2365–2374, 2007.

[5] Corbo P., Migliardini F. and Veneri O. “Experimental analysis of a 20 kWe PEM fuel cell system in dynamic conditions representative of automotive applications”. *Energy Conversion and Management*, Vol. 49 n^o 10, pp. 2688–2697, 2008.

[6] Rabbani R. A. “Dynamic Performance of a PEM Fuel Cell System”. *DTU Mechanical Engineering. DCAMM Special Report*, n^o No. S154, 2013.

[7] Teng Teng, Zhang Xin, Dong Han and Xue Qicheng. “A comprehensive review of energy management optimization strategies for fuel cell passenger vehicle”. *International Journal of Hydrogen Energy*, Vol. 45 n^o 39, 2020.

[8] Hyundai. “Hyundai Nexo - Technical Specifications”.

[9] Ballard. “Product Data Sheet - FCMove-HD”, 2016.

[10] Ballard. “Product Data Sheet - FCVelocity-MD”. 2016.

[11] U.S. Department Of Energy. “DOE Technical Targets for Fuel Cell Systems and Stacks for Transportation Applications”, 2015.

[12] U.S. Department Of Energy. “DOE Technical Targets for Onboard Hydrogen Storage for Light-Duty Vehicles”, 2015.

[13] FuelCellsWorks. “World’s first fuel cell heavy-duty truck, Hyundai XCIENT Fuel Cell, heads to Europe for commercial use”, 2020.

[14] Onori Simona, Serrao Lorenzo and Rizzoni Giorgio. *Hybrid electric vehicles: Energy management strategies.* Springer, 2016.

[15] Sciarretta Antonio and Guzzella Lino. “Control of hybrid electric vehicles”. *IEEE Control Systems Magazine*, Vol. 27 n^o 2, pp. 60–70, 2007.

[16] Luján Jose Manuel, Guardiola Carlos, Pla Benjamín and Reig Alberto. “Cost of ownership-efficient hybrid electric vehicle powertrain sizing for multi-scenario driving cycles”. *Proceedings of the Institution of Mechanical Engineers, Part D: Journal of Automobile Engineering*, Vol. 230 n^o 3, pp. 382–394, 2016.

[17] Serrao Lorenzo, Onori Simona and Rizzoni Giorgio. “ECMS as a realization of Pontryagin’s minimum principle for HEV control”. In *2009 American control conference*, pp. 3964–3969. IEEE, 2009.

[18] Tsotridis Georgios, Pilenga Alberto, Marco Giancarlo De and Malkow Thomas. “EU Harmonised Test Protocols for PEMFC MEA Testing in Single Cell Configuration for Automotive Applications: JRC Science for Policy report”. Technical report, European Commission, JRC Science for Policy report, 2015.

[19] Garland Nancy, Benjamin Thomas and Kopasz John. "DOE Fuel Cell Program: Durability Technical Targets and Testing Protocols". *ECS - The Electrochemical Society, ECS Transactions*, Vol. 11 n^o 1, pp. 923, 2007.

[20] Desantes J.M., Novella R., Pla B. and Lopez-Juarez M. "A modeling framework for predicting the effect of the operating conditions and component sizing on fuel cell degradation and performance for automotive applications". *Applied Energy*, Vol. 317, pp. 119137, 2022.

[21] Molina S., Novella R., Pla B. and Lopez-Juarez M. "Optimization and sizing of a fuel cell range extender vehicle for passenger car applications in driving cycle conditions". *Applied Energy*, Vol. 285 n^o December 2020, pp. 116469, 2021.

[22] DoE - Department of Energy. "DOE Technical Targets for Polymer Electrolyte Membrane Fuel Cell Components".

[23] Pei Pucheng, Chang Qianfei and Tang Tian. "A quick evaluating method for automotive fuel cell lifetime". *International Journal of Hydrogen Energy*, Vol. 33 n^o 14, pp. 3829–3836, 2008.

[24] Lu Languang, Ouyang Minggao, Huang Haiyan, Pei Pucheng and Yang Fuyuan. "A semi-empirical voltage degradation model for a low-pressure proton exchange membrane fuel cell stack under bus city driving cycles". *Journal of Power Sources*, Vol. 164 n^o 1, pp. 306–314, 2007.

[25] Song Ke, Chen Huan, Wen Peimin, Zhang Tao, Zhang Boqiang and Zhang Tong. "A comprehensive evaluation framework to evaluate energy management strategies of fuel cell electric vehicles". *Electrochimica Acta*, Vol. 292, pp. 960–973, 2018.

[26] Hu Zunyan, Li Jianqiu, Xu Liangfei, Song Ziyou, Fang Chuan, Ouyang Minggao, Dou Guowei and Kou Gaihong. "Multi-objective energy management optimization and parameter sizing for proton exchange membrane hybrid fuel cell vehicles". *Energy Conversion and Management*, Vol. 129, pp. 108–121, 2016.

[27] Sun Zhendong, Wang Yujie, Chen Zonghai and Li Xiyun. "Min-max game based energy management strategy for fuel cell/supercapacitor hybrid electric vehicles". *Applied Energy*, Vol. 267, pp. 115086, 2020.

[28] Song Ke, Wang Xiaodi, Li Feiqiang, Sorrentino Marco and Zheng Bailin. "Pontryagin's minimum principle-based real-time energy management strategy for fuel cell hybrid electric vehicle considering both fuel economy and power source durability". *Energy*, Vol. 205, pp. 118064, 2020.

[29] Peng Fei, Zhao Yuanzhe, Chen Ting, Zhang Xuexia, Chen Weirong, Zhou Donghua and Li Qi. "Development of robust suboptimal real-time power sharing strategy for modern fuel cell based hybrid tramways considering operational uncertainties and performance degradation". *Applied Energy*, Vol. 226 n^o April, pp. 503–521, 2018.

[30] Benjamin Tom, Borup Rod, Garland Nancy, Gittleman Craig, Habibzadeh Bahman, Hirano Shinichi, Ho Donna, Kleen Greg, Kopasz John, Lakshmanan Balsu, Masten David, Mehall Mark, Myers Deborah, Onorato Shaun, Papageorgopoulos Dimitrios, Peterson David, Spendelow Jacob, Waldecker Jim, Wilson Adria and Zou Max. "U.S. DRIVE Fuel Cell Technical Team Roadmap", 2017.

[31] Marocco Paolo, Sundseth Kyrre, Aarhaug Thor, Lanzini Andrea, Santarelli Massimo, Barnett Alejandro Oyarce and Thomassen Magnus. "Online measurements of fluoride ions in proton exchange membrane water electrolysis through ion chromatography". *Journal of Power Sources*, Vol. 483 n^o October 2020, pp. 229179, 2021.

[32] Kusoglu Ahmet, Calabrese Michelle and Weber Adam Z. “Effect of mechanical compression on chemical degradation of Nafion membranes”. *ECS Electrochemistry Letters*, Vol. 3 n^o 5, 2014.

[33] Bhosale Amit C., Meenakshi S. and Ghosh Prakash C. “Root cause analysis of the degradation in a unitized regenerative fuel cell”. *Journal of Power Sources*, Vol. 343, pp. 275–283, 2017.

[34] Hu Zunyan, Xu Liangfei, Huang Yiyuan, Li Jianqiu, Ouyang Minggao, Du Xiaoli and Jiang Hongliang. “Comprehensive analysis of galvanostatic charge method for fuel cell degradation diagnosis”. *Applied Energy*, Vol. 212 n^o October 2017, pp. 1321–1332, 2018.

[35] Kangasniemi K. H., Condit D. A. and Jarvi T. D. “Characterization of Vulcan Electrochemically Oxidized under Simulated PEM Fuel Cell Conditions”. *Journal of The Electrochemical Society*, Vol. 151 n^o 4, pp. E125, 2004.

[36] Feng Yanbiao and Dong Zuomin. “Integrated design and control optimization of fuel cell hybrid mining truck with minimized lifecycle cost”. *Applied Energy*, Vol. 270 n^o March, pp. 115164, 2020.

[37] Zhao Jian and Li Xianguo. “A review of polymer electrolyte membrane fuel cell durability for vehicular applications: Degradation modes and experimental techniques”. *Energy Conversion and Management*, Vol. 199 n^o September 2019, pp. 112022, 2019.

[38] Zawodzinski Thomas A., Springer Thomas E., Davey John, Jestel Roger, Lopez Cruz, Valerio Judith and Gottesfeld Shimshon. “A Comparative Study of Water Uptake By and Transport Through Ionomeric Fuel Cell Membranes”. *Journal of The Electrochemical Society*, Vol. 140 n^o 7, pp. 1981–1985, 1993.

[39] Barbir Frano. *PEM Fuel Cells Theory and Practice Chapter 4 - Main Cell Components, Material Properties, and Processes.* 2013.

[40] Bi Wu and Fuller Thomas. F. “Temperature Effects on PEM Fuel Cells PtâC Catalyst Degradation”. *Journal of The Electrochemical Society*, Vol. 155 n^o 2, pp. B215, 2008.

[41] Jia Nengyou, Dutta Monica, Lu Suzy and Colbow Vesna. “Voltage Degradation Associated with Operational Conditions: Upper Potential and Lower Potential Limits”. *Journal of The Electrochemical Society*, pp. 2–3, 2009.

[42] Borup Rod L., Davey John, Wood David, Garzon Fernando and Inbody Michael. “DOE Hydrogen Program FY 2005 Progress Report - VII.I.3 PEM Fuel Cell Durability”. Technical report, 2005.

[43] Mathias Mark F., Makharia Rohit, Gasteiger Hubert A., Conley Jason J., Fuller Timothy J., Gittleman Craig J., Kocha Shyam S., Miller Daniel P., Mittelsteadt Corky K., Xie Tao, Van Susan G. and Yu Paul T. “Two fuel cell cars in every garage?”. *Electrochemical Society Interface*, Vol. 14 n^o 3, pp. 24–35, 2005.

[44] Dutta M, Jia N, Lu S, Colbow V and Wessel S. “Effects of Upper Potential Dwell Time, Transients and Relative Humidity on PEM Fuel Cell Cathode Catalyst Degradation”. *The Electrochemical Society 217th Meeting (c)*, 2010.

[45] Li Yunqi, Chen Xiran, Liu Yuwei, Xiong Danping, Li Jing, Yin Sha, Chen Liang, Li Congxin and Xu Jun. “Analytical modeling framework for performance degradation of PEM fuel cells during startup-shutdown cycles”. *RSC Advances*, Vol. 10 n^o 4, pp. 2216–2226, 2020.

[46] Wu Jinfeng, Yuan Xiao Zi, Martin Jonathan J., Wang Haijiang, Zhang Jiujun, Shen Jun, Wu Shaohong and Merida Walter. “A review of PEM fuel cell durability: Degradation mechanisms and mitigation strategies”. *Journal of Power Sources*, Vol. 184 n^o 1, pp. 104–119, 2008.

[47] Bezmalinovic Dario, Simic Boris and Barbir Frano. “Characterization of PEM fuel cell degradation by polarization change curves”. *Journal of Power Sources*, Vol. 294, pp. 82–87, 2015.

[48] Office of energy efficiency and renewable energy - Department of Energy. “Durability Working Group - Hydrogen and Fuel Cell Technologies Office”.

[49] Desantes J. M., Molina S., Novella R. and Lopez-Juarez M. “Comparative global warming impact and NOX emissions of conventional and hydrogen automotive propulsion systems”. *Energy Conversion and Management*, Vol. 221, pp. 113137, 2020.

[50] IPCC. “Climate Change 2014”. Technical report, Cambridge, 2015.

[51] Boningari Thirupathi and Smirniotis Panagiotis G. “Impact of nitrogen oxides on the environment and human health: Mn-based materials for the NOx abatement”. *Current Opinion in Chemical Engineering*, Vol. 13 n^o x, pp. 133–141, 2016.

[52] Cheng Fangwei, Porter Michael D. and Colosi Lisa M. “Is hydrothermal treatment coupled with carbon capture and storage an energy-producing negative emissions technology?”. *Energy Conversion and Management*, Vol. 203 n^o August 2019, pp. 112252, 2020.

[53] Choi Wonjae and Song Han Ho. “Well-to-wheel greenhouse gas emissions of battery electric vehicles in countries dependent on the import of fuels through maritime transportation: A South Korean case study”. *Applied Energy*, Vol. 230 n^o August, pp. 135–147, 2018.

[54] Obnamia Jon Albert, Dias Goretty M., MacLean Heather L. and Saville Bradley A. “Comparison of U.S. Midwest corn stover ethanol greenhouse gas emissions from GREET and GHGenius”. *Applied Energy*, Vol. 235 n^o October 2018, pp. 591–601, 2019.

[55] Wu Xiaohua, Hu Xiaosong, Yin Xiaofeng, Li Lei, Zeng Zhaowei and Pickert Volker. “Convex programming energy management and components sizing of a plug-in fuel cell urban logistics vehicle”. *Journal of Power Sources*, Vol. 423 n^o March, pp. 358–366, 2019.

[56] Al-Qahtani Amjad, Parkinson Brett, Hellgardt Klaus, Shah Nilay and Guillen-Gosalbez Gonzalo. “Uncovering the true cost of hydrogen production routes using life cycle monetisation”. *Applied Energy*, Vol. 281, pp. 115958, 2021.

[57] European Environmental Agency (EEA). “Overview of electricity production and use in Europe - Indicator Assessment”, 2018.

[58] Council of European Energy Regulators (CEER). “CEER Report on Power Losses”. Technical report, 2017.

[59] Notter Dominic A., Kouravelou Katerina, Karachalios Theodoros, Daletou Maria K. and Haberland Nara Tudela. “Life cycle assessment of PEM FC applications: Electric mobility and μ-CHP”. *Energy and Environmental Science*, Vol. 8 n^o 7, pp. 1969–1985, 2015.

[60] Keoleian Gregory, Miller Shelie, Kleine Robert De, Fang Andrew and Mosley Janet. “Life Cycle Material Data Update for GREET Model - Report No. CSS12-12”. Technical report, 2012.

[61] Sherwood Steven C., Dixit Vishal and Salomez Chryséis. “The global warming potential of near-surface emitted water vapour”. *Environmental Research Letters*, Vol. 13 n^o 10, pp. 104006, 2018.

Chapter 4

Fuel Cell Electric Vehicle Powerplant Optimization

Contents

4.1 Introduction

The results in this chapter constitute the multi-scale optimization process of the FCV powertrain considered in this thesis. It can be divided into two parts, each focused on optimizing the FCV powertrain at different levels.

The first part, comprising section 4.2, is focused on the optimization of the FCS so that the FC-part of the powertrain offers the maximum efficiency at any load demand. The optimization of the FCS through the management of the components of the BoP implies that, for any load, the FCS net efficiency is ideally maximum, which ensures that the results of driving cycle simulations in the following chapters would be representative of the best FCS efficiency behavior, which is in line with using an iterative EMS optimizer that ensures minimum H_2 consumption. Along section 4.2, the results of such optimization in terms of the energy balance are presented for the FCS designed for the passenger car and heavy-duty applications. The main differences between both FCS are analyzed and different operating regions along the current density operation space were identified based on the relative consumption of each component of the BoP and the FC stack electrochemical losses.

Once the FCS performance was optimized at the BoP level in the first part (section 4.2), the second part, comprising sections 4.3 and 4.4 aims at optimizing the architecture of both passenger car and heavy-duty vehicles with the resulting combination of the FCS model, the vehicle modelling platform, the EMS optimizer and the FC degradation model. For the passenger car application, FCREx architecture was considered and the change in performance and durability was analyzed by considering different sizing for the FC stack, battery and H_2 and different constraints in the dynamics or in the operational space (section 4.3). In contrast, for the heavy-duty application, an alternative architecture consisting of two FCS integrated in the same powertrain was analyzed. The analysis of such architecture was carried out in section 4.4 and was focused on evaluating the changes in both durability and performance that the new degrees of freedom of the multi-FCS architecture offered by considering the differential control and sizing of the two FCS while maintaining the sum of the total power of both FCS.

4.2 Fuel cell system energy balance optimization

4.2.1 Optimization space

Prior to the sizing of the FCS, it is required to optimize the operating conditions of the BoP. There are various aspects impacting the efficiency of the FC stack like the temperature, the stoichiometry, the pressure and the relative humidity at both the anode and the cathode. Among these factors, the cathode stoichiometry and pressure has a substantial influence on the FCS performance as its value is connected with the compressor consumption, which is much greater than that of the H_2 recirculating pump or the coolant pump. As such, in this work, the optimization of the BoP was accomplished by optimizing the air management strategy with the FC stack load to enhance the FCS efficiency. The optimization was accomplished under steady-state conditions with various limits to prevent operating scenarios during transient operation that may compromise the integrity of the FC. As such, the cathode stoichiometry was always kept over or equal to 1.8 to avoid cathode starvation during sudden load increases, the pressure at the anode was always kept over the cathode pressure with a Δp limited to 0.3 bar while the minimum cathode inlet pressure was set to 1.2 bar to overcome the pressure losses of the inner channels in the FC stack and auxiliary devices and ensure atmospheric cathode pressure at the outlet of the system.

Regarding the other factors impacting the FC stack efficiency, several constraints were added:

- Anode stoichiometry was always 3 to minimize anode starvation and maximize H_2 diffusion via the GDL, thereby optimizing the FC efficiency. The stoichiometry was maintained this high since the power consumption of the H_2 pump which regulates it has a little influence on the overall FCS. Some studies indicate that the optimum anode stoichiometry that minimizes the voltage losses is around 2-2.5 [1]. Nonetheless, these studies refer to steady-state condition where no local anode starvation may happen. In the case of driving conditions, the highly dynamic FC behavior could imply local anode starvation, which has as a consequence severe degradation. As such, given the lack of detailed studies that

Methodology	Design of experiments	
Control input (u)	Cathode inlet pressure	p_{cath}
	Cathode stoichiometry	λ_{cath}
Objective	Efficiency maximization	η_{FCS}
Constraints	Defined in section 3.4.2	

Table 4.1. *BoP management optimization characteristics.*

identify these local phenomena under different conditions of anode stoichiometry, it was decided to keep it at a higher value than what is usually found in the literature to ensure that no local anode starvation is present even during highly dynamics operation.

- The relative humidity at the input of the cathode was 80% at any current density, provided that there is enough water at the outlet of the cathode to humidify the inlet. The rise in air temperature and pressure from atmospheric conditions after the compressor was properly considered to compute the relative humidity. This value was selected since it was deemed that a high value of RH (>80%) is required to minimize the ohmic voltage losses, thus maximizing the FCS power density [2]. However, the FC stack and degradation models used for this research are not capable of predicting the loss in performance and durability when membrane flooding happens (water saturation when RH>100%). Therefore, given the water produced in the CCL and the necessity to evacuate the water with the air flow, the upper limit in the RH at the cathode inlet was set to 80%.

- The coolant temperature at the exit of the FC stack was regulated to 70-75°C.

All these parameters were controlled by means of PID controllers as explained in section 3.4.2. An overview of the major aspects of the optimization process may be found in table 4.1.

The optimization process was carried out for both the passenger car and the heavy-duty vehicle application in the baseline design since it is intended to be scalable. The baseline FCSs were designed with a 20 kW FC stack for the case of the passenger car application (following the traditional philosophy of range-extender: small power generation system and moderate battery capacity) and with a 120 kW FC stack for the heavy-duty application, based on the Hyundai

XCIENT FCV [3]. The change in the FCS efficiency was identified by varying the cathode stoichiometry (mass flow rate) and pressure along the compressor map in the range of 1.8 to 60 (the highest value corresponds to the minimum current density) and 1.2 to 2.5 bar, respectively, for a set of values of current density. The purpose of this was to identify the combination of compressor pressure ratio and corrected mass flow rate that maximized the FCS efficiency as a trade-off between the compressor power consumption and the decrease in the electrochemical losses of the FC stack, which, as can be seen in figure 3.1, allows for higher cell voltage if the pressure at the cathode increases. The main difference between both FCS is the compressor map, showed in sections 4.2.2.1 and 4.2.2.2. In the case of the passenger car, a standard compressor map representative of a light-duty internal combustion engine vehicle application was used by applying the compressor map parametrization tool in GT-Suite. The key reason behind this choice is that the sizing study aimed at FCREx architecture for passenger cars comprises a wide range of FC stack maximum output power (from 20 to 100 kW), which implies that selecting a non-scalable specific compressor map would not be useful for all the FC stacks and would not provide further insight in the FCS optimization process, which main objective is to identify trends in the FCS performance according to the systems sizing and provide design recommendations for the industry. In the case of the heavy-duty vehicle application, the compressor map was based on the ROTREX EK10AA-PT54 compressor, which was designed specifically for FCS, since the FC technology is expected to be integrated in the short term in the heavy-duty transportation industry. Therefore obtaining a more accurate prediction of the H_2 consumption to verify the feasibility of the proposed designs is critical. Furthermore, the minimum and maximum current density values for each application were slightly modified. The first optimization study was carried out for the passenger car application and allowed to identify that extremely low values of current density implied low FCS efficiency and that from a current density of 1.4 A/cm^2 (close to the limiting current density of 1.44 A/cm^2), the model behaved unstably. Therefore this operation region should be avoided. Furthermore, the first driving cycle simulations with the SUV FCREx (section 4.3.1) allowed to identify that, when high-power driving cycles are considered, the EMS tends to avoid operating at the minimum current density, and that low current density operation increases noticeably FC degradation. As such, current density limits for the FCS integrated in the heavy-duty vehicle were updated to 0.01 and 1.3 A/cm^2.

As it is explained in sections 4.2.2.1 and 4.2.2.2, the design of experiments methodlogy carried out by varying the cathode stoichiometry and inlet pressure allowed to identify how the efficiency of the FCS is usually maximized

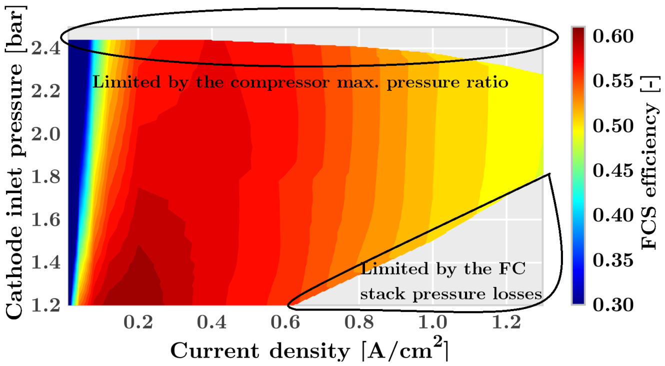

Figure 4.1. *Mathematical space for the EMS of the heavy-duty FCS: evoluation of the FCS efficiency as a function of the cathode inlet pressure and the FC current density.*

when the cathode stoichiometry is minimum and the compressor pressure ratio is maximum, provided that it does not imply a significant decrease in the compressor efficiency (trade-off). This allowed fixing the cathode stoichiometry evolution and identify the change in the FCS efficiency with the cathode pressure ratio. This was performed mainly to obtain the dynamics-informed mathematical spaces explained in section 3.6 on which the decision space for the control variable u relating the current density to the FCS efficiency changed with the cathode inlet pressure predicted from the previous time step.

This relation can be perceived in figure 4.1, in which the evolution of the FCS efficiency with the cathode inlet pressure and the current density for the FCS used in the heavy-duty application studies is presented. As can be seen, the mathematical space is limited by the compressor maximum pressure ratio at each current density (which, together with the cathode stoichiometry, determines the compressor mass flow rate) and by the FC stack pressure losses when the air mass flow rate (proportional to the current density when the stoichiometry is constant). In this last limited region, the pressure needs to be over a certain value (increasing with air mass flow rate) to overcome the FC stack losses produced in the inner cathode flow channels. Note that the operation region in which the compressor is at surge, identified by a sudden drop in FCS efficiency at low current density, is maintained in the operation space, although the management strategy of the BoP integrated in the FCS model prevents the compressor from operating in this region. The motivation behind this was that the EMS needs to be capable of decreasing the current density of the FC stack to its minimum value since there may be time steps along a driving cycle simulation in which the e-motor power demand is zero and the battery has relatively high energy stored. In this case, even though the EMS can choose to change from high current density to almost zero in 1 time step, it does not mean that the compressor is going to suffer from surge. This is possible since the time step used in the simulations of this work is 0.1 s and, in the case such a sudden drop in the current density happens, the management strategy in the BoP will adjust the pressure ratio through the cathode exhaust valve at the next time step so that the compressor operates close to the points in which the FCS efficiency is maximize at each current density. In contrast, in order to avoid cathode starvation when the EMS takes the decision of increasing abruptly the current density in a given time step, the minimum target cathode stoichiometry was set to 1.8. This value was tested in the complete modeling platform with highly dynamic power demand profiles (driving cycles) and lowered to 1.3-1.4 occasionally due to the delay between the electric compressor and the stack air consumption. The fact that it is kept over but close to 1 (not global starvation but potentially local starvation, only detectable with detailed 3D computational fluid dynamics simulations) is possible thanks to the highly dynamics behaviour of electric compressors that do not depend on the inertia of a turbine. The reader should note that this may only happen when there are not restrictions on the FCS dynamics, and that the values of anode and cathode stoichiometry are kept much closer to their target values when the dynamics are limited to preserve the FC stack durability.

4.2.2 Optimum Energy Balance Identification

In this section, after performing the simulations to understand how the FCS efficiency changes with the cathode stoichiometry and the cathode inlet pressure, the optimum air management strategy was selected and the energy balance was analyzed for each FCS. Since the conclusions extracted for the FCS considered for the passenger car application can also be applied to the heavy-duty vehicle FCS, the energy balance will be analyzed in detail in section 4.2.2.1, while only the main conclusions will be highlighted in section 4.2.2.2.

4.2.2.1 Passenger car

The optimum air manamgent strategy for the baseline design for the passenger car application can be seen over a compressor map in figure 4.2.

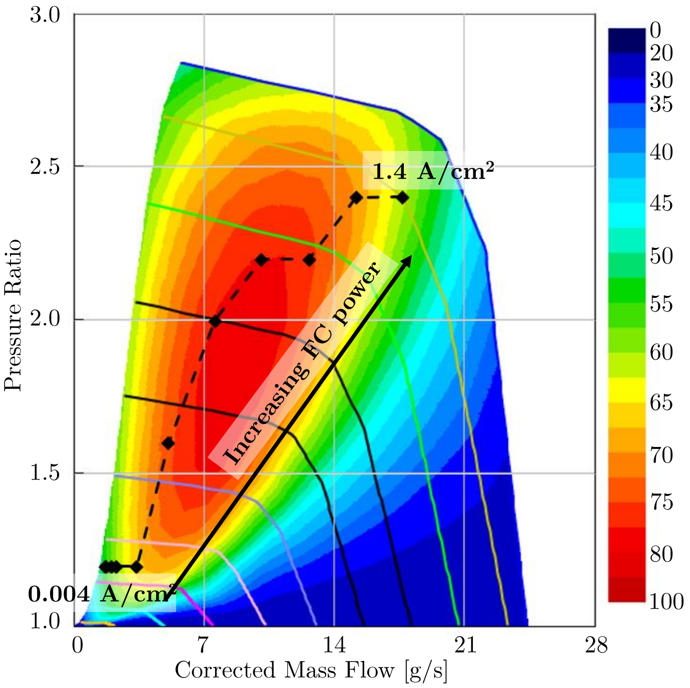

Figure 4.2. *Parametrized compressor map with optimum operating conditions for the passenger car FCS, baseline design of 20 kW.*

This figure shows how the net power of a FCS is maximized by minimizing the compressor power consumption by operating in regions of the map close to the maximum efficiency. Nonetheless, as can be observed, the optimum air management strategy does not pass exactly over the points where the compressor efficiency is maximum, but rather it comprises slightly higher pressure ratios than those offering maximum compressor efficiency. This is mainly due to the trade-off between minimizing the compressor power consumption and the FC electrochemical losses with both cathode pressure and stoichiometry, but more importantly with pressure. In this case, increasing the cathode pressure implies an increase in the partial pressure of oxygen, which increases the exchange current density and decreases the activation losses, thus maximizing the power produced by the FC stack. In contrast, this implies an increase in the power consumed by the compressor, which affects the FCS net power. This trade-off makes the compressor operate at slightly higher pressure ratios than those offering the maximum efficiency for a given mass flow rate. As a consequence, the optimum compressor map for FCS would be one whose

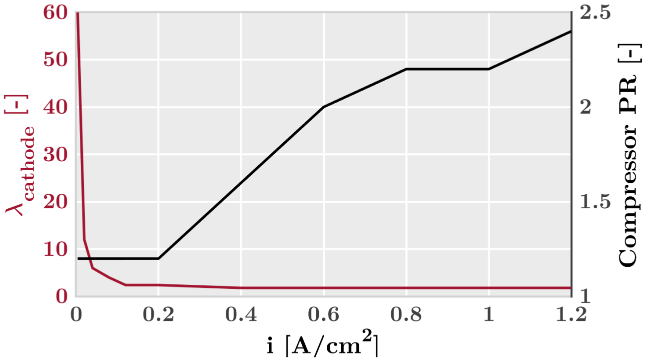

Figure 4.3. *Evolution of the optimum cathode stoichiometry and inlet pressure with the FC stack current density.*

maximum efficiency region is close to the surge line (high pressure ratios), as can be identified in the scaled compressor map based on the ROTREX EK10AA-PT54 model for the heavy-duty vehicle application (figure 4.5).

Analogously, figure 4.3 demonstrates how for low loads high cathode stoichiometry was necessary to prevent compressor surge and the consequent inefficiency. High pressure at high load was necessary mainly to maximize the FC efficiency given a mass flow rate, since minimizing voltage losses becomes more important at high current density to improve the performance of the system. However, as soon as the compressor can give low stoichiometry without suffering from surge (from 0.2-0.4 A/cm^2), the cathode stoichiometry evolves towards the self-imposed lower bound of 1.8, thereby lowering the compressor mass flow rate and power consumption. From this, it is reasonable to deduce that the main driver when optimizing the air management strategy of an FCS is the compressor power consumption and efficiency, being the rise in FC stack efficiency with cathode pressure and stoichiometry only affecting as a second-order effect.

The optimum energy balance of the FCS is displayed in fig 4.4. The red bar, depicting the FCS net power (FC stack power minus the power consumption of the BoP), also indicates the FCS efficiency. The other bars reflect the power losses owing to diverse factors such as the FC stack inefficiencies and the power consumption of the BoP (primarily compressor power consumption) . Therefore , the curve formed by combining the red bars is the power curve of the FCS. In this graph it is feasible to discern four operating areas depending on the current density:

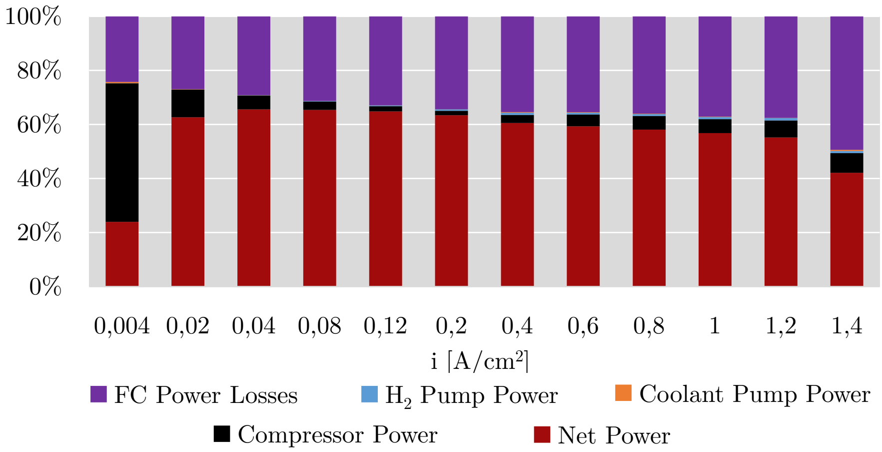

Figure 4.4. *Evolution of the optimum energy balance of the FCS for the passenger car application with the current density in relative terms.*

- Ultra-low load I $\approx$ 0.004 A/cm^2): the compressor receives most of the power delivered by the FC stack while the FC efficiency is maximal since electrochemical losses are minimal. The FCS efficiency is the lowest. This area is analogous to the idle state for ICE. If possible, a solution to increase the performance of an FCS in this region could be to use RAM air, i.e., air introduced to the FC stack by bypassing the compressor (to mitigate the pressure loss under the low-load condition) and compressed when stopped due to the relative speed between the air and the vehicle.
- Low load I $\in$ [0.02, 0.04] A/cm^2): relative to the preceding region the FC stack losses grow because ohmic losses begin to have a significant influence. However, FCS efficiency rises with load since the FC electrical power increases considerably relative to the compressor power.
- Medium load I $\in$ [0.04, 0.4] A/cm^2): FCS efficiency is maximized (desired operating conditions) because FC losses are moderate while the compressor power is minimal in relative terms. Overall system efficiency might reach around 60-65%. Note that the efficiencies achieved here do not include the loss in power in the DC-DC converters and that the BoP operation was optimized and sized according to the FC maximum power. This explains the rather higher results of the efficiency in this investigation.
- High load I $\in$ [0.4, 1.4] A/cm^2): FC losses are essentially constant up to 1.2 A/cm^2 because compressor pressure ratio rises with load. Around

1.4 A/cm^2 mass transport losses rise considerably resulting to increasing FC stack inefficiency. Furthermore, total FCS efficiency declines with load because, for a given cathode stoichiometry, increasing the current density implies increasing the needed air mass flow rate, thus increasing the compressor power consumption.

4.2.2.2 Heavy-duty vehicle

As explained before, the main difference between the FCS used for the heavy-duty vehicle and the one used for the passenger car is the compressor. Besides the significantly different location of the maximum efficiency region with respect to the surge line in both compressors, they are different in the maximum efficiency value. The compressor used for the passenger car had a nominal (maximum) efficiency of 80%, corresponging to the approximate upper efficiency limit of a centrifugal compressor for automotive applications. As such, this compressor could provide lower consumption and could be representative of the best-case scenario, reason for which it was chosen to evaluate the FCREx architecture. Nonetheless, for the heavy-duty application, the expectations of the short-term integration of heavy-duty vehicles powered by FCS motivate the use of a commercial compressor map designed for FCS technology. This map, based on the ROTREX EK10AA-PT54 compressor, is presented in figure 4.5 with the optimum air management strategy on it. The maximum efficiency of this compressor is 79% [4], which is close to the one of the compressor used for the passenger car application. The last difference, which implies a noticeable deviation with respect to the values of maximum FCS efficiency, is the control of the compressor mass flow rate when the current density of the stack is low ($\leqslant 0.12$ A/cm^2). These points are represented over the compressor map of the passenger car (figure 4.2) as the points in the lower part of the map forming a horizonal line. These points try to approach the surge line as much as possible to minimize the compressor power consumption. However, after carrying out numerous driving cycles with the FCREx model, it was determined that, for the heavy-duty appplication at the lower values of the current density, the compressor should maintain a certain margin with respect to the surge line to avoid instabilities and inefficiencies in the compressor during highly dynamic driving cycles, so a lower bound in terms of compressor mass flow rate was imposed over the air management strategy for the heavy-duty application. Note that, as commented in section 4.2.1, the FCS needs to be aware of the performance of the FCS at this region (figure 4.1), but does not necessarily operates there. This, which was identified for the passenger car application, was limited in the air management strategy

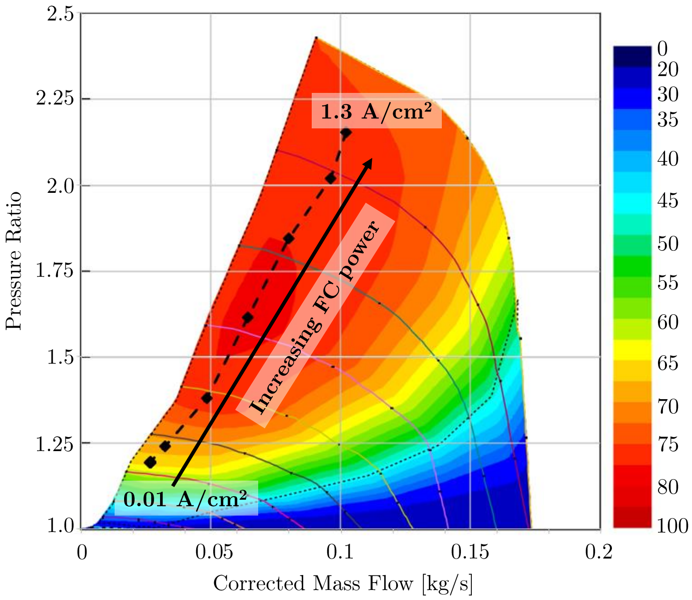

Figure 4.5. *Parametrized compressor map with optimum operating conditions for the heavy-duty vehicle FCS, baseline design of 120 kW.*

of the FCS during driving cycle simulations and had small influence on the H_2 in the mean values model.

The main differences in the air management strategy between the two applications are basically the pressure ratio for each value of stoichiometry, the compressor efficiency and the lower bound limit for the compressor mass flow rate.

As a result, and analogous to the optimum air management strategy for the passenger car compressor, the optimum combination of PR and corrected mass flow rate is that passing throught the maximum efficiency region of the compressor map (figure 4.5). In this case, the trade-off between the efficiency and the PR is not that important since the compressor designed for FCS has the maximum efficiency region closer to the surge line and thus it is achieved with higher PR.

The optimum energy balance for the FCS used for the heavy-duty vehicle is depicted in figure 4.6, in which the same regions identified for the the pasenger car FCS are found as well. The main difference between figures 4.4 and 4.6 (apart from those explained previously with respect to the updated considerations for the heavy-duty application) are the values for the FCS

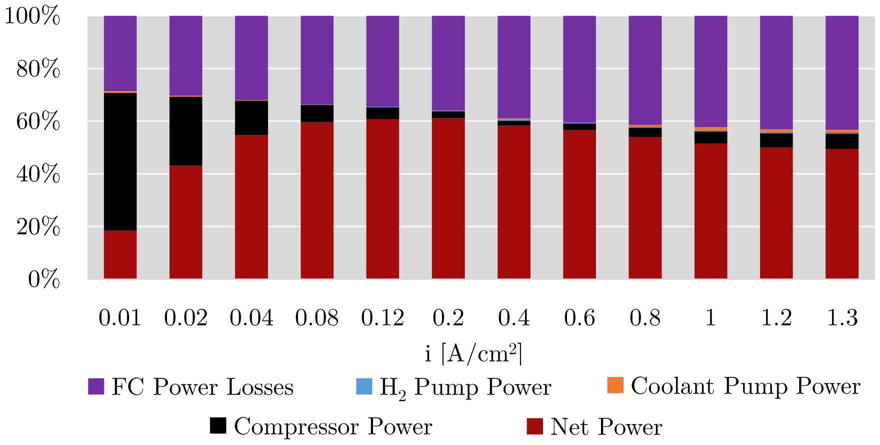

Figure 4.6. *Evolution of the optimum energy balance of the FCS for heavy-duty vehicle application with the current density in relative terms.*

net efficiency, identified as the value that the red bar (net power) reaches. As can be seen, up to a current density of 0.2 A/cm^2, the efficiency of the passenger car application is higher because of the lower mass flow rates the compressor map reaches. Nonetheless, the efficiency of the FCS for the heavy-duty application reaches a high value of 60% at 0.08 A/cm2, offering slightly higher efficiencies at 0.12-0.2 A/cm2 and starting to decline noticeably from 0.6 A/cm2. Nevertheless, the optimization process allowed to have always a FCS net efficiency over 50%, even at maximum current density, which far exceeds the thermal efficiency of internal combustion engines. The flat behaviour of the efficiency with the load depicted in figures 4.4 and 4.6 allows to understand that even though there may be some inefficiencies due to the dynamic operation during any driving condition, the FCS net efficiency is not expected to decline in such a magnitude as for internal combustion engines.

In the high current density region, the FCS for the heavy-duty application offered lower efficiency than the passenger car FCS since overall pressure losses across most of the components, such as the air filter located at the inlet of any FCS, become more relevant for higher-power FCS due to the higher mass flow rates required for their operation. This happens even though the compressor technology was designed to be compatible with FC stacks and maximize their efficiency, which implies that using other type of compressors would have a negative impact on the FCS efficiency. As a last comment, note that the maximum efficiency of the heavy-duty FCS is in the range of 60-62%, which is competitive and slightly superior to the maximum FCS efficiency of vehicles such as the Hyundai Nexo with similar power FC stack (60%).

4.3 FCREx architecture for the passenger car application

As commented in chapters 1 and 2, the novelty of this thesis is the optimization of the FCREx architecture applied to a passenger car application. This powertrain configuration has been applied to other applications such as heavy-duty trucks [5], urban logistic vehicles [6], and city bus [7] applications, but prior to this thesis it still needed to be further explored and optimized.

The reader should note that FCREx architecture traditionally implied a low-power FC stack and a battery with moderate to high capacity. Nonetheless, it is actually not limited by such constraints since the main reason behind FCREx architecture is to be able to use the FC as a range-extender but also the battery along during driving, like a BEV. In this situation, the main advantages of the FCREx architecture and the potential to be optimized arise from having a high-enough battery capacity. Integrating a fully autonomous electric propulsion system such a chargable battery along with a FC has several benefits:

- Decreases the dependency of the vehicle on H_2, which is indeed worthy in the short-term while the Hydrogen Economy is rising but far from being fully established. As a consequence, the actual range of the vehicle may increase since it may be used to access regions where there are not hydrogen refueling stations.
- Adds an additional degree of freedom in terms of operation modes, being able to use the battery as in a plug-in vehicle to cover the user's daily movements across the city so that it can be charged overnight and the FC as a range-extender when the user needs to travel between cities.
- The flexibility highlighted in the previous point may also allow the manufacturers design control strategies and driving modes to minimize factors such as the cost along the vehicle life (H_2 is significantly more expensive than electricity) and the life cycle emissions (some H_2 production pathways may imply more emissions than using the electricity from the grid in some countries). This means that the FCREx architecture may potentially imply lower total cost of ownership

and cradle-to-grave emissions than a conventional FCV, if optimized properly.

- Relying on two power generation systems in the same powertrain (FCS and battery) implies that the load dynamics may be absorbed by any of the two systems, which implies that the FC stack durability, which is reduced significantly due to abrupt load-changes (section 3.7), can be increased if the battery is used to provide the highly dynamic power supply, thus minimizing again factors such as the total cost of ownership and the life cycle emissions.

In this context, this section aims at understanding the effect of the sizing of the components of the FCREx powertrain on performance (section 4.3.1), the effect of constraining the dynamics and the operation of the FCS on durability 4.3.2, and the combined effect of these two design factors (operation strategy and sizing) on both performance and durability simultaneously to identify any cross-effect that may be found among them (section 4.3.3). These results of these sections were included in the scientific articles [8], [9] (section 4.3.1), [10] (section 4.3.2) and [11] (section 4.3.3).

4.3.1 Effect of powertrain components sizing on performance

The sizing of FCREx is rather more difficult than that of a normal FCV as the battery capacity also impacts considerably the best energy management strategy of the systems in the vehicle, the cost, and the range. As such, for this type of architecture, it is imperative to provide a comprehensive and wide analysis on the range, performance, and cost of systems for different combinations of FC stack maximum power output, battery capacity, and H_2 tank storage capacity in order to better understand the real potential and limitations of such configuration, relative to conventional FCVs.

The global space design consisted of altering 3 independent design parameters: the FC stack maximum power output, the capacity of the battery, and the H_2 tanks storage capacity. As such, the data in figures 4.7, 4.8 and 4.9 have 1 out of these 3 parameters fixed. In figure 4.9, the fixed parameter is the H_2 tank capacity which was chosen properly to achieve a certain vehicle range with an error of ± 20 km. Battery capacity was modified among 30 and 60 kWh, FC stack maximum power output within 20 and 100 kW and the H_2 mass stored in the tank within 1 and 5 kg. The ratio between both the energy stored in the battery and the energy stored as H_2 in the tank is indicative of the H_2 utilization to cover the complete vehicle range. The results reported

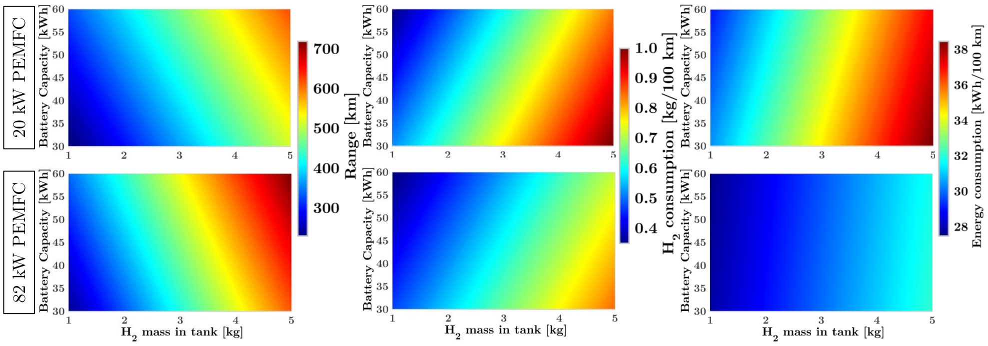

Figure 4.7. *Range, H_2 consumption and energy consumption of FCREx with 20 and 82 kW PEMFC.*

in these figures were influenced by the inaccuracy after simplifying the entire model to the mean values model. Therefore, the real values of range may be somewhat lower than those given in figures 4.7 and 4.9.

Along this discussion, alternative FCREx designs are assessed against state-of-the-art commercial FCV. The FCV are referenced as FCV1 and FCV2, and their performance statistics and characteristics can be obtained at [12] and [13], respectively.

Figure 4.7 illustrates the range, H_2 consumption and energy consumption as a function of the H_2 tank and battery capacities with 20 and 82 kW FC stacks. Range was determined assuming the operation with the battery until SOC=0.3, then operation with optimal energy management strategy as described in section 3.6 until H_2 exhaustion, followed subsequently by operation until complete battery discharge. In figure 4.7, FC stack maximum power was the fixed design factor in the analysis since it has the lowest effect in the range compared with the other two sized components. However, raising the FC stack power increases the vehicle range.

When the FC stack maximum power is increased, the FCS works under reduced current density for the power demand. According to figure 4.4, this implies improved FCS efficiency as the stack runs mainly in the medium current density area, i.e., reduced H_2 consumption. The increased efficiency at lower current density is explained by the decreased electrochemical losses and BoP power consumption in this region. On one hand, both ohmic and activation losses decrease with current density because the flow of protons through the MEA and the intensity of the surface reaction per unit of surface area at the catalyst layer decline, thus reducing the losses associated with the membrane protonic conductivity (ohmic losses) and the activation overpotential necessary to initiate the electrochemical reaction (activation losses). On the other side, because the compressor was scaled with the FC maximum power, while the needed mass flow may grow, the relative compressor energy consumption lowers since the FC stack is more efficient (see figure 4.4). Opposite to this benefit, this also entails increasing the FCS weight, therefore the vehicle weight. The increase in weight also has the consequence of raising the needed load for a given vehicle acceleration or velocity and, consequently, H_2 consumption. The data in the left-side and centre graphs on figure 4.7 demonstrate that the rise in FCS efficiency balances the increase in the vehicle weight, therefore improving range and lowering H_2 consumption as the FC stack maximum power grows. The left-side graphs also demonstrate how the range varies with the energy stored as H_2 and the energy stored stored in the battery. With 20 kW PEMFC, if an iso-range line is traced from the X axis at 2 kg of H_2 (66.6 kWh as H_2) it would cross the Y axis at around 50 kWh of energy stored in the battery. This indicates that given the design of 30 kWh battery and 1 kg of H_2, it would be required to increase the energy stored as H_2 by 33.3 kWh to have the same gain in range as increasing the battery capacity by 20 kWh. Therefore, in terms of energy use and performance, increasing the energy stored in the battery is more efficient to extend the range than increasing it in the form of H_2 owing to the greater efficiency of batteries. This extra benefit was also observed with those designs which FC stack maximum power was 82 kW, although it was less significant as the FCS efficiency rose. Despite this, the weight, volume and cost constraint of batteries makes attaining ranges equivalent to those of FCVs with BEVs impossible for passenger car applications. As such, to minimize H_2 and energy consumption in FCREx vehicles, the battery capacity should be moderate and therefore not lowered to the minimum capacity like in current commercial FCVs, in other words, the FCREx architecture can also be used to maximize energy utilization in FCVs and hence minimize consumption and maximize range.

The two middle graphs of figure 4.7 reveal a comparable drop in H_2 consumption as the FC stack maximum power is increased. As discussed earlier, this is due to the outweigh of the FCS efficiency improvement against the increase in power demand as the vehicle weight grows. In this scenario, H_2 consumption was estimated as H_2 mass stored in the tank divided by the whole range of the vehicle. Therefore, this definition is reflective of the whole performance of the vehicle, not simply of the FC+battery mode, and is of the highest relevance given the current situation with few H_2 refueling stations around the world.

As indicated earlier, increasing the H_2 mass in the tank also improved the range. However, it also increased the H_2 consumption because of the vehicle increase in weight. This was caused because raising the stored fuel mass did not have any influence on the efficiency of the systems directly, but elevated the power demand for a given operation due to the additional weight. Conversely, increasing the battery capacity considerably lowers H_2 consumption as it implies that a higher portion of the range was covered exclusively with the battery, which means that the range grows while the stored fuel mass is maintained constant. The H_2 consumption for all the configurations with 82 kW PEMFC was below 0.9 kg H_2/100 km. The fuel consumption of FCV1 [12] (state-of-the-art FCV) is 0.95 kg H_2/100 km (31.6 kWh/100 km) assuming 6.33 kg of H_2 stored and a range of 666 km (WLTP). Compared to this vehicle, in the design space shown in figure 4.7, the FCREx design that is equivalent-in range with minimum H_2 consumption (4.97 kg of H_2, a battery of 44.5 kWh and 82 kW FC stack) offers a H_2 consumption of 0.79 kg H_2/100 km and a total energy consumption of 31.56 kWh/100 km. Hence, this design compared to FCV1 performance is capable of attaining roughly 16.8% save in H_2 consumption and comparable total energy consumption to cover the complete range. This comparison permits emphasizing the potential of FCREx, which may give comparable performance in terms of energy usage and range with reduced H_2 consumption and the flexibility to employ alternative driving modes based on H_2 availability.

As an additional part of this analysis, state-of-the-art BEVs offer around 455-484 km following the WLTP procedure (based on the Hyundai Kona electric and KIA e-Niro with a battery capacity of 64 kWh), which implies an energy consumption of roughly 13.2-14 kWh/100 km (considering a 100% depth of discharge, which is actually lower), which is significantly lower than that of FCVs [14, 15]. However, the charging times of these vehicles may oscillate from 30 min to several hours, depending on the C-rate while charging, which may be an inconvenient given that the actual range in highway of these vehicles could drop to 250-350 km. As such, even though the energy consumption may be higher for conventional FCVs or FCREx vehicles, the higher range and the lower refueling duration may make them more suitable then BEV for long-range operation.

The right-hand side pair of graphs in figure 4.7 depict the total energy consumption of every design with FCREx architecture. Energy consumption was determined as the total energy carried in the vehicle (considering both the H_2 and the battery) divided by the complete range. Increasing the FC stack maximum power implies a huge reduction in energy usage. This reveales that the FCS, relative to the battery, is the most limiting system in terms of

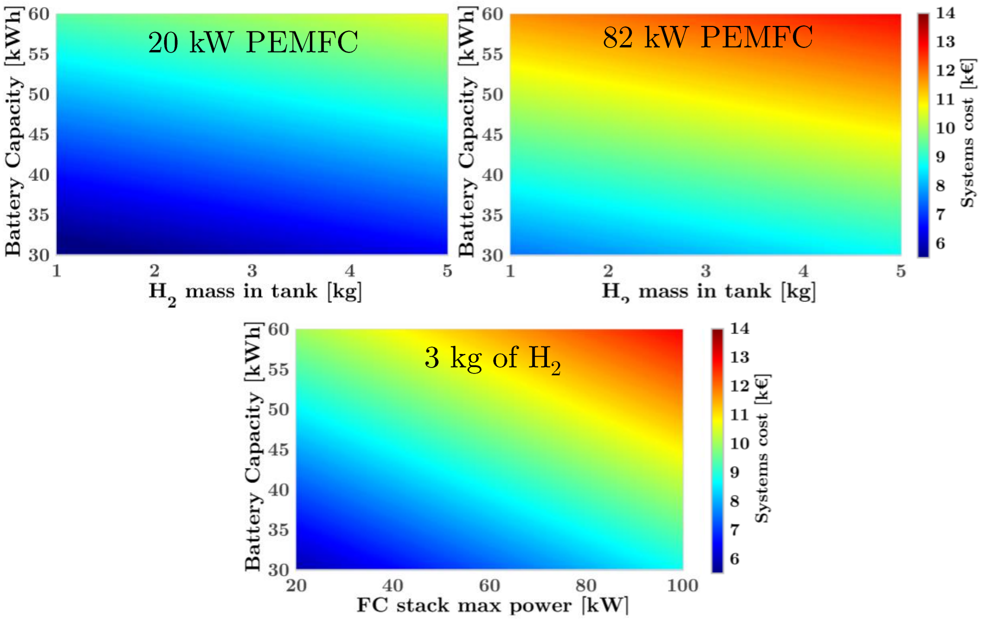

Figure 4.8. Total cost variation of the FCS, battery and H_2 tank for a FCREx architecture considering the designs with 20 kW PEMFC, 82 kW PEMFC and 3 kg of H_2 as fixed variables.

performance since it has lower efficiency. The impact of increasing the capacity of the battery and the H_2 tank on energy consumption is the same as that seen on H_2 consumption. However, the impact of increasing the battery size on lowering energy consumption is less important since for H_2 consumption the H_2 mass in the tank was maintained constant. From this data, FCREx manufacturers should prevent the usage of low-power FC stacks in their vehicle designs in order to optimize the energy consumption and range. Note that FCREx also enable lower FC maximum power compared to conventional FCV while achieving similar range and performance.

The graphs in figure 4.8 illustrate the overall cost change of the FCS, the battery and the H_2 tank. The two upper graphs demonstrate the cost variance while increasing the vehicle range by adding battery or H_2 tank capacity. Analogously, the cost variation while raising the maximum FC stack power and the battery capacity was displayed in the third graph as these two factors have the biggest influence on H_2 and energy consumption. From these data, increasing the energy stored in the vehicle was much more costly if it was done by expanding the battery capacity rather than increasing the H_2 tank capacity.

This indicates that the purchase cost of any BEV with the same range as any FCV could be significantly higher, which might enable greater H_2 cost to have the same TCO. For the designs with 82 kW PEMFC (upper right-hand side graph) increasing the H_2 capacity from 1 kg to 5 kg with a battery of 30 kWh was equal in cost to raising the battery capacity from 30 kWh to 40 kWh with 1 kg of H_2. These two systems with comparable cost had dramatically different performance in terms of consumption. The design with 5 kg of H_2 and a battery capacity of 30 kWh has a range, energy and H_2 consumption of 616 km, 32.1 kWh/100 km and 0.85 kg H_2/100 km, respectively. In comparison, the design with 1 kg of H_2 and a battery capacity of 40 kWh has a range, energy and H_2 consumption of 272 km, 27.8 kWh/100 km and 0.43 kg H_2/100 km, respectively. These designs are diametrically opposed and give such differing performance and range because the ratio of energy stored as H_2 to the total energy stored (battery included) is entirely different. This ratio was highlighted as another decision parameter for prospective that FCREx manufacturers may alter based on the vehicle application. With similar volume of the systems, if this ratio is low (low H_2 stored), the range is dramatically decreased alongside H_2 and energy consumption. This indicates significantly more efficient energy utilization to cover a given range, thereby decreasing operational expenses. This design might be useful for captive fleets application such as those founds at ports and airports or for low-power cars, therefore lowering the refueling/recharging time of these vehicles compared to BEV. In contrast, if the ratio is high, FCREx might be ideal for passenger cars by giving a high-enough range coupled with a flexible operation (battery for urban driving and FC+battery for long journeys) and low H_2 consumption compared to commercial FCVs. Finally, the data in figure 4.8 indicate that raising the FC stack maximum power also had a considerable influence on the vehicle manufacturing cost. Therefore, for every vehicle manufacturer, the ultimate decision of the FC stack maximum power should be taken by evaluating the vehicle application, the rise in manufacturing price and the reduction in H_2 consumption to minimize the TCO.

In figure 4.9, the design spaces for the FCREx architecture with range of 500, 600, and 700 km are presented. The mass of H_2 in the tank was set based on the battery capacity to give adequate on-board energy to accomplish the desired range (± 20 km). As such, it is reasonable to see that FCREx could possibly attain a range of roughly 700 km with 5 kg of on-board H_2, a battery of >50 kWh and an FC stack maximum power >30 kW if its performance was optimized. All the designs whose systems characteristics were lower than these could not attain a range of 700 km because of the absence of on-board energy or the poor efficiency of the systems. However, this range or somewhat

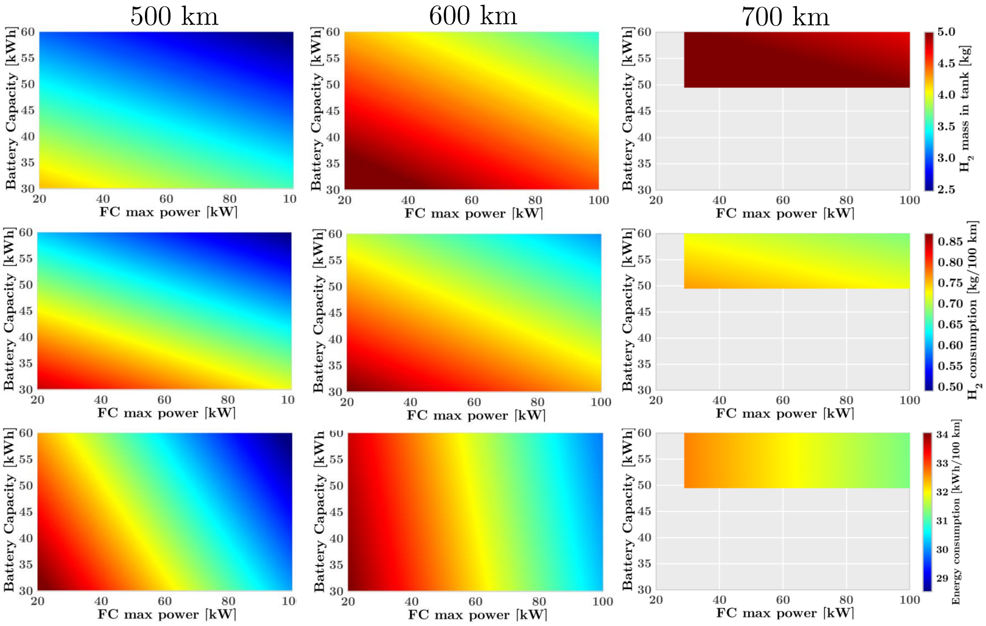

Figure 4.9. *Design spaces showing H_2 consumption and required H_2 mass capacity for FCREx with 500, 600, 700 km of range.*

better range appears to be the present limit for FCREx as the needed space to hold 5 kg of H_2 and a battery of >50 kWh may only be possible for large size passenger cars.

Based on the finding of this research, a properly optimized and designed FCREx could attain a range of 500 km with barely 3.76 kg of H_2 and a battery capacity of 30 kWh (155.3 kWh of total stored energy, i.e., 0.75 kg H_2/100 km of H_2 consumption and 31.06 kWh/100 km of energy consumption). Compared to FCV2, which has a range of 500 km with 5 kg of H_2 (166.5 kWh, i.e., 1 kg H_2/100 km of energy and H_2 consumption and 33.3 kWh/100 km), this indicates a much more efficient power usage of around 6.8% in terms of energy saving and around 25% in terms of H_2 consumption saving. As a result, FCREx might provide significantly lower operating expenses.

The advantage achieved after optimizing both FCV1 and FCV2 turned into an FCREx architecture and imposing the same total range is larger in the case of the FCV2. In this scenario the savings in energy use are bigger (around 6% saving vs. almost no saving), and the reason is the higher proportion of the total energy stored in the battery (30 kWh out of 155.3 kWh against 44.5 kWh out of 210.15 kWh). This gives a better optimization potential as the proportion of energy consumed from the battery to reach the prescribed range grows, hence the total vehicle efficiency also improves appropriately. Nonetheless, it would be necessary to integrate the same FC technology as in FCV1 and FCV2 to refine the quantification of the advantages or disadvantages of the FCREx architecture.

As demonstrated in figure 4.9, raising the FC stack maximum power lowers H_2 consumption (second row of graphs in figure 4.9). As such, the desing space reveals that larger FC stack maximum power can lower the quantity of H_2 stored to attain the same range (first row of graphs in figure 4.9), thereby decreasing the operating cost but raising the manufacturing costs. Energy usage exhibits variable sensitivity with the battery capacity depending on the vehicle range. For FCREx designs with 500 km of range, the drop in energy consumption with the increase in battery capacity (due to the improved battery efficiency) is smaller than for designs with 600 km of range. This occurs when the ratio of stored H_2 energy with respect to the total on-board energy must grow to achieve larger ranges, consequently a bigger percentage of the range is covered using just H_2 thus diminishing the impact of battery capacity over energy consumption. FCREx vehicle manufacturers should consider this to reduce the TCO. Based on the design spaces in figure 4.9 together with more precise data regarding the overall cost of a single FCREx manufacturing, it would be possible to produce equivalent graphs displaying the TCO. With the data in hand, the minimal TCO would presumably be situated around moderate values of battery capacity (cheaper operation with just energy from the battery) and relatively high FC maximum power to lower the H_2 consumption. The optimum design to minimize the total cost depends on the H_2 refueling price. If it is low, the optimum would shift towards lower FC maximum power, higher H_2 tank capacity and lower battery capacity to decrease manufacturing costs while, if H_2 is expensive, the optimum would relocate towards higher FC stack power, lower H_2 tank capacity and higher battery battery capacity. Estimating the TCO is a challenging task which depends on the H_2 cost, therefore on the region where the refueling station is located among other factors, and on the vehicle usage and driver profile, i.e., if the vehicle is used mainly in cities (BEV-like mode) and occasionally for long trips (FC+battery mode) or otherwise. This calculation is beyond the scope of this research and might give a significant and insightful analysis regarding the advantages, in terms of TCO, of FCREx compared to similar FCVs and BEVs. As such, it is proposed as a future work in chapter 6.

The development of the design spaces permitted to grasp the effects of modifying the systems size in terms of range, manufacturing costs and consumption. Only in terms of performance, the best design would be one with a battery capacity of 60 kWh and an FC stack maximum power of 100 kW (figure 4.9), and the H_2 tank capacity would be changed according to the required range. Nonetheless, this design would also indicate greater production costs, compared to lower FC power options. Following this argument, the ideal FCREx design would not only rely on performance considerations but on the TCO, as stated, and the cradle-to-grave emissions, which would depend greatly on the H_2 manufacturing route and the systems scaling. For this reason, the primary outcomes of this study are the design spaces themselves including the performance analysis of FCREx architectures relative to modern commercial FCVs, and the identification of the optimum systems sizing: moderate battery capacity ($\sim$30 kWh) and moderate-to-high FC stack maximum power ($\geqslant$80 kW). Although the highest performance was attained for 60 kWh batteries, the increase in systems costs practically doubled when raising the battery capacity from 30 kWh to 60 kWh (figure 4.8). For that reason, the best design, as a trade-off between TCO and performance would most certainly include a battery of 30 kWh in these design areas. Finally, as H_2 prices decrease and the FCS become more efficient, it would be conceivable to lower the FC stack maximum power output without substantial change in performance and operating expenses to minimize manufacturing costs, reason for which the FC maximum power of future FCREx may be around 60 kW rather than 80 kW.

The results reported in this section might be of interest for the scientific community and the industry for numerous reasons. First, any anyone from research institutes or industry who wants to know which would be the ideal H_2 and/or energy consumption and range of a particular FCREx design might directly utilize the design spaces (figures 4.7-4.9) to acquire fair and direct information. These data may be utilized effectively in the earliest phases of the FCREx vehicle development process to choose a basic design that would be enhanced with costs and emissions related data. TCO and cradle-to-grave emissions might also be derived using H_2 and energy usage statistics, as in section 5.2. Furthermore, the value of FCREx architecture was demonstrated against commercial FCVs, indicating that the lower the range, the bigger the benefit in consumption of FCREx compared to FCV (see the comparisons with FCV1 and FCV2). The maximum attainable range for an FCREx passenger with 5 kg of H_2 was also estimated (700 km), suggesting that FCREx architecture is adequate for passenger car applications. All in all, the conclusions reported in this section may be utilized widely in both scientific research and commercial applications.

4.3.2 Effect of energy management strategy dynamic and operational limits on performance and FC durability

The discussion in this section aims at understanding the effect of limiting the dynamics and the operation space of a FCREx vehicle on the EMS on performance and durability. As such, the selected design for this analysis, among those presented in section 4.3.1, is that representative of the future trend for the FCREx architecture with a FC stack maximum power offering close-to-optimum performance (60 kW) a battery capacity that minimizes the manufacturing cost (30 kWh) and 5 kg of H_2 to provide enough range.

Centered in this particular FCREx design, this section is divided into three different parts in which different constraints are imposed over the FCS control strategy, following the simulation matrix presented in table 3.7. In the first study, the dynamics of the FCS are limited in terms of $|\mathrm{di/dt}|_{\mathrm{max}}$. In the second part, the operation space, defined in terms of current density, is reduced by imposing a lower limit $\mathrm{i}_{\mathrm{min}}$. The last analysis consists of imposing the constraints in terms of dynamics and operation space defined in the previous parts to understand whether there exists any cross-effect between these restrictions in the EMS. In these three parts the consequences of set of constraints imposed over the EMS in terms of H_2 consumption and FC stack durability are evaluated.

4.3.2.1 Effect of limiting |di/dt|

Limiting |di/dt| during drive cycle operation has a direct influence on how the EMS optimizer manages the energy flows produced by the FCS. Taking into consideration that the boundary condition on the EMS is to keep the SOC of the battery at the same value at the start and at the end of the driving cycle (charge sustaining mode), any constraint on the EMS that does not allow the FCS to operate at the optimum condition must be compensated by increasing the total power generated (current density) at other operating conditions. As such, implementing constraints on the FCS dynamics has an influence not only on those conditions that the FCS can not attain because of the EMS limitations but also on the full cycle. This suggests that the current density development during the driving cycle is likely to be greatly altered, not solely in the high-dynamics region of the cycle. Figure 4.10 illustrates both the current density and the current density change rate during the simulated driving cycle. The development of the current density with time is fairly similar in the simulations where |di/dt| is not restricted and when the restriction is 0.1 $\mathrm{A/cm^2s}$ as high-dynamics is also attainable with such limitation. Therefore, the amplitude of

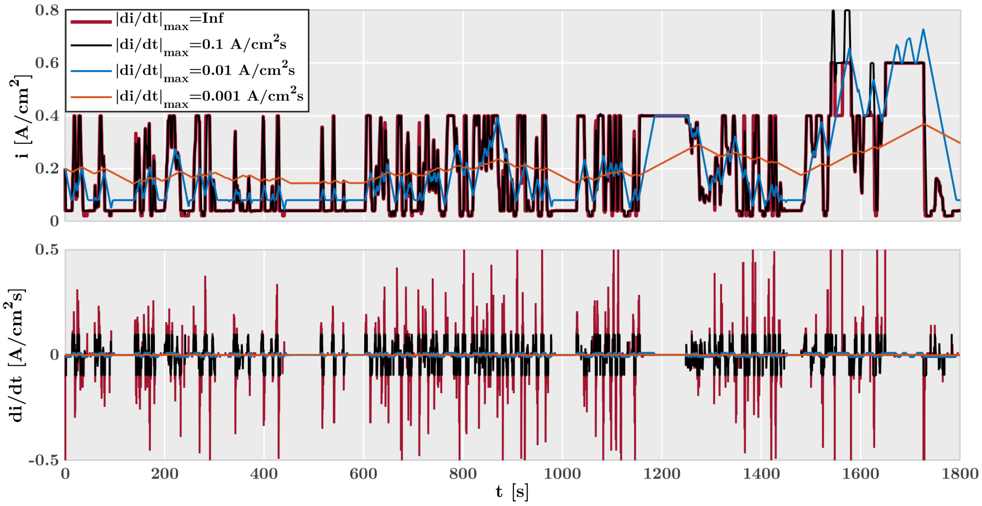

Figure 4.10. *Current density and current density variation rate evolution along the WLTC 3b driving cycle with different restrictions on |di/dt|.*

the load-change oscillations and their intensity is comparable in both cases. Nevertheless, it is feasible to notice certain discrepancies between these two control strategies. First, the current density peaks are greater until 1500 s for the non-limited simulation, implying that to accomplish that current density evolution, high dynamics are necessary. Therefore, at these points, the operation of the case with |di/dt| $\leqslant$0.1 A/cm^{2}s is sub-optimal. To compensate for this departure from the optimal operation the |di/dt| $\leqslant$0.1 A/cm^{2}s case has to provide extra power from 1500 s, in the high-power demand region of the cycle, when the current density increases to 0.8 A/cm^2. Compared to these two examples, those with |di/dt| $\leqslant$0.01 A/cm^{2}s and |di/dt| $\leqslant$0.001 A/cm^{2}s offer a smoother current density evolution. In both cases, the dynamics of the load-change (expressed through |di/dt|) are clearly reduced by imposition while the magnitude of such oscillations is lower in both simulations. For both scenarios, it is feasible to define how the minimum current density throughout the cycle grows to compensate for the areas when its operation is sub-optimum. This trend is reinforced the greater the limits on |di/dt|. Nonetheless, aside from slower dynamics, the scenario with |di/dt| $\leqslant$0.001 A/cm^{2}s also shows much smaller load-change oscillations amplitude because the slower dynamics prohibit the FCS from achieving large current densities. The minimal change in the absolute value of the FC current density shows that the behavior of the

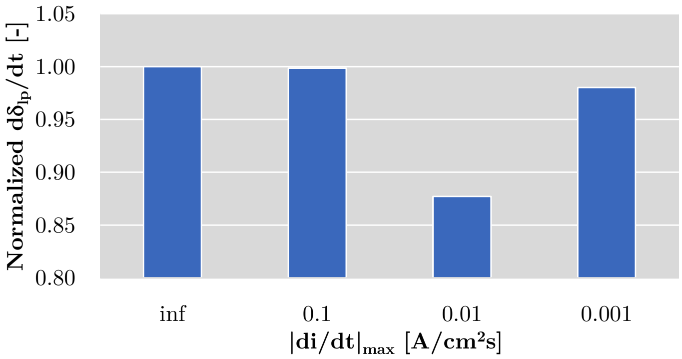

Figure 4.11. *Normalized low-power degradation rate variation with* $|di/dt|_{max}$.

FCS may be impacted by the value of the current density at the beginning of the driving cycle.

The second graph in figure 4.10 demonstrates how the dynamics of each simulation vary with the constraints. This graph, besides from serving to confirm that the |di/dt| limitations are implemented correctly, is helpful to understand that in the modeled FCREx vehicle the |di/dt| along the driving cycle without any restrictions on the EMS is mostly kept below 0.5 (reaching values around 1 occasionally). As such, mild constraints on |di/dt| such as restricting it to 0.1 A/cm^{2}s enable high dynamics and an FCS behavior near to the non-restricted situation. This means that, to observe substantial changes in both degradation and H_2 consumption, |di/dt| should be restricted to values around 0.01 A/cm^{2}s or lower.

The impact of altering the current density evolution (as seen in figure 4.10) on degradation can be observed in the various degradation rates by source in figures 4.11-4.14. Although it is expected that the biggest impact of restricting the dynamics of the FCS is identified in the load-change degradation rate, the subsequent change in the current density evolution to compensate for the sub-optimum operation influences other degradation rate sources such as low-power and natural/medium-power degradation.

Regarding the low-power degradation rate source (figure 4.11), following the change in the current density evolution when restricting |di/dt|, the simulations with no dynamic constraints and $|di/dt| \geqslant 0.1$ A/cm^{2}s have similar behavior in the low-power current density operating region $i<0.33$ A/cm^2, which explains the values of the normalized degradation rate for these designs in figure 4.11. Increasing further the dynamic restriction to 0.01 A/cm^{2}s

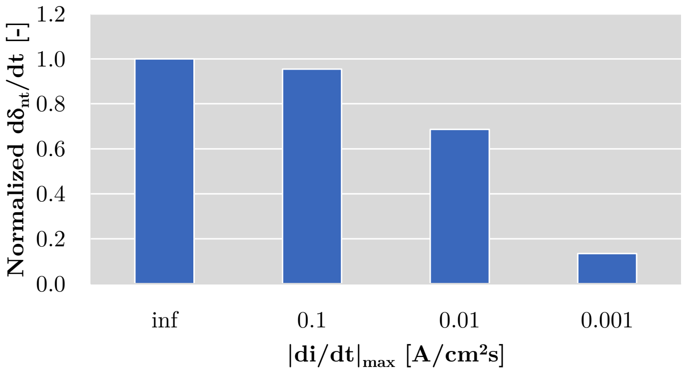

Figure 4.12. *Normalized natural (medium-power) degradation rate variation with* $|di/dt|_{max}$.

raises the minimum current density, thereby minimizing the degradation rate produced by electrochemical scaling as in equation 3.34. This suggests a drop in the degradation rate caused under steady-state low-power conditions. Nevertheless, if the dynamic constraint is even further raised to 0.001 A/cm^{2}s the slower development of the FC current density does not enable obtaining medium or high-power conditions frequently, thus the FC stack functions mainly under low-power conditions. This fact, even if it may reduce the operating temperature of the stack (due to the lower electrochemical losses), it increases the degradation rate caused under low-power conditions.

Following the same explanation as for low-power degradation, medium-power or natural degradation decline the higher the dynamic limitation (figure 4.12) because the overall current density profile becomes lower, thus the FC stack is less time at conditions at which steady-state degradation can be attributed only to the natural decay of the properties of the membrane and the catalysts.

As predicted, load-change degradation is the most-affected degradation rate source when restricting the dynamics because of both the reduction in the rate of change of the current density (|di/dt|) and in the amplitude of load-change oscillations.

The overall impact of placing dynamic limitations on FC stack durability may be observed in figure 4.14, in which the normalized total degradation rate change is illustrated. As explained in figures 4.11-4.13, small dynamic limitations (0.1 A/cm^{2}s) do not influence durability significantly while increasing them to 0.01 and 0.001 A/cm^{2}s could decrease the total degradation

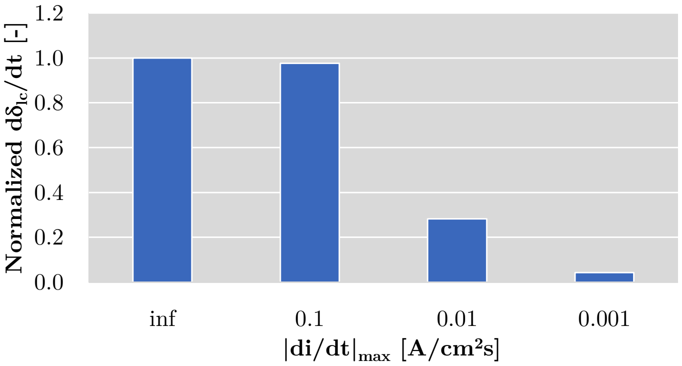

Figure 4.13. *Normalized load-change degradation rate variation with* $|di/dt|_{max}$.

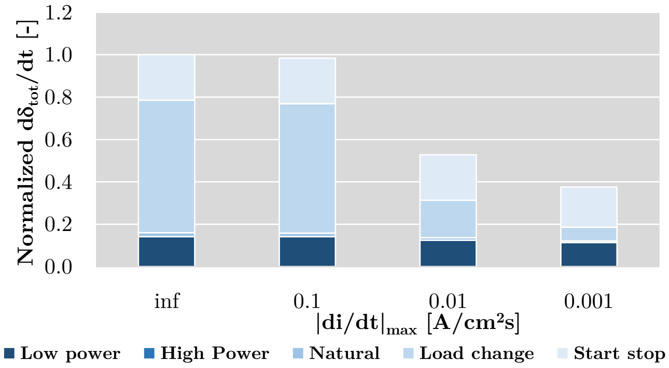

Figure 4.14. *Normalized total degradation rate variation with* $|di/dt|_{max}$ *segmented by source.*

rate by 47% and 62%, respectively. This suggests an increase in the FC stack lifetime of 89% and 166%. In agreement with most of the research in the literature, load-change degradation is the largest degradation cause, therefore limiting it via dynamic restrictions in the energy management strategy entails a considerable improvement in the stack durability. As can be observed in figure 4.14, load-change degradation is by far the most impacted degradation source.

Nonetheless, even if the degradation rate has fallen dramatically when restricting the dynamics, placing limits on the control strategy whose main purpose is to lower H_2 consumption has an influence on the overall vehicle efficiency. Figure 4.15 displays this effect in terms of H_2 consumption. The

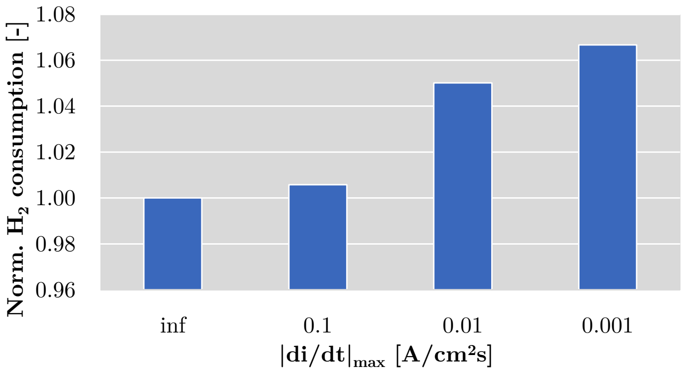

Figure 4.15. *Normalized H_2 consumption variation with $|di/dt|_{max}$.*

larger the dynamic constraint, the bigger the penalty in H_2 consumption, attaining increments of 5% and 6.7% in the cases of 0.01 and 0.001 A/cm^{2}s, respectively. This is reflective of how much of a trade-off imposing dynamic constraints is. Apart from the sub-optimum operation of the FCS, it is important to note that, if the dynamics of the FCS are lower than the dynamics of the e-motor power demand, the battery would need to provide additional power to cover for the lack of FCS power. This means that the battery will be discharged more and thus, in order to fulfill the charge-sustaining condition, additional power will need to be provided by the FCS. For that reason, considering the penalties in terms of H_2 consumption, the FCREx vehicle manufacturers should implement the dynamic limitation in the EMS that allows the FC stack of the designed vehicle to meet the target lifetime for a specific application and avoid restricting further the dynamics of the FCS to optimize H_2 consumption.

4.3.2.2 Effect of limiting i_{min}

The second constraint on the EMS that has yet to be studied is to limit the FC to work under a particular value of current density, i.e., restricting the minimum current density (i_{min}). This limitation is essential and has a demonstrable influence on durability since it dramatically affects the EMS optimizer behavior. As can be observed in the first graph of figure 4.16, the high dynamics are generally conserved throughout the various simulated cycles. Nevertheless, while detecting a high rate of change in the load-change oscillations (di/dt), it is obvious that the load-change cycle amplitude declines, implying that there should be a considerable influence on the major FC

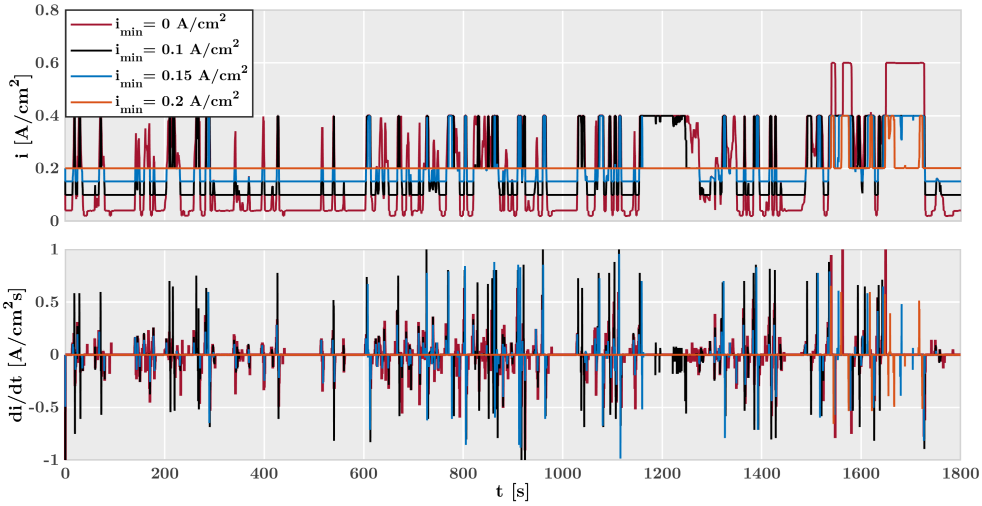

Figure 4.16. *Current density and current density variation rate evolution along the WLTC 3b driving cycle with different restrictions on i_{min}.*

degradation cause, i.e., load-change degradation. Moreover, the sub-optimum operation caused when imposing limitations on $\mathrm{i_{min}}$ encourages on one hand, smaller current density peaks and, on the other hand, fewer oscillations (see case with $\mathrm{i_{min}}$=0.15 A/cm^2 compared against cases with $\mathrm{i_{min}}$=0.1 A/cm^2 and $\mathrm{i_{min}}$=0 A/cm^2). The smaller and less frequent current density peaks are attributable to the fact that a considerable amount of additional power is produced when the FC is trying to operate under low current densities but remains at the restricted $\mathrm{i_{min}}$, hence the EMS does not require the FC to operate under high peak current densities that frequently to fulfill the charge sustaining boundary condition. As it is expected, operating at higher current densities may lower the FC degradation rate originating from the low-power (idle) degradation processes that are more significant the higher the FC voltage.

Despite detecting the aforementioned variations in the load-change oscillations and on the overall current density evolution during the driving cycle, excessive constraints on $\mathrm{i_{min}}$ are not suggested, although they may bring considerable advantages in terms of durability. This is the situation of restricting the $\mathrm{i_{min}}$ to 0.2 A/cm^2, where the FC operates at i=$\mathrm{i_{min}}$ for most of the cycle, except during the high-power region of the WLTC 3b cycle. With this current density evolution, the charge sustaining requirement could not be achieved with higher limits on $\mathrm{i_{min}}$ or at different driving cycles when

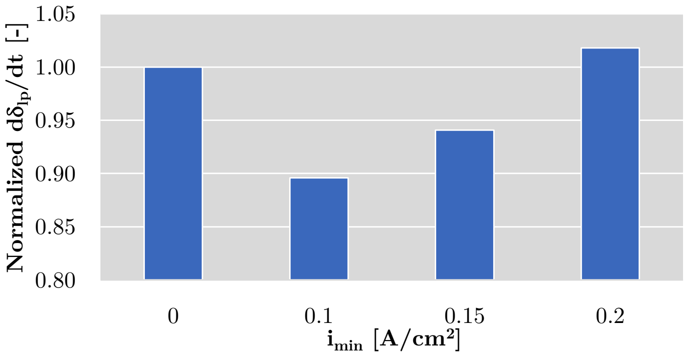

Figure 4.17. *Normalized low-power degradation rate variation with* i_{min}.

the brake power requirement of the electric motor is lower. As such, placing constraints on the minimum current density must be done thoughtfully, as it may impact considerably the operating mode of the FCREx vehicle, rendering it impracticable for specific driving conditions.

The intensity of the load-change oscillations, depicted in the second graph of figure 4.16, rises in general when limiting $\mathrm{i_{min}}$ compared to the non-restricted case at the high current density peaks to compensate for the sub-optimum operation. Nonetheless, the non-restricted case presents more locations where di/dt≠0 since the optimal operation that the EMS optimizer is enforcing is that of the FC following, up to a certain degree, the electric motor power demand. In general, except for the scenario in which $\mathrm{i_{min}}$=0.2 A/cm^2, it is impossible to extract a conclusion about what occurs with the impact of load-change oscillations intensity over durability only by looking at the current density evolution. However, an overall reduction in load-change degradation may be predicted given that a noticeable drop in load-change oscillations amplitude is observed.

Based on the change in the evolution of the current current density and its rate of change (figure 4.16) it is possible to understand the variation of the multiple degradation rates by source. Low-power degradation (figure 4.17) displays two tendencies depending on the limitation. It is possible to notice a drop in low-power degradation rate when comparing the non-limited and the $\mathrm{i_{min}}$=0.1 A/cm^2 cases. This drop is largely due to the global increase in the current density profile, which allows the FC stack to work at lower voltages, thereby decreasing the intensity of the degradation mechanisms that occur at low current density (equation 3.34). However, by raising further the constraint in the minimum current density, the low-power degradation rises. This fact,

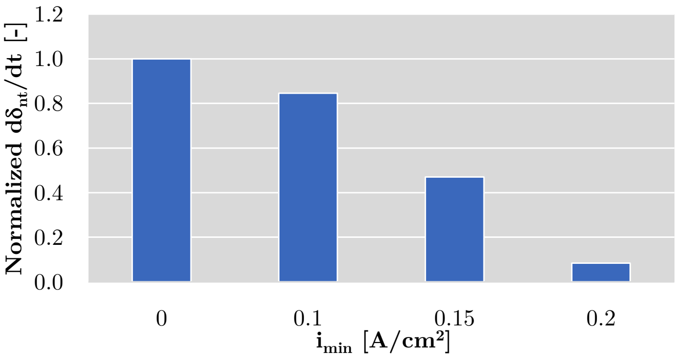

Figure 4.18. *Normalized natural (medium-power) degradation rate variation with* i_{min}.

while it appears contradictory, is caused for two reasons. First, the overall rise in the current density means larger electrochemical losses which, irretrievably, entails higher dissipated heat in the stack and the consequent increase in the temperature of operation. The rise in the temperature increases the degradation rate as in equation 3.41. Second, following the charge sustaining boundary condition set in the control strategy, raising the minimum current density implies increased power output during most of the driving cycle, which prevents the FC from running at medium or high current densities. In this situation, this has as a result that the FC stack works longer at <0.33 A/cm^2, thereby prolonging the timeframe under which the FC stack experiences low-power degradation.

Natural or medium-power degradation rate is reduced the higher the $\mathrm{i_{min}}$ (figure 4.18) because the overall increase in the current density in the low-power region makes the FC no longer need to reach the operating regions considered as medium or high-power to fulfill the charge sustaining constraint.

Although the dynamics of the FC stack are not constrained when applying limits in $\mathrm{i_{min}}$, a considerable reduction in load-change degradation is seen in figure 4.19 the higher value defining the lower bound for the current density. This is largely due to the lower amplitude of the load-change oscillations depicted in figure 4.16. As shown earlier, setting constraints in $\mathrm{i_{min}}$ has a direct influence on the total current density evolution, lowering even its maximum value over the driving cycle. Furthermore, in the extreme scenario of limiting the minimum current density to 0.2 A/cm^2, almost all of the load-change oscillations disappear since the additional power supplied when the current density is 0.2 A/cm^2 causes the optimum FC stack behavior no longer pursue

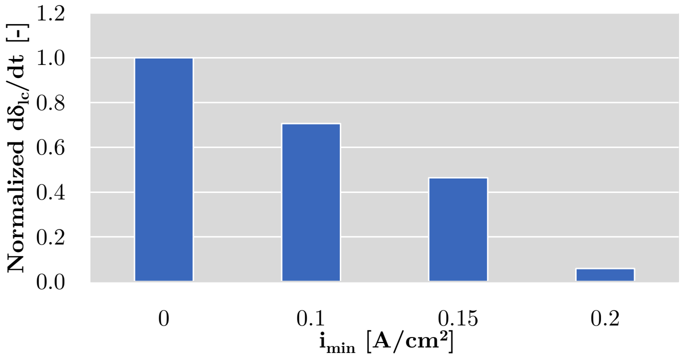

Figure 4.19. *Normalized load-change degradation rate variation with* i_{min}.

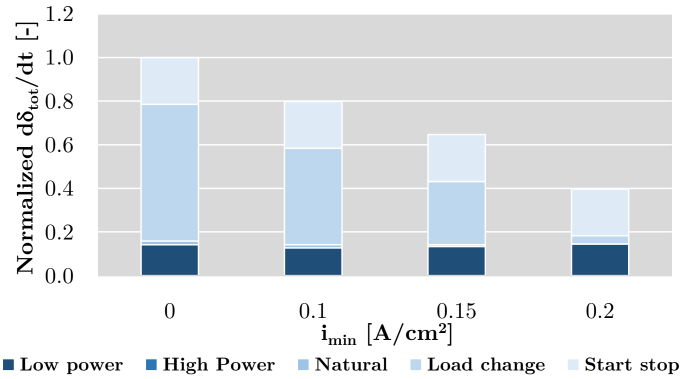

Figure 4.20. *Normalized total degradation rate variation with* i_{min}.

the e-motor power demand to fulfill the constant battery SOC condition. Nevertheless, after testing this restrictive condition in various driving cycles such as ARTEMIS Motorway, it was found too limiting as it may not enable satisfying the charge sustaining mode in high-dynamics driving profiles.

The overall effect of constraining the minimum current density is a reduction in the total degradation rate (figure 4.20), particularly caused by the decrease in load-change degradation which compensates for the rise in low-power degradation. Therefore , depending on the constraint, the degradation rate may reduce by 21% with moderate limitations (i_{min}=0.1 A/cm^2) or by 60% when severe constraints are placed (0.2 A/cm^2).

Analogous to figure 4.15, figure 4.21 exhibits the rise in H_2 consumption after implementing constraints on the minimum current density. Note that

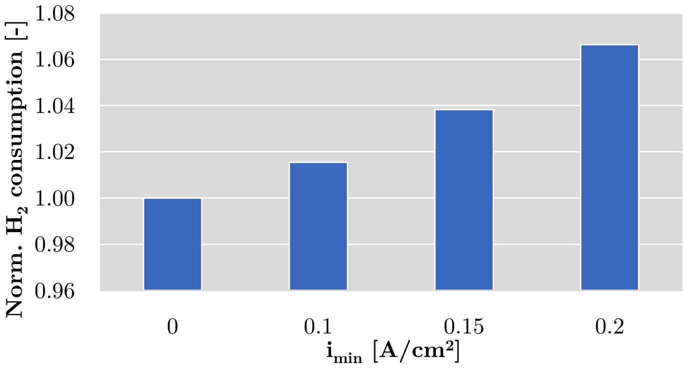

Figure 4.21. *Normalized* H_2 *consumption variation with* i_{min}.

setting any constraint on $\mathrm{i}_{\mathrm{min}}$ involves reducing the operating space of the FCS. Particularly, increasing the lower limit of the operation space of any power generation system implies ignoring the possibility to optimize the fuel consumption locally, which in turn, has severe consequences in terms of fuel consumption optimization penalty. For that reason, even the lowest restriction in the minimum current density examined in this research (0.1 $\mathrm{A/cm^2}$) has as a result a considerable rise in $\mathrm{H_2}$ consumption of 1.5%. Interestingly, when comparing the two simulations in which the limitations on the EMS are extreme ($\mathrm{i}_{\mathrm{min}}$=0.2 $\mathrm{A/cm^2}$ or $|\mathrm{di/dt}|_{\mathrm{max}}$=0.001 $\mathrm{A/cm^2s}$) the $\mathrm{H_2}$ consumption increases similarly by 6.6%-6.7% with respect to the non-constrained case. This value for the $\mathrm{H_2}$ consumption increment can be regarded as the highest penalty for the best-case control strategy when severe restrictions are put on it and it becomes unable to meet the charge-sustaining condition under high-dynamics driving situations.

From these data, it is reasonable to deduce that even a minor constraint in the minimum current density gives a considerable drop in degradation rates at the price of a slight penalty on $\mathrm{H_2}$ consumption. Nonetheless, setting constraints on $\mathrm{i}_{\mathrm{min}}$ narrows the operating space of the FCS, therefore hampering the fulfillment of the charge-sustaining condition.

4.3.2.3 Simultaneous limitation of |di/dt| and $\mathbf{i}_{\mathbf{min}}$

The effect of constraining |di/dt| and $\mathrm{i}_{\mathrm{min}}$ on performance and durability has been investigated in sections 4.3.2.1 and 4.3.2.2, respectively. As explained, the implications of putting separately each constraint on the control method are comparable yet caused by differing behavior on the current density

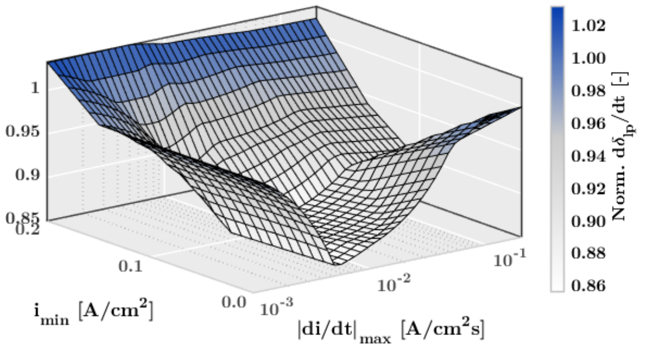

Figure 4.22. *Normalized low-power degradation rate variation with* $|di/dt|_{max}$ *and* i_{min}.

evolution over the driving cycle. Load-change degradation was the most impacted degradation rate source as the imposed limits had an influence on the FCS dynamics (|di/dt|) or in the load-change oscillation amplitude ($\mathrm{i_{min}}$). In this section, the cross-effect of both limitations on the energy management strategy is explored to determine if it is preferable to apply simply one of these limitations or a combination of both to optimize durability and decrease consumption.

Low-power degradation is both influenced by setting limitations on the dynamics of the FCS (|di/dt|) and on the minimum current density because in both situations the overall current density profile rises, thereby decreasing the degradation rate due to high-voltage operation. Figure 4.22 demonstrates how the trends in figures 4.11 and 4.17 continue to appear except for the cases when severe constraints are implemented. As a result, the minimum low-power degradation rate is reported with $\mathrm{|di/dt|_{max}}$=0.01 A/cm^{2}s and $\mathrm{i_{min}}$=0.1 A/cm^2, i.e., agreeing with the minimums observed in figures 4.11 and 4.17. This suggests that the ideal combination of both limits on the control method may stimulate the further reduction of the low-power deterioration. Nonetheless, when extreme limitations are applied ($\mathrm{|di/dt|_{max}}$=0.001 A/cm^{2}s or $\mathrm{i_{min}}$=0.2 A/cm^2) the low-power degradation rate becomes maximal and almost insensitive to any other constraint. This, again, reinforces the argument for avoiding excessive limits in the EMS.

Similarly to low-power degradation, natural or medium-power degradation rate also retains the individual trends when imposing restrictions on the

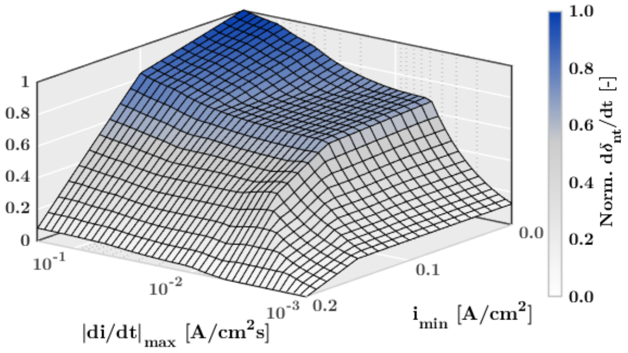

Figure 4.23. *Normalized natural (medium-power) degradation rate variation with* $|di/dt|_{max}$ *and* i_{min}.

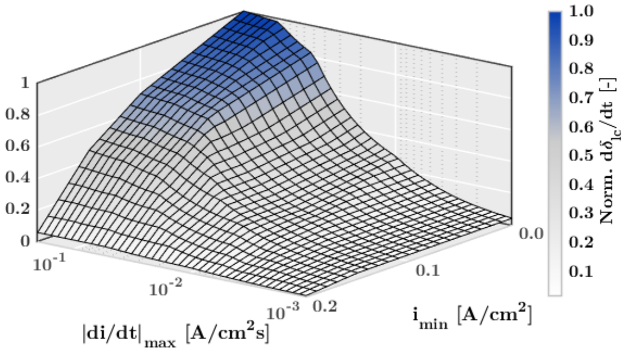

Figure 4.24. *Normalized load-change degradation rate variation with* $|di/dt|_{max}$ *and* i_{min}.

dynamics or on the lower limit of the operating space except for severe constraints (figure 4.23).

As anticipated, load-change degradation is more impacted when restricting the dynamics than when imposing limitations on the minimum current density (figure 4.24). Nevertheless, its minimal value is always obtained at severe restrictions, no matter whether they are in the dynamics or in the operational space. Load-change degradation rate dominates the overall degradation, given the similarity of figures 4.24 and 4.25, although the latter is greater at each restriction because of the inclusion of the other degradation rates. This is

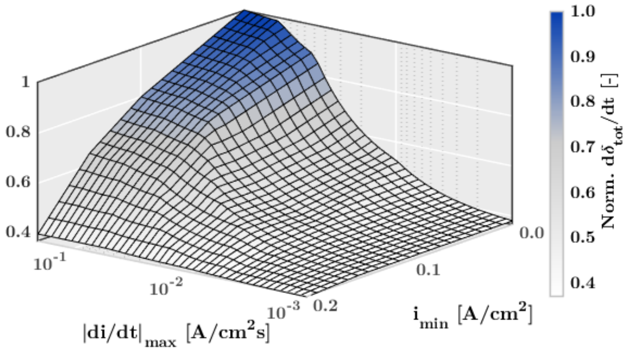

Figure 4.25. *Normalized total degradation rate variation with $|di/dt|_{max}$ and i_{min}.*

attributable to the fact that even knowing that there are other degradation rate sources that may vary with the constraints imposed on the energy management strategy, load-change degradation continues to dominate the FC stack durability even when alternative constraints oriented to mitigating other degradation sources (such as limiting i_{min}) are imposed. Nonetheless, it is essential to quantify the contribution of the other degradation sources to the total degradation as they may become more relevant as the EMS is more restricted (figures 4.14 and 4.20). This indicates that any research that analyzes the change in FC stack durability via modifications in the control strategy and that considers solely load-change degradation as the only degradation source may surely overestimate the improvement in FC stack durability.

H_2 consumption suffers a comparable increase when applying any constraint, be it in the dynamics or in the operation space (figure 4.26). The maximum increase in H_2 consumption with the control strategies considered is observed when extreme limitations are implemented ($|di/dt|_{max}$=0.001 A/cm^{2}s or i_{min}=0.2 A/cm^2) and is around 6.6-6.7% with respect to the non-limited case. Furthermore, only small limits in the operation space (i_{min}=0.1 A/cm^2) indicate 1.5% higher H_2 consumption and 20% lower degradation rate, i.e., 25% greater durability. The cause for this modest increase in H_2 consumption is that, although the limitation prevents the FCS from working at a very low load where the fuel consumption is low, this operation region usually implies low efficiency because the auxiliary components integrated into the BoP have considerable consumption compared to the power produced by the FC stack at such a low load.

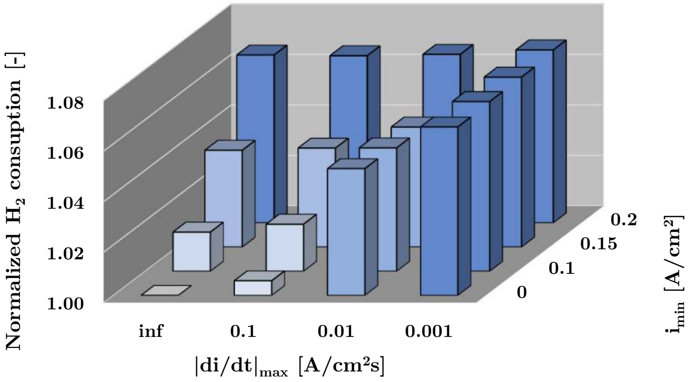

Figure 4.26. *Normalized* H_2 *consumption variation with* $|di/dt|_{max}$ *and* i_{min}.

Interestingly, once the constraint in the dynamics achieves a value of 0.01 A/cm^{2}s or the minimum current density is restricted to 0.15 A/cm^2, the H_2 consumption remains between 3.8% and 5% higher than the non-limited case, except when any of the two constraints is increased. Among these strategies, that with $|di/dt|_{max}$=0.01 A/cm^{2}s and i_{min}=0.15 A/cm^2 offers the highest decrease in degradation rate (53%), thus the highest increase in durability (110%) with an increase in H_2 consumption of 4.7%. In this situation, it is possible to discern a cross-effect between the two limitations since a modest drop in H_2 consumption was discovered when restricting the dynamics to a fixed value of 0.01 A/cm^{2}s and raising the i_{min}. This drop in H_2 consumption was due to the fact that the dynamic restriction does not permit the FC stack to run under high loads when the e-motor experiences a rapid increase in the load demand if the FC stack is working at low current densities. However, if the FC stack runs at greater current densities in the low load region because the i_{min} is restricted, then the FCS power supply will attain higher loads under rapid increases in the e-motor power demand. This helps the FCS to follow better e-motor operation in the high current density zone where the battery has to deliver extra power when the FCS is not capable. As a result, if the battery is less depleted, the FCS will not have to supply extra power to satisfy the charge-sustaining mode, thereby lowering the H_2 consumption.

From the results obtained in this section, the control strategy with $|di/dt|_{max}$=0.01 A/cm^{2}s and i_{min}=0.15 A/cm^2 offered the largest increase in durability (110%) with just an increase in the H_2 consumption of 4.7%.

As such, this design might be regarded *recommended* for the passenger car application and vehicle architecture by the authors for the following reasons:

- The dynamics are high enough to meet the constant SOC restriction that is typical of FCREx design even under high-load and high-dynamics driving profiles.
- Minimum current density is high enough to reduce the influence of the degradation mechanisms that arise during high-voltage operation and appears to offer a reduction in H_2 consumption due to a cross-effect with the constraints in the dynamics.
- The increase in H_2 consumption is minor and below 5% in exchange for a large improvement in FC durability.

Nevertheless, it is important to remember that this research was undertaken for a particular application and driving cycle condition. As such, if the vehicle design, size or application change, the optimal restrictions in the EMS may likewise vary. For example, if the FCS is used for other applications such as forklift captive fleets for which the propulsion system power demand is lower and the dynamics are not critical or frequent, then the optimum EMS may consist of a set of hybrid operation modes: extremely low dynamics ($|\mathrm{di/dt}|_{\mathrm{max}}$=0.001 A/cm^{2}s) to move the vehicle and permitted high-dynamics during short periods for cargo-lifting. In this regard, altering the driving conditions and the driver profile will surely influence the FC stack durability and performance. As such, any EMS developed for actual driving should consider self-adaptation to the most typical driving profiles and power demands it is utilized for, hence the optimal constraints may vary. With these considerations, this research serves as a foundation to further develop improved EMS aimed at maximizing durability and H_2 consumption based on the patterns revealed from these data.

The insights from the results presented in this section bring light to the implementation of constraints in the energy management strategy for FCREx vehicles. As may be noticed in figure 4.26, every constraint in the EMS indicates an increase in H_2 consumption. Hence, the advice that can be drawn from these data is that the EMS should be restricted in such a manner that the FC stack achieves a desired value of durability, without over-constraining the EMS to decrease consumption. Furthermore, it may be desirable to set constraints on the minimum current density if the dynamics are constrained to a value near 0.01 A/cm^{2}s because both durability and performance improve. This suggests that FCREx producers should consider extra constraints in the control strategy of their FCREx vehicles aside from enforcing slower dynamics in the FCS. Given the highly-dynamic behavior that the FCS reveals when the dynamics are limited to 0.1 A/cm^2s, it is suggested for both conventional FCVs and FCREx vehicles to implement at least this limitation in the dynamics to minimize the potential appearance of anode or cathode starvation that may increase degradation. Finally, given an FC stack technology with specific durability, the FCREx manufacturers could predict the rise in H_2 consumption and durability while applying diverse control strategies in such a manner that they could minimize the degradation rate and the OPEX simultaneously. The change in the FC durability may be done individually for each degradation source, therefore the durability can be evaluated for each FC stack technology.

FC stack or FCS designers might also utilize these data when in collaboration with OEMs if they want to develop FCREx vehicles. If the OEM considers the use of a specific control strategy with a particular set of constraints in the dynamics or in the minimum current density based on these data, the FC stack manufacturers could aim for a stack design that improves the water and flow management at low-dynamic operation or that reduces the high-voltage degradation (low-power) to minimize costs, maximize performance and durability. Analogously, FCS manufacturers might modify the balance of plant design in such a manner that the needs in terms of the dynamics for the cathode and/or anode humidification or for the compressor are reduced, thereby decreasing the manufacturing costs of the powertrain.

4.3.3 Cross-effect of dynamics-limited energy management strategy sizing on performance and FC durability

4.3.3.1 Effect over the FCS behaviour

In agreement with the results in the previous sections, the evolution of the current density along the driving cycles changes when adjusting the FC maximum power by modifying the number of cells and the dynamic limitations of the FCS. As such, and given the significance of the FCS operation on degradation and performance, it is essential to understand and evaluate the FC behavior and how it changes when acting over any of these factors. For that reason, figure 4.27 displays the current density evolution for the 40 kW and 100 kW FC stack maximum power designs with dynamic constraints ranging from 1 A/cm^2s(nearly infinite dynamics) to 0.001 A/cm^2s (very high restriction) . Although the 60 kW and 80 kW designs were included in the study as well, their current density evolution is not illustrated in fig 4.27 to enhance the readability and clarity of the graphs. In contrast, the highest-

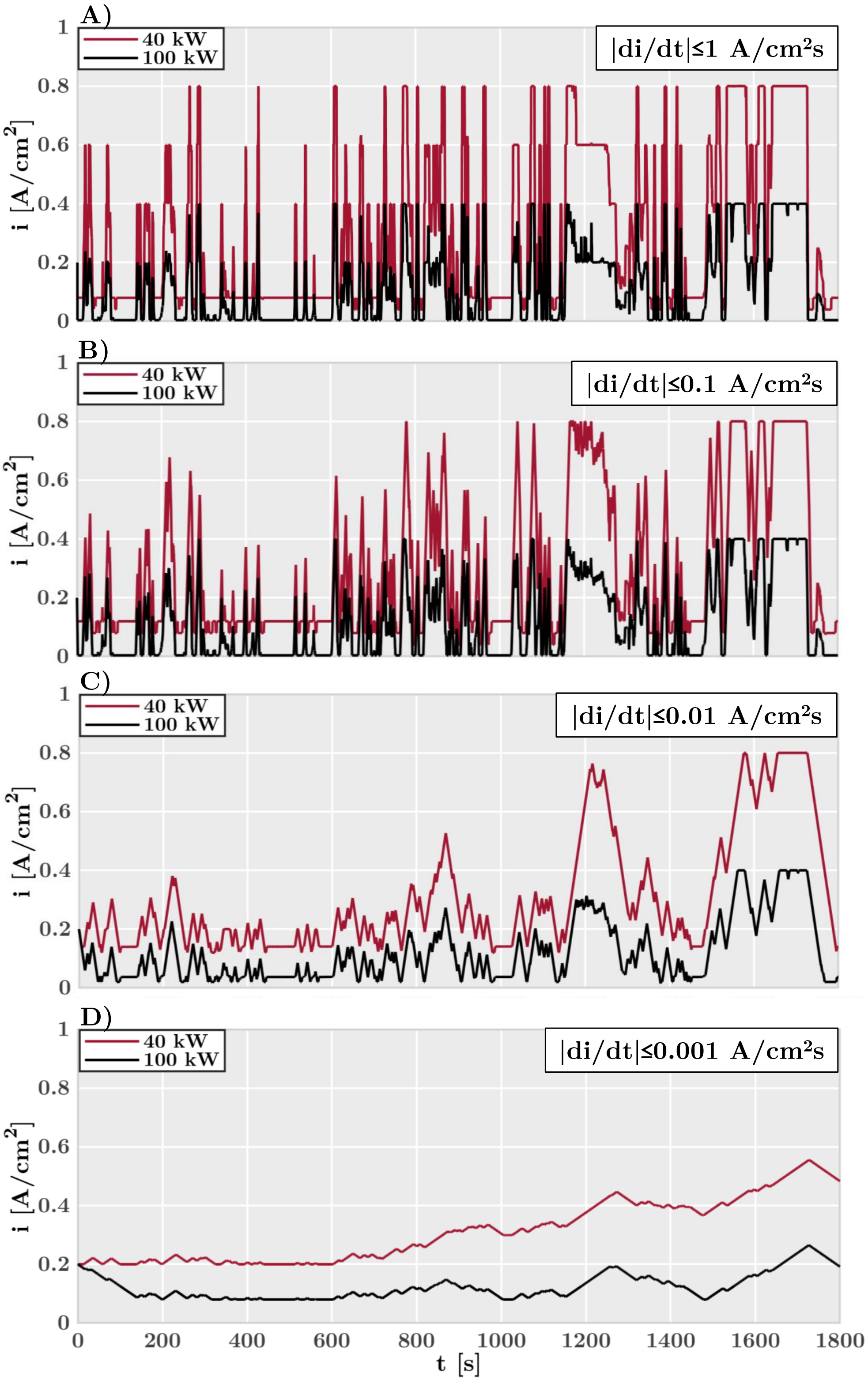

Figure 4.27. *Current density evolution along WLTC 3b driving cycle for 40 kW and 100 kW FC stack maximum power with dynamic limitations ranging from 1 A/cm^2 to 0.001 A/cm^2.*

power and lowest-power designs were utilized to show the influence of FC stack power. This figure is used to supplement the information in figures 4.28 and 4.31 demonstrating how the H_2 consumption and degradation rate change.

The selection of the dynamic constraints to 1, 0.1, 0.01, and 0.001 A/cm^2 was influenced by the various scenarios they represent. The first restriction (1 A/cm^2) reflects the scenario of practically unlimited dynamics since throughout the simulation of the non-restricted FCV in WLTC 3b cycles without any dynamic constraint the $|di/dt|$ was usually below 1. The second value (0.1 A/cm^2) was identified as a dynamic restriction representative of high dynamics with a certain limitation to avoid cathode/anode starvation because the stoichiometries were more stable and nearer to the target values while retaining the highly-dynamic operation. The scenario with 0.001 A/cm^2 (severe dynamics limitations) illustrates the predicted operation of a range-extender in which the power demand oscillations are slow (see figure 4.27, graph D). This shows the dynamic limit within which the condition set in the EMS of maintaining the battery SOC at the same value at the start and the end of the driving cycle is not met in aggressive driving patterns (calculated by considering the ARTEMIS Motorway driving cycle). Finally, the limitation of 0.01 A/cm^2 is a number in between the high and low dynamics (moderate dynamics) that permits the FC attain higher current densities while reducing the severity and the amplitude of load-changing cycles (see figure 4.27, graph C).

The influence of FC stack size on the current density evolution may be evaluated using the data in figure 4.27. A, where the dynamic limitations are minimal and the FCS operates near the optimal behavior to reduce H_2 consumption because the EMS is not limited by the FC dynamics. In contrast, given the relevance of load-change degradation in driving cycle conditions, FC durability is anticipated to be worse compared to other scenarios with lower dynamics. An overall drop in current density is seen while raising the FC maximum power. This is justified by the fact that an FC stack with a large number of cells (100 kW) running at a specific current density generates more power than a stack with a lesser number of cells (40 kW) at the same current density. Therefore, because both FCV designs are being utilized in the same driving cycle (WLTC 3b) the power demand by the electric motor would be similar, given that it rises slightly for the case of the 100 kW FC stack design because of the larger powertrain weight. Lower H_2 consumption is expected for the design with 100 kW as it works at lower current densities, which suggests improved FCS efficiency. Interestingly, the maximum current density throughout the cycle for the 40 kW design is 0.8 A/cm^2 whereas it is 0.4 A/cm^2 for the 100 kW despite the number of cells increasing by a factor of 2.5. This occurs because the energy management strategy optimizer that reduces H_2 consumption restricts the 40 kW stack to run in the lowest efficiency region, i.e., at high current density (>0.8 A/cm^2). Instead, to compensate for this lack of power supplied by the 40 kW FC when the e-motor power demand is substantial the minimum current density rises to meet the charge sustaining condition, compared to the 100 kW design.

Increasing the FC dynamic restriction to 0.1 A/cm^{2}s (figure 4.27.B) does not imply substantial changes in the current density distribution as the limitation is still modest and allows for high dynamic behavior. Nevertheless, certain differences in both the 40 kW and the 100 kW designs may be detected at the high current density peaks and in the lowest current density. In this sense, due to the dynamic limitations, certain peaks in figure 4.27.A with a value of 0.8 A/cm^2 for the 40 kW design can not be attained in figure 4.27.B, implying that the operation, in terms of minimizing H_2 consumption, is sub-optimum. In order to compensate for this temporary shortage of power supplied by the FCS and fulfill the charge sustaining condition, the minimum current density rises, thereby supplying more power along the driving cycle. These modifications are more obvious for the 40 kW design but are also present, albeit to a reduced level, for the 100 kW design. Given the current density evolution in figure 4.27.B, some loss in terms of H_2 consumption and some advantage in terms of durability may be anticipated. Nonetheless, the influence on both parameters should be minimal as the dynamic limitation is not severe.

When the dynamics are visibly limited to values of 0.01 A/cm^{2}s and 0.001 A/cm^{2}s (figures 4.27.C and 4.27.D, respectively), the evolution of the current density along the driving cycle significantly changes and has important effects on both H_2 consumption and FC stack durability. In the case of figure 4.27.C, both designs experience an increase in the minimum current density to compensate for the sub-optimum operation and the maximum current density peaks are less frequent, which may result in a large penalty on H_2 consumption. This may reflect an overall decline in medium-power or natural degradation, followed by a drop in low-power or idle degradation due to high-potential cell values. Furthermore, load-change intensity is clearly altered. Therefore, an overall reduction in the total degradation rate should be predicted since the principal source of degradation (load-change) is effectively acted on. Nevertheless, the increase in the minimum current density also indicates an increase in the rejected heat of the FC stack throughout the cycle, thus an increase in the FC temperature and a probable rise in all the degradation rates. The final degradation rate will consist of a trade-off between these impacts.

The case with the most restrictive dynamic limitation (figure 4.27.D) provides a smooth current density variation along the driving cycle. In this case, for both designs, a decrease in the load-change cycle intensity and amplitude, a drop in the maximum current density, an increase in the minimum current density are observed. Following the same reasoning as with the results in figure 4.27.C, H_2 consumption should increase while degradation rate should decreasesignificantly, but the effect over durability should be determined taking into account the FC stack physical conditions of temperature and relative humidity, not only the current density evolution. Nonetheless, this highly-restricted dynamics limitation was evaluated throughout several FC stack size designs and drive cycles. As in section 4.3.2, it was determined that high-dynamics restrictions may prevent the controller from fulfilling the charge sustaining condition when low-power FC stacks are considered (20-40 kW) in high-power and high-dynamics driving cycles and that it will significantly depend on the initial current density at the beginning of the cycle. Nonetheless, the charge sustaining mode might be feasible with high-power FC stacks since a given change in the current density for a 100 kW stack implies a larger variation in the power supply than in a 40 kW stack. Therefore, this limitation is not suggested for automotive applications as it may hinder the flexible operation of FCREx vehicles, but may be interesting for applications such as heavy-duty transportation in which long routes with lower dynamics in the power demand may be found often.

4.3.4 Effect on FCV performance

The impact of FC sizing and dynamics limitations on H_2 consumption and FC stack degradation rate may be primarily due to the change in the FC current density evolution (figure 4.27). However, it is critical to distinguish between the impact of implementing dynamic limits and the effect of raising the FC maximum power both in degradation rate and performance.

In this section, normalized results are reported as they offer advantages for comparative analyses. Nevertheless, the absolute value of H_2 consumption is within the predicted range of FCV because this model was utilized in prior research where it was validated and compared against commercial FCVs [8, 9]. The same can be stated for degradation rates which, even in the scenario that the FC technology advances in durability, the tendencies in relative terms should be conserved since they are scaled with the tendencies followed by the electrochemical and physical degradation phenomena.

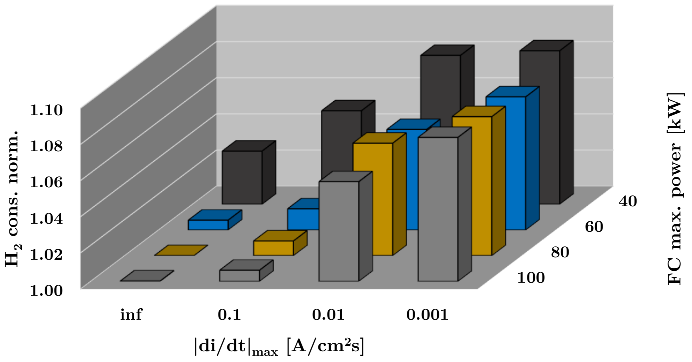

Figure 4.28. *Normalized H_2 consumption evolution as a function of the FC stack maximum power and the dynamic limitations.*

Figure 4.28 illustrates the normalized H_2 consumption of each design with different constraints on the rate of change of the current density. As mentioned in section 4.3.3.1, greater FC maximum power indicates lower current density, thus a more efficient operation despite of the slightly larger load. Therefore, H_2 consumption falls with increasing FC maximum power, but nearly no advantage is noticed when raising the FC power further from 80 kW since, for the specified vehicle application, this stack already works at the highest-efficiency current density range (medium load). From this value of FC stack power, increasing the number of cells of the stack should not bring considerable advantages in terms of H_2 consumption but rather it might increase due to the higher weight. In this respect, H_2 consumption is 3% greater with the 40 kW FC stack compared to the 100 kW design when no dynamic restriction is implemented. In contrast, with a constant FCV design, raising the dynamic restriction to 0.01 and 0.001 A/cm^{2}s increases H_2 consumption by 5-8% depending on the design. In the case of the 40 kW design, consumption only rises by 5% (for both 0.01 and 0.001 A/cm^{2}s scenarios) compared to its value with infinite dynamics as it is high already without any dynamic limits. For higher-power designs, there is a noticeable variation in H_2 consumption between the 0.01 A/cm^{2}s and the 0.001 A/cm^{2}s because the former allows for higher dynamics in terms of power variation rate, thus lowering H^2 consumption and experiencing higher penalties when increasing the constraint.

4.3.5 Effect on FC stack durability

As with H_2 consumption, the data obtained from the simulations illustrate how the impact of adjusting the FC maximum power on the durability is different from that observed when implementing dynamic constraints on the control strategy. Figures 4.29 and 4.30 represent the change of the relative importance of each degradation source for various designs and dynamic limits. These data, coupled with those in figure 4.31 are helpful to comprehend the difference in durability between different designs and dynamic constraints as well as the specific impact of modifying the FC maximum power or implementing dynamic limitations on each degradation source. Lifetime was determined following the end of life (EOL) standard defined by the Department of Energy through which an FC stack is deemed to have reached the EOL when the voltage decreases by 10% with respect to its nominal condition at a current density of 1 A/cm^2 [16].

The direct impact of the change in the current density evolution when increasing the FC stack maximum power (figure 4.27) and the decrease in FC stack temperature due to the lower electrochemical losses when operating at low current density yields the increase in FC stack durability with infinite dynamics shown in figure 4.31. This implies an improvement in FC durability of 53% when comparing the 40 kW and the 100 kW configurations. The specifics on how the degradation rate by source change with this design factor (figure 4.29) shows how the load-change degradation, responsible for 72% of the total degradation rate with the 40 kW design, decreases below 53% of he ttotal degradation due to the lower amplitude of the load-change cycles (figure 4.27.A). Star-stop cycling remains as the second main source of degradation for all the designs and its relative impact tends to increase with FC stack power since it is constant and does not depend on the FC behavior along the driving cycle (only 1 start-stop cycle was considered per cycle) and it depends mainly on the start-stop sequence and the FC stack technology. As the FC stack maximum power grows, low-power degradation becomes more critical while medium-power or natural degradation diminishes as the FC stack needs to run at lower current densities to meet the same power requirement.

Imposing dynamic restrictions has been a common method to reduce degradation in FC stacks for automotive applications since load-change degradation is the major source of FC degradation. As such, the largest increase in the durability is observed when imposing limitations over the current density dynamics rather than when increasing the FC maximum power (figure 4.31), with a maximum increase in FC durability of 294% and 123% for the 40 kW and the 100 kW comparing the infinite dynamics with the highest

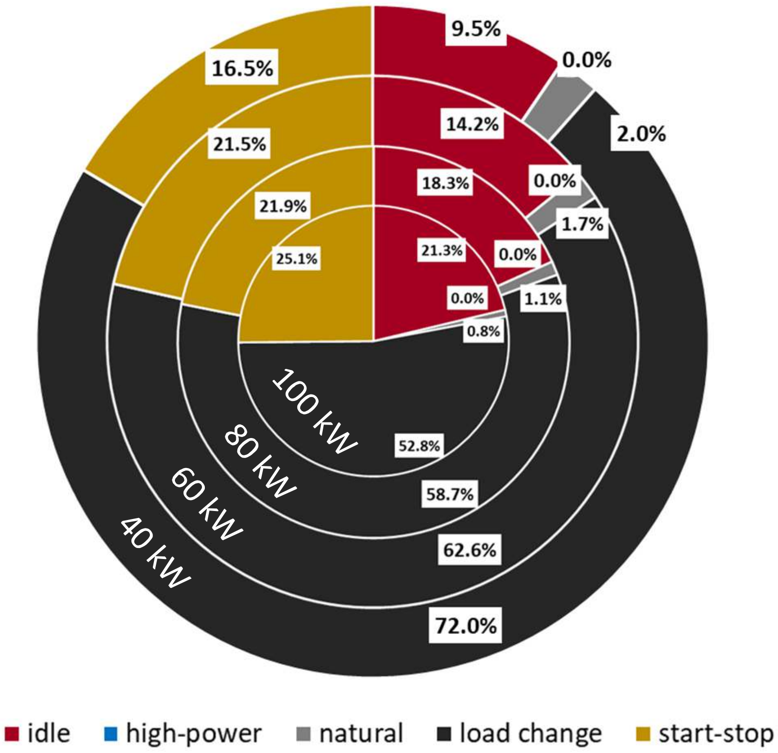

Figure 4.29. *Degradation source relative effect on FC stack durability decrease for the 40, 60, 80, and 100 kW designs.*

dynamic limitation cases, respectively. Nevertheless, similar durability is observed for all the designs when the highest dynamic limitations are imposed over the FC control (0.01 A/cm^{2}s and 0.001 A/cm^{2}s), meaning that the positive impact in the durability of operating under lower current density and lower load-change cycle amplitude becomes negligible when the load-change intensity (dynamics) is limited no matter the FC stack maximum power. The considerable improvement in durability is largely due to the reduction in load-change degradation that ranges from 62.6% to 6.9% of total degradation in the case of the 60 kW design (figure 4.30). This drop in load-change degradation suggests a considerable rise in the prominence of other degradation sources. Start-stop degradation can become the largest degradation source, followed by low-power degradation prior to load-change degradation.

The change in the relative importance of each degradation source may be important information for FC stack manufacturers for OEMs designing

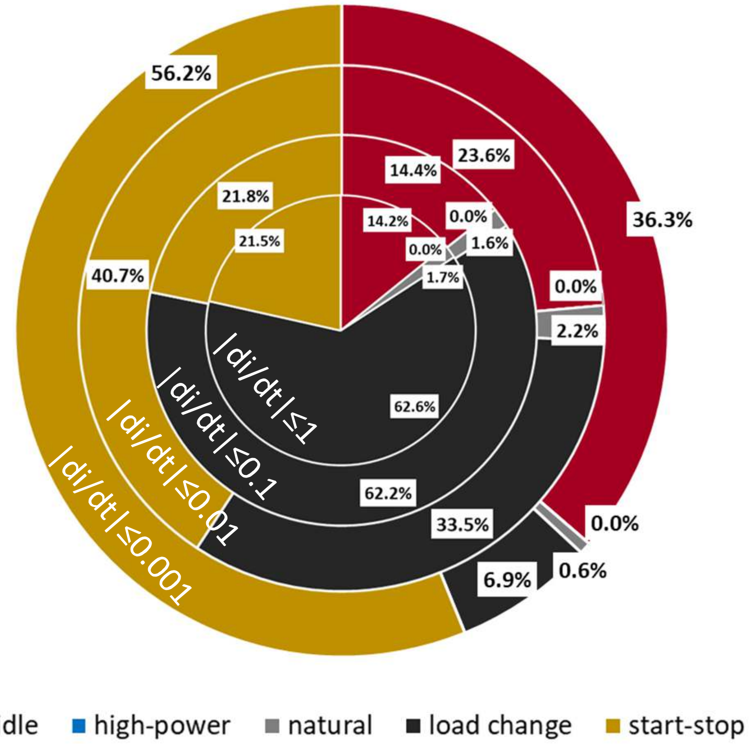

Figure 4.30. *Degradation source relative effect on FC stack durability decrease for the 60 kW design with different dynamic limitations.*

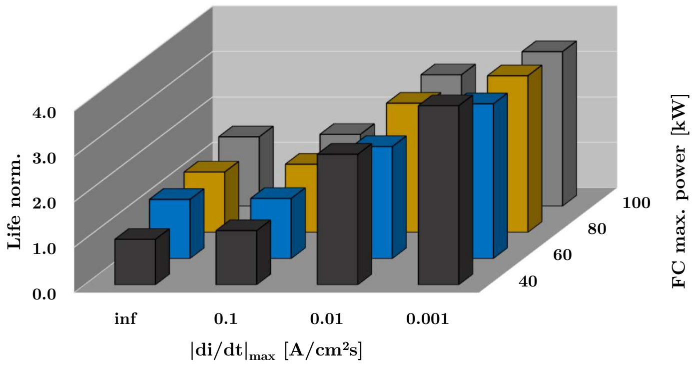

Figure 4.31. *Normalized FC stack durability (life) evolution as a function of the FC stack maximum power and the dynamic limitations.*

FCREx vehicles with dynamic restrictions since they could focus their development and innovation efforts in mitigating star-stop or low-power degradation through start-stop sequence management or improvement of the material properties rather than on improving the internal geometry of the FC stack flow channels to improve water management to reduce load-change degradation. This change might offer better FC stack durability for FCREx stacks with reduced costs provided that the energy management strategy of the vehicle is designed appropriately.

In light of these findings, FCREx vehicle manufacturers should take into consideration the diverse effects of raising the FC stack power and applying dynamic constraints throughout the vehicle design process. Increasing the FC stack power means higher production costs (↑ CAPEX) [8], lower H_2 consumption (↓ OPEX), and greater FC stack durability. In contrast, raising the dynamic restrictions implies equivalent manufacturing costs (= CAPEX), higher H_2 consumption (↑ OPEX), and higher durability. Vehicle manufacturers should therefore establish a trade-off to reduce costs with appropriate FC stack durability when assessing the vehicle design and should take into consideration the dynamic restrictions on the control strategy, if any, in the sizing process of the FC stack.

As a closing comment, it has been investigated how H_2 consumption is heavily penalized while raising the dynamic restrictions, independent of the FC stack power. In this line, durability has also risen by imposing dynamic restrictions, although good durability is already obtained for the 0.01 A/cm^2s limitation. As previously noted, raising the dynamic constraint to 0.001 A/cm^2s may affect negatively the durability of the FC stack, prohibiting the control strategy from maintaining the charge sustained mode under aggressive and high-power driving profiles. Therefore, the manufacturers of FCREx vehicles should design the FCV control strategy in such a way that the FCS operation ensures durability close to the desired expected life for the vehicle since over-constraining the dynamics of the FCS would imply higher H_2 consumption and might compromise the accomplishment of the charge sustaining mode.

4.4 Multi-FCS architecture for heavy-duty vehicle applications

This second part of the analysis, aimed at optimizing the architecture of heavy-duty FCV, describes the effect over performance and FC durability of considering a powertrain composed by multiple FCS, instead of one. This architecture provides additional degrees of freedom in terms of controlling the sizing of the different FCS and integrating differential energy management strategies, i.e., the control strategy of each FCS could integrate different dynamic limitations. In this sense, section 4.4.1 is focused on analyzing the impacts on durability and H_2 consumption of imposing differential control strategies on a powertrain composed by two identical FCS whose FC stack maximum power is 120 kW. This study is then extended in section 4.4.2 to other architectures which the same total maximum power (240 kW) but composed of FCS with different maximum power output: 100+140 kW and 80+160 kW (as presented in table 3.2. These two studies will serve to identify whether including more than one FCS in a powertrain brings advantages in terms of consumption and durability by exploring the differential sizing and differential control degrees of freedom that it can provide. This information is intended to be valuable to understand whether the trend of the industry of designing modular FCS that can be combined to get a higher-power powerplant is optimum in terms of vehicle architecture as well as to provide design guidelines for future heavy-duty FCV.

4.4.1 Effect of dynamics-limited energy management strategy on performance and FC durability

This first section is focused on the analysis of the multi-FCS architecture applied to heavy-duty vehicle when different dynamic limitations are applied over each FCS. In this case, both FCS have the same power (120 kW) and were integrated into the vehicle body described in section 3.5.2. The dynamic limits were similar to those imposed on the analysis of section 4.3.2 and 4.3.3.1, i.e., ranging from 0.1 to 0.001 A/cm^{2}s. The performance and durability of each design were compared after simulating the vehicle in the HDDT driving cycle which, as can be seen in figures 4.32 and 4.33 require the multi-FCS powertrain to be operated at medium-to-high load.

The current density evolution along the driving cycle of each FCS with different dynamics are presented in figures 4.32 and 4.33. Figure 4.32 considers the FCS_1 to be operated with a maximum rate of change of the current density of 0.1 A/cm^{2}s (high dynamics) while the constraint of the FCS_2 is varied from 0.1 to 0.001 A/cm^{2}s. In contrast, the results in figure 4.33 are representative of the behavior of the same FCS powertrain but with moderate-to-high dynamic restrictions imposed in every FCS (0.01-0.001 A/cm^{2}s). In this sense, the control strategies yielding the behaviors of figure 4.32 could be representative of a design in which H_2 consumption is prioritized over durability since one of

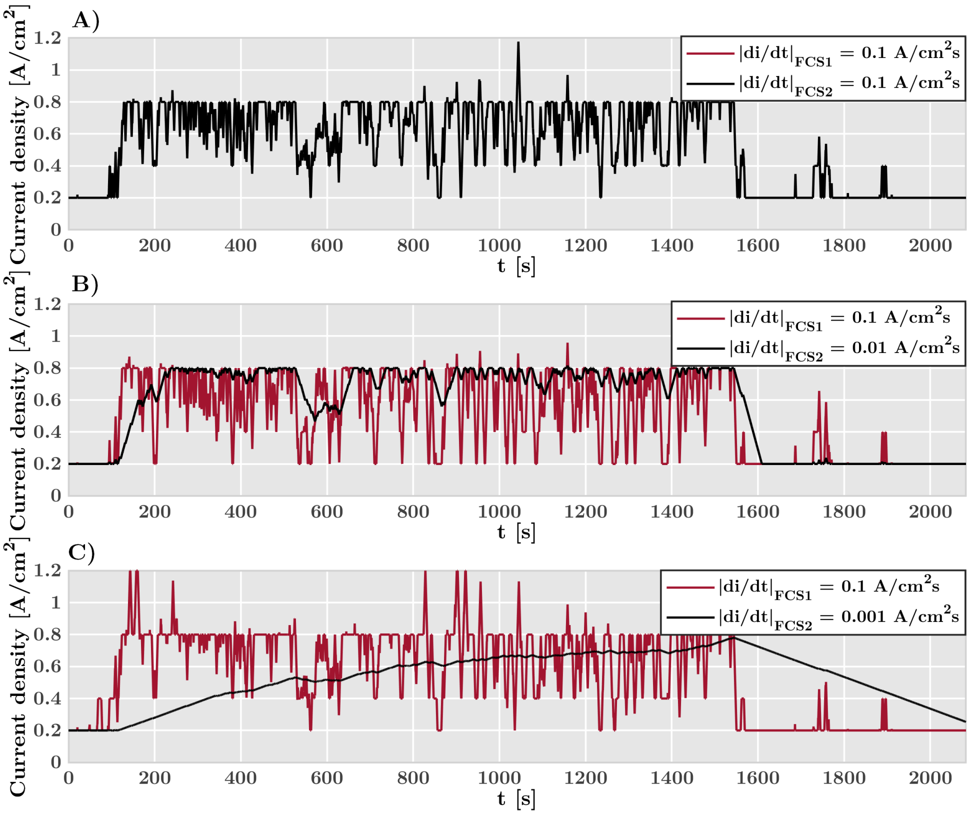

Figure 4.32. *Part 1: Evolution of the current density for the FCS_1 and FCS_2 (120 kW both) along the HDDT driving cycle with differential control dynamics ranging from 0.1 to 0.001 A/cm^{2}s.*

the FCS is clearly affected by load-change degradation while those resulting in the current density evolutions in figure 4.33 could represent a design aimed at maximizing the FC stack durability.

The evolution of the current density along the HDDT driving cycle shows the optimum behavior of each FCS to minimize the H_2 consumption, within the dynamic limitations imposed, as it is aimed with EMS optimizer integrated in the vehicle modeling platform 3.6. Therefore, the behavior of the current density in graphs 4.32.A, 4.33.A and 4.33.C is meaningful since it shows how, when both FCS are operated under the same dynamic constraints, the EMS optimizer finds that to minimize H_2 consumption, both FCS should operate following the same current density evolution, i.e., they are operated as if they were only one FCS capable of producing double the single-FCS maximum power output.

Graphs 4.32.B and 4.32.C are representative of an architecture that uses one FCS to absorb most of the dynamics (low durability) while the other is used to generate power following the traditional behaviour of a range-extender (high durability). When the dynamics are limited to 0.1 A/cm^{2}s for FCS$_2$ (figure 4.32.B), it is possible to observe how both the minimum and maximum values of current density in the load-change cycles of the FCS$_1$ decrease. This is due to the fact that when the e-motor power demand suddenly decreases the FCS$_2$ can not reduce its power production at the same rate, so the FCS$_1$ needs to absorb such a power demand shortage by decreasing as much as possible its current density (minimum current density in some load-change oscillations decrease). In this sense, when the e-motor power demand suddenly rises, the sub-optimal behavior of FCS$_2$ implies that it is already producing high power and that the battery has higher SOC, which has as a consequence that it can be used to absorb the power demand peak and thus the current density of FCS$_1$ does not need to increase abruptly (maximum current density decrease). Nonetheless, this behavior is not perceived in figure 4.32.C since the dynamics of FCS$_2$ are that low that when the power demand peaks of the e-motor happen the battery SOC is not high to absorb them and the FCS$_1$ is forced to increase the rate of change of the current density, hence implying a higher number of load-change oscillations with higher amplitude, which may be detrimental in terms of FC durability.

When FCS$_1$ is operated with the dynamic constraint of 0.01 A/cm^2 and FCS$_2$ under 0.001 A/cm^2, the evolution of the current density of the slower FCS changes compared when both FCS are operated under very low dynamics (figures 4.33.B and 4.33.C). From these results, it is possible to notice how the FCS$_2$ in 4.33.B operates under lower values of current density when is supported by another FCS whose dynamics are higher than when both FCS operate under very low dynamics (figure 4.33.C). This is produced since when the e-motor power demand suddenly increases, FCS$_1$ is already operating at at higher load which permits the FCS$_2$ not to increase its current density to produce the same total power. This behavior, which is aimed at optimizing the H$_2$ consumption is meaningful of how the EMS optimizer controls the FCS with ultra-low dynamics to maximize the performance of the powertrain. When the dynamics are low, if possible, the EMS makes the FCS to operate under lower current density, which implies higher FCS efficiency (figure 4.6), since they can not follow the e-motor power demand evolution. Therefore, it would not be strange if, when comparing the efficiency of both FCS along the driving cycle, it is higher at lower dynamics. Nonetheless, even though the

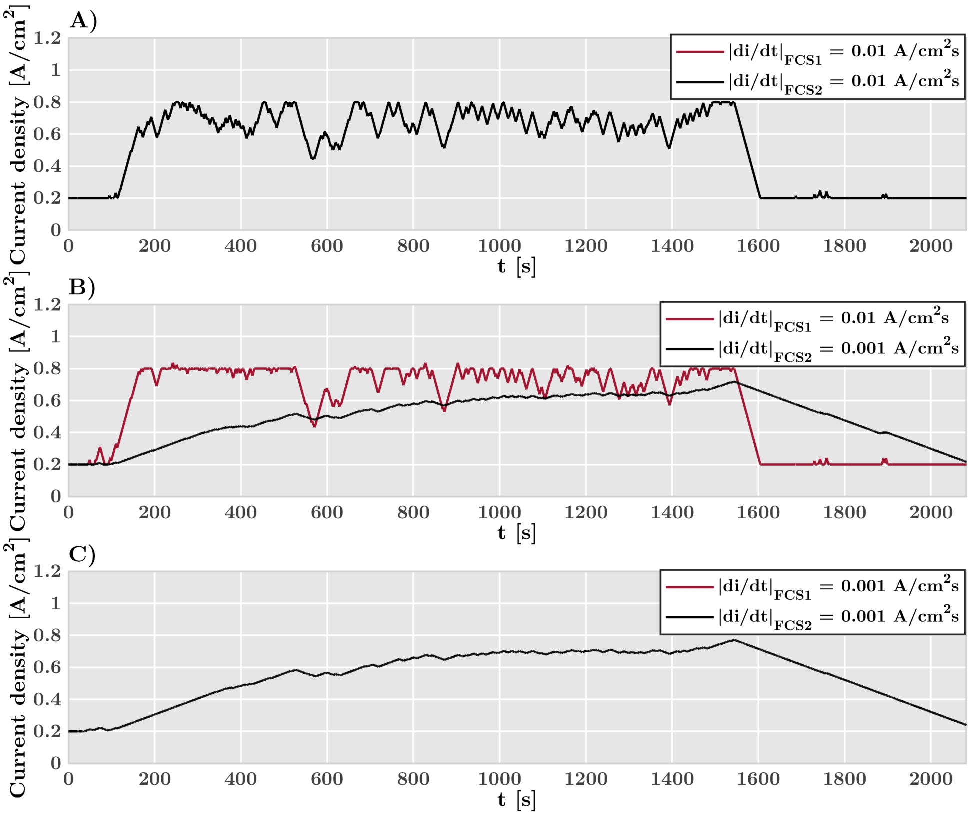

Figure 4.33. *Part 2: Evolution of the current density for the FCS_1 and FCS_2 (120 kW both) along the HDDT driving cycle with differential control dynamics ranging from 0.1 to 0.001 A/cm^2s.*

efficiency may be higher the H_2 consumption would still be higher as well since the sub-optimum behavior that low-dynamics imply makes the battery being discharged to cover up the power demand peaks of the e-motor, and thus the FCS need to provide more power later to fulfill the constant-SOC constraint.

The results in terms of consumption and durability of both FCS following the current density evolution in figures 4.32 and 4.33 are showed in figures 4.34 and 4.35, respectively. Note that the results of figure 4.35 are only given for one FCS, following the dynamic limitations in the right-hand bottom axis. The durability of the other FC stack was not presented in another figure because it would be redundant (both FCS present the same behaviour since both are identical).

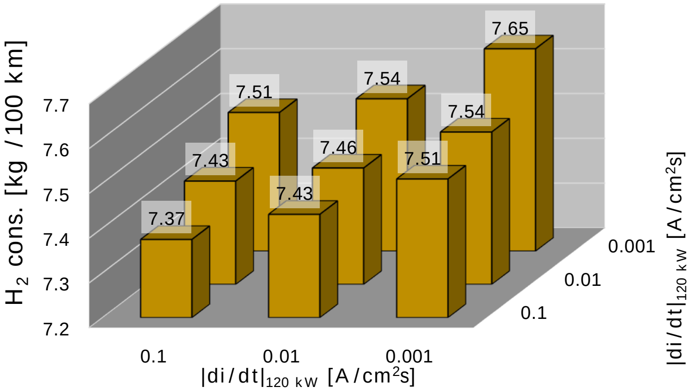

Figure 4.34. *H_2 consumption of the different dynamics limitations considered for the powertrain composed of two 120 kW FCS.*

The influence of applying dynamic restrictions on H_2 consumption can be clearly identified in figure 4.34. Comparing the case with both FCS being used with high dynamics to the case with the lowest dynamics, it is possible to notice that the H_2 consumption increases from 7.37 to 7.65 kg H_2/100 km, which implies an increase of 3.8%. Interestingly, this is lower than the increase in H_2 consumption noticed for FCREx architecture when changing the high-dynamic behaviour to a very low dynamic control in section 4.3.2 (7-8%). This may be due to the fact that the HDDT driving cycle requires a more steady high-power supply than the WLTC 3b cycle, so the dynamics are not that critical. Nevertheless, this change in the dynamics implies that both FCS only last for 98000 km while, if low dynamics are imposed, the durability increases to 558000 km, i.e., and increase of 471% according to the data in figure 4.35. The reader should note the difference in the increase of consumption and durability. The effect of this in the total life cycle emissions or in the total cost of ownership should be studied carefully, since, depending on the emissions or cost generated when producing H_2 or when manufacturing a FCS, the design minimizing the cradle-to-grave emissions or the total cost may either be that with the FCS operating in high or low dynamics. This discussion in terms of cradle-to-grave emissions is further discussed in section 5.3, but it should be further explored in terms of costs, which is left for future studies.

In the case of using one of the FCS with high dynamics and the other one with very low dynamics, the total H_2 consumption increases 7.51 kg H_2/100 km, i.e., by 1.8%, while the durability of the slow-dynamics FCS increases to 560000 km (+473%). The discrepancies in terms of durability

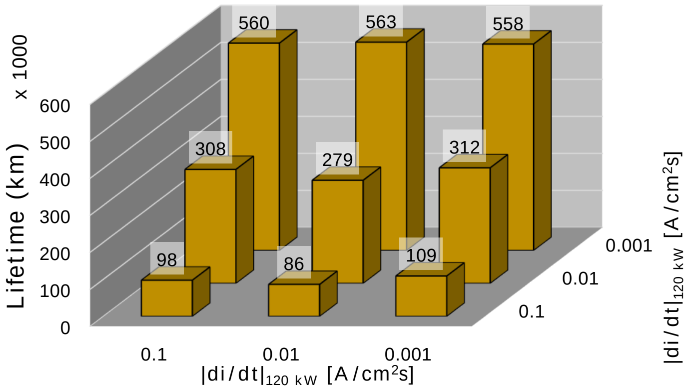

__Figure 4.35.__ Durability of the different dynamics limitations considered for the powertrain composed of two 120 kW FCS.

when a given FCS is operated with a fixed dynamics and the limitations over the dynamics of the other FCS are changed are due to the aforementioned effects over the current density evolution in figures 4.32 and 4.33. For instance, in the case of considering both FCS with high dynamics (0.1 A/cm^2), the current density evolution would be that of figure 4.32.A and their durability 98000 km. However, when the dynamics of one of the FCS is maintained to high and they are limited to a value of 0.01 A/cm^2 for the other FCS, the current density evolution of the former FCS changes as in figure 4.32.B, yielding in a higher number of load-change cycles and thus degradation to cover up for the lack of dynamics of the other FCS. This results in a drop of durability to 86000 km. If the dynamics of the second FCS are further constrained to a value of 0.001 A/cm^2, the suboptimum behaviour of this FCS provides additional energy to the battery when the e-motor power demand is under the supply of this FCS, thus fostering the usage of the battery to absorb the dynamics and therefore increasing the durability of the FCS operated under high dynamics to 109000 km. As can be see in this discussion, it is not simple to identify the effects over durability on a FCS whose dynamics do not change but the dynamics of the other FCS are modified. Nevertheless, in all the cases these variations are mostly kept withing 12%, droping to below 1% when the dynamics are low, which is negligible compared to the variation suffered when changing the dynamics of the analyzed FCS.

If instead of high or low dynamics, moderated dynamics are considered (0.01 A/cm^2). The durability of both FCS increase to 279000-312000 km (+185%) while the H_2 consumption rises to 7.46 kg H_2/100 km (+1.2%).

It is important to note that, depending on the dynamics of each FCS, differential control may make sense or may not be useful. For instance, if one FCS if operated with $|di/dt|_{max} \leqslant 0.1$ A/cm^{2}s and the other with $|di/dt|_{max} \leqslant 0.01$ A/cm^{2}s, the H_2 consumption becomes 7.43 kg H_2/100 km, while the durability of one of the FCS is 86000 km. Then, if the both FCS have moderate dynamics ($|di/dt|_{max} \leqslant 0.01$ A/cm^{2}s), the consumption only rises by 0.4% to 7.46 kg H_2/100 km while the durability of both FCS become 279000 km. In this case, there seems to be no advantage in terms of differential control since with moderate dynamics allow to almost triple the life of the FC stacks with a very small penalty in the H_2 consumption. However, there may be other cases in which differential control may be useful. If the dynamics of one FCS is limited to 0.01 A/cm^2 while the other is restricted to 0.001 A/cm^2, the H_2 consumption becomes 7.54 kg H_2/100 km, while the lowest durability of one of the FCS is 312000 km. If this design is compared againts the case in which both FCS have their dynamics limited to 0.001 A/cm^2 (7.65 kg H_2/100 km and a durability of 558000 km), it is possible to realize that it would imply an increase in H_2 consumption of 1.5% with an increase in the durability of 79%. In this case, the increase in durability is not that high with respect to the increase in H_2 consumption which may lead to use the differential control if the depending on the combination of emissions/cost in the H_2 production and the FCS manufacturing.

4.4.2 Cross-effect of dynamics-limited energy management strategy and FCS sizing on performance and FC durability

The results in the previous section allowed to understand the effect of considering the differential control strategies in a multi-FCS powertrain composed by two FCS with the same maximum power output. However, the combination of differential control with differential FCS sizing in a multi-FCS may bring synergies to minimize factors such as the life cycle emissions and the total cost of ownership of any heavy-duty FCV. This is partly due to the fact that differential control allow operate one FCS with high dynamics to absorb the e-motor power demand peaks while the other FCS can be used in a more steady operation. This in itself may not sound interesting to minimize the aforementioned factors, but when coupled with differential FCS sizing its potential increases. Differential sizing allows to select the power specification of both the high-dynamics and the low-dynamics FCS. Given that a FCS with higher maximum output power undoubtedly implies a higher environmental impact and cost, it is reasonable to try to maximize the life of the higher-power

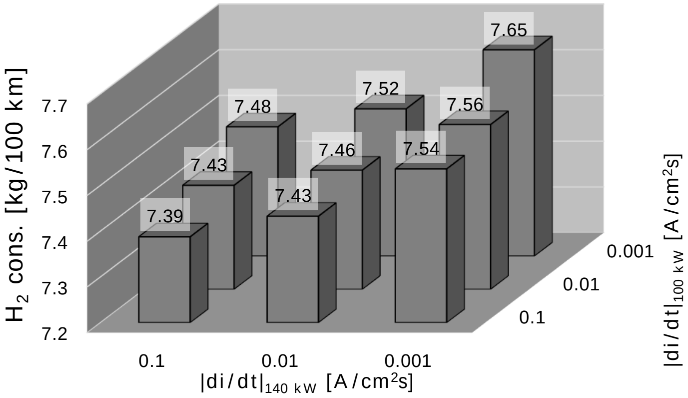

Figure 4.36. *H_2 consumption of the different dynamics limitations considered for the powertrain composed of a 100 kW and a 140 kW FCS.*

FCS. Furthermore, as seen in section 4.3.1, increasing the FCS maximum power implies higher efficiency in general and higher rate of change in the power output given a limited rate of change of current density, compared with a FCS with lower maximum power output. Therefore, if the multi-FCS powertrain is composed of two FCS with very different maximum power output, it may be interesting from the point of view of minimizing the life cycle emissions and cost to use the FCS with high power with slow dynamics and the lower-power FCS with high dynamics. With this design strategy the replacement cost of the FCS may be significantly decrease since the one to be replaced more often is that with lower power while the operation cost may not be as high as other designs with lower dynamics in both stacks. Following this line of thought, this section aims at analyzing the impact of combining differential sizing and differential control strategies in both performance and FCS stack durability through the results obtained by simulating the designs in table 3.2 with dynamic limitations ranging from 0.1 to 0.001 A/cm^{2}s.

Figures 4.36 and 4.37 show the consumption of each design (100+140 kW and 80+160V kW) when imposing different limitations on the dynamics of each FCS. As it was analyzed in figures 4.32 and 4.33, when the dynamics of both FCS are identical the system tends to behave as if it was controlling a FCS whose maximum power output is the sum of that of both FCS. This is not only perceived for the 120+120 kW powertrain, but for all the designs considered in this study since the H_2 consumption for all the designs when the dynamics of both FCS are the same offer similar H_2 consumption (see the results with both FCS operating under the same dynamic restrictions on

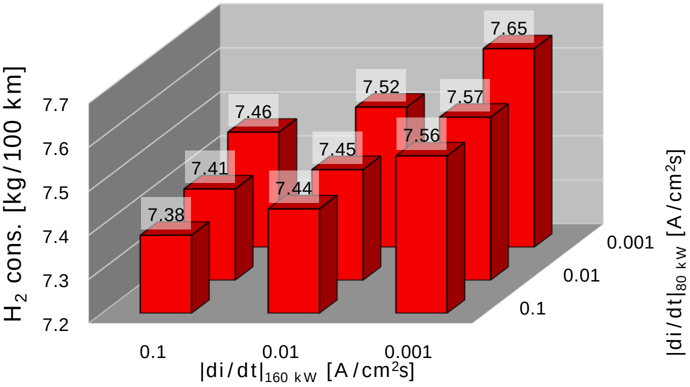

Figure 4.37. *H_2 consumption of the different dynamics limitations considered for the powertrain composed of a 80 kW and a 160 kW FCS.*

figures 4.34, 4.36 and 4.37). Hence, in all these cases the EMS finds optimum to minimize H_2 consumption to operate the powertrain as if it was only composed of a 240 kW FCS. The conclusion extracted from these results is important since they imply that differential sizing does not provide any benefit in terms of performance if both FCS operate with the same dynamics.

H_2 consumption is lower the higher the difference between the power of both FCS only when the dynamics of the smaller FCS are lower than the dynamics of the high-power FCS. This was to be expected since the lower the dynamics the higher the penalty in H_2 consumption. Therefore, it is only reasonable to expect that the limitations on the dynamics of the high-power FCS imply a higher penalty in H_2 consumption. When comparing these differential control strategies, it is possible to identify how in the case on which the dynamics of both FCS are the most different, the change in H_2 consumption is still small. In the case of operating the high-power FCS with $|\mathrm{di/dt}|_{\max} \leqslant 0.1$ A/cm^{2}s and the low-power FCS with $|\mathrm{di/dt}|_{\max} \leqslant 0.001$ A/cm^{2}s the maximum change in H_2 consumption due to differential sizing is of 0.7% (7.51 vs 7.46 kg H_2/100 km).

In contrast, when the dynamics of the high-power FCS are lower than that of the low-power FCS, the designs with differential sizing present higher H_2 consumption. As explained before, this is because the FCS with higher power has more influence over the overall performance of the powertrain. Therefore, the higher the constraints in the dynamics of this FCS, the higher the penalty in H_2 consumption. Nevertheless, the variation is still small and contained below 0.7% as well (7.51 vs 7.56 kg H_2/100 km). Apart from comparing

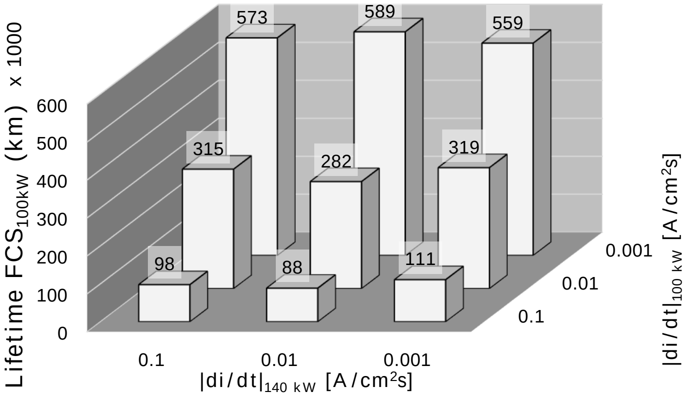

Figure 4.38. *Durability of the 100 kW FC stack with different dynamics limitations considered for the powertrain composed of a 100 kW and a 140 kW FCS.*

designs, it is important to also understand the variation in performance when changing the dynamics in the same design. In the case of the 80+160 kW if one of the FCS is operated with low dynamics and the other with high dynamics, the consumption may change from 7.46 to 7.56 kg H_2/100 km (1.6%), which means that the control strategy of both FCS has a higher degree of flexibility when optimizing durability or performance. This is critical not only if each FCS has different maximum power (and thus imply different cost and emissions in their manufacturing) but may become even more relevant if the technology of each FC stack is not the same with very different manufacturing cost or emissions (for instance a SOFC combined with a PEMFC).

After analyzing the effect of combining differential sizing and differential control on performance, the durability of each FCS is presented in figures 4.38, 4.39, 4.40 and 4.41. The trends identified in these figures coincide with those in figure 4.35 and the durability of each FC stack is in the same range when the dynamic limitation is the same, provided that there are small variations that arise mainly from the different evolution of the FC stack temperature after being calibrated as in figure 3.15. This is mainly due to using the rate of change of the current density as a parameter representative of the dynamics, which is directly related to load-change degradation (section 3.7).

Just with these results it is possible to make prospections about how the emissions or costs in the manufacturing of the powertrain (with the corresponding FCS replacements) or in the operation of the vehicle would change. This can be analyzed by considering a vehicle lifetime of 1000000 km. For instance, in the case of the design with two 120 kW in which one of the FCS

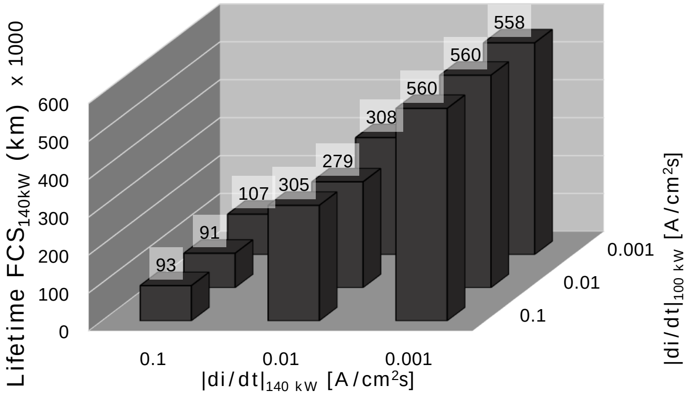

Figure 4.39. *Durability of the 140 kW FC stack with different dynamics limitations considered for the powertrain composed of a 100 kW and a 140 kW FCS.*

system is operated at $|di/dt|_{max} \leqslant 0.1$ A/cm^{2}s (high dynamics) and the other at $|di/dt|_{max} \leqslant 0.001$ A/cm^{2}s (low dynamics), the H_2 consumption is 7.51 kg H_2/100 km and the durability results imply that during the life of the vehicle the high-dynamics FC stack should be replaced 10 times while the FC stack operated under low-dynamics only 1, i.e., it would be necessary 13 FCS during the life of the heavy-duty vehicle. If the cost of one 120 kW FCS is X, then the cost would be:

$$11 \cdot X + 2 \cdot X = 13 \cdot X$$

Comparing this case with the design of 80+160 kW in which the 80 kW FCS is operated with high-dynamics and the 160 kW FCS is operated under low-dynamic conditions, it is impossible to understand the change in both operation and manufacturing cost. In this case, the H_2 consumption rises to 7.56 kg H_2/100 km which implies an increase in the operation costs of 0.7%. In terms of durability, the 80 kW requires 10 replacements while the 160 kW only 1, i.e., a total of 13 FCS again. In this case, if the manufacturing cost is considered to be scaled with the FCS power, the manufacturing cost of the 80 kW FCS would be 80/120·X and that of the 160 kW one 160/120·X. This implies a total cost of:

$$11 \cdot 80/120 \cdot X + 2 \cdot 160/120 \cdot X = 7.333 \cdot X + 2.667 \cdot X = 10 \cdot X$$

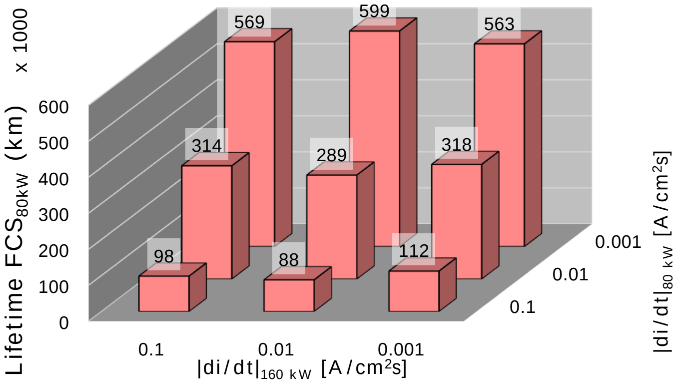

Figure 4.40. *Durability of the 80 kW FC stack with different dynamics limitations considered for the powertrain composed of two a 80 kW and a 160 kW FCS.*

This simple calculation, albeit not accurate since the manufacturing costs would probably not scale linearly with the FCS power, provides an insight about the benefits of the combination of differential control and differential sizing. The manufacturing costs were reduced by 23% while the operation costs increased by 0.7%. Still, only with these data it is not possible to determine whether the combination of such design strategies may bring benefits in terms of total life cycle emissions or costs since it will mainly depend on the emissions associated to the H_2 production and the FCS manufacturing. This will be assessed in detail following the LCA framework described in section 3.8 in the analysis of section 5.3.

4.5 Summary and conclusions

In the first part of chapter, the results for the optimization of the FCS for both the passenger car and the heavy-duty applications were presented and discussed. This part entails a critical step in the multi-scale optimization process followed in this work. The results here were integrated in the air management strategy of the BoP to run the driving cycle simulations in sections 4.3 and 4.4 to optimize the FCV architecture. If the BoP management was not optimum and representative of the maximum efficiency achievable by a FCS for automotive application, the results and tendencies identified in the sizing and control strategy analyses would undoubtedly be biased. The main conclusions extracted from the first part of this chapter can be summarized as:

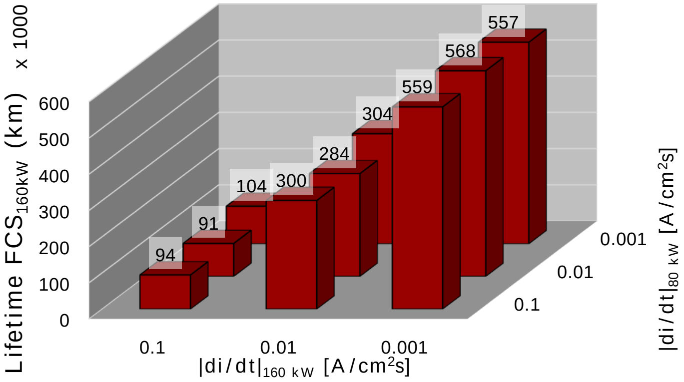

Figure 4.41. *Durability of the 160 kW FC stack with different dynamics limitations considered for the powertrain composed of two a 80 kW and a 160 kW FCS.*

optmum energy balance for the passenger car FCS was presented in figure 4.4 while that for the heavy-duty application in figure 4.6. These energy balances, showing the power consumption/generation by each component in the FCS, were obtained by optimizing the air management strategy as in figures 4.2 and 4.5.These results served to identify different regions of operation as a function of the current density, being the highest efficiency of the FCS in the medium-load region ([0.04, 0.4] A/cm^2). Therefore, the operation of the FCS during driving conditions could be aimed by the EMS mainly at this region, particularly for designs on which the FC stack dynamics are limited. The use of the optimum energy balance for the passenger application in driving conditions (carried out in sections 4.3 and 4.4) served to identify limits in the minimum compressor mass flow rate for the heavy-duty FCS that were integrated in the optimization procedure. This implied slightly lower efficiency in the low-load region but higher stability in the compressor operation. The overall efficiency of the heavy-duty FCS was lower than that of the passenger car FCS due to the higher mass flow rates and the subsequent higher pressure losses. Still, both FCS show maximum net efficiencies over 60% in the same current density interval (0.12-0.2 A/cm^2), which is in line with FCS efficiency achieved by state-of-the-art FC technolgy.

This second part of this chapter was aimed at optimizing the vehicle architecture for the passenger car application by considering the FCREx configuration (section 4.3) and for the heavy-duty vehicle application by exploring the potential of the multi-FCS powertrain (section 4.4). For both applications, the impact of the sizing of the FCS and the limitations on the control dynamics on performance and durability were evaluated. However, the approach for the heavy-duty vehicle was slightly different since the sum of the maximum power of the two FCS integrated in the vehicle was maintained constant. From this part, the following conclusions may be highlighted for the FCREx architecture optimization:

- Raising both the FC maximum power and the battery capacity lowers H_2 and energy consumption because the efficiency of both systems rise. Between these two sizing factors, consumption is more sensitive to the FC maximum power since most of the stored energy in the FCREx vehicle is in the form of H_2.

- FCREx designs were compared against state-of-the-art commercial FCVs with equivalent range (FCV1 and FCV2) . From this analysis, it was established that FCREx architecture might give a more efficient energy utilization, consequently lower H_2 consumption, implying a possible drop in the TCO. The design with 4.97 kg of H_2, a FC stack of 82 kW, and 44.5 kWh stored in the battery was equal in range to the FCV1 and provided 16.8% lower H_2 consumption and similar total energy consumption. Compared to the FCV2, the entire energy use of the equivalent-in-range FCREx (30 kWh of energy in the battery and 3.76 kg of H_2) was roughly 6.8% lower. Therefore, FCREx architecture might considerably minimize H_2 and energy consumption compared to standard FCV.

- The recommended FCREx design is with moderate-to-high FC maximum power ($\geqslant$60 kW) to maximize performance (operation costs) since the H_2 and energy consumption was more sensitive to FC maximum power than to battery capacity and with minimum but high-enough battery capacity (around 30 kWh) to reduce production costs. Still, an ideal design was not chosen from the design spaces as it may rely on other parameters such as H_2 or energy price (important to compute the TCO) and cradle-to-grave emissions.

- Excessive limitations in the dynamics and/or minimum current density ($|di/dt|_{max}$=0.001 A/cm^{2}s or i_{min}=0.2 A/cm^2) were regarded unpractical since, even though after applying them the durability increased significantly, they also implied 6.6-6.7% additional H_2 consumption and could hinder the fulfillment of the charge-sustaining operation in high-dynamics or high-load driving cycles.

- The optimum combination of restrictions that maximizes FC stack durability without affecting the vehicle operational capability was identified to be $|di/dt|_{max}$=0.01 A/cm^{2}s and i_{min}=0.15 A/cm^2 because it offers the highest decrease in degradation rate (53%), thus the highest increase in durability (110%) with an increase in H_2 consumption of 4.7%. This was found for the specific combination of FC stack power and battery size in the FCREx architecture, but may change depending on the vehicle design and driving conditions. As such, it was recommended for the manufacturers of FCREx vehicles to carry out the operational limits and dynamic restrictions optimization for their particular design.
- Given the large rise in H_2 consumption when applying constraints in the control strategy, the authors advocate evaluating the restrictions in the control strategy that assures a targeted life, defined by the vehicle manufacturer or the legislation, without over-constricting it. As a reference, FCREx vehicle manufacturers should initially consider an EMS limiting the dynamics and the operational space to $|di/dt|_{max}$=0.01 A/cm^{2}s and i_{min}=0.15 A/cm^2 and then further optimize the H_2 and durability, according to the specific targets for the vehicle application by refining the these limits.
- It was noticed a change in degradation rate source relevance when high dynamic limits were imposed. In this situation, load-change degradation became a minor degradation factor, becoming start-stop and low-power degradation more significant. This might influence the project process of FC stack manufacturers for FCREx vehicles because they may be willing to prioritizing the design of low-degradation start-stop sequence or to considering materials with low degradation under high-voltage conditions instead of focusing on designing the FC stack internal channels to reduce water management issues in highly dynamic operation.
- All the designs with low dynamics ($|di/dt|_{max}$=0.001 A/cm^{2}s) offered similar H_2 consumption, which implied that the FC stack sizing is not that important if the dynamic limitations on the FCS are significant.

As for the optimization of the heavy-duty multi-FCS architecture:

- It was identified that H_2 consumption and durability increased by +3.8% and +471%, respectively, when increasing the dynamic limitation of both 120 kW FCS from $|di/dt|_{max}$=0.1 A/cm^{2}s to 0.001 A/cm^{2}s. This implies that significant increase in durability can be achieved with relatively low penalties in H_2 consumption. These changes in durability and performance were deemed different from those identified for the FCREx architecture applied to passenger cars since the driving profile of heavy-duty vehicles is more steady.

- When the dynamic limitations were equal for both FCS, H_2 consumption, no matter the relative sizing of each FCS, was almost identical. This implies that differential sizing might only provide benefits in terms of costs and life cycle emission if coupled with differential control strategies.

- In the designs with differential sizing, lower H_2 consumption was achieved when the high-power FCS operated under high dynamics since it is used to provide most of the power of the powertrain and restricting it has a higher impact on performance.

- A simple example was raised to understand the potential of coupling differential sizing with differential control. This example, in which two designs (120+120 kW and 80+160 kW) whose FCS were operated with very different dynamics (the lower power one with $|di/dt|_{max}$=0.1 A/cm^{2}s and the higher power FCS with $|di/dt|_{max}$=0.001 A/cm^{2}s), illustrated how the 80+160 kW could offer 23% lower manufacturing costs/emissions with only an increase of 0.7% in the operation costs/emissions. This implied that depending on the cost or emissions associated to the manufacturing of the FCS or to the production of H_2, the multi-FCS architecture with differential control and sizing might minimize the life cycle cost/emissions.

References

[1] Emmanuel Balogun O., Barendse Paul and Chamier Jessica. "Effect of Anode Stoichiometry and Back Pressure on the Performance of PEMFCs". In *2018 IEEE PES/IAS PowerAfrica*, pp. 1–6, 2018.

[2] Zhang Jianlu, Tang Yanghua, Song Chaojie, Xia Zetao, Li Hui, Wang Haijiang and Zhang Jiujun. "PEM fuel cell relative humidity (RH) and its effect on performance at high temperatures". *Electrochimica Acta*, Vol. 53, pp. 5315–5321, 6 2008.

[3] FuelCellsWorks. "World's first fuel cell heavy-duty truck, Hyundai XCIENT Fuel Cell, heads to Europe for commercial use", 2020.

[4] ROTREX. "Rotrex EK10AA Fuel Cell Compressor Technical Datasheet".

[5] Sim Kyuhyun, Vijayagopal Ram, Kim Namdoo and Rousseau Aymeric. "Optimization of component sizing for a fuel cell-powered truck to minimize ownership cost". *Energies*, Vol. 12 n^o 6, 2019.

[6] Lü Xueqin, Wang Peisong, Meng Lingzheng and Chen Chao. "Energy optimization of logistics transport vehicle driven by fuel cell hybrid power system". *Energy Conversion and Management*, Vol. 199 n^o June, pp. 111887, 2019.

[7] Xu Liangfei, Mueller Clemens David, Li Jianqiu, Ouyang Minggao and Hu Zunyan. "Multi-objective component sizing based on optimal energy management strategy of fuel cell electric vehicles". *Applied Energy*, Vol. 157, pp. 664–674, 2015.

[8] Molina S., Novella R., Pla B. and Lopez-Juarez M. "Optimization and sizing of a fuel cell range extender vehicle for passenger car applications in driving cycle conditions". *Applied Energy*, Vol. 285 n^o December 2020, pp. 116469, 2021.

[9] Desantes J.M., Novella R., Pla B. and Lopez-Juarez M. "Impact of fuel cell range extender powertrain design on greenhouse gases and NOX emissions in automotive applications". *Applied Energy*, Vol. 302, pp. 117526, 2021.

[10] Desantes J.M., Novella R., Pla B. and Lopez-Juarez M. "Effect of dynamic and operational restrictions in the energy management strategy on fuel cell range extender electric vehicle performance and durability in driving conditions". *Energy Conversion and Management*, Vol. 266, pp. 115821, 2022.

[11] Desantes J.M., Novella R., Pla B. and Lopez-Juarez M. "A modeling framework for predicting the effect of the operating conditions and component sizing on fuel cell degradation and performance for automotive applications". *Applied Energy*, Vol. 317, pp. 119137, 2022.

[12] Hyundai. "Hyundai Nexo - Technical Specifications".

[13] Argonne National Laboratory. "Technology Assessment of a Fuel Cell Vehicle: 2017 Toyota Mirai Energy Systems Division". *US DOE -Energy Systems Division*, 2017.

[14] Database EV. "Kia e-Niro 64 kW (2020-2022) price and specifications", 2022.

[15] Europe Hyundai Motor. "Hyundai KONA Electric Features", 2022.

[16] DoE - Department of Energy. "DOE Technical Targets for Polymer Electrolyte Membrane Fuel Cell Components".

Chapter 5

Life cycle emissions optimization

Contents

5.1 Introduction

This chapter focuses on evaluating the environmental impact of the novel architectures proposed for the passenger car and heavy-duty vehicle applications. The LCA framework followed to obtain the results presented in this chapter is that defined in section 3.8 while the H_2 consumption results for each architecture were those obtained in chapter 4.

The analysis aimed at the FCREx architecture for the passenger car application (section 5.2), is focused on understanding the change in the GHG-100 and NO_X emissions in the vehicle manufacturing cycle, the fuel production cycle and the cradle-to-grave process when changing the FC stack maximum power, the H_2 tank capacity and the battery capacity in driving cycle conditions. The consumption data were those obtained in section 4.3.1 without any restriction in the dynamics. This study was not aimed at understanding the effect of including FC stack degradation in the LCA calculation since considering infinite-durability stacks is representative of the ideal long-term scenario for this technology. This makes the results of this study representative of the potential of this technology to decrease cradle-to-grave emissions only through the FCREx powertrain design. Furthermore, since one of the main concerns of the industry and the scientific community is to improve FC durability, it is expected that for the relatively short lifetimes of passenger cars, the FC stack can last the whole life by the time the technology fully penetrates the light-duty transport sector. Green H_2 is included in a separated subsection since it is a production pathway that is not representative of the short-term for the light-duty passenger car application.

The second part of this chapter is aimed at the analysis of the environmental impact of the heavy-duty vehicle application integrating a multi-FCS architecture. The main objective behind this analysis is to identify whether the multi-FCS architecture should follow the industry trend or if there is any room of improvement to minimize the cradle-to-grave emissions by considering the design strategies of differential control and sizing. In this case, given the long lifetime of the heavy-duty vehicles, the similarity of these vehicle fleets with captive fleets (fixed collection/discharge locations, usually in industrial parks our of cities), and the predicted short-term penetration of FC technology in the heavy-duty sector, both FC durability and green H_2 were integrated in the study. The data about the FC durability and performance were obtained from the results of section 4.4, and were used to calculate the total H_2 and electricity consumption (considering that 10% of the lifetime is covered with the batteries in urban driving conditions). Green H_2 was included since the fixed routes of long-haul heavy-duty trucks and the collecting/drop-off locations, usually out of the cities, enable the short-term development of infrastructure to produce renewable energy and generate H_2 to refuel the tanks of these vehicles. Furthermore, FC technology is projected to penetrate the heavy-duty sector in the short-term, which encourages the inclusion of all the H_2 production pathways in the study.

5.2 Cradle-to-grave emissions of FCREx vehicles

This section is divided in 5 different parts. In the first part (section 5.2.1), the H_2 and energy consumption for each design are presented together with the emissions related to the vehicle manufacturing cycle. Then, these data are combined with the fuel production cycle data to understand the impact of the FCREx design in the cradle-to-grave emissions in terms of GHG-100 emissions (section 5.2.2) and NO_X (section 5.2.3). Since green H_2 (from renewable sources) is not feasible in the short-term for the passenger car application (high demand and not enough renewable energy production infrastructure) and may lead to a bias against BEV since the electricity in the batteries comes from the EU electricity mix, a separate section is used to compare the cradle-to-grave emissions when comparing blue with green H_2 (section 5.2.4). Finally, a discussion about the potential of FCREx to decrease cradle-to-grave emissions is carried out in section 5.2.5, thus elaborating a set of recommendations for FCREx vehicle manufacturers.

5.2.1 Impact of FCREx design on consumption and the manufacturing cycle

In this section, the design spaces in terms of H_2 consumed, total energy consumed along the life and H_2 storage capacity are presented in figure 5.1 as a function of the battery capacity and the FC maximum power output for the FCREx designs with ranges of 600, 500 and 700 km. The design spaces are equivalent to those presented in section 4.3.1 but representative of the vehicle lifetime consumption. They are briefly discussed here again to provide a preliminary explanation on how the design and consumption change to justify the tendencies in the emissions produced in each phase of the life cycle. Then, GHG-100 and NO_X emissions in the vehicle manufacturing cycle for the multiple design spaces are presented in figure 5.2 and analyzed.

Different powertrain component design has a significant influence on both the performance of the vehicle in terms of range and consumption and on the emissions generated in the cradle-to-grave process. Among the effects the powertrain sizing has on emissions, it is feasible to distinguish different effects. First, there is a direct influence on the emissions produced during the vehicle manufacturing. Second, an indirect consequence given the fact that a different powertrain design may change substantially the H_2 or electricity consumption of the vehicle, therefore needing a lower or a larger quantity of energy over the complete vehicle lifetime. As such, the second effect solely increases the emissions originating from the fuel production cycle since utilizing H_2

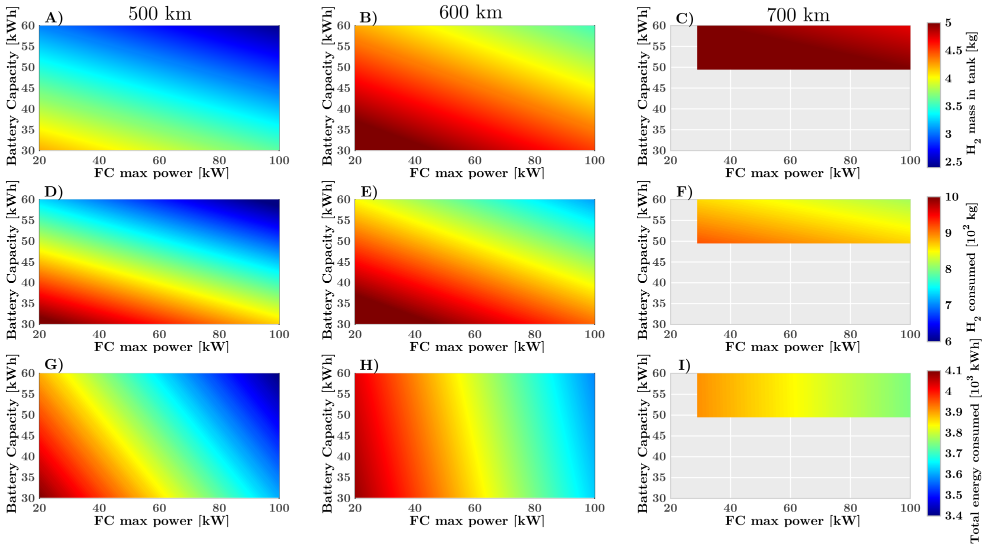

Figure 5.1. *Design spaces for 500, 600, and 700 km of range FCREx. Contours show: H_2 mass in tank to achieve the target range (1^{st} row), H_2 consumed along the whole life (2^{nd} row), and NO_X total energy consumed along the whole life, including H_2 and electricity in the operation cycle (3^{rd} row).*

or electricity from batteries to power a vehicle does not generate any tailpipe GHG-100 or NO_X emissions (operation cycle). However, in the case of FCREx, there is a third consequence arising from the versatility and complexity of the powertrain as it consists of two power sources: a battery and a FCS. The third effect is also indirect and impacts significantly the fuel production cycle because there are two types of energy carriers (H_2 and electricity) and the overall percentage of H_2 or electricity utilization along the whole lifetime depends on the ratio between the energy in the vehicle stored in the tank and in the battery. Therefore, the fuel production cycle might also be influenced by the relative quantity of energy carrier produced as H_2 or as electricity since the emissions released in the H_2 production pathway could be much bigger than those emitted to produce electricity and vice versa.

Figure 5.1 illustrates in the first row (graphs A-C) how the H_2 tank capacity was adjusted depending on the battery capacity and the FC stack maximum power output to meet the desired range (estimated using the WLTC 3b driving cycle). In the second row (graphs D-F) the quantity of H_2 consumed throughout the 120000 km of life is presented while the third row (graphs G-I) displays the total energy consumed during the complete lifetime, including both H_2 and the electricity.

FCREx performance and H_2 sizing change considerably depending on the range (figure 5.1). As the H_2 tank capacity is increased with the target range, given a fixed FC maximum power and battery capacity, the total vehicle weight increases while the efficiency of the systems remains constant, hence both H_2 and total energy consumption increase with the target range (figure 5.1, D-I). As such, it is important to mention that depending on the application and the desired range for which the vehicle is designed, the H_2 and energy consumption may be altered. This is essential and must be taken into consideration by FCV designers and manufacturers as, unlike traditional vehicles, altering the capacity of the fuel storage system of an FCREx vehicle may have a significant influence on consumption.

As the battery capacity is increased in the FCREx architecture for a fixed target range, the H_2 tank capacity decreases because the fraction of the range that can be assumed by the battery alone increases, thus allowing the decrease in the H_2 mass stored (figure 5.1, A-C). As a result, the required quantity of H_2 to travel 120000 km lowers as well when increasing the battery capacity (figure 5.1, D-F). Furthermore, the larger the percentage of energy generated by the battery the higher the total system efficiency, given the higher efficiency of the battery relative to that of the FCS. Hence, the overall vehicle efficiency improves despite the increasing vehicle weight, thereby lowering the total energy needed to travel 120000 km (figure 5.1, G-I). It is imperative to note here that the reduction in the H_2 consumed is not attributable to an improvement in the FCS efficiency. In reality, the increased vehicle weight means higher brake power demand during the driving cycle, indicating that the FCS would work at higher current densities, thereby diminishing the efficiency. Rather, the drop in H_2 comes from the lowest demand of H_2 to cover a specific range, because the distance that can be covered just with the battery grows.

The major benefit of raising the FC stack maximum power is to improve the FCS efficiency since, for the same power demand, a higher-power FC stack runs with lower current density, thereby minimizing the electrochemical losses related to the FC stack operation and the BoP energy consumption. This indicates that H_2 consumption decreases by increasing FC maximum power despite the rise in vehicle weight, hence reducing the required H_2 tank capacity (figure 5.1, A-C), the H_2 and total energy consumed during the lifetime (figure 5.1, D-I). Differently from what was indicated previously, the trend of reducing H_2 consumption, in this situation, is caused by a rise in the FCS efficiency during the driving cycle. When raising the FC stack maximum power, the

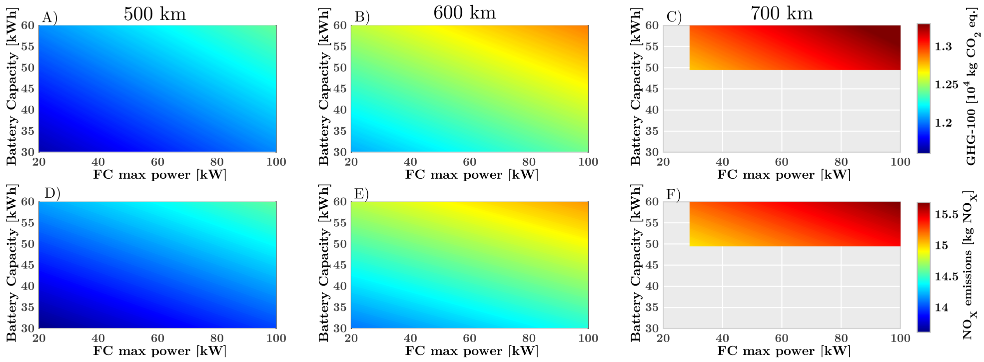

Figure 5.2. *Design spaces for 500, 600, and 700 km of range FCREx: GHG-100 emissions in the manufacturing cycle (1st row), and NO_X in the manufacturing cycle (2nd row). Functional unit is 1 vehicle. Life is set to 120000 km.*

range that can be achieved using the battery alone is slightly lower, given the rise in the vehicle weight. Nevertheless, this appears to be balanced by the improvement in the FCS efficiency.

It is essential to notice that, although the iso-H_2-consumed lines are parallel across graphs with different vehicle range (figure 5.1, D-F), in the case of the total energy consumption they do not have the same slope between graphs (G-I). This occurs because as the objective range increases, the quantity of necessary H_2 grows, thereby increasing the proportion of energy stored as H_2. If the proportion of the total energy as H_2 grows, the vehicle total efficiency and overall consumption would become more sensitive to improvements in the FCS efficiency. This answers why the iso-lines in graphs G-I in figure 5.1 get more vertical as the objective range rises, indicating increased sensitivity to the FC maximum power output relative to the battery capacity. Therefore, for high-range FCREx, it would be more favorable in terms of total energy consumption to pursue high-power FC stack designs.

As explained in section 4.3.1, the ideal design of FCREx passenger car in terms of consumption and performance was determined to have large battery capacity and high FC stack maximum power. This conclusion shows that, solely in terms of performance, the FCREx architecture could have higher performance than the traditional FCV configurations. Nonetheless, it is still necessary to identify whether the cradle-to-grave emissions are minimum with the optimum-performance design or if there are other factors such as the vehicle manufacturing that are more relevant in terms of life cycle emissions. It is expected that the optimum design in terms of cradle-to-grave emissions is dependent on the H_2 production pathway and the vehicle manufacturing process.

As noted earlier, the first effect of FCREx design on life cycle emissions is obtained from the rise in emissions originating in the vehicle manufacturing cycle. This is depicted in figure 5.2 in terms of GHG-100 (A-C) and NO_X emissions (D-F). If comparing designs with the same battery capacity and FC stack maximum power output but different target range, those with greater range entail higher GHG-100 and NO_X emissions as the H_2 tank capacity rises, therefore producing more emissions throughout its manufacturing process. Nevertheless, the relative rise of GHG-100 emissions with target range is more substantial compared to NO_X since the GHG-100 emissions in the H_2 tank manufacturing process scale more with its storage capacity than NO_X. Both increasing the FC maximum power and the battery capacity imply higher emissions because the increase in emissions produced when manufacturing higher-power FC stacks and higher-capacity batteries outweighs the reduction in emissions due to the decrease in the required H_2 tank capacity shown in figure 5.1, graphs A-C. Bare in mind how the emissions shown in figure 5.2 are remarkably high compared to those produced in the manufacturing process of any fossil-fueled conventional ICE vehicle since the emissions originated from the battery, the FCS, and the H_2 tanks are large in comparison to the emissions required to produce an ICEV. This disparity is likely to reduce with time as the H_2-based technology develops more and the industry manufacturing them is more mature, therefore decreasing the prices and emissions thanks to economies of scale. Nevertheless, the manufacturing cycle is only one component of the cradle-to-grave process, therefore the fuel production cycle should also be considered for (the emissions during the operating cycle are practically negligible and are only GHG-100).

5.2.2 Cradle-to-grave and fuel production GHG-100 emissions

In this section, the design spaces were represented as a function of GHG-100 emissions for the fuel production cycle and the cradle-to-grave process. First, the design spaces for the FCREx cars with a goal range of 600 km were displayed considering various H_2 production pathways (figure 5.3): electrolysis with the existing EU electricity mix (black), and SMR with (blue) and without CCS (grey). With these information, it is discussed how the emissions change for a constant design space while altering the H_2 production pathway. Afterward, the GHG-100 emissions associated to the design spaces for FCREx with target range of 500, 600 and 700 km in the fuel production and the cradle-to-grave processes were shown in figure 5.4 by considering blue H_2

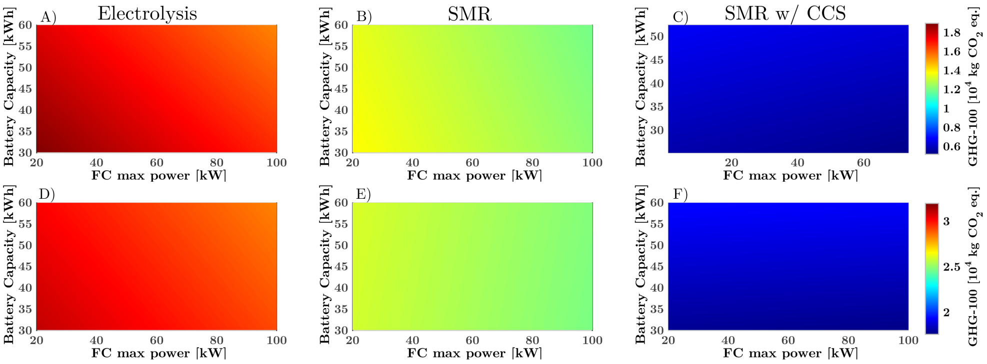

Figure 5.3. *Design spaces for 600 km of range FCREx: GHG-100 emissions originated in the fuel cycle (1st row) and in the cradle-to-grave cycle (2nd row) considering* ***black*** *(1st column), grey (2nd column) and blue (3rd column)* H_2 *production pathways. Functional unit is 120000 km and 1 vehicle produced.*

(generated through SMR with CCS) as most of the H_2 used currently is produced with SMR technology which can be enhanced in the short-term with CCS, consequently being a more plausible option to reduce emissions in the short-term than green H_2 (produced entirely from renewable energy).

The strongest change in GHG-100 emissions in the graphs of figure 5.3 is caused by modifying the H_2 production pathway. This fluctuation in emissions is considerably higher than that produced by modifying the design in terms of FC maximum power or battery capacity output, thus the variation in emissions in the fuel production cycle per kg of H_2 or per kWh of electricity when switching the H_2 production pathway is much more important than the decrease in H_2 or electricity consumption as a result of changing the powerplant design. In general, the GHG-100 emissions produced in the fuel production cycle rise by ∼184% and ∼111% comparing those produced with SMR and CCS with those generated if considering electrolysis with the EU electricity mix and SMR, respectively. Analogously, the average increase in GHG-100 emissions in the cradle-to-grave cycle with the H_2 production pathway is ∼60 % and ∼36 % comparing SMR with CCS with electrolysis and SMR, respectively. The high relative growth in emissions in the fuel production cycle and the large increase in the cradle-to-grave process demonstrate how the fuel production pathway has a big impact on the overall emissions. The GHG-100 emissions in the fuel production cycle constitute roughly ∼33% of the total emissions in the case of SMR with CCS, ∼51% in the case of SMR, and ∼58% in the case of electrolysis. According to this results, it is reasonable to infer that the emissions produced during the vehicle manufacturing cycle are a significant component of those produced in the FCREx cradle-to-grave process and could constitute more than 50% of them if low-emissions production pathways such as SMR with CCS (blue H_2) are considered. Therefore, the FCREx design has a higher impact on the total emissions if H_2 production pathways imply high emissions (electrolysis with the EU mix and SMR) since the emissions during the fuel production are sensitive to the powertrain efficiency through fuel and electricity consumption (figure 5.1). This suggests that in a scenario with blue or green H_2 the effort to decrease cradle-to-grave emissions for conventional FCV and FCREx vehicles should mainly be focused on the vehicle manufacturing process.

The slope of the iso-lines in figure 5.3 reflects the sensitivity of the GHG-100 emissions generated in the fuel production cycle or in the cradle-to-grave process to the designd of the FCREx components. The slope varies substantially with the H_2 production route as there are two energy sources in the vehicle (electricity in the battery and H_2 in the tank) with differing emissions per kWh of energy. Therefore , how GHG-100 emissions vary with the design of the FCREx powertrain would depend on what energy carrier entails more emissions per useful[1] kWh of energy carrier produced. For H_2 produced through electrolysis or SMR (figure 5.3: A,B,D & E), the production of 1 $\text{kWh}_{\text{useful}}$ in the form of H_2 generates more emissions than 1 $\text{kWh}_{\text{useful}}$ in the form of electricity due to both the better efficiency of batteries and the lower emissions per actual kWh. Therefore, in this scenario, as the battery capacity is increased, the GHG-100 emissions in the fuel cycle are reduced (A-B). In figure 5.3, the slope of graph A's iso-lines is close to the slope of the iso-lines in the figure showing the total H_2 consumption during the lifetime (figure 5.1, graph E) because the emissions generated when producing H_2 through electrolysis with the current EU electricity mix dominate the total emissions in the fuel production cycle. In contrast, the iso-lines of figure 5.3 graph B are similar to those found in figure 5.1 graph H which represents the overall energy consumption since producing 1 $\text{kWh}_{\text{useful}}$ of H_2 generates comparable but higher emissions than producing 1 $\text{kWh}_{\text{useful}}$ of electricity to be used with a battery. The trend of GHG-100 emissions when comparing graphs A and D (electrolysis, figure 5.3) are similar, therefore the fuel cycle dominates most of the cradle-to-grave cycle. In the case of SMR (graphics B and E) the trends vary: increasing the battery capacity increases total emissions in spite of lowering both the H_2 and the power used throughout the life. This suggests that if SMR is considered, GHG-100 emissions would decline in such a manner

---

[1] Useful kWh is the energy stored as electricity or H_2 multiplied by the average efficiency of the related system (battery or FCS)

that the vehicle production cycle dominates the cradle-to-grave process as the battery capacity is increased. Nonetheless, with both electrolysis and SMR as the fuel production pathways, cradle-to-grave emissions still decline with FC maximum power since the efficiency of the FCS improves and most of the energy in the vehicle is stored as H_2. Consequently, the fuel production cycle dominates the global GHG-100 whenever the FC maximum power is changed.

Interestingly, if production pathways for H_2 that impy high emissions are considered, the optimum design for the FCREx architecture in terms of cradle-to-grave emissions is the same as that minimizing the H_2 and energy consumption determined in section 4.3.1 (high battery capacity and high FC stack maximum power) because in this case, the fuel cycle dominates the global emissions (figure 5.3, graphs A & D). Hence, limiting H_2 consumption also implies minimizing cradle-to-grave emissions. This tendency is also seen for NO_X emissions in the next section (figure 5.5, graphs A & D).

The trends observed for SMR with CCS in the fuel production cycle are considerably different from those with other production strategies. In the fuel production cycle (figure 5.3, graph C), the GHG-100 emisions generated per kWh_{useful} of H_2 are much lower than those per kWh_{useful} of electricity, thereby increasing the fuel production cycle emissions as the battery capacity increases (higher fraction of energy stored as electricity in the vehicle). With all the production paths studied, as most of the energy stored is in form of H_2, raising the FC maximum power significantly lowers the emissions in the fuel production cycle (figure 5.3 graph F). Again, the rise in battery capacity implies larger cradle-to-grave emissions. In the case of considering SMR with CCS, the total GHG-100 emissions are significantly more sensitive to battery capacity than SMR without CCS. This is attributable to the fact that both in the fuel production cycle and the cradle-to-grave process GHG-100 emissions grow with the battery capacity. This is representative of the implications of employing low-emission fuels such as blue or green H_2 to power FCV. First, the focus to minimize emissions moves towards the vehicle manufacturing cycle because it dominates the cradle-to-grave emissions. Second, utilizing power from batteries if the renewable share of the electricity mix does not increase may merely raise the cradle-to-grave emissions.

Figure 5.4 illustrates the fuel production cycle and the cradle-to-grave emissions for various FCREx vehicle ranges with H_2 generated via SMR with CCS. Note again that the GHG-100 emissions of blue H_2 are lower than those of electricity. The graphs A-C are comparable to graph C in figure 5.3, illustrating the GHG-100 emissions grow with the battery capacity and decline with the FC maximum power due to the low emissions generated in

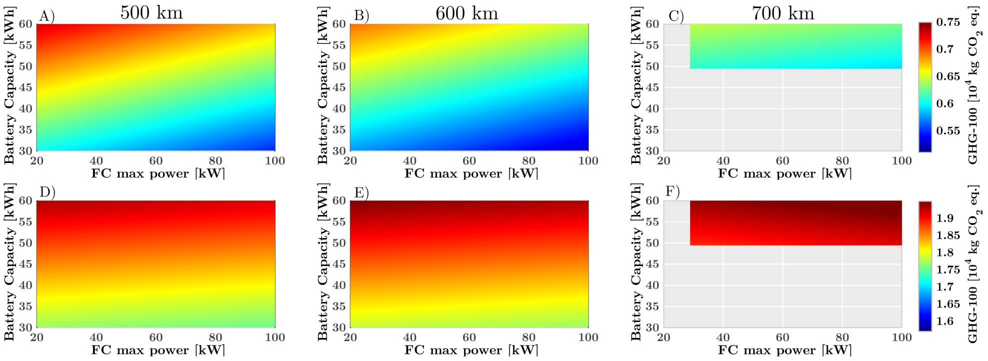

Figure 5.4. *Design spaces for 500, 600, and 700 km of target range FCREx: GHG-100 emissions produced in the fuel cycl (1^{st} row) and in the cradle-to-grave cycle (2^{nd} row) considering SMR with CCS (blue) as H_2 production pathway. Functional unit is 120000 km and 1 vehicle produced.*

the SMR with CCS process. In these figures, it is possible to observe how the GHG-100 emissions in the fuel production cycle decrease with the desired range for a given configuration. Interestingly this occurs because, for a given battery capacity, as the targeted range grows, the mass of H_2 in the tank increases, thereby increasing the proportion of the lifetime (distance) that is covered using just H_2. If GHG-100 emissions per kWh_{useful} of H_2 were greater than those generated per kWh_{useful} of electricity (SMR or electrolysis) in the fuel production cycle, then the total GHG-100 in the fuel cycle would grow with the target range.

In the case of cradle-to-grave GHG-100 emissions, extending the range for a given combination of battery capacity and FC maximum output power increases GHG-100 emissions (figure 5.4 graphs D-F). This takes place since the decrease in emissions in the fuel production cycle (figure 5.4 graphs A-C) is smaller than the increase in the vehicle manufacturing cycle emissions due to the requirement of bigger H_2 tanks (figure 5.2 graphs A-C) when increasing the target range. When the range is held constant at 500 or 600 km, graphs D-E illustrate how GHG-100 emissions grow with battery capacity and decrease with FC maximum power, as mentioned for figure 5.3, graph F. In contrast, for the design space with a range of 700 km the trend of the emissions with respect to the FC maximum power is inverted, showing a rise in GHG-100 with this sizing parameter. The transformation of this trend is caused by the high weight of the FCREx vehicles with such target range, which restricts the decrease in H_2 consumption (figure 5.1, graph F) with the FC maximum power, making the rise in the emissions associated to the vehicle manufacturing cycle surpass the decrease in the fuel production cycle.

From the results in figure 5.4 cradle-to-grave GHG-100 emissions could vary up to 10% depending on the size of each component and the desired range the FCREx is designed for. Although 10% might seem small, it is actually considerable if it is regarded that the comparison is conducted between vehicles that use the same energy carriers (H_2 and electricity) with the same production pathway and similar architecture, albeit the sizing of the components of the powertrain may vary.

In conclusion, the usage of FCREx architecture implies significant variability in cradle-to-grave GHG-100 emissions with the design choice, the desired range and the H_2 production pathway. Hence, such emissions must be taken into consideration in the vehicle design process. With low-emission H_2 production pathways, limiting the FCREx target range and decreasing the battery capacity might minimize emissions because the vehicle manufacturing cycle becomes the dominating phase in the cradle-to-grave process. As such, based on how the H_2 production infrastructure develops in the coming decades, the optimal FCREx powertrain in terms of GHG-100 emissions may move towards moderate-to-high FC stack power and moderate-to-low battery capacity. This optimal design may indicate lower-than-BEV manufacturing costs and low but not minimal H_2 and total energy consumption (figure 5.1) [1]. This optimal could be similar to the optimum design in terms of TCO.

5.2.3 Cradle-to-grave and fuel production NO_X emissions

This section focuses on studying NO_X emissions since they have recently been an important concern for society due to their harmful effects on human health and ozone depletion at higher altitudes and generation at lower altitudes. This section follows the same structure as section 5.2.2 but particularly focused on the NO_X emissions produced along the cradle-to-grave process. Note that, unlike in GHG-100, the production pathway SMR without CCS implies the lowest NO_X emissions (figure 5.5) since SMR with CCS requires additional energy for the the CO_2 capturing and the renewable share in the EU electricity mix is low to produce low-NO_X H_2 from electrolysis. Consequently, compared to the H_2 produced from SMR with CCS, the NO_X emissions vary in the fuel production cycle approximately by $\sim$95% and $\sim -16\%$ considering electrolysis and SMR without CCS, respectively. Analogously, the total NO_X associated to the cradle-to-grave process change by $\sim$38% and $\sim -6\%$. According to the change in the emissions when the production pathway is modified, it is possible to deduce that their influence is by much less considerable than for GHG-100 emissions. Given the little variance in NO_X emissions and the significant difference in GHG-100 emissions between SMR without and with CCS, it could be desirable to consider SMR with CCS as the optimum production pathway to minimize the total emissions (among those included in this research).

The production of H_2 from electrolysis implies significantly higher NO_X emissions as an important part of the EU electricity mix is produced using non-renewable energy sources. In the SMR process, the NO_X are formed in the combustion process used to heat the reactor to achieve high-enough temperatures to dissociate the CH_4 molecule. For this technology, low-NO_X burners and selective catalyst reduction (SCR) after treatment systems for exhaust gases are a possible option to minimize NO_X in SMR plants, despite their usage not being extensively spread [2].

When H_2 is generated from electrolysis (figure 5.5, graphs A & D), NO_X emissions decrease as the battery capacity and the FC stack maximum power are increased, both in the fuel production cycle (graph A) and in the total life cycle (graph D). As outlined before, the trend of the NO_X emissions in the fuel production cycle is motivated by the decrease in the energy and the H_2 consumption. The emissions generated in the H_2 production pathway are higher than those produced during the generation of the electricity used to charge the battery. As such, the decline in NO_X emissions when increasing the FC stack maximum power is much important than when raising the battery capacity. The evolution of the emissions in the fuel cycle and the cradle-to-grave process are opposed to that found in the vehicle manufacturing cycle (figure 5.2, graph E), where the NO_X emissions increase with the battery capacity and the FC maximum power. This implies that the overall trend of the emissions generated in the cradle-to-grave process are dominated by the fuel production cycle. Particular to this case, more emissions are generated in the fuel production cycle than in the vehicle manufacturing cycle (16.4-19.7 kg NO_X against 14.1-15.1 kg NO_X), which means that the fuel production pathway dominates the total emissions both in amount and trend.

The evolution of NO_X emissions and their absolute value are similar in the cases of generating H_2 through SMR with or without CCS (figure 5.5, graphs B, C, E & D). In the fuel production cycle (graphs B & C), the NO_X emissions are reduced when increasing the FC maximum output power due to the lower H_2 consumption. Opposed to this, they increase with the capacity of the battery as electricity production implies more emissions than H_2 generation. When this happens the portion of energy stored as H_2 declines,

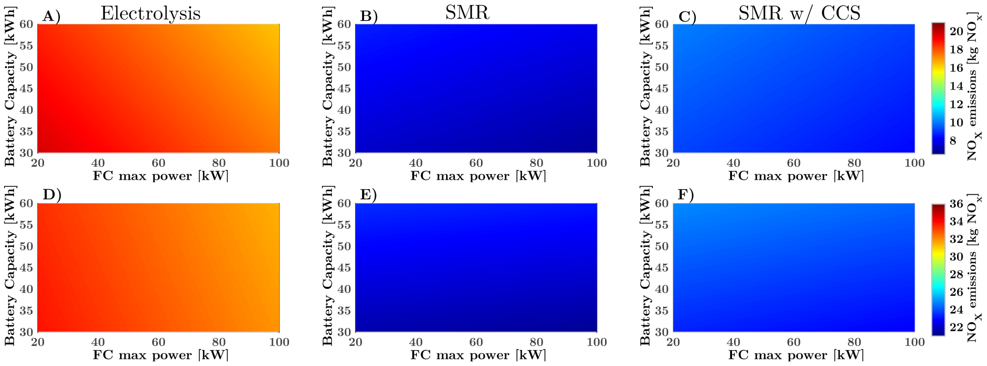

Figure 5.5. *Design spaces for 600 km of range FCREx: NO$_X$ emissions originated in the fuel cycle (1st row) and in the cradle-to-grave cycle (2nd row) considering* ***black*** *(1st column), grey (2nd column) and blue (3rd column) H$_2$ production pathways. Functional unit is 120000 km and 1 vehicle produced.*

thus fostering the battery utilization to achieve the target range. In regard to the cradle-to-grave emissions, they present the same trend when changing the sizing of the components as the fuel production cycle, implying that they are mainly dominated by the fuel production cycle emissions. Nevertheless, the emissions generated in the fuel production cycle are considerably lower than those observed in the vehicle manufacturing cycle, therefore although most of NO$_X$ emissions are produced in the vehicle manufacturing cycle, the sensitivity of the fuel production cycle to the FCREx design is larger, hence dominating the evolution of the cradle-to-grave emission without entailing the highest contribution to their total amount.

Supplementing figure 5.5, figure 5.6 presents the NO$_X$ emissions generated in the fuel production cycle and the cradle-to-grave process for the FCREx designs with target range of 500, 600 and 700 km considering blue H$_2$ (SMR with CCS). The trends of the NO$_X$ emissions in the graphs A-C are similar to that in figure 5.5 graph C and the justification for that is elaborated in the previous paragraph. For a fixed design in terms of FC stack maximum power and battery capacity, increasing the desired range means lower NO$_X$ emissions in the fuel production cycle since higher H$_2$ tank capacity is needed to rise the range and the emissions associated to blue H$_2$ generation are lower than those releases in the electricity production with the EU mix. This tendency in the fuel production cycle is similar to that observed in GHG-100 emissions, figure 5.4. In the design space with a range of 700 km, the NO$_X$ emissions are less responsive to the change in the FC stack maximum power since the

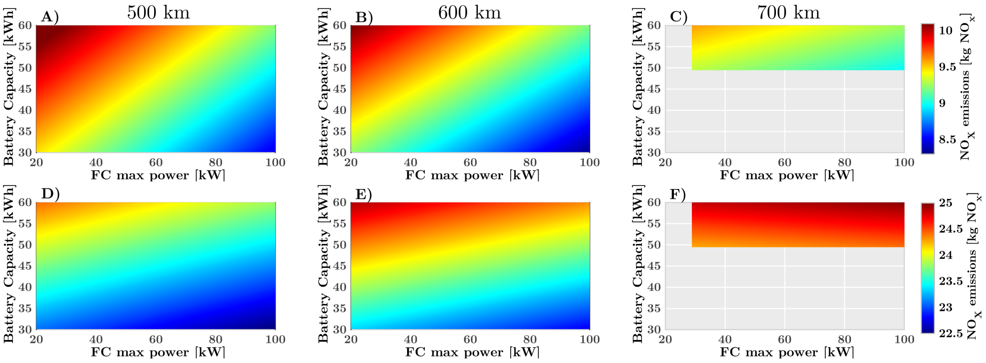

Figure 5.6. *Design spaces for 500, 600, and 700 km of target range FCREx: NO_X emissions produced in the fuel cycle (1^{st} row) and in the cradle-to-grave cycle (2^{nd} row) considering SMR with CCS (blue) as H_2 production pathway. Functional unit is 120000 km and 1 vehicle produced.*

gain in FCS efficiency when rising the FC maximum power is less important due to the significant vehicle weight (high battery and H_2 tank capacities). This could also be perceived in the total H_2 consumption estimated with this design space (figure 5.1, graph F).

Figure 5.6 graphs D-F provide information about how the cradle-to-grave NO_X emissions of a fixed combination of FC maximum power and battery capacity grow with the target range because of the additional emissions generated when increasing the H_2 tank capacity. Furthermore, the variation in the NO_X evolution when comparing graphs D-E with graph F is due to the lower sensitivity of the emissions in the fuel production cycle to the FC stack maximum power, hence making the vehicle manufacturing cycle dominate the trend. As a consequence, in the design space with a target range of 700 km, the NO_X emissions grow with the FC stack maximum power.

The change in cradle-to-grave NO_X emissions between worst and best designs could be up to 10% among the designs included in the design spaces of this research. This variation is close to that found in the analysis for GHG-100 emissions, which is due to the similar trend they follow when modifying the sizing of the FCREx components.

In conclusion, unlike GHG-100 emissions, the cradle-to-grave NO_X emissions of FCREx vehicles are mainly dominated by the fuel cycle, except for the designs with 700 km target range in which the vehicle weight becomes an hindrance to decrease considerably H_2 consumption when rising the FC stack maximum power. Therefore, the designs with the lowest cradle-to-grave NO_X

emissions are those with high FC stack maximum power and moderate battery capacity (30 kWh), except for the design space of 700 km. Among electrolysis, SMR and SMR with CCS, the production pathway that offered the lowest NO_X was SMR without CCS since CCS process needs an additional amount of energy to for the capture of CO_2. Nonetheless, the variation between SMR with and without CCS in NO_X is significantly smaller than that found in section 5.2.2 for GHG-100. Therefore, looking at the total emissions, SMR with CCS might still be the optimum H_2 production pathway among those considered in sections 5.2.2 and 5.2.3.

5.2.4 Blue and green H_2 comparison

As a supplementary section of the study aimed at evaluating the environmental impact of FCREx vehicles, this part is focused on analyzing the GHG-100 and NO_X emissions of the FCREx architecture comparing blue and green H_2 are compared. The set of processes defining the green H_2 production pathway were exactly those for black H_2 presented in figure 3.14 but changing the source of the electricity from the EU mix to solar energy. As a consequence, the emissions associated to green H_2 production are considerably smaller compared to those of any other H_2 production pathway (0.056 kg CO_2 eq./kWh H_2 and $6.8 \cdot 10^{-5}$ kg NO_X/kWh H_2). Nonetheless, the data in figures 5.7 and 5.8 must be interpreted carefully baring in mind the scenario they represent. As commented before, the source of energy is renewable for green H_2, while the electricity in the battery was obtained from the EU mix. As such, these results are representative of a scenario that may be biased towards FCV compared to BEV as it could be questioned that the renewable energy could rather be part of the EU mix to decrease the emissions due to the battery utilization. This is why these results were included in a separate section of the study focused on FCREx for completeness and should be analyzed while taking into account the specific scenario just described.

It is essential to note that the emission generated during the production of green H_2 are not completely zero since some of the processes included in the production pathway need the use of non-renewable energy for H_2 refinement and distribution. Nevertheless, the total emissions of the production pathway are still much lower than with other H_2 production technology.

Figure 5.7 presents the GHG-100 emissions generated during the fuel production cycle and cradle-to-grave process for both blue (SMR w/ CCS, left column) and green (electrolysis with solar energy, right column) H_2 for the FCREx designs with 600 km of range. These data are also illustrated for

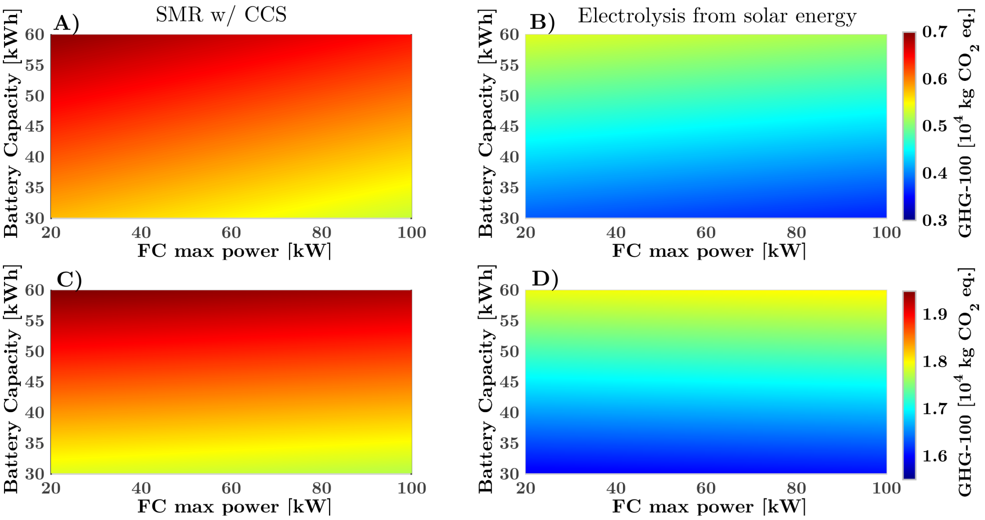

Figure 5.7. *Design spaces for 600 km of range FCREx: GHG-100 emissions produced in the fuel cycle (1st row) and in the cradle-to-grave cycle (2nd row) considering blue (1st column) and green (2nd column) H_2. Functional unit is 120000 km.*

NO_X emissions in figure 5.8. The evolution of the emissions when changing any sizing parameter in both figures is similar. As discussed previously for blue H_2, increasing the capacity of the battery implies a rise in GHG-100 and NO_X emissions as the emissions released when producing 1 kWh of H_2 are much lower than those generated when producing 1 kWh of electricity with the current EU electricity mix. as a result, both emissions decline when the battery capacity is increased, which implies a higher utilization of electricity and a lower H_2 tank capacity (figure 5.1). The change in the emissions when modifying the FC stack maximum power was already explained along the study: rising the FC maximum power output means a more efficient usage of H_2, hence decreasing the fuel consumption and emissions.

As explained in section 5.2.2, modifying the H_2 production pathway does not only mean a change in the cradle-to-grave emissions but also in the fraction of the fuel production cycle emissions over the total emissions. Blue H_2 production implies ~33% of the overall emissions while the production of green H_2 entails ~26%. This implies, again, a reason to justify that as the industry moves towards low-emissions energy carriers and/or propulsion systems, the vehicle manufacturing processes will become more relevant in the overall cradle-to-grave emissions.

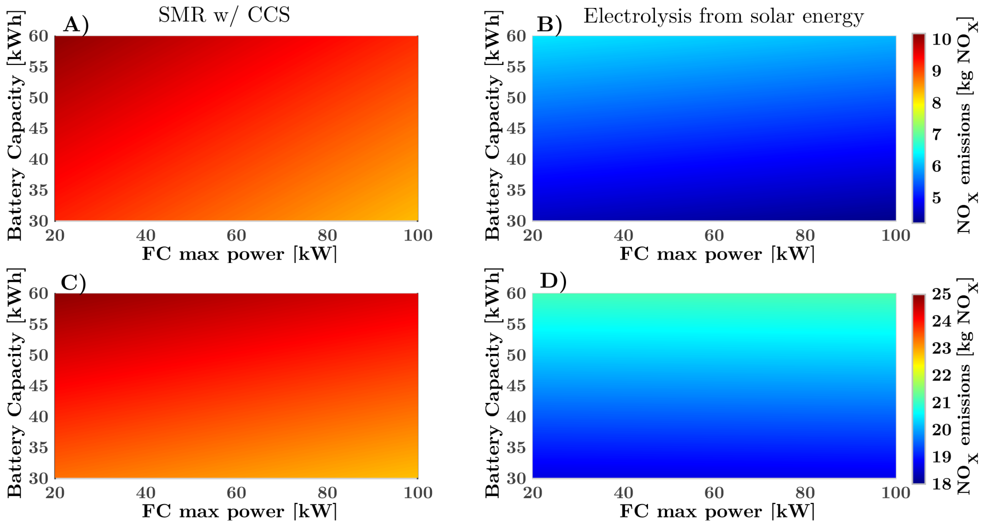

Figure 5.8. *Design spaces for 600 km of range FCREx: NO_X emissions produced in the fuel cycle (1^{st} row) and in the cradle-to-grave cycle (2^{nd} row) considering blue (1^{st} column) and green (2^{nd} column) H_2. Functional unit is 120000 km.*

In figures 5.7 and 5.8, it is possible to identify how increasing the FC stack maximum power with green H_2 means higher emissions. This is motivated by the low emissions that green H_2 entails in the fuel production cycle, which change when increasing FC stack power in the FCREx architecture is even smaller than the variation in emissions in the vehicle manufacturing cycle. As a consequence, the cradle-to-grave emissions when considering green H_2 show a similar evolution to that of the emissions in the vehicle manufacturing cycle (figure 5.2, graphs B & E).

Finally, it is essential to comprehend that cradle-to-grave GHG-100 and NO_X emissions may vary up to 11.8% and 12.5% for green H_2 depending on the FCREx design, respectively. In contrast, they may change up to 9.1% and 8.8% with blue H_2, respectively. This is due to the lower fuel production cycle emissions for green H_2, which makes the vehicle manufacturing cycle dominate the cradle-to-grave process.

5.2.5 Potential of FCREx architecture to decrease cradle-to-grave emissions

From the results shown along sections 5.2.2 and 5.2.3, it was concluded that with low-emissions H_2 production pathways (SMR with CCS or blue

H_2), the trend that FCREx manufacturers should follow to minimize cradle-to-grave emissions should aim at decreasing the battery capacity as much as possible but providing high-enough range in BEV mode (so that the emissions generated in the battery manufacturing are low) and high FC stack maximum power to minimize H_2 consumption. This trend might imply that using the FCREx architecture could generate higher cradle-to-grave GHG-100 and NO_X emissions than conventional FCV architectures.

However, if high-emissions H_2 production pathways are considered (electrolysis with electricity from the EU electricity mix), the FCREx architecture would decrease considerably the GHG-100 and NO_X emissions with higher battery capacity (figure 5.3 and 5.5, graph D). This puts forward that the interest of considering the FCREx architecture, only emissions-wise, would mainly depend on the balance between the emissions released in the production of electricity and those generated when producing H_2. Nevertheless, there exists another key factor that could impact noticeably the cradle-to-grave emission of FCREx architecture: the battery manufacturing process. Hence, it is feasible to deduce that, in the short term, if H_2 is mainly produced with electrolysis and EU electricity mix, FCREx vehicles could offer important advantages over conventional FCVs in terms of cradle-to-grave emissions. Projecting this into the future, in the medium and long-term it is unpredictable if FCREx or traditional FCV architectures will imply lower emissions as this will depend on the rate at which the H_2 production pathways, the EU electricity mix, and the battery manufacturing process are decarbonized and become cleaner. If the decarbonization of the battery production processes and the increase in the renewable share in the electricity mix are prioritized, then FCREx architecture may be superior to conventional FCV, while if the focus is on producing cleaner H_2 conventional FCV may imply lower emissions. The results obtained in this study will be useful for FCV manufacturers to identify and understand the cradle-to-grave emissions and performance of FCREx vehicles and their change when modifying the FC stack maximum power, H_2 tank capacity and battery capacity. This may also suppose an starting point in the design process of FCREx vehicles to preliminary select a set of design choices to be further iterated as the vehicle development process progresses. The importance of producing such data not only relies in the benefits for FCV manufacturers, but also for the society as the existence of these design spaces, presented not only in terms of performance but in terms of cradle-to-grave emissions as well, could shorten considerably the FCREx vehicle development process, thus accelerating the pathway towards the H_2 economy and reducing the environmental impact of the transportation sector and industry.

Finally, from the data in the previous sections, a set of recommendations to minimize the cradle-to-grave emissions of vehicle with the FCREx architecture can be extracted. In the first place, it is essential to decarbonize and decrease the overall emissions of the vehicle and subcomponents manufacturing processes, particularly the battery manufacturing, as it is responsible for a substantial fraction of the cradle-to-grave emissions. In second place, the share of renewable energy on the EU electricity mix ought to be increased as it has a direct impact on both electricity and H_2 production. Last but not least, in other to significantly reduce the cradle-to-grave emissions of FCVs (both FCREx and conventional), it is required to implement CCS technology in SMR plants, because this it would enable the increase in the renewable energy share of the EU electricity mix at a faster path while decarbonizing the SMR H_2 production pathway which will imply a higher rate of decrease of the global emissions, affecting the cradle-to-grave emissions of BEV as well, rather than devoting all the renewable energy infrastructure the will be developed in the coming years to produce green H_2.

5.3 Cradle-to-grave emissions of Multi-FCS HDV

After exploring the FCREx architecture and its potential to decrease cradle-to-grave emissions, this section focuses on the analysis of the multi-FCS architecture for the heavy-duty application and how it can be used to minimize the GHG-100 and NO_X life cycle emissions. The results presented along this section use the consumption and durability data obtained previously in section 4.4. As such, the emissions showed here do not only comprise those required to produce the fuel and electricity for the vehicle's lifetime but also for all the FCS replacements required to fulfill the vehicle target operation life. As commented before, these results will serve to identify whether the multi-FCS architecture should integrate differential control or differential sizing design approaches and to critically assess if the trend of the industry of using a fixed-power modular FCS standard that can be stacked for higher-power applications is optimum or can be improved by applying them.

Similar to section 5.2, the LCA analysis in this section are divided into two: the first focused on GHG-100 emissions (section 5.3.1) and the second on NO_X emissions (section 5.3.2). Differently from the previous analysis focused on passenger cars and the FCREx architecture, the results along the following discussion include the production pathways of black, grey, blue and green H_2 simultaneously. The reason for including green H_2 together with the rest of the production strategis is that, for the heavy-duty sector, some the long-haul trucks are designed to run between two or more predetermined points constantly to transport goods. These locations are usually out of the cities, near or inside industrial parks, in which a constant an foreseen flow of trucks is established. In this situation, the planned operation of the heavy-duty vehicle fleet and the separate location of the goods collection/drop points, make it possible to develop infrastructure to refuel the heavy-duty vehicles with green H_2 (obtained from a solar or wind powerplant near these locations) and to identify the arrival times of each vehicle to ensure there is no lack of H_2. For such reasons, the heavy-duty transport sector could integrate green H_2 in the short-term more easily than the passenger car application, as it is planned in the Hydrogen Roadmap for Europe [3].

5.3.1 GHG-100 cradle-to-grave emissions of heavy-duty FCV

The results presented in this and the following section are the cradle-to-grave emissions of the heavy-duty vehicle powered with a multi-FCS powertrain. In each graph, the fraction of the total emissions pertaining to a specific process is indicated in the legend. As such, these graphs are also useful to identify the % of the emissions that comes from each of the phases composing the cradle-to-grave process: fuel production and vehicle manufacturing, mainly. In the case of the vehicle manufacturing, the emissions are broken down into *vehicle body, e-motor, battery manufacturing, H_2 tank* and *FCS manufacturing*, while the fuel production cycle is divided into *H_2 production* and *electricity production*. It is important to note that the emissions associated to the *FCS manufacturing* comprise all the emissions that are released when manufacturing all the FCS required during the vehicle's lifetime, derived from the durability results in section 4.4. Furthermore, the lower limit of the Y axis in figures 5.9, 5.10, 5.12 and 5.13 was not the same when comparing different H_2 production pathways purposely to provide enough resolution to identify the segmentation of the cradle-to-gate process (vehicle manufacturing).

The structure in both sections 5.3.1 and 5.3.2 is similar. First, the cradle-to-grave emissions for the 120+120 kW design are presented for each of the different H_2 production pathways and control dynamics, showing the contribution of each phase of the life cycle to the total emissions. Then, the overall cradle-to-grave emissions are compiled numerically in a table, highlighting the best and the worst control dynamics depending on the H_2 production pathway. This is then repeated for the 160+80 kW configuration to present how differential sizing would affect the results. This configuration was chosen while the 140+100 kW one was omitted since it is the design that is the furthest with respect to the 120+120 kW architecture and to improve readability. Finally, the optimum control dynamics for both the 120+120 kW and the 160+80 kW configurations for each production pathway are presented in a graph, in which the differences in cradle-to-grave emissions with different H_2 can be clearly identified.

The results in figure 5.9 show the breakdown of the cradle-to-grave emissions depending on the H_2 production pathway. The vehicle manufacturing cycle amounts to 2.6-3.5% for black H_2, 3.6-4.8% for grey H_2, 9.4-12.1% for blue H_2, and 15-19% for green H_2 of the cradle-to-grave emissions. As can be seen, the vehicle manufacturing processes become less relevant as the emissions in the fuel production cycle increase. Note that the lower limits in the % intervals just presented correspond to the differential control strategies in which the dynamics of both FCS are limited to $|\mathrm{di/dt}|_{\mathrm{max}} = 0.001\ \mathrm{A/cm^2s}$ while the upper limits correspond to the cases in which both FCS operate with high dynamics ($|\mathrm{di/dt}|_{\mathrm{max}} = 0.1\ \mathrm{A/cm^2s}$). The change in this percentages is meaningful, as it represents the effect of optimizing the durability of the FC stacks instead of the consumption on the cradle-to-grave emissions. Similarly, the H_2 production cycle may be originating 96.5-97.4% for black H_2, 95.2-96.4% for grey H_2, 87.9-90.6% for blue H_2, and 81-85% for green H_2 of the cradle-to-grave emissions. The higher limits of these intervals correspond to the very-low control dynamics (high H_2 consumption) while the lower limits to the high dynamics cases. Given these percentages, it is clear how the performance of the vehicle is key to minimize the cradle-to-grave emissions since it minimizes the amount of H_2 consumed and thus the emissions coming from H_2 production. Nevertheless, it is important to note that the variation in this percentages is very similar to the variation in the relative value of the vehicle manufacturing emissions. This means that in the cases that were considered in this study, the emissions associated to the vehicle manufacturing and the H_2 production suffer similar variations when changing the dynamics. This means that, although H_2 production is the origin for most of the emissions, it would be an error to consider that minimizing H_2 consumption at the expense of lower FC stack durability implies minimizing cradle-to-grave emissions,

In this sense, the data from these graphs and those in table 5.1 show the trade-off between consumption and durability in terms of cradle-to-grave emissions and what control dynamics minimize them. For the high-emissions H_2 production pathways (black and grey), the emissions in the fuel production cycle are that high that the optimum dynamics are those minimizing the H_2 consumption for both FCS, i.e., high dynamics. In contrast, the lowest-dynamics control strategy implied the highest emissions despite offering the

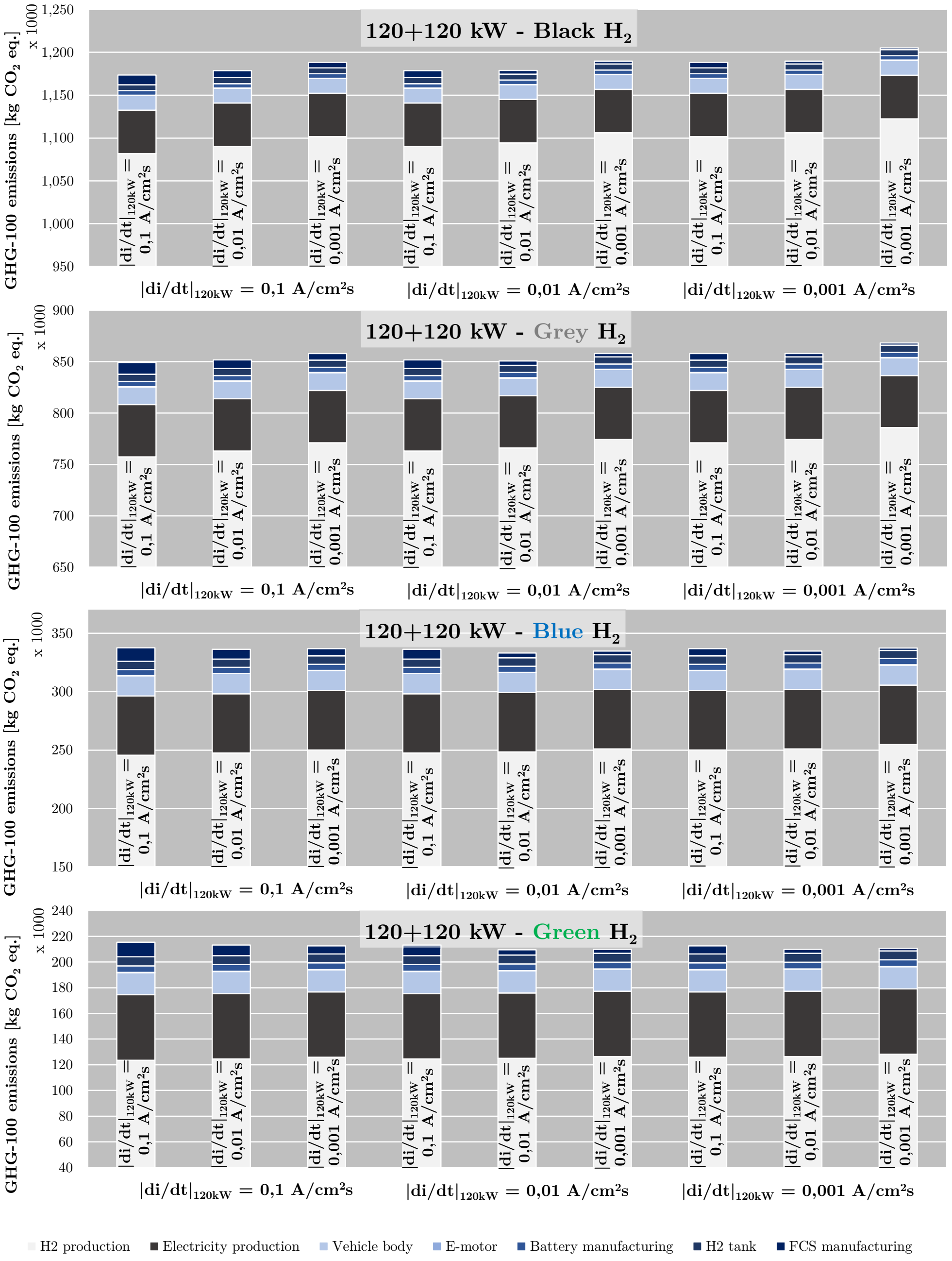

Figure 5.9. *Cradle-to-grave GHG-100 emissions of the heavy-duty multi-FCS architecture with the 120+120 kW configuration and different control dynamics considering* ***black****, grey,* ***blue*** *and* ***green*** H_2*. Functional unit is 1000000 km and 1 vehicle produced.*

	$\lvert di/dt \rvert$ [A/cm^2s]								
120 kW	0.1	0.01	0.001	0.1	0.01	0.001	0.1	0.01	0.001
120 kW	0.1	0.1	0.1	0.01	0.01	0.01	0.001	0.001	0.001
	Ctg GHG-100 emissions [$\cdot$1000 kg CO_2 eq.]								
Black H_2	1174	1179	1188	1179	1179	1190	1188	1190	**1205**
Grey H_2	**849.1**	851.7	857.8	851.7	850.6	857.8	857.8	857.8	**868.2**
Blue H_2	**337.4**	336.1	336.7	336.1	**333.0**	334.6	336.7	334.6	337.3
Green H_2	**215.4**	213.2	212.5	213.2	**209.6**	209.9	212.5	209.9	210.7

Table 5.1. *Cradle-to-grave GHG-100 emissions of the 120+120 kW with* ***black****, grey,* ***blue*** *and* ***green*** *H_2. Optimum control with lowest cradle-to-grave emissions for each production pathway is highlighted in green while the worst control is in* ***red****. Functional unit is 1000000 km and 1 vehicle produced.*

highest FC stack durability. This means that for high-emission H_2 production pathways the fuel cycle dominates the cradle-to-grave emissions. The change in the total emissions between the best and the worst control dynamics is of 2.7% for black H_2 and 2.3% for grey H_2. The relative values are low since the lifetime of the vehicles is large, but in absolute terms they imply 31.3 t CO_2 eq. for black H_2 and 19.2 t CO_2 eq. for grey H_2, which is not negligible.

With the low-emission H_2 production pathways (blue and green), the optimum control is the trade-off between consumption and FC durability. In this case, the minimum cradle-to-grave emissions are found when both FCS are operated with moderate dynamics ($|di/dt|_{max} = 0.01$ A/cm^{2}s). This is due to the fact that the GHG-100 emissions per kg of H_2 produced lowered significantly, so the FC stack durability is more relevant in the overall cradle-to-grave emissions. With these production pathways, the difference between the best and worst control dynamics is 1.3% (4.4 t CO_2 eq.) in the case of blue H_2 and 2.8% (5.8 t CO_2 eq.) with green H_2. The lowest variation in the case of blue H_2 is motivated by the fact that with the value of emissions per kg of H_2 in this production pathway the gain in the high-dynamics case in the fuel production is compensated by the loss in the vehicle manufacturing cycle. This happens again in the lowest-dynamics case for this particular pathway. As a consequence, as can be seen in table 5.1, the cradle-to-grave emissions of the highest and lowest dynamics cases are very similar.

Nonetheless, even though low-emissions H_2 production pathways are considered, the emissions of the fuel production cycle are still the origin of most of the cradle-to-grave emissions. For this reason, the optimum control strategy comprises moderate dynamics: a trade-off between FC durability and performance. This bring light about one important conclusion related to the use of FC technology in the heavy-duty sector: even with renewable H_2, since it is not zero-emissions, the way of minimizing the cradle-to-grave emissions is not to only improve FC durability at the expense of performance, but rather to find a compromise between consumption and durability. This is important since it may be thought that the emissions coming from green H_2 production are that low that only the vehicle manufacturing cycle is contributing to the overall emissions and that the focus should be only on minimizing them by increasing the FC stack durability. Nevertheless, the lifetime of a heavy-duty transport vehicles are that high that even with renewable H_2 the fuel production cycle is the origin of most of the emissions.

The results in figure 5.10 and table 5.2 are analogous to those presented in figure 5.9 and table 5.1 but for the 160+80 kW configuration.

As commented in section 4.4, the cases in which both FCS operate with the same dynamics, the results in terms of consumption and durability are similar to those obtained for the 120+120 kW architecture. As a consequence, since the optimum designs seem to be those with the same control dynamics in both FCS, the main differences arise when comparing the cases with differential control. As an example, the following discussions is focused in the case in which one of the FCS has moderate dynamics ($|\mathrm{di/dt}|_{\mathrm{max}} = 0.01$ A/cm^{2}s) while the other behaves with low dynamics ($|\mathrm{di/dt}|_{\mathrm{max}} = 0.001$ A/cm^{2}s), but is also applicable to the rest of the cases with differential control. When the 160 kW is operated with low-dynamics and the 80 kW is operated under moderate-dynamics the 120+120 kW with the same differential control exhibits lower cradle-to-grave emissions. It could be thought that in this case the high-power FCS has higher durability, so the vehicle manufacturing emissions would fall significantly compared to the 120+120 kW configuration. This is true, but since the 160 kW FCS is producing most of the power in the powertrain, imposing significant constraints on its dynamics implies a higher penalty in the H_2 consumption, which is translated into a noticeable increase in the fuel production cycle emissions. Since the lifetime of this application is very high, the fuel production cycle is mostly dominant with all the H_2 production pathways, which implies that the increase in the fuel production cycle emissions outweighs the decrease in the vehicle manufacturing cycle emissions. As a consequence, this design with differential control and differential sizing does not offer any advantage in terms of life cycle emissions with respect to the 120+120 kW architecture.

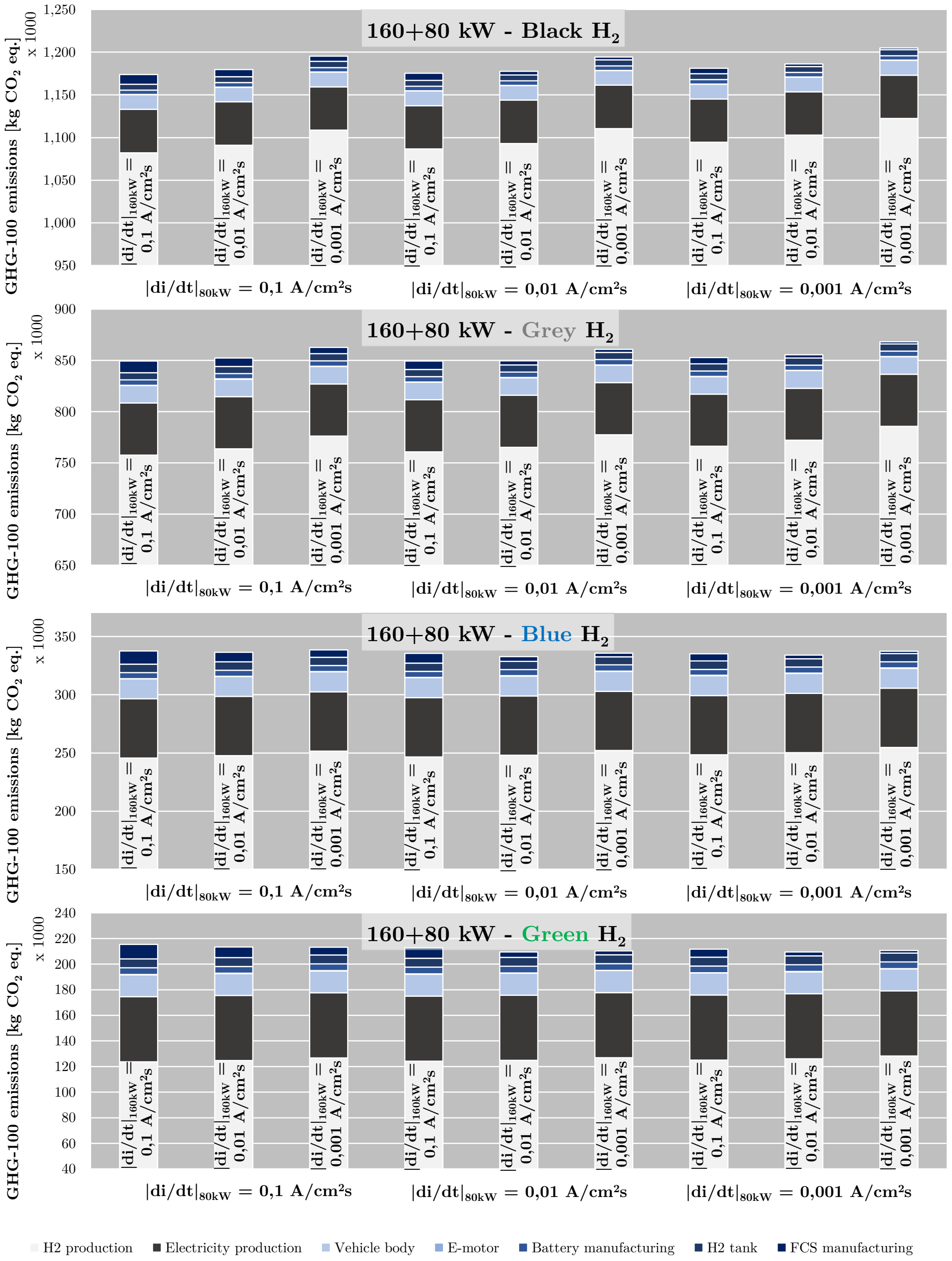

__Figure 5.10.__ Cradle-to-grave GHG-100 emissions of the heavy-duty multi-FCS architecture with the 160+180 kW configuration and different control dynamics considering __black__, grey, __blue__ and __green__ H_2. Functional unit is 1000000 km and 1 vehicle produced.

	$\|di/dt\|$ [A/cm^{2}s]								
160 kW	0.1	0.01	0.001	0.1	0.01	0.001	0.1	0.01	0.001
80 kW	0.1	0.1	0.1	0.01	0.01	0.01	0.001	0.001	0.001
	Ctg GHG-100 emissions [$\cdot$1000 kg CO_2 eq.]								
Black H_2	**1174**	1178	1194	1176	1178	1194	1183	1187	**1205**
Grey H_2	**849.4**	851.0	861.0	850.0	849.7	860.6	854.2	855.9	**868.1**
Blue H_2	**337.5**	335.0	336.6	336.0	**332.7**	335.3	336.5	334.2	337.3
Green H_2	**215.4**	212.0	211.6	213.5	**209.4**	210.0	213.0	209.9	210.7

Table 5.2. *Cradle-to-grave GHG-100 emissions of the 160+80 kW with* ***black****, grey,* ***blue*** *and* ***green*** *H_2. Optimum control with lowest cradle-to-grave emissions for each production pathway is highlighted in green while the worst control is in* ***red****. Functional unit is 1000000 km and 1 vehicle produced.*

Nevertheless, the case in which the 160 kW FCS is operated with moderate dynamics and the 80 kW one with low dynamics the situation changes. In this case, even thought the vehicle manufacturing emissions may rise since the durability of the 160 kW FC stack decreases, the H_2 consumption improves since the higher-power FCS is less constrained in terms of the rate of change of the current density, which implies that the rate of change of the FCS power output is greater. This makes the multi-FCS powertrain approach their optimum behavior due to the lower restriction in the dynamics and thus decrease H_2 consumption. As a consequence, the fuel production emissions are reduced more than the increase in the vehicle manufacturing emissions, resulting in a overall decrease in the cradle-to-grave emissions. Therefore, in this case the differentially controlled and sized powertrain may imply lower cradle-to-grave emissions than the 120+120 kW configuration. This trend and the opposite one discussed in the previous paragraph are common to all the H_2 production pathways but the difference between the designs is less significant the cleaner the H_2 production technology. Nevertheless, in all the cases the change in the cradle-to-grave emissions when considering the differential control and differential sizing strategies is below 0.2%. This is meaningful of the fact that these design methodologies may be important only if the difference in the manufacturing costs or emissions of the multiple FCS is large enough. This may happen when the costs and emissions do not scale linearly with the FCS power and when the technology of both FCS is significantly different. For example, if a SOFC system is used together with a PEMFC system to decrease the amount of rejected heat by the powertrain

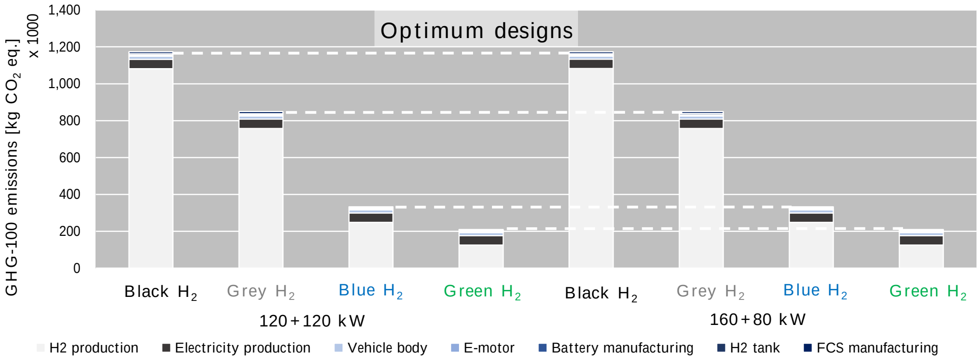

Figure 5.11. *Cradle-to-grave GHG-100 emissions of the optimum-control multi-FCS with the 120+120 kW configuration with **black**, grey, **blue** and **green** H_2. Functional unit is 1000000 km and 1 vehicle produced.*

(decrease the radiator size) and to use the high-temperature flows of the SOFC stack for other purposes. In this case, the dynamics and manufacturing costs and emissions of the two FCS are significantly different, hence differential control and sizing may bring benefits in terms of cradle-to-grave emissions. Other situation in which this may be interesting is for applications with lower lifetimes in which the fuel production cycle is less relevant. This would be the case of passenger car application, but the size of each FCS should be significantly smaller, given the lower power demand requirements of these vehicles.

Once the optimum dynamics for each production pathway and configuration are identified, the are gathered and presented in figure 5.11. Note that the cradle-to-grave emissions of each configuration and production pathway in this figure correspond to those highlighted in green in tables 5.1 and 5.2. As can be seen, the optimum designs for both the 120+120 kW and 160+80 kW configurations present similar cradle-to-grave GHG-100 emissions since they have both FCS operating with the same dynamics. When changing the H_2 production pathway the total cradle-to-grave emissions change, compared with the black H_2 case, by -28% with grey H_2, -72% with blue H_2 and -82% with green H_2. Therefore, as discussed in section 5.2.2 for passenger car application, the highest changes in the cradle-to-grave emissions are motivated by the change in the H_2 production pathway, being the rest of the effects due to changes in the control dynamics or the FCS sizing minor compared to it.

	$\lvert$di/dt$\rvert$ [A/cm^{2}s]								
120 kW	0.1	0.01	0.001	0.1	0.01	0.001	0.1	0.01	0.001
120 kW	0.1	0.1	0.1	0.01	0.01	0.01	0.001	0.001	0.001
	Ctg NO_X emissions [kg NO_X]								
Black H_2	1250	1249	1255	1249	1242	1251	1255	1241	**1265**
Grey H_2	**474.8**	468.2	465.7	468.2	457.4	458.0	465.7	458.0	460.1
Blue H_2	**583.0**	577.2	575.9	577.2	566.8	568.6	575.9	568.6	572.4
Green H_2	**285.7**	277.4	272.9	277.4	265.8	264.4	272.9	264.4	263.6

Table 5.3. *Cradle-to-grave NO_X emissions of the 120+120 kW with* ***black****, grey,* ***blue*** *and* ***green*** *H_2. Optimum control with lowest cradle-to-grave emissions for each production pathway is highlighted in green while the worst control is in* ***red****. Functional unit is 1000000 km and 1 vehicle produced.*

5.3.2 NO_X cradle-to-grave emissions of heavy-duty FCV

This section is analogous to section 5.3.1 but focused on NO_X. Since some of the trends are similar to those identified previously, the discussion is slightly simplified and mainly focused on the differences with respect to the GHG-100 results.

Figure 5.12 shows the change in the cradle-to-grave NO_X emissions for the 120+120 kW configuration with different control dynamics and H_2 production pathways. In this case, the vehicle manufacturing cycle NO_X emissions amounts to 3.9-6.1% for black H_2, 10.6-16.1% for grey H_2, 8.5-13.1% for blue H_2, and 18.6-26.8% for green H_2 of the cradle-to-grave emissions. As can be seen, the effect vehicle manufacturing cycle in the total emissions is much more relevant than for GHG-100 emissions since H_2 production is usually a low-NO_X emissions process, mainly coming from the electricity production, the combustion in SMR processes and the distribution of the H_2. As in the analysis for GHG-100 the lower limits of the previous intervals correspond to the cases with the lowest dynamics (high FC stack durability and low number of replacements) while their higher bound is representative of the high-dynamics cases (low FC stack durability and high number of replacements).

The results in figure 5.12 are compile in table 5.3 to improve the readability. The data presented in this table shows the total cradle-to-grave NO_X emissions for each control dynamics with the optimum case highlighted in green and the worst case in red. Differently from GHG-100, the vehicle manufacturing cycle is that important in terms of NO_X emissions that the optimum control

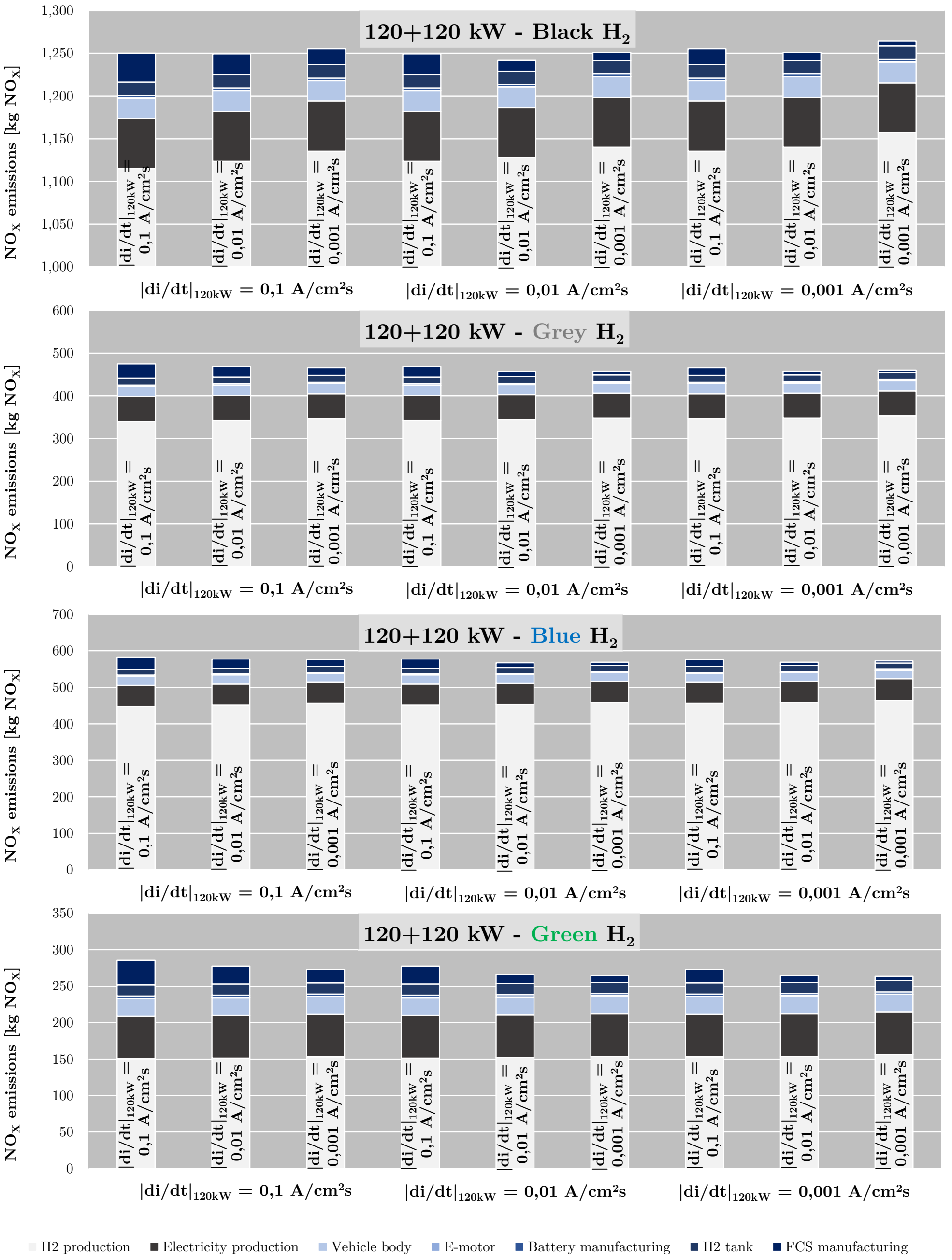

Figure 5.12. *Cradle-to-grave* NO_X *emissions of the heavy-duty multi-FCS architecture with the 120+120 kW configuration and different control dynamics considering* ***black****, grey,* ***blue*** *and* ***green*** H_2*. Functional unit is 1000000 km and 1 vehicle produced.*

dynamics for black and grey H_2 are no longer high-dynamics for both stacks. In this sense, the control dynamics for black, grey and blue H_2 is that with both FCS operating under moderate dynamics. This is caused by the relatively lower emission of the fuel production cycle compared to the vehicle manufacturing cycle in the when the emissions under analysis are NO_X instead of GHG-100. As can be seen, NO_X emissions for blue H_2 are higher than those for grey H_2 since the CCS process implies additional resource utilization and does not affect NO_X emissions. In contrast to the analysis focused on GHG-100 emissions, the control dynamics that minimize NO_X emissions for green H_2 are those maximizing the FC stack durability, i.e., both FCS operating under low-dynamics.

The worst cases for NO_X are the one with both FCS in low-dynamics for black H_2 since the emissions in the fuel production cycle are still low, and the cases with high-dynamics in both FCS for grey, blue and green H_2 since the NO_X emissions in the fuel production cycle become less sensitive to the control strategy than those in the vehicle manufacturing cycle. In this case, the different between the total cradle-to-grave NO_X emissions of the best and the worst control dynamics is 1.8% for black H_2, 3.8% for grey H_2, 2.9% for blue H_2, and 8.3% for green H_2.

The cradle-to-grave emissions of the 120+120 kW (figure 5.12) and the 160+80 kW (figure 5.13) configurations are very similar, particularly in the cases in which the dynamics of both FCS are identical. For both configurations, the fuel production cycle imply the 89.2-81.5% for black H_2, the 71.6-76.6% for grey H_2, the 76.9-81.2% for blue H_2, and the 52.7-59.2% for green H_2 of the total cradle-to-grave emissions. Note that, compared to GHG-100, the relevance of H_2 production on the cradle-to-grave emissions is significantly smaller. In the case of green H_2, the fuel production cycle implied a minimum of 81% of the total GHG-100 emissions while it falls to 52.7% for NO_X emissions. Similar decrease in the relevance of the fuel production cycle can be found with other H_2 production pathways (96.5% to 89.2% in the case of black H_2, for example).

The cradle-to-grave NO_X emissions of the optimum designs for the 160+80 kW configuration are slightly lower than those obtained with the 120+120 kW configuration since a higher-power FCS with the same dynamics restrictions in the current density allows higher changes in the power output for a given time window without penalizing significantly the FCS efficiency. Again, this change is small. Interestingly, one of the differential control strategies in the 160+80 kW configuration with grey H_2 (low dynamics for the 80 kW FC stack and moderate dynamics for the 160 kW one) presents

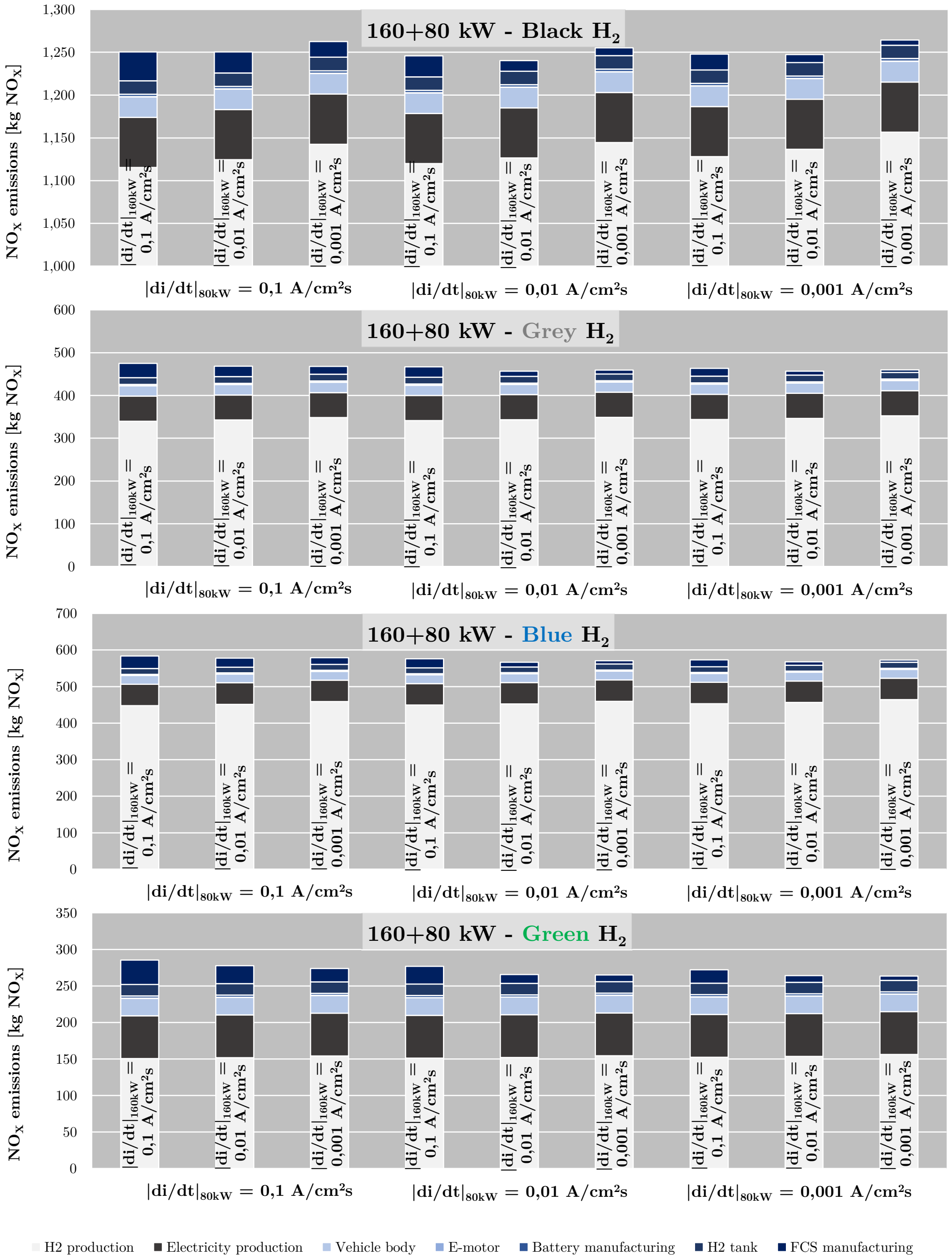

Figure 5.13. *Cradle-to-grave NO_X emissions of the heavy-duty multi-FCS architecture with the 160+80 kW configuration and different control dynamics considering* ***black****, grey,* ***blue*** *and* ***green*** *H_2. Functional unit is 1000000 km and 1 vehicle produced.*

	|di/dt| [A/cm²s]								
160 kW	0.1	0.01	0.001	0.1	0.01	0.001	0.1	0.01	0.001
80 kW	0.1	0.1	0.1	0.01	0.01	0.01	0.001	0.001	0.001
	Ctg NO_X emissions [kg NO_X]								
Black H_2	1250	1250	1261	1244	1240	1255	1248	1247	**1264**
Grey H_2	**474.9**	468.5	466.4	465.6	457.0	459.4	463.5	457.0	460.1
Blue H_2	**583.1**	577.6	577.3	574.3	566.3	570.5	573.0	567.3	572.3
Green H_2	**285.5**	277.5	272.4	275.4	265.6	265.0	271.9	264.0	263.6

Table 5.4. *Cradle-to-grave NO_X emissions of the 160+80 kW with* ***black****,* *grey,* ***blue*** *and* ***green*** *H_2. Optimum control with lowest cradle-to-grave emissions for each production pathway is highlighted in green while the worst control is in red. Functional unit is 1000000 km and 1 vehicle produced.*

the similar emissions to the optimum control dynamics. This is caused due to the aforementioned trade-off between fuel production cycle and vehicle manufacturing cycle. The evidence that the optimum control strategy for green H_2 are that with both FCS operating under low dynamics is indicative of the fact that if the H_2 production NO_X emissions are between those of grey and green H_2, the differential control and differential sizing could offer minimum emissions for the selected lifetime as well. Nonetheless, the benefit in NO_X emissions would be that small that most likely other factors such as the infrastructure cost of producing 2 different-size FCS assembly lines would outweigh this benefit, thus moving towards the design with 2 FCS with the same FC stack maximum output power.

Finally, the optimum control dynamics for each production pathway were compiled in figure 5.14, showing the effect of changing the production strategy of H_2 by comparing the optimum design cases. Therefore, according to figure 5.14, when changing the H_2 production pathway the variation in the total cradle-to-grave NO_X emissions, compared with the black H_2 case, by -63% with grey H_2, -54% with blue H_2 and -79% with green H_2. Again, the significant variation in the cradle-to-grave NO_X emissions with the production pathway indicates that this is the most significant factor affecting NO_X emissions and that the effect of any design strategy of the powertrain implies a second-order effect.

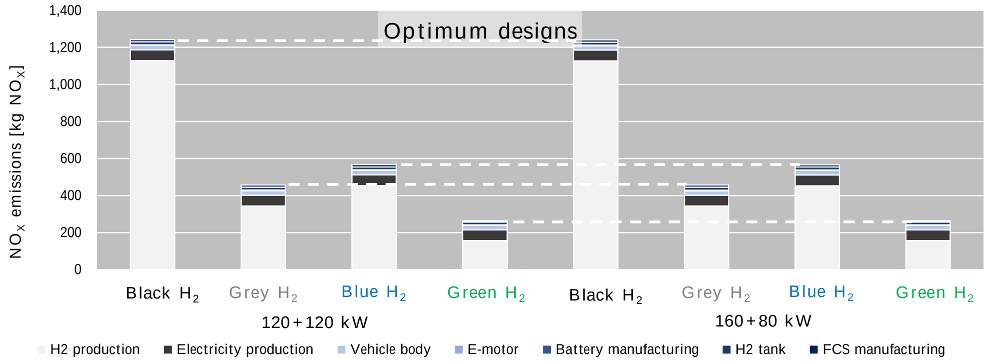

Figure 5.14. *Cradle-to-grave NO$_X$ emissions of the optimum-control multi-FCS with the 120+120 kW configuration with* ***black****,* ***grey****,* ***blue*** *and* ***green*** *H$_2$. Functional unit is 1000000 km and 1 vehicle produced.*

5.4 Summary and conclusions

Along this chapter, the cradle-to-grave GHG-100 and NO$_X$ emissions were evaluated with the LCA framework defined in section 3.8 and the results obtained in chapter 4 for passenger car application with the FCREx architecture (section 5.2) and heavy-duty vehicle application with multi-FCS configuration (section 5.3).

The conclusions that can be extracted for the passenger car application analysis are:

- Cradle-to-grave emissions were significantly affected by the H$_2$ production pathway. GHG-100 emissions increased by ~60% and ~36% with electrolysis from the EU mix and SMR without CCS compared to SMR with CCS (blue H$_2$). In this line, the total NO$_X$ emissions change by ~38% and ~ −6%.

- For both GHG-100 and NO$_X$ emissions, the vehicle manufacturing cycle was the origin of most of the cradle-to-grave emissions, although the fuel production cycle could also dominate the trend of the cradle-to-grave emissions depending on the fuel production pathway.

- With blue H$_2$, the vehicle manufacturing cycle dominated together with the fuel production cycle the evolution of the cradle-to-grave emissions when the battery capacity was changed but the trend in emissions when the FC stack maximum power varied was dominated by the fuel production cycle, except for NO_X emissions in the FCREx designs with 700 km of target range.

- Both cradle-to-grave GHG-100 and NO_X emissions may change up to 10% when comparing the best and worst designs among those considered in the design spaces.
- The optimum FCREx design should have a moderate-to-small battery capacity enough to cover an objective range only with the battery and a moderate-to-high FC stack maximum power. This contrasts with the optimum design in terms of performance and consumption, which had high battery capacity and high FC stack maximum power.
- The cradle-to-grave emissions of FCREx vehicles changed considerably with the design choice, the objective range and the H_2 production pathway. Hence, such emissions must be taken into consideration in the FCREx vehicle design process. With low-emission H_2 production pathways (blue or green), decreasing the battery capacity and limiting the FCREx target range might minimize the overall emissions as the vehicle manufacturing cycle becomes the dominating phase in the cradle-to-grave process. In this line, based on how the H_2 production infrastructure develops in the coming years, the optimal FCREx powertrain in terms of GHG-100 emissions may move towards moderate-to-high FC stack power and moderate-to-low battery capacity. This optimal design may indicate lower-than-BEV manufacturing costs and low but not minimum H_2 and total energy consumption.

As for the heavy-duty vehicle LCA, the main conclusions are:

- For most of the configurations and H_2 production pathways, the optimum dynamics had both FCS operating with the same rate of change in the current density.
- It was identified that depending on the H_2 production pathway, the optimum control dynamics minimizing the cradle-to-grave emissions changed since the relative importance of the fuel production cycle with respect to the vehicle manufacturing cycle changed. As such, it was possible to identify the optimum control dynamics for each production pathway in terms of both GHG-100 and NO_X emissions.
- As for the passenger car application, the H_2 production pathway was the factor influencing the most the cradle-to-grave emissions. Therefore, it

was determined that the powertrain design choices had a second-order effect on the total life cycle GHG-100 and NO_X emissions.

- The vehicles with 120+120 kW configuration showed similar GHG-100 and NO_X emissions to those with the 160+80 kW. Even though the 160+80 kW could be slightly superior depending on the H_2 production pathway and the lifetime, this implied that if both FCS were of the same technology (PEMFC) there would probably would be other factors such as the infrastructure development cost that would benefit the 120+120 kW configuration.

- The potential of the differential control and sizing design strategy could be when different technology was used for each FCS. For instance, combining a SOFC with a PEMFC FCS in the same powertrain. But it did not provided enough advantages in terms of cradle-to-grave emissions to make this architecture superior to the current trend of the industry.

- Finally, from these results, it was verified that the current trend of the industry of making the FCS modular with a fixed power specification may be optimum depending on the H_2 production pathway and the lifetime, and that considering differential control and sizing of the heavy-duty powertrain may imply additional complexity in the industry development without bringing significant benefits to the life cycle emissions. As such, the trend of the industry can be considered correct and the differential control and sizing disregarded unless several FCS with different FC technology are integrated in the same powertrain.

References

[1] Molina S., Novella R., Pla B. and Lopez-Juarez M. "Optimization and sizing of a fuel cell range extender vehicle for passenger car applications in driving cycle conditions". *Applied Energy*, Vol. 285 n^o December 2020, pp. 116469, 2021.

[2] Bradley Stephen, Ducrocq Jean, Gallarda Jean, Mineur Bernard, Ott Wolfgang, Ritter Andre and Brickell Philip. "Best available techniques for the co-production of hydrogen, carbon monoxide & their mixtures by steam reforming". Technical report, EUROPEAN INDUSTRIAL GASES ASSOCIATION AISBL, Brussels, 2013.

[3] Fuel Cells & Hydrogen (FCH). *Hydrogen Roadmap Europe - a Sustainable Pathway for the European Energy Transition.* Publications Office of the European Union, 1st edition, 2019.

Chapter 6

General conclusions and future work

Contents

6.1 Introduction

This last chapter is written with two main purposes. On one hand, the general conclusions of each of the results and discussion chapters (4 and 5) are gathered and summarized in section 6.2. On the other hand, the future work that was not included in this thesis because of being out of the scope and due to time constraints is described for each chapter in section 6.3 so that this thesis can become the basis to pave the way of the future research focused on FC technology applied to the transportation sector.

6.2 Conclusions

Along this thesis, the FC powerplant architectures for a passenger car and a heavy-duty vehicle application were analyzed and optimized in three different levels: FC stack and its interaction with the BoP (chapter 4, part 1, section 4.2), powertrain architecture (chapter 4, part 2, sections 4.3 and 4.4) and environmental impact of the vehicle (chapter 5). For that purpose, a complex FCV modeling framework was developed, integrating simulation tools capable of describing the FC stack, BoP and vehicle mechanical components behavior. These basic models were supplemented with a semi-empirical FC stack degradation model and an energy management optimizer algorithm so that the simulation framework could be used to predict the best performance of the powertrain and the FC stack degradation rate in driving cycle conditions. Two versions of this modeling platform were developed: one for a passenger car application and one for a heavy-duty vehicle application. The studies about the passenger car application aimed at understanding the potential benefits of the FCREx architecture for this particular application by considering different sizing for the FC stack, the battery and the H_2 tank, and different constraints in the control of the vehicle to further improve the durability of the stack. In contrast, the multi-FCS architecture coupled with differential control and sizing design strategies was considered for the heavy-duty application in order to understand whether this powertrain configuration could be further optimized, thus evaluating if the industry trend of modularizing the FCS to a fixed power specification is sub-optimum. The specific conclusions of each results chapter can be found in the following subsections.

6.2.1 Fuel Cell Electric Vehicle Powerplant Optimization

This chapter, divided into two parts, was focused on analyzing and optimizing the performance and durability of the novel FCV powerplant architectures in at different scales. The first part aimed at optimizing the FCS operation for both passenger car and heavy-duty vehicle applications so that for each value of current density, the BoP management, particularly the air management strategy, offered the higher FCS efficiency or net power. Analogously, the second part aimed at understanding how the FCREx architecture for passenger cars and the multi-FCS configuration for heavy-duty vehicle application could be further optimized by acting over the sizing of the components and imposing limits in the EMS to constrain the dynamics or the operating space of the FCS. These studies aimed at maximizing both performance and durability and at analyzing the trade-off between them.

The specific conclusions extracted from the first part of the study were:

- The optimum energy balance for both applications was identified and presented in figures 4.4 and 4.6. This energy balance included both the electrochemical power losses as well as the power consumption of the BoP components.
- Different operating regions were identified as a function of the current density. The highest-efficiency region was called medium-load region and it comprises the operating conditions under which the FC current density is within [0.04, 0.4] A/cm^2. It was expected that the EMS aimed at operating as much as possible withing this range of current density during driving cycle operation.
- The overall efficiency of the heavy-duty FCS was slightly lower than that for the passenger car application due to the higher pressure caused by the higher mass flow rates.
- The maximum efficiency of both FCS was slightly above 60%, in line with the state-of-the-art FCS net efficiency.

In the second part, the main conclusions extracted for the passenger car application were:

- Increasing the FC stack maximum power or the battery capacity decreased the H_2 consumption. Among these two sizing parameters, H_2 consumption was more sensitive to changes in the FC stack maximum power since it implied an increase in the efficiency when utilizing H_2, which is the form in which most of the energy in the vehicle is stored as.
- FCREx vehicle designs were compared against equivalent-in-range commercial FCV. This architecture could provide 16.8-25% lower H_2 consumption and up to 6.8% lower total energy consumption.
- The optimum FCREx design, only in terms of performance, should have high FC stack maximum output power and battery capacity. Nevertheless, since it may be prohibitive in cost, it was recommended to lower the battery capacity to around 30 kWh so that it can provide high-enough battery-only range without increasing significantly the manufacturing cost.

- High limitations in the dynamics or in the operation space of the FCS ($|di/dt|_{max}$=0.001 A/cm^{2}s or i_{min}=0.2 A/cm^2) were determined to be unpractical since they may not permit the fulfillment of the charge-sustained condition depending on the driving cycle.
- The combination of constraints $|di/dt|_{max}$=0.01 A/cm^{2}s and i_{min}=0.15 A/cm^2 was determined to be adequate since it offered the highest increase in durability without compromising the operation modes (110%) with an increase in H_2 consumption of 4.7%.
- It was determined that FCREx manufacturers should only apply constraints in the dynamics and operation space of the FCS to achieve a certain value of durability but refrain from further limiting the EMS since it will penalize significantly H_2 consumption.
- A change in the relevance of all the degradation sources was identified and presented depending on the constraints imposed in the EMS. This would serve to help FC stack manufacturers focus their work to improve durability depending on the expected FCS application.
- FC stack sizing had smaller impact the higher the dynamic restrictions, having it very small influence when the dynamics were constrained to low ($|di/dt|_{max}$=0.001 A/cm^{2}s).

Analogously, the conclusions extracted for the heavy-duty vehicle application were:

- For the particular driving pattern for heavy-duty vehicle (HDDT driving cycle), imposing low dynamics ($|di/dt|_{max}$=0.001 A/cm^{2}s) implied an increase in both H_2 consumption and durability of +3.8% and +471%, respectively. This dynamic restriction could be suitable for the heavy-duty application.
- Differential sizing was determined to be only practical when coupled with differential control since using the same control for both FCS implied similar H_2 consumption and durability, regardless of the relative sizing of both FCS.
- Differentially-sized powertrains offered the lowest H_2 consumption when the high-power FCS was operated with high dynamics.
- 160+80 kW design could offer 23% lower manufacturing costs/emissions with only an increase of 0.7% in the operation costs/emissions, compared to the 120+120 kW configuration.

6.2.2 Life cycle emissions optimization conclusions

Once the performance and durability of each powertrain was determined in chapter 4, this chapter was aimed at translating this data into the environmental impact, in terms of GHG-100 and NO_X emissions, of each technology with different H_2 production patways: electrolysis with energy from the EU mix (black H_2), SMR without CCS (grey H_2), SMR with CCS (blue H_2), and electrolysis from renewable energy sources (green H_2). Again, similar to the analysis, the conclusions can be divided into those for the passenger car application and those for the heavy-duty vehicle application. For the former, the specific conclusions are:

- The highest factor affecting cradle-to-grave emissions for both the passenger car and the heavy-duty vehicle application was the H_2 production pathway. For FCREx vehicles, GHG-100 and NO_X emissions could increase by ∼60% and ∼38% respectively when comparing black and blue H_2.
- The vehicle manufacturing cycle was responsible for a significant share of the cradle-to-grave emissions, particularly when low-emissions H_2 production pathways were considered (blue and green).
- With blue H_2, both GHG-100 and NO_X cradle-to-grave emissions may vary up to 10% when comparing the best and the worst configurations among those considered in the design spaces.
- Given the significant change in the cradle-to-grave emissions with the design choices and the H_2 production pathway, such emissions must be considered in the design process of any FCREx vehicle. With blue or green H_2, decreasing the battery capacity and limiting the FCREx target range could help minimize the total life cycle emissions since the vehicle manufacturing cycle becomes the dominating set of processes in the cradle-to-grave cycle.
- Depending on how the H_2 production infrastructure is developed in the coming years, the optimal FCREx powertrain in terms of emissions may change to moderate-to-high FC stack power and moderate-to-low battery capacity.

Similarly, for then heavy-duty vehicle application, the analysis of the multi-FCS architecture allowed to obtain the following conclusions:

- Most of the configurations offered the lowest emissions when both FCS had equal dynamics constraints with any H_2 production pathway.
- The optimum control dynamics for each H_2 production pathway minimizing GHG-100 and NO_X emissions was determined, since they varied significantly when the relative weight of the vehicle manufacturing cycle and the fuel production cycle on cradle-to-grave emissions changed.
- The 120+120 kW configuration offered similar cradle-to-grave emissions than the 160+80 kW architecture. Therefore, differential sizing and control was determined to be more relevant when different FC technology is used for each FCS (PEMFC+SOFC, for instance).
- It was identified that the tendency of the industry of designing fixed-power FCS and stack them for higher power application may be optimum since it this architecture is only overtaken by the differentially-sized configuration at very specific lifetime intervals depending on the H_2 production pathway with only a small advantage in terms of cradle-to-grave emissions.

6.3 Future work

The scope of any research work, such as the one contained in this thesis, is finite and constrained by the tools, the previous state-of-the-art and the timeframe. This makes possible, and even necessary, to identify and describe the activities that could not be carried out in the final report of any research work. This last section of this thesis serves the purpose of presenting the activities that could arise using this work as the baseline for future research. Given the structure of this thesis, they can be classified according to the optimization level of the FC technology, following the scales considered in chapters 4 and 5.

The activities related to the FCS management optimization could be complemented or further improved by considering the following research paths:

- Development of optimization methodologies for other FC technology such as high-temperature PEMFC or SOFC. For this purpose, it would be necessary to identify the requirements of the BoP for a these stacks depending on the transport or power generation application. Then, a sensitivity analysis should be carried out to identify which components of the FCS affect the most the net FCS efficiency, given a current density value. It is recommended to simplify and automatize the optimization process as much as possible so that it can be applied to different applications, as it was done in this thesis. For this reason, it is essential to identify the safety limits for the operation of the FCS with a each FC technology and minimize the number of components to be optimized .

- Design of BoP management strategies that could improve the FCS overall performance at extremely high values of current density. The state-of-the-art FC stacks may reach current densities close to 2 A/cm^2, for which the requirements in terms of mass flow rate could be different. As such, the optimum energy balance may be different and the design methodology for the BoP and its management should be refined.

- Analysis of the FCS performance decay at different altitudes for aerospace application. With this objective in mind, it would be necessary to use the FCS modeling platform developed in this thesis and change the pressure and temperature boundary conditions at the inlet and outlet of the system according to the ISA model in such a way that they replicate different altitude conditions. Then, the initial BoP air management strategy should be used to understand the fall in the FCS net power with altitude. Finally, the optimization of the BoP management should be carried out at each altitude to understand how it should be modified to preserve the maximum FCS efficiency, thus identifying the minimum decline in the FCS net power and comparing it with the case in which the BoP air management strategy is kept constant.

Along this thesis, the activities aimed at the optimization of the FC-based powertrains considered for the passenger car and heavy-duty vehicle applications could be further improved with the following research:

- The light-commercial vehicle (LCV) application could be considered as an additional road transport vehicle to integrate FC technology. The sizing study carried out in section 4.3.1 could be repeated for this particular application by just modifying the vehicle modeling platform and selecting an adequate and representative driving cycle. It is recommended to combine this sizing with the integration of dynamic constraints as in section 4.3.3 since the penetration of the FC technology in the LCV sector is expected in the short-to-medium term.

- Analysis of the use of different control strategies for several architectures by considering different variations in the state-of-charge of the battery per km. This would allow to understand the changes in both FC stack durability and vehicle total range when considering hybrid control strategies other than battery-only mode and FCREx modes.

- Application of the optimum architectures to captive fleets through holistic control strategies. This could consider not only the exchange of information between the different FCVs in the same fleet but the planned work routines, the routes of each vehicle and the global H_2 consumption of the fleet. In order to outline the advantages or disadvantages of FC technology in this application, the same vehicle fleet and operation should be simulated with BEV. This would enable the quantification of the operating costs of the fleet under different scenarios as well as the estimation of the minimum number of vehicles required to carry out a certain fleet operation routine, provided that the refueling duration of a FCV is lower than the charging time of a BEV.
- The sizing methodology should be adapted to other transport applications out of the road transport sector. Particularly to aerospace, maritime and railway application. In the case of aerospace application, the sizing methodology should consider the simulation of all the phases of a missions, particularly the take-off and the cruise. Cruise should be used to estimate a preliminary FC stack maximum power since it would require a steady power demand. For this purpose, the FCS optimization should be carried out at different altitude as mentioned before to minimize the FCS efficiency decay. Then, the take-off part should be simulated carefully to adjust the FC stack maximum power and size the battery, since the propulsion system will probably require additional power besides that provided by the FCS.
- The multi-FCS architecture for the heavy-duty vehicle application should be considered with different FC technology, primarily high-temperature PEMFC and SOFC stacks. This would provide a deeper insight on how complex FC-based powertrain architectures should be designed, and on whether differential control and sizing may bring advantages in terms of performance and durability.

Regarding the additional activities that could complement the LCA results in chapter 5, it is possible to identify the following ones:

- Development a parallel and analogous methodology to use the results of chapter 4 to carry out a TCO analysis and compare the results against the TCO of state-of-the-art equivalent FCVs and BEVs. This study should have the same structure as that in chapter 5 by considering the same H_2 production pathways as well as manufacturing processes, if possible.

- Identification of the H_2 mixes combining different production pathways according to the hydrogen roadmap [1] in several scenarios and application of such mixes to calculate the total cost and life cycle emissions of the FC technology applied to the transport sector from the current scenario until 2050. This could be done by applying the fuel production cycle emissions presented in section 3.8.4, and will be useful to identify when the FC technology would provide lower cradle-to-grave emissions than any other technology according to the hydrogen roadmap, similar to the research carried out in [2].

- Broadening of the LCA to other applications such as LCV or those in the aerospace sector (drone/short-range aircraft) and comparing their environmental impact with that of other technologies, including alternative FC stacks (high-temperature PEMFC and SOFC) and conventional propulsion systems such as ICE or batteries. Part of the future work described for the previous chapters must be carried out in order to make this activity possible and a more complex modeling platform should be developed, which implies that this activity would comprise the long-term horizon of the research line started in this thesis.

- Integration of the FCS replacement in the LCA for the passenger car application, not only by understanding the impact of replacing the FCS (manufacturing cycle) but also the effect on the H_2 consumed due to the performance decay (fuel production cycle).

The modeling platform developed in this thesis was planned from the beginning to be as flexible as possible so that it can be applied to most of the transport and power-generation applications. Therefore, since it may be updated and improved, the aforementioned future research work entail just a slight portion of the activities that could be developed by using this thesis as the basis to develop advanced FCV architectures and push forward the state-of-the-art of FC technology applied to the transport sector.

References

[1] Fuel Cells & Hydrogen (FCH). *Hydrogen Roadmap Europe - a Sustainable Pathway for the European Energy Transition.* Publications Office of the European Union, 1st edition, 2019.

[2] Desantes J. M., Molina S., Novella R. and Lopez-Juarez M. "Comparative global warming impact and NOX emissions of conventional and hydrogen automotive propulsion systems". *Energy Conversion and Management*, Vol. 221, pp. 113137, 2020.

References

Al-Qahtani Amjad, Parkinson Brett, Hellgardt Klaus, Shah Nilay and Guillen-Gosalbez Gonzalo.
Uncovering the true cost of hydrogen production routes using life cycle monetisation.
Applied Energy, Vol. 281, pp. 115958, 2021. (cited on p. 79)

Anselma Pier Giuseppe and Belingardi Giovanni.
Fuel cell electrified propulsion systems for long-haul heavy-duty trucks: present and future cost-oriented sizing.
Applied Energy, Vol. 321, 9 2022. (cited on p. 24)

Argonne National Laboratory.
Technology Assessment of a Fuel Cell Vehicle: 2017 Toyota Mirai Energy Systems Division.
US DOE -Energy Systems Division, 2017. (cited on pp. 20, 106)

Ballard.
Product Data Sheet - FCMove-HD, 2016. (cited on pp. xi, 49)

Ballard.
Product Data Sheet - FCVelocity-MD.
2016. (cited on pp. xi, 49)

Barbir Frano.
PEM Fuel Cells Theory and Practice Chapter 4 - Main Cell Components, Material Properties, and Processes.
2013. (cited on pp. 2, 67)

Benajes J., Antonio Garcia, Monsalve-Serrano Javier, Balloul Iyad and Pradel Gérard.
Evaluating the reactivity controlled compression ignition operating range limits in a high-compression ratio medium-duty diesel engine fueled with biodiesel and ethanol.
International Journal of Engine Research, Vol. 18, pp. 60–88, 02 2017. (cited on p. 15)

Benjamin Tom, Borup Rod, Garland Nancy, Gittleman Craig, Habibzadeh Bahman, Hirano Shinichi, Ho Donna, Kleen Greg, Kopasz John, Lakshmanan Balsu, Masten David, Mehall Mark, Myers Deborah, Onorato Shaun, Papageorgopoulos Dimitrios, Peterson David, Spendelow Jacob, Waldecker Jim, Wilson Adria and Zou Max.
U.S. DRIVE Fuel Cell Technical Team Roadmap, 2017. (cited on p. 62)

Bezmalinovic Dario, Simic Boris and Barbir Frano.
Characterization of PEM fuel cell degradation by polarization change curves.
Journal of Power Sources, Vol. 294, pp. 82–87, 2015. (cited on pp. vi, 71, 72)

Bhosale Amit C., Meenakshi S. and Ghosh Prakash C.
Root cause analysis of the degradation in a unitized regenerative fuel cell.
Journal of Power Sources, Vol. 343, pp. 275–283, 2017. (cited on p. 63)

Bi Wu and Fuller Thomas. F.
Temperature Effects on PEM Fuel Cells PtâC Catalyst Degradation.
Journal of The Electrochemical Society, Vol. 155 n^o 2, pp. B215, 2008. (cited on p. 68)

Boningari Thirupathi and Smirniotis Panagiotis G.
Impact of nitrogen oxides on the environment and human health: Mn-based materials for the NOx abatement.
Current Opinion in Chemical Engineering, Vol. 13 n^o x, pp. 133–141, 2016.
(cited on p. 78)

Borup Rod L., Davey John, Wood David, Garzon Fernando and Inbody Michael.
DOE Hydrogen Program FY 2005 Progress Report - VII.I.3 PEM Fuel Cell Durability.
Technical report, 2005. (cited on p. 69)

Bradley Stephen, Ducrocq Jean, Gallarda Jean, Mineur Bernard, Ott Wolfgang, Ritter Andre and Brickell Philip.
Best available techniques for the co-production of hydrogen, carbon monoxide & their mixtures by steam reforming.
Technical report, EUROPEAN INDUSTRIAL GASES ASSOCIATION AISBL, Brussels, 2013. (cited on p. 169)

Bressel Mathieu, Hilairet Mickael, Hissel Daniel and Ould Bouamama Belkacem.
Extended Kalman Filter for prognostic of Proton Exchange Membrane Fuel Cell.
Applied Energy, Vol. 164, pp. 220–227, 2016. (cited on p. 28)

Breuer Janos Lucian, Samsun Remzi Can, Stolten Detlef and Peters Ralf.
How to reduce the greenhouse gas emissions and air pollution caused by light and heavy duty vehicles with battery-electric, fuel cell-electric and catenary trucks.
Environment International, Vol. 152, 7 2021. (cited on p. 24)

Chen Ben, Cai Yonghua, Shen Jun, Tu Zhengkai and Chan Siew Hwa.
Performance degradation of a proton exchange membrane fuel cell with dead-ended cathode and anode.
Applied Thermal Engineering, Vol. 132, pp. 80–86, 2018. (cited on p. 26)

Chen Huicui, Song Zhen, Zhao Xin, Zhang Tong, Pei Pucheng and Liang Chen.
A review of durability test protocols of the proton exchange membrane fuel cells for vehicle.
Applied Energy, Vol. 224 n^o April, pp. 289–299, 2018. (cited on p. 27)

Chen Kui, Laghrouche Salah and Djerdir Abdesslem.
Degradation model of proton exchange membrane fuel cell based on a novel hybrid method.
Applied Energy, Vol. 252 n^o May, pp. 113439, 2019. (cited on p. 28)

Cheng Fangwei, Porter Michael D. and Colosi Lisa M.
Is hydrothermal treatment coupled with carbon capture and storage an energy-producing negative emissions technology?
Energy Conversion and Management, Vol. 203 n^o August 2019, pp. 112252, 2020.
(cited on p. 78)

Cherevko Serhiy, Kulyk Nadiia and Mayrhofer Karl J.J.
Durability of platinum-based fuel cell electrocatalysts: Dissolution of bulk and nanoscale platinum.
Nano Energy, Vol. 29, pp. 275–298, 2016. (cited on p. 26)

Choi Wonjae and Song Han Ho.
Well-to-wheel greenhouse gas emissions of battery electric vehicles in countries dependent on the import of fuels through maritime transportation: A South Korean case study.
Applied Energy, Vol. 230 n^o August, pp. 135–147, 2018. (cited on p. 78)

Corbo P., Migliardini F. and Veneri O.
Experimental analysis of a 20 kWe PEM fuel cell system in dynamic conditions representative of automotive applications.
Energy Conversion and Management, Vol. 49 n^o 10, pp. 2688–2697, 2008. (cited on pp. 42, 46)

Corbo Pasquale, Migliardini Fortunato and Veneri Ottorino.
Experimental analysis and management issues of a hydrogen fuel cell system for stationary and mobile application.
Energy Conversion and Management, Vol. 48 n^o 8, pp. 2365–2374, 2007. (cited on pp. 42, 43, 46)

Council of European Energy Regulators (CEER).
CEER Report on Power Losses.
Technical report, 2017. (cited on p. 79)

Database EV.
Kia e-Niro 64 kW (2020-2022) price and specifications, 2022. (cited on p. 108)

de las Nieves Camacho María, Jurburg Daniel and Tanco Martín.
Hydrogen fuel cell heavy-duty trucks: Review of main research topics.
International Journal of Hydrogen Energy, 7 2022. (cited on p. 23)

Desantes J. M., Molina S., Novella R. and Lopez-Juarez M.
Comparative global warming impact and NOX emissions of conventional and hydrogen automotive propulsion systems.
Energy Conversion and Management, Vol. 221, pp. 113137, 2020. (cited on pp. 16, 21, 75, 201)

Desantes J.M., Novella R., Pla B. and Lopez-Juarez M.
Impact of fuel cell range extender powertrain design on greenhouse gases and NOX emissions in automotive applications.
Applied Energy, Vol. 302, pp. 117526, 2021. (cited on pp. 2, 105, 134)

Desantes J.M., Novella R., Pla B. and Lopez-Juarez M.
Effect of dynamic and operational restrictions in the energy management strategy on fuel cell range extender electric vehicle performance and durability in driving conditions.
Energy Conversion and Management, Vol. 266, pp. 115821, 2022. (cited on p. 105)

Desantes J.M., Novella R., Pla B. and Lopez-Juarez M.
A modeling framework for predicting the effect of the operating conditions and component sizing on fuel cell degradation and performance for automotive applications.
Applied Energy, Vol. 317, pp. 119137, 2022. (cited on pp. 58, 105)

DoE - Department of Energy.
DOE Technical Targets for Polymer Electrolyte Membrane Fuel Cell Components. (cited on pp. 60, 136)

Dutta M, Jia N, Lu S, Colbow V and Wessel S.
Effects of Upper Potential Dwell Time, Transients and Relative Humidity on PEM Fuel Cell Cathode Catalyst Degradation.
The Electrochemical Society 217th Meeting (c), 2010. (cited on pp. vi, 69, 70, 71)

Emmanuel Balogun O., Barendse Paul and Chamier Jessica.
Effect of Anode Stoichiometry and Back Pressure on the Performance of PEMFCs.
In *2018 IEEE PES/IAS PowerAfrica*, pp. 1–6, 2018. (cited on p. 93)

Europe Hyundai Motor.
Hyundai KONA Electric Features, 2022. (cited on p. 108)

European Commission.
A hydrogen strategy for a climate-neutral Europe, 2020. (cited on p. 6)

European Parliament.
European Parliament resolution of 15 January 2020 on the European Green Deal (2019/2956(RSP)), 2020. (cited on p. 6)

European Environmental Agency (EEA).
Overview of electricity production and use in Europe - Indicator Assessment, 2018. (cited on p. 79)

Feng Yanbiao and Dong Zuomin.
Integrated design and control optimization of fuel cell hybrid mining truck with minimized lifecycle cost.
Applied Energy, Vol. 270 n^o March, pp. 115164, 2020. (cited on pp. 23, 24, 64)

Feroldi Diego and Carignano Mauro.
Sizing for fuel cell/supercapacitor hybrid vehicles based on stochastic driving cycles.
Applied Energy, Vol. 183, pp. 645–658, 2016. (cited on p. 22)

Fuel Cells & Hydrogen (FCH).
Hydrogen Roadmap Europe - a Sustainable Pathway for the European Energy Transition.
Publications Office of the European Union, 1st edition, 2019.
(cited on pp. 6, 14, 15, 16, 23, 177, 201)

FuelCellsWorks.
World's first fuel cell heavy-duty truck, Hyundai XCIENT Fuel Cell, heads to Europe for commercial use, 2020. (cited on pp. xi, 49, 51, 94)

Futter Georg A., Latz Arnulf and Jahnke Thomas.
Physical modeling of chemical membrane degradation in polymer electrolyte membrane fuel cells: Influence of pressure, relative humidity and cell voltage.
Journal of Power Sources, Vol. 410-411 n^o November 2018, pp. 78–90, 2019.
(cited on p. 29)

Gaikwad Shrihari D. and Ghosh Prakash C.
Sizing of a fuel cell electric vehicle: A pinch analysis-based approach.
International Journal of Hydrogen Energy, Vol. 45 n^o 15, pp. 8985–8993, 2020.
(cited on p. 23)

García Antonio, Monsalve-Serrano Javier, José Sanchís Enrique and Fogué-Robles Álvaro.
Exploration of suitable injector configuration for dual-mode dual-fuel engine with diesel and OMEx as high reactivity fuels.
Fuel, Vol. 280, pp. 118670, 2020. (cited on p. 15)

García Antonio, Monsalve-Serrano Javier, Villalta D., Lago Sari Rafael, Gordillo Zavaleta Victor and Gaillard Patrick.
Potential of e-Fischer Tropsch diesel and oxymethyl-ether (OMEx) as fuels for the dual-mode dual-fuel concept.
Applied Energy, Vol. 253, pp. 113622, 2019. (cited on p. 15)

Garland Nancy, Benjamin Thomas and Kopasz John.
DOE Fuel Cell Program: Durability Technical Targets and Testing Protocols.
ECS - The Electrochemical Society, ECS Transactions, Vol. 11 n^o 1, pp. 923, 2007. (cited on pp. 57, 67)

Gordon Meghan and Weber Maya.
Global energy demand to grow 47top, 10 2021. (cited on pp. v, 3)

Hu Zunyan, Li Jianqiu, Xu Liangfei, Song Ziyou, Fang Chuan, Ouyang Minggao, Dou Guowei and Kou Gaihong.
Multi-objective energy management optimization and parameter sizing for proton exchange membrane hybrid fuel cell vehicles.
Energy Conversion and Management, Vol. 129, pp. 108–121, 2016. (cited on pp. 23, 27, 60, 64)

Hu Zunyan, Xu Liangfei, Huang Yiyuan, Li Jianqiu, Ouyang Minggao, Du Xiaoli and Jiang Hongliang.
Comprehensive analysis of galvanostatic charge method for fuel cell degradation diagnosis.
Applied Energy, Vol. 212 n^o October 2017, pp. 1321–1332, 2018. (cited on p. 63)

Hyundai.
Hyundai Nexo - Technical Specifications. (cited on pp. 48, 106, 108)

Ilio G. Di, Giorgio P. Di, Tribioli L., Bella G. and Jannelli E.
Preliminary design of a fuel cell/battery hybrid powertrain for a heavy-duty yard truck for port logistics.
Energy Conversion and Management, Vol. 243, 9 2021. (cited on p. 25)

International Council Of Clean Transportation.
Vision 2050: A strategy to decarbonize the global transport sector by mid-century, 2020. (cited on pp. v, 4, 5)

International Energy Agency.
Africa Energy Outlook 2019 World Energy Outlook Special Report. (cited on p. 3)

International Energy Agency.
Technology Roadmap Hydrogen and Fuel Cells. (cited on pp. v, 3, 4)

International Energy Agency.
Net Zero by 2050 - A Roadmap for the Global Energy Sector, 2021. (cited on pp. v, 6, 7)

International Energy Agency.
The Future of Hydrogen.
Technical Report June, 2019. (cited on pp. 14, 16, 20)

IPCC.
Climate Change 2014.
Technical report, Cambridge, 2015. (cited on p. 78)

IPCC.
Special report: global warming of 1.5 °C - Summary for Policymakers, 6 2018. (cited on p. 4)

Jha Mayank Shekhar, Bressel Mathieu, Ould-Bouamama Belkacem and Dauphin-Tanguy Genevieve.
Particle filter based hybrid prognostics of proton exchange membrane fuel cell in bond graph framework.
Computers and Chemical Engineering, Vol. 95, pp. 216–230, 2016. (cited on p. 28)

Jia Nengyou, Dutta Monica, Lu Suzy and Colbow Vesna.
Voltage Degradation Associated with Operational Conditions: Upper Potential and Lower Potential Limits.
Journal of The Electrochemical Society, pp. 2–3, 2009. (cited on pp. v, 69)

Kangasniemi K. H., Condit D. A. and Jarvi T. D.
Characterization of Vulcan Electrochemically Oxidized under Simulated PEM Fuel Cell Conditions.
Journal of The Electrochemical Society, Vol. 151 n^o 4, pp. E125, 2004. (cited on p. 63)

Keoleian Gregory, Miller Shelie, Kleine Robert De, Fang Andrew and Mosley Janet.
Life Cycle Material Data Update for GREET Model - Report No. CSS12-12.
Technical report, 2012. (cited on p. 80)

Knights S.
Polymer Electrolyte Membrane and Direct Methanol Fuel Cell Technology: 6 - Operation and durability of low temperature fuel cells.
Woodhead Publishing Limited, 2012. (cited on pp. v, vi, 41, 63, 64, 68, 69, 71)

Kregar Ambrož, Tavčar Gregor, Kravos Andraž and Katrašnik Tomaž.
Predictive system-level modeling framework for transient operation and cathode platinum degradation of high temperature proton exchange membrane fuel cells â.
Applied Energy, Vol. 263 n^o February, pp. 114547, 2020. (cited on p. 29)

Kusoglu Ahmet, Calabrese Michelle and Weber Adam Z.
Effect of mechanical compression on chemical degradation of Nafion membranes.
ECS Electrochemistry Letters, Vol. 3 n^o 5, 2014. (cited on p. 62)

Kwon Jun Hwa, Jo Seunghyun, Cho Ki Yeop and Eom Kwang Sup.
Deconvolution of the dehydration degradation mechanism in polymer electrolyte membrane fuel cells using electrochemical impedance analysis combined with the transmission line model under low humidity.
Journal of Power Sources, Vol. 473 n^o March, pp. 228587, 2020. (cited on p. 29)

Lane Blake, Shaffer Brendan and Samuelsen Scott.
A comparison of alternative vehicle fueling infrastructure scenarios.
Applied Energy, Vol. 259 n^o June 2019, pp. 114128, 2020. (cited on p. 21)

Lee Dong Yeon, Elgowainy Amgad, Kotz Andrew, Vijayagopal Ram and Marcinkoski Jason.
Life-cycle implications of hydrogen fuel cell electric vehicle technology for medium- and heavy-duty trucks.
Journal of Power Sources, Vol. 393, pp. 217–229, 7 2018. (cited on p. 24)

Li Huan, Ravey Alexandre, N'Diaye Abdoul and Djerdir Abdesslem.
Online adaptive equivalent consumption minimization strategy for fuel cell hybrid electric vehicle considering power sources degradation.
Energy Conversion and Management, Vol. 192 n^o March, pp. 133–149, 2019.
(cited on p. 26)

Li Yunqi, Chen Xiran, Liu Yuwei, Xiong Danping, Li Jing, Yin Sha, Chen Liang, Li Congxin and Xu Jun.
Analytical modeling framework for performance degradation of PEM fuel cells during startup-shutdown cycles.
RSC Advances, Vol. 10 n^o 4, pp. 2216–2226, 2020. (cited on pp. 29, 70)

Liu Feiqi, Mauzerall Denise L., Zhao Fuquan and Hao Han.
Deployment of fuel cell vehicles in China: Greenhouse gas emission reductions from converting the heavy-duty truck fleet from diesel and natural gas to hydrogen.
International Journal of Hydrogen Energy, Vol. 46, pp. 17982–17997, 5 2021.
(cited on p. 24)

Lu Languang, Ouyang Minggao, Huang Haiyan, Pei Pucheng and Yang Fuyuan.
A semi-empirical voltage degradation model for a low-pressure proton exchange membrane fuel cell stack under bus city driving cycles.
Journal of Power Sources, Vol. 164 n^o 1, pp. 306–314, 2007.
(cited on pp. vi, 27, 28, 60, 74)

Lü Xueqin, Wang Peisong, Meng Lingzheng and Chen Chao.
Energy optimization of logistics transport vehicle driven by fuel cell hybrid power system.
Energy Conversion and Management, Vol. 199 n^o June, pp. 111887, 2019.
(cited on pp. 22, 104)

Luján Jose Manuel, Guardiola Carlos, Pla Benjamín and Reig Alberto.
Cost of ownership-efficient hybrid electric vehicle powertrain sizing for multi-scenario driving cycles.
Proceedings of the Institution of Mechanical Engineers, Part D: Journal of Automobile Engineering, Vol. 230 n^o 3, pp. 382–394, 2016. (cited on p. 50)

Ma Rui, Yang Tao, Breaz Elena, Li Zhongliang, Briois Pascal and Gao Fei.
Data-driven proton exchange membrane fuel cell degradation predication through deep learning method.
Applied Energy, Vol. 231 n^o July, pp. 102–115, 2018. (cited on p. 28)

Marocco Paolo, Sundseth Kyrre, Aarhaug Thor, Lanzini Andrea, Santarelli Massimo, Barnett Alejandro Oyarce and Thomassen Magnus.
Online measurements of fluoride ions in proton exchange membrane water electrolysis through ion chromatography.
Journal of Power Sources, Vol. 483 n^o October 2020, pp. 229179, 2021. (cited on p. 62)

Mathias Mark F., Makharia Rohit, Gasteiger Hubert A., Conley Jason J., Fuller Timothy J., Gittleman Craig J., Kocha Shyam S., Miller Daniel P., Mittelsteadt Corky K., Xie Tao, Van Susan G. and Yu Paul T.
Two fuel cell cars in every garage?
Electrochemical Society Interface, Vol. 14 n^o 3, pp. 24–35, 2005. (cited on p. 69)

McKinsey.
A portfolio of power-trains for Europe: a fact-based analysis - The role of Battery Electric Vehicles, Plug-in Hybrids and Fuel Cell Electric Vehicles.
Technical report, 2020. (cited on p. 25)

Ministerio para la Transición Ecológica y el Reto Demográfico (MITERD).
Hoja de Ruta del Hidrógeno: Una apuesta por el hidrógeno renovable, 2020. (cited on p. 6)

Moein-Jahromi M. and Kermani M. J.
Three-dimensional multiphase simulation and multi-objective optimization of PEM fuel cells degradation under automotive cyclic loads.
Energy Conversion and Management, Vol. 231 n^o February, pp. 113837, 2021.
(cited on p. 26)

Molina S., Novella R., Pla B. and Lopez-Juarez M.
Optimization and sizing of a fuel cell range extender vehicle for passenger car applications in driving cycle conditions.
Applied Energy, Vol. 285 n^o December 2020, pp. 116469, 2021.
(cited on pp. 59, 60, 105, 134, 139, 168)

Murschenhofer Dominik, Kuzdas Dominik, Braun Stefan and Jakubek Stefan.
A real-time capable quasi-2D proton exchange membrane fuel cell model.
Energy Conversion and Management, Vol. 162 n^o January, pp. 159–175, 2018.
(cited on p. 41)

Notter Dominic A., Kouravelou Katerina, Karachalios Theodoros, Daletou Maria K. and Haberland Nara Tudela.
Life cycle assessment of PEM FC applications: Electric mobility and μ-CHP.
Energy and Environmental Science, Vol. 8 n^o 7, pp. 1969–1985, 2015. (cited on p. 80)

Obnamia Jon Albert, Dias Goretty M., MacLean Heather L. and Saville Bradley A.
Comparison of U.S. Midwest corn stover ethanol greenhouse gas emissions from GREET and GHGenius.
Applied Energy, Vol. 235 n^o October 2018, pp. 591–601, 2019. (cited on p. 78)

Office of energy efficiency and renewable energy - Department of Energy.
Durability Working Group - Hydrogen and Fuel Cell Technologies Office. (cited on pp. 25, 75)

Onori Simona, Serrao Lorenzo and Rizzoni Giorgio.
Hybrid electric vehicles: Energy management strategies.
Springer, 2016. (cited on pp. 50, 54)

Ou Mingyang, Zhang Ruofan, Shao Zhifang, Li Bing, Yang Daijun, Ming Pingwen and Zhang Cunman.
A novel approach based on semi-empirical model for degradation prediction of fuel cells.
Journal of Power Sources, Vol. 488 n^o December 2020, pp. 229435, 2021. (cited on p. 28)

Pan Tianyao, Shen Jiong, Sun Li and Lee Kwang Y.
Thermodynamic modelling and intelligent control of fuel cell anode purge.
Applied Thermal Engineering, Vol. 154 n^o March, pp. 196–207, 2019. (cited on p. 25)

Pei Pucheng, Chang Qianfei and Tang Tian.
A quick evaluating method for automotive fuel cell lifetime.
International Journal of Hydrogen Energy, Vol. 33 n^o 14, pp. 3829–3836, 2008.
(cited on pp. vi, 27, 28, 60, 61, 73, 74, 76)

Peng Fei, Zhao Yuanzhe, Chen Ting, Zhang Xuexia, Chen Weirong, Zhou Donghua and Li Qi.
Development of robust suboptimal real-time power sharing strategy for modern fuel cell based hybrid tramways considering operational uncertainties and performance degradation.
Applied Energy, Vol. 226 n^o April, pp. 503–521, 2018. (cited on pp. 27, 60)

Pourabdollah M., Egardt B., Murgovski N. and Grauers A.
Convex Optimization Methods for Powertrain Sizing of Electrified Vehicles by Using Different Levels of Modeling Details.
IEEE Transactions on Vehicular Technology, Vol. 67 n^o 3, pp. 1881–1893, 2018.
(cited on p. 22)

Qin Yanzhou, Liu Guokun, Chang Yafei and Du Qing.
Modeling and design of PEM fuel cell stack based on a flow network method.
Applied Thermal Engineering, Vol. 144 n^o August, pp. 411–423, 2018. (cited on p. 25)

Rabbani R. A.
Dynamic Performance of a PEM Fuel Cell System.
DTU Mechanical Engineering. DCAMM Special Report, n^o No. S154, 2013.
(cited on p. 46)

ROTREX.
Rotrex EK10AA Fuel Cell Compressor Technical Datasheet. (cited on p. 101)

Sciarretta Antonio and Guzzella Lino.
Control of hybrid electric vehicles.
IEEE Control Systems Magazine, Vol. 27 n^o 2, pp. 60–70, 2007. (cited on p. 50)

Serrao Lorenzo, Onori Simona and Rizzoni Giorgio.
ECMS as a realization of Pontryagin's minimum principle for HEV control.
In *2009 American control conference*, pp. 3964–3969. IEEE, 2009. (cited on p. 54)

Sherwood Steven C., Dixit Vishal and Salomez Chryséis.
The global warming potential of near-surface emitted water vapour.
Environmental Research Letters, Vol. 13 n^o 10, pp. 104006, 2018. (cited on p. 81)

Shi Shouwen, Sun Xiaoyi, Lin Qiang, Chen Jian, Fu Yuanjie, Hong Xiaodong, Li Cong, Guo Xiang, Chen Gang and Chen Xu.
Fatigue crack propagation behavior of fuel cell membranes after chemical degradation.
International Journal of Hydrogen Energy, Vol. 45 n^o 51, pp. 27653–27664, 2020.
(cited on p. 26)

Sim Kyuhyun, Vijayagopal Ram, Kim Namdoo and Rousseau Aymeric.
Optimization of component sizing for a fuel cell-powered truck to minimize ownership cost.
Energies, Vol. 12 n^o 6, 2019. (cited on pp. 24, 104)

Song Ke, Chen Huan, Wen Peimin, Zhang Tao, Zhang Boqiang and Zhang Tong.
A comprehensive evaluation framework to evaluate energy management strategies of fuel cell electric vehicles.
Electrochimica Acta, Vol. 292, pp. 960–973, 2018. (cited on p. 60)

Song Ke, Wang Xiaodi, Li Feiqiang, Sorrentino Marco and Zheng Bailin.
Pontryagin's minimum principle-based real-time energy management strategy for fuel cell hybrid electric vehicle considering both fuel economy and power source durability.
Energy, Vol. 205, pp. 118064, 2020. (cited on pp. 27, 60)

Sun Zhendong, Wang Yujie, Chen Zonghai and Li Xiyun.
Min-max game based energy management strategy for fuel cell/supercapacitor hybrid electric vehicles.
Applied Energy, Vol. 267, pp. 115086, 2020. (cited on pp. 20, 27, 60)

Teng Teng, Zhang Xin, Dong Han and Xue Qicheng.
A comprehensive review of energy management optimization strategies for fuel cell passenger vehicle.
International Journal of Hydrogen Energy, Vol. 45 n^o 39, 2020. (cited on pp. 19, 47)

Terada Ichiro and Nakagawa Hideki.
Polymer Electrolyte Fuel Cell.
Kobunshi, Vol. 57 n^o 7, pp. 498–501, 2008. (cited on pp. 26, 40, 67)

Tsotridis Georgios, Pilenga Alberto, Marco Giancarlo De and Malkow Thomas.
EU Harmonised Test Protocols for PEMFC MEA Testing in Single Cell Configuration for Automotive Applications: JRC Science for Policy report.
Technical report, European Commission, JRC Science for Policy report, 2015. (cited on p. 57)

United Nations.
World population projected to reach 9.8 billion in 2050, and 11.2 billion in 2100, 2017. (cited on p. 3)

U.S. Energy Information Administration.
International Energy Outlook 2021, 10 2021. (cited on pp. v, 3)

U.S. Department Of Energy.
DOE Technical Targets for Fuel Cell Systems and Stacks for Transportation Applications, 2015. (cited on pp. xi, 49)

U.S. Department Of Energy.
DOE Technical Targets for Onboard Hydrogen Storage for Light-Duty Vehicles, 2015. (cited on pp. xi, 49)

Verhelst Sebastian and Wallner Thomas.
Hydrogen-fueled internal combustion engines.
Progress in Energy and Combustion Science, Vol. 35 n^o 6, pp. 490–527, 2009. (cited on p. 14)

Wikner Evelina and Thiringer Torbjörn.
Extending battery lifetime by avoiding high SOC.
Applied Sciences (Switzerland), Vol. 8 n^o 10, 2018. (cited on p. 20)

Wu Jinfeng, Yuan Xiao Zi, Martin Jonathan J., Wang Haijiang, Zhang Jiujun, Shen Jun, Wu Shaohong and Merida Walter.
A review of PEM fuel cell durability: Degradation mechanisms and mitigation strategies.
Journal of Power Sources, Vol. 184 n^o 1, pp. 104–119, 2008. (cited on p. 70)

Wu Xiaohua, Hu Xiaosong, Yin Xiaofeng, Li Lei, Zeng Zhaowei and Pickert Volker.
Convex programming energy management and components sizing of a plug-in fuel cell urban logistics vehicle.
Journal of Power Sources, Vol. 423 n^o March, pp. 358–366, 2019. (cited on pp. 22, 23, 78)

Wu Xiaohua, Hu Xiaosong, Yin Xiaofeng, Peng Yiqiang and Pickert Volker.
Convex programming improved online power management in a range extended fuel cell electric truck.
Journal of Power Sources, Vol. 476 n^o 2019, pp. 228642, 2020. (cited on p. 23)

Xu Liangfei, Mueller Clemens David, Li Jianqiu, Ouyang Minggao and Hu Zunyan.
Multi-objective component sizing based on optimal energy management strategy of fuel cell electric vehicles.
Applied Energy, Vol. 157, pp. 664–674, 2015. (cited on pp. 22, 104)

Xu Liangfei, Ouyang Minggao, Li Jianqiu, Yang Fuyuan, Lu Languang and Hua Jianfeng.
Optimal sizing of plug-in fuel cell electric vehicles using models of vehicle performance and system cost.
Applied Energy, Vol. 103, pp. 477–487, 2013. (cited on p. 22)

Yan Jianjun and Zhao Jia.
Willingness to pay for heavy-duty hydrogen fuel cell trucks and factors affecting the purchase choices in China.
International Journal of Hydrogen Energy, 2022. (cited on p. 23)

Yuan Xiao Zi, Nayoze-Coynel Christine, Shaigan Nima, Fisher David, Zhao Nana, Zamel Nada, Gazdzicki Pawel, Ulsh Michael, Friedrich Kaspar Andreas, Girard Francois and Groos Ulf.
A review of functions, attributes, properties and measurements for the quality control of proton exchange membrane fuel cell components.
Journal of Power Sources, Vol. 491 n^o January, pp. 229540, 2021. (cited on p. 26)

Zawodzinski Thomas A., Springer Thomas E., Davey John, Jestel Roger, Lopez Cruz, Valerio Judith and Gottesfeld Shimshon.
A Comparative Study of Water Uptake By and Transport Through Ionomeric Fuel Cell Membranes.
Journal of The Electrochemical Society, Vol. 140 n^o 7, pp. 1981–1985, 1993.
(cited on p. 67)

Zhang Hongtao, Li Xianguo, Liu Xinzhi and Yan Jinyue.
Enhancing fuel cell durability for fuel cell plug-in hybrid electric vehicles through strategic power management.
Applied Energy, Vol. 241 n^o January, pp. 483–490, 2019. (cited on p. 20)

Zhang Jianlu, Tang Yanghua, Song Chaojie, Xia Zetao, Li Hui, Wang Haijiang and Zhang Jiujun.
PEM fuel cell relative humidity (RH) and its effect on performance at high temperatures.
Electrochimica Acta, Vol. 53, pp. 5315–5321, 6 2008. (cited on p. 94)

Zhao Jian and Li Xianguo.
A review of polymer electrolyte membrane fuel cell durability for vehicular applications: Degradation modes and experimental techniques.
Energy Conversion and Management, Vol. 199 n^o September 2019, pp. 112022, 2019.
(cited on p. 66)

Zheng Weibo, Xu Liangfei, Hu Zunyan, Ding Yujie, Li Jianqiu and Ouyang Minggao.
Dynamic modeling of chemical membrane degradation in polymer electrolyte fuel cells: Effect of pinhole formation.
Journal of Power Sources, Vol. 487 n^o December 2020, pp. 229367, 2021. (cited on p. 26)

Zhou Yue, Obeid Hussein, Laghrouche Salah, Hilairet Mickael and Djerdir Abdesslem.
A novel second-order sliding mode control of hybrid fuel cell/super capacitors power system considering the degradation of the fuel cell.
Energy Conversion and Management, Vol. 229 n^o September 2020, pp. 113766, 2021.
(cited on p. 28)